JACOBS UNIVERSITY

The circulation and distribution of heat within Warm Deep Water in the Weddell Gyre: an Argo float perspective

by

Krissy Anne Reeve

A Thesis submitted in partial fulfilment of the requirements for the degree of

Doctor of Philosophy in Geosciences

Approved Dissertation Committee:
Prof. Dr. Rüdiger Gerdes[1,2] *(chair)*
Prof. Dr. Laurenz Thomsen[1]
Prof. Dr. Torsten Kanzow[2,3]
Prof. Dr. Andreas Muenchow[4]

[1]Jacobs University Bremen, Germany
[2] Alfred Wegener Institute, Bremerhaven, Germany
[3] Bremen University, Germany
[4] University of Delaware Newark, USA

Date of Defence: December 14th 2018

Statutory Declaration

Family Name, Given/First Name	**Reeve, Krissy Anne**
Matriculation number	**20329691**
What kind of thesis are you submitting: Bachelor-, Master- or PhD-Thesis	**PhD Thesis**

English: Declaration of Authorship:

I hereby declare that the thesis submitted was created and written solely by myself without any external support. Any sources, direct or indirect, are marked as such. I am aware of the fact that the contents of the thesis in digital form may be revised with regard to usage of unauthorized aid as well as whether the whole or parts of it may be identified as plagiarism. I do agree my work to be entered into a database for it to be compared with existing sources, where it will remain in order to enable further comparisons with future theses. This does not grant any rights of reproduction and usage, however.
The Thesis has been written independently and has not been submitted at any other university for the conferral of a PhD degree; neither has the thesis been previously published in full.

German: Erklärung der Autorenschaft (Urheberschaft)

Ich erkläre hiermit, dass die vorliegende Arbeit ohne fremde Hilfe ausschließlich von mir erstellt und geschrieben worden ist. Jedwede verwendeten Quellen, direkter oder indirekter Art, sind als solche kenntlich gemacht worden. Mir ist die Tatsache bewusst, dass der Inhalt der Thesis in digitaler Form geprüft werden kann im Hinblick darauf, ob es sich ganz oder in Teilen um ein Plagiat handelt. Ich bin damit einverstanden, das s meine Arbeit in einer Datenbank eingegeben werden kann, um mit bereits bestehenden Quellen verglichen zu werden und dort auch verbleibt, um mit zukünftigen Arbeiten verglichen werden zu können. Dies berechtigt jedoch nicht zur Verwendung oder Vervielfältigung.
Diese Arbeit wurde in der vorliegenden Form weder einer anderen Prüfungsbehörde vorgelegt noch wurde das Gesamtdokument bisher veröffentlicht.

.....

Date, Signature

Abstract

The Weddell Gyre supplies heat towards the Antarctic ice shelves and regulates the density of water masses that feed the deepest limb of the global overturning circulation, and is therefore a fundamental component in the global climate system. Our understanding of the Weddell Gyre hydrography is limited due to sparse data availability. Furthermore, long-term trends are masked by significant variability, and previous estimates show a large range in the strength of the Weddell Gyre's horizontal circulation, for reasons that are unclear.

In this thesis, Argo float profile and trajectory data spanning the entire Weddell Gyre from 2002 to 2016 are utilised in order to determine the horizontal circulation and distribution of heat within the Warm Deep Water (WDW) layer, which is the primary heat source to the Weddell Gyre. Objective mapping is applied to Argo float profiles, to provide gridded maps of temperature and salinity on fixed pressure levels from 50 to 2000 dbar. A 3-dimensional grid of the horizontal stream function is obtained, from which horizontal circulation is described. Volume transports throughout the gyre are calculated and placed into context of existing estimates in the literature. The heat budget for a 1000 m thick layer encompassing the core of WDW is presented, to investigate the mechanisms by which heat is redistributed throughout the WDW layer of the Weddell Gyre.

The horizontal sub-surface temperature distribution, i.e. core of the WDW layer, shows the warmest WDW entering the gyre in the southern limb from the east, and the coldest WDW within the interior. The Taylor column situated over Maud Rise is distinguished by a cold, deep WDW core. The circulation describes an elongated, cyclonic, double-cell gyre, in which the western cell is weaker and virtually barotropic, and the eastern cell is stronger and is influenced by baroclinic shear. This is the first time a detailed, comprehensive view of the double-cell structure is obtained purely from in-situ measurements. There is an inflow of 83 ± 22 Sv into the Weddell Gyre, of which 28 ± 7 Sv is WDW. Significant recirculation in the gyre interior is observed (15 ± 8 Sv in the WDW layer, 71 ± 28 Sv in the full water column), owing to the strong eastern circulation cell. It is shown that the large variation in previous estimates of the Weddell Gyre strength is likely due to the zonal variation in the gyre structure. While the heat

budget does not close at the resolution of the grid cells, it does almost close when integrated over large areas. In general, there is a balance between mean horizontal advection and horizontal turbulent heat diffusion (representative of eddy processes), whereas the vertical terms contribute relatively little. Horizontal turbulent diffusion contributes towards redistributing heat throughout the gyre, by diffusing heat northward from the southern limb into the interior circulation cell (6.5 ± 3 TW), and coastward towards the ice shelves (inferred as 12.5 ± 10 TW). 20 ± 10 TW of heat enters the gyre across the northern boundary from the Antarctic Circumpolar Current by horizontal turbulent diffusion. The influence of eddy processes is implied in the lee of Maud Rise, where heat divergence due to horizontal turbulent diffusion is observed. This may be due to baroclinic instabilities on the flanks of Maud Rise, which leads to enhanced convection. One outstanding question from this thesis concerns the response of the double-cell circulation to long-term changes in the wind field, and how this might alter the mechanisms by which heat is injected into and subsequently redistributed throughout the Weddell Gyre.

Table of Contents

List of Figures

List of Tables

List of Acronyms

Antarctic Bottom Water	AABW
Antarctic Circumpolar Current	ACC
Antarctic Coastal Current	ACoC
Antarctic Slope Current	ASC
Antarctic Slope Front	ASF
Circumpolar Deep Water	CDW
Full depth	FD
Horizontal Drift	HD
Julian Day Ascent End	JAE
Julian Day Descent Start	JDS
Northern Limb	NL
Prime Meridian	PM
Southern Limb	SL
Warm Deep Water	WDW
Weddell Sea Deep Water	WSDW
Weddell Sea Bottom Water	WSBW
Sub-surface temperature maximum	Tmax, Θ_{max}
Temperature mean for the WDW layer	Θ_{WDW}
Depth-Averaged temperature	Θ_{AVE}
World Ocean Atlas	WOA
World Ocean Circulation Experiment	WOCE
Surface drift	SD
Full depth (of the water column)	FD
Volume transport	VT
Cross-section	CS
Southern Annular Mode	SAM
Mid-thermocline depth	mT
Net air-sea-heat flux	Q_{net}

1 Introduction

1.1 Global ocean circulation

The ocean plays an important role in the Earth's climate system through the regulation, transport and storage of heat, freshwater, carbon and oxygen (i.e. Rhein et al., 2013). As such, understanding the drivers and pathways of large-scale ocean circulation is a fundamental component of climate science.

The thermohaline circulation (THC) describes the component of ocean circulation driven by density differences that arise from heat and freshwater fluxes at the sea surface (Sandström, 1916; Jeffreys, 1925). However, at steady state on a global scale, surface buoyancy fluxes alone will not sustain the Meridional Overturning Circulation (MOC): a mechanical energy input is required to mix heat downwards in order to maintain horizontal pressure gradients necessary to drive the MOC. Turbulent mixing of heat and salt in the ocean interior, driven, for example, by the initiation of internal waves from winds, tides and bathymetry, and wind-driven upwelling play an important role in sustaining the MOC (Munk & Wunsch, 1998; Rahmstorf, 2003). At the global scale, the MOC is characterised by (1) the sinking of water-masses in localised deep-water formation regions, (2) the spreading of these deep-water masses, for example, within deep western boundary currents, and (3) the wind-driven upwelling of deep waters. Wind-driven upwelling in the Southern Ocean and diapycnal upwelling in the deep Indian and Pacific Oceans are essential for allowing the deep and bottom water masses formed in the North Atlantic (North Atlantic Deep Water; NADW) and the Southern Ocean (Antarctic Bottom Water; AABW) to once again return to the surface (Marshall & Speer, 2012; Talley, 2013). The focus here is on the Southern Ocean.

1.2 The Southern Ocean

The Southern Ocean is a unique feature of the Earth's climate system, in that it links all major ocean basins and has no meridional boundaries. It is also the region of the so-called roaring forties, furious fifties and screaming sixties; strong westerly winds which dominate the wind stress field between 40 and 60º S, for the most part unhindered by landmass. Meridional temperature gradients and the strong westerly winds drive the Antarctic Circumpolar Current (ACC), the world's strongest ocean current, whose eastward transport has been estimated to be stronger than 150 Sv (Park

et al., 2009; Koenig et al., 2014). The ACC has a banded jet-like structure, where the bulk of the transport is concentrated within a series of fronts that run along the ACC (Deacon, 1937; Baker et al., 1977; Nowlin & Klinck, 1986; Orsi et al., 1995). The northern boundary of the ACC is identified by the Subantarctic Front, north of which the downwelling of surface waters occurs due to Ekman convergence (e.g. Koshlyakov & Tarakanov, 2011). Within the central ACC there is the Polar Front, characterised by the onset of a sub-surface temperature minimum layer southwards of the Polar Front (Taylor et al., 1978; Orsi et al., 1995). South of the ACC, Ekman divergence results in the upwelling of water masses at the interface between the strong westerly winds and the polar easterly winds at the Antarctic coast (Taylor et al., 1978; Deacon, 1982; Hayakawa et al., 2012). Other fronts include the Southern ACC Front and the southern boundary of the ACC. Poleward of these fronts, along the continental slope of Antarctica, the Antarctic Slope Front is distinguished by a westward counter flow, which protects the continental shelf seas from being breached by warmer waters from the north (Jacobs, 1991; Orsi et al., 1995; Whitworth et al., 1998; Chevanne et al., 2010). A basic schematic of the Southern Ocean circulation is provided in Fig. 1.1, originally from Rintoul et al., 2001.

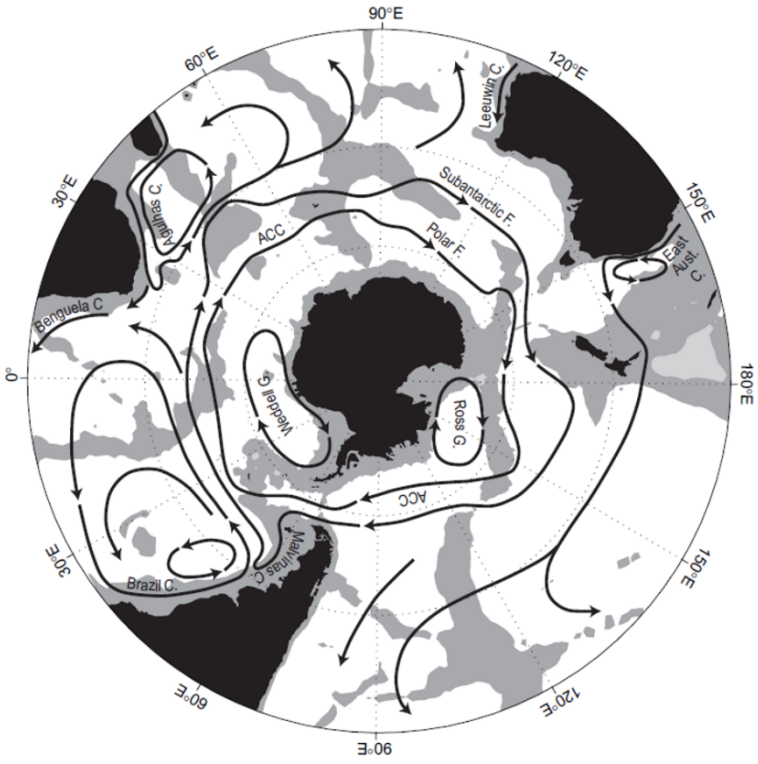

Figure 1.1. Schematic of the main Southern Ocean currents, from Rintoul et al., 2001. Grey regions indicate bottom depths of less than 3500 m. The Polar Front and Subantarctic Front present the main cores of the banded structure of the ACC. The Weddell and Ross Gyres are labelled, in the Atlantic and Pacific sectors of the Southern Ocean respectively.

Since there are limited meridional boundaries in the upper 2000 m (the depth of the water column within Drake Passage is below 2000 m), there are no east-west pressure gradients within the latitude band of Drake Passage, which means that within this upper layer, there can be no meridional geostrophic flow. Thus, Ekman upwelling is able to occur from great depths, driving a northward flow that can only be returned below 2000 m, where meridional boundaries enable an east-west pressure gradient, which can drive a southward return flow (Gill & Bryan, 1971; Cox, 1989; Toggweiler & Samuels, 1995). Thus, the Southern Ocean is the only place in the global ocean where direct large-scale upwelling of deep water (Circumpolar Deep Water; CDW) to the sea surface occurs, helping to connect the upper and lower cells of the MOC (Marshall & Speer, 2012; Talley, 2013). The impact of this large-scale upwelling is most distinct in maps of near-surface nutrient concentrations, such as nitrate (Levitus et al., 1993; Sarmiento et al., 2004). CDW is formed by modification of North Atlantic Deep Water (NADW), which is drawn into the ACC. While circulating the ACC, NADW interacts with water from other ocean basins, forming CDW. There are two classes of CDW characterised by their density; the lighter component of CDW, upper CDW (UCDW) is upwelled and transported northwards, whereas the denser component, lower CDW (LCDW) is advected southwards towards the poles (Callahan, 1972; Whitworth & Nowlin, 1987; Smith et al., 1999).

The ACC has previously been described as “equivalent barotropic”, which essentially means unidirectional, but with shear reducing velocity magnitude with increasing depth (Killworth, 1992; Killworth & Hughes, 2002; Gille, 2003). Thus, at 2000 dbar, the ACC shows a similar circulation to the surface, with weaker magnitudes (Gille, 2003). However, topographic obstacles below 2000 m result in strong topographic steering of the circulation (Gille, 2003), and the meridional boundary below 2000 m at Drake Passage results in horizontal pressure gradients. This leads to deep western boundary currents as a distinctive feature of the circulation at 4000 dbar through the Scotia Sea, which transport deep and bottom water masses northward to begin the return journey to the source location in the North Atlantic (Sloyan & Rintoul, 2001; Talley, 2013).

Peña-Molino et al., (2014) challenge the view of the ACC as “equivalent barotropic”, except within jet centres, where flow rotation is weak. Conversely, on the flanks of these jet streams and at depth, rotation is large. They show that, if we consider

the zonal flow of the ACC in terms of its barotropic and baroclinic components, the geostrophic transport is predominantly baroclinic, with the barotropic component of flow not exceeding 25% at any point in the ACC. Away from the ACC, the barotropic/baroclinic ratio is strongest in the centre of basins, at 10/90%, and least pronounced within the vicinity of complex topography (50/50%). The barotropic and baroclinic components act in opposite directions, and supports significant cross-stream transports (Peña-Molino et al., 2014). More recent research highlights topographic features as regions of enhanced upwelling of deep waters into the surface Southern Ocean, which has been associated with heightened mesoscale eddy activity (Tamsitt et al., 2017). These findings suggest that surface velocity data alone are not enough to determine the circulation and mass transports within the Southern Ocean (Peña-Molino, 2014).

South of the South ACC Front, polar gyres are a distinct feature of the Southern Ocean circulation. The two most prominent polar gyres are found to either side of the Antarctic Peninsula: the Ross Gyre and the Weddell Gyre, located in the Pacific and Atlantic sectors of the Southern Ocean respectively. These gyres play a pivotal role in the MOC (e.g. Mazloff et al., 2010), through the modification of LCDW, which is advected into the polar gyres, supplying heat to the continental ice shelves at the Antarctic coastline. In this thesis, the focus will be on the Weddell Gyre.

1.3 The Weddell Gyre

1.3.1 Structure, circulation and water masses of the Weddell Gyre

The Weddell Gyre is located in the Atlantic sector of the Southern Ocean, south of the ACC (Fig. 1.1). The gyre is cyclonic and encompasses the Weddell and Enderby basins, with open boundaries to the north and east, and closed boundaries of the Antarctic continent to the south and west. The open boundaries pose a substantial challenge in observing the mean state of the Weddell Gyre circulation, due to the dynamic, highly variable nature of the ACC (Fahrbach et al., 2004; Klatt et al., 2005; Donnelly et al., 2017), and the sensitivity of the ACC and gyre peripheries to the wind field (Armitage et al., 2018). A basic schematic of the Weddell Gyre circulation in provided in Fig. 1.2. The presence of sea-ice and the bathymetric feature Maud Rise further contribute towards the challenge of observing the mean state of the Weddell Gyre circulation (Leach et al., 2011; Donnelly et al., 2017). Regardless, we have a good

understanding of the general structure of the gyre, thanks to observations from as far back as the early 1900's, when Brennecke (1918) first described the cyclonic nature of the Weddell Gyre, through combining measurements within the region from expeditions of several countries between 1901 and 1912.

The Weddell Gyre is primarily wind-driven, driving a cyclonic (clockwise) circulation, where eastward flowing westerly winds are superimposed over the northern limb of the gyre, and westward flowing easterly winds are superimposed over the southern limb of the gyre (Schwerdfeger, 1970; Fahrbach et al., 2011). The wind forcing results in upwelling in the gyre centre due to the Ekman divergence of surface waters, and downwelling at the gyre periphery, in particular along the Antarctic coast due to the easterly winds "piling" the water up onto the coast (Deacon, 1979). Thus, when looking at meridional cross-sections of potential density, the Weddell Gyre is characterised by the doming of its isopycnals; the isopycnals shoal towards the surface along the central axis of the gyre and deepen along the gyre periphery (Schröder & Fahrbach, 1999; also see Figs. 3.29-3.31). The upwelling at the surface along the gyre axis and the downwelling along the gyre periphery establishes an overturning circulation within the Weddell Gyre, where the upwelling of the upper cell acts as a source of carbon dioxide and loss of heat to the atmosphere, whereas the downwelling of the lower cell acts as a sink for carbon dioxide and heat (Naveira Garabato et al., 2016; Jullion et al., 2014; Brown et al., 2015). Thus, the Weddell Gyre contributes towards the lower limb of the global overturning circulation and plays an important role in the regulation of climate, in supplying heat to the global ocean interior (Jullion et al., 2014; Naveira Garabato et al., 2016).

Defining the eastern boundary of the gyre is not straightforward, and estimates range from 30 to 60° E (Gouretski & Danilov, 1993; Schröder & Fahrbach, 1999; Ryan et al., 2016). The ACC turns sharply southwards at about 26° E due to the topographic boundary of the mid-ocean ridge (Gouretski & Danilov, 1993). Some of this water is deflected westwards and forms the inflow region at the open eastern boundary of the Weddell Gyre. It is a highly dynamic region where topographic constraints result in an intense mesoscale eddy field between 15 and 30° E (Schröder & Fahrbach, 1999; Ryan et al., 2016; Donnelly et al., 2017), which poses a challenge in quantifying the inflow of heat into the Weddell Gyre. Ryan et al. (2016) show that the inflow of warm water to the Weddell Gyre occurs through two different pathways, which are distinct as separate

cores at 20° E but become indistinguishable at 0° E. Eddy-mixing in the north-eastern corner of the Weddell Gyre drives an inflow at about 60° S, while horizontal advection drives an inflow closer to the coast, which first extends eastwards past 30° E before turning westward into the Weddell Gyre (Ryan et al., 2016). This area remains an under-sampled region and the long-term mean of the inflow east of the Prime Meridian represents an important gap in our knowledge from an observational viewpoint.

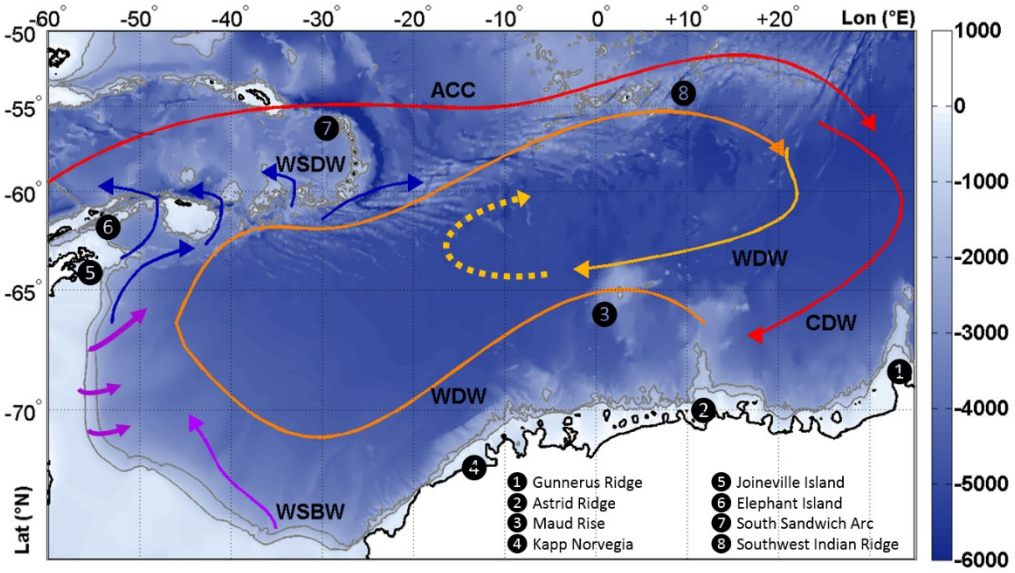

Figure 1.2. Schematic of the Weddell Gyre circulation overlying bathymetry (IOC, IHO and BODC, 2003). The red arrows indicates the relatively warm and salty Circumpolar Deep Water, which enters the Weddell Gyre to the east from the ACC. As CDW enters the gyre, where it is named WDW (orange), it undergoes modification as it circulates the gyre (light orange arrow). WSBW spills into the Weddell Gyre basin from underneath the ice shelves in the southwestern Weddell Sea (purple arrows). The dark blue arrows indicate the export routes of WSDW. The legend provides the names of prominent bathymetric features. The grey contours provide the 1000 and 2000 m isobaths. From Reeve et al. (in review).

LCDW is injected westwards into the southern limb of Weddell Gyre at a depth of about 800 to 1000 dbar (Orsi et al., 1993; Donnelly et al., 2017), though intrusions of CDW from the ACC also occurs to a lesser extent along the northern boundary (Klatt et al., 2005). Upon entering the Weddell Gyre, LCDW is locally known as Warm Deep Water (WDW), and is gradually modified, through entrainment and mixing of the underlying and overlying water masses as it circulates the Weddell Gyre (Orsi et al., 1993; Leach et al., 2011). It is also gradually upwelled towards the surface in the centre of the gyre, where it has been identified at its shallowest point at about ~100 dbar (Orsi et al., 1993; Reeve et al., 2016; Donnelly et al., 2017). WDW is distinguished by a sub-surface temperature and salinity maximum at its core (for example, see Figs. 3.28 to 3.30). WDW is the primary source water mass, which supplies heat towards the ice shelves in the western sector of the Weddell Gyre, leading to the formation of Antarctic

Bottom Water (AABW). Intrusions of WDW onto the continental shelf through submarine troughs leads to basal melting of the Filchner Ronne Ice Shelf, the largest ice sheet in terms of volume surrounding Antarctica (Artun et al., 2012; Ryan et al., 2017).

Directly above WDW is the surface mixed layer, which experiences large seasonal variation due to air-sea-ice interaction. A sequence of feedback events that are relevant for the role of the Weddell Gyre in the climate system occurs throughout the year. In the approach to Austral winter, the atmosphere cools, and gradually becomes cooler than the surface of the ocean, resulting in a heat flux from the ocean to the atmosphere, i.e. surface cooling. Due to surface cooling, convective overturning leads to a relatively deep surface mixed layer. As the atmosphere continues to cool, and the surface of the ocean cools, a critical point is reached where sea-ice begins to form. When sea-ice is formed, salt is rejected from the ice and brine water is released to the underlying water. The temperature of this water is close to its freezing point. Then, as the atmosphere begins to warm in the approach to Austral summer, the surface of the ocean is heated and sea-ice melts, creating a surface lens of relatively warm and fresh water. Owing to the stratification of the water column, the heat is unable to penetrate far into the water column. Thus, the cold and fresh water formed at the surface in the winter persists at the sub-surface throughout the summer months, and is easily recognisable by a sub-surface temperature minimum layer from the surface to about 50 to 150 m (Behrendt et al., 2011). The salinity of this sub-surface water mass, Winter Water (WW), plays a role in the stability of the upper Weddell Gyre, directly influencing the amount of convective overturning (Gordon & Huber, 1990; Behrendt et al., 2011). WW is entrained by the underlying WDW, and is also sensitive to freshwater fluxes due to variations in sea-ice formation (Behrendt et al., 2011).

Weddell Sea Deep Water (WSDW) and Weddell Sea Bottom Water (WSBW) are the water masses found below WDW. WSBW is the coldest and densest water mass in the Weddell Gyre, primarily produced within the vicinity of the Filchner-Ronne ice shelves, and the ice shelves that line the eastern flank of the Antarctic Peninsula, where plumes of cold High Salinity Shelf Water (HSSW) cascade down the continental slope to fill the bottom of the Weddell basin with WSBW (Foster & Carmack, 1976; Foster et al., 1980; Foldvik et al., 2004). WSDW is formed both by entrainment of WDW into WSBW as it cascades down the continental slope, and more directly through the mixing

of WDW with shelf waters at the shelf edge (Farhbach et al., 1995; Fahrbach et al., 2011).

WSBW is too dense to be able to directly escape the Weddell Gyre as a result of topographic constraints to the north (Gordon et al., 2001). WSDW is able to directly escape the Weddell Gyre, by flowing northwards along the continental slope towards the tip of the Antarctic Peninsula, where it is able to exit the Weddell Gyre through gaps in the South Scotia Ridge and the eastern flank of the Scotia Arc (Locarnini et al., 1993; Gordon et al., 2001; Naveira Garabato et al., 2002; Schodlok et al., 2002). Here, WSDW feeds into AABW, which is then dispersed throughout much of the global ocean abyss. The water that does not escape the Weddell Gyre continues its circulation along the northern limb of the gyre, forming the return flow to the northeast of the Weddell Gyre, continuing to cool on-route. The WDW that reaches the northeastern quadrant of the Weddell Gyre cools considerably, forming the so-called "cold regime" east of the Prime Meridian (Gordon & Huber, 1984), which partially recirculates about the easternmost part of the gyres central axis, mixing with the warmer incoming WDW, i.e. the "warm regime" waters (Gordon & Huber, 1984). A cross-section along the Prime Meridian showing the Weddell Gyre water masses as indicated by their neutral density ranges is provided in Fig. 1.3, from Fahrbach et al. (2011).

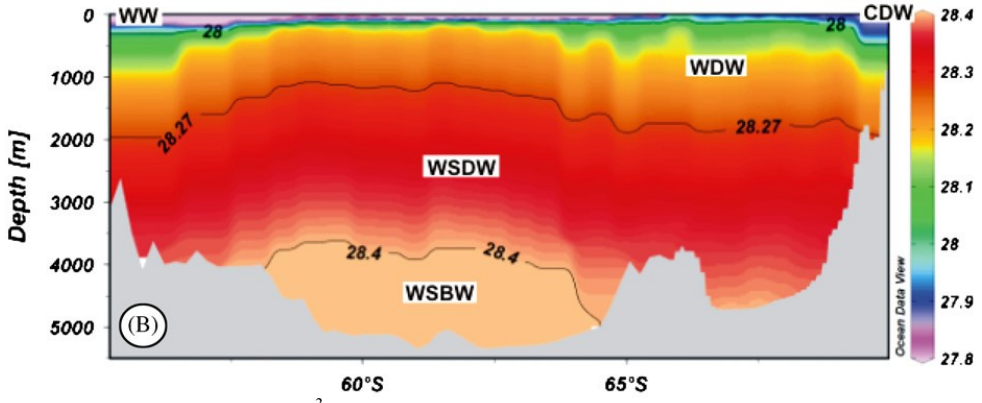

Figure 1.3. Neutral density (kg m^{-3}) for a section along the Prime Meridian from the cruise ANT-X/4 in 1992, from Fahrbach et al., 2011. The water masses are indicated by their neutral density ranges: Circumpolar Deep Water (CDW) at the northern boundary, Winter Water (WW), Warm Deep Water (WDW), Weddell Sea Deep Water (WSDW) and Weddell Sea Bottom Water (WSBW).

The strongest currents within the Weddell Gyre are found at the periphery of the gyre. As much as 90% of the volume transport along the Kapp Norvegia-Joineville Island transect has been attributed to boundary currents along the shelf edge in Fahrbach et al., (1994). The Antarctic Coastal Current (ACoC) is a westward fast-flowing current over the continental shelf, with a primarily barotropic transport (Núñez-Riboni &

Fahrbach, 2009). While poorly observed, observations have shown that the ACoC displays significant seasonal variability, with the strongest transports occurring during the Austral winter (Núñez-Riboni & Fahrbach, 2009; Cisewski et al., 2011). The ACoC is primarily driven by the wind field, but thermohaline forcing as a result of heating/cooling and sea-ice formation/melt are also driving mechanisms which contribute towards the seasonal variability of the ACoC (Núñez-Riboni & Fahrbach, 2009). The Antarctic Slope Front (ASF) sits at the continental shelf-edge, which separates the cold and relatively fresh coastal waters from the warmer, saltier waters farther offshore (Heywood et al., 2004). A barotropic jet is located at the ASF, and constitutes a powerful component of flow within the boundary currents, which can be twice as strong during austral autumn than other seasons (Armitage et al. 2018). The ACoC and ASF are found all around the coast of Antarctica. The ASF allows for the export of WSDW through the Weddell-Scotia Confluence, some of which continues westwards north of the Weddell Gyre (Heywood et al., 2004). The ACoC plays an important role in protecting the ice shelves surrounding Antarctica from direct contact with CDW, or in the Weddell Gyre, WDW. The amount of WDW that is able to cross the shelf break governs the amount of heat that is supplied to beneath the ice shelves. Studies have shown that the wind, in combination with the seasonally varying thermocline depth, plays an important role in controlling the amount of WDW that reaches the shelves (Arthun et al., 2014; Zhou et al., 2014; Darelius et al., 2016). However, the actual pathways of WDW under the ice shelves are still poorly understood (Meredith et al., 2016). A modelling study by Hellmer et al., (2012, 2017) suggests that thinning of sea-ice in the southwestern Weddell Gyre could induce changes to the ocean surface stress, resulting in a redirection of the coastal current into the Filchner Trough, bringing WDW into direct contact with the Filchner-Ronne ice shelf. This could result in a substantial increase in basal melting under the ice shelf, from the current average of 0.2 m/year, to over 4 m/year, potentially contributing to sea-level rise (Hellmer et al., 2012).

1.3.2 The role of wind and sea-ice on Weddell Gyre dynamics

In addition to driving the gyre-scale ocean circulation, the wind also drives spatial variability in sea-ice cover within the Weddell Gyre. The presence of sea-ice influences the underlying ocean in two main ways:

1. "shielding" the ocean from the direct influence of the wind
2. contributing towards driving the freshwater budget.

The transport of sea-ice from the Antarctic coast northwards towards the ACC results in a freshwater conveyor belt, where sea-ice formation/brine rejection at the coast and sea-ice melt/freshwater input further north results in horizontal gradients in salinity, driving freshwater fluxes (Holland & Kwok, 2012). These freshwater fluxes influence seawater density and subsequently the stratification and circulation of the Southern Ocean (Abernathey et al., 2016). The katabatic winds play a role in driving sea-ice away from the continental shelf around Antarctica, driving/sustaining polynyas and leads (Zwally et al., 2013). Numerical model studies have linked meridional sea-ice transports with the strength of the lower branch of the Southern Ocean overturning circulation cell (Stoessel et al., 1998; Komuro & Hasumi, 2003). Other studies suggest that the sea-ice component of the freshwater budget contributes to Antarctic Intermediate Water formation (AAIW; Saenko et al., 2002), and that wind-driven sea-ice transport is tightly coupled to the upper branch of the overturning circulation cell (Abernathey et al., 2016). Additionally, anomalies in the wind forcing entering over the Weddell gyre from the west, can lead to perturbations in sea-ice circulation, causing the accumulation of sea-ice in the south eastern part of the Weddell Gyre every 4-6 years, which is then circulated north-north-eastwards, joining the northern limb of the Weddell Gyre circulation (Venegas et al. 2001).

The wind has also been shown to control the export of WSDW (AABW) from the Weddell Gyre (Jullion et al., 2010). Decadal variability in AABW properties in the Scotia Sea has been linked to the baroclinic adjustment of the Weddell Gyre in response to changes in the wind stress field, where vertical variations in the density structure influences the export of AABW over the South Scotia Ridge (Jullion et al., 2010). The wind-controlled regulation of the export of AABW from the Weddell Gyre therefore has important implications on the long-term changes in AABW properties, where observed AABW warming (Coles et al., 1996; Zenk and Morozov, 2007; Meredith et al., 2008; Johnson et al., 2008) has been attributed to changing density classes of AABW exported from the Weddell Gyre (Meredith et al., 2008). Indeed, a seasonal cycle in the export of AABW from the Weddell Gyre has been suggested by Gordon et al. (2010), based on 8 years of observations south of the South Orkney Islands. Gordon et al. (2010) found a pronounced seasonal cycle in bottom waters where a warm pulse occurred in May/June,

followed by a cold pulse in October/November, which the authors suggest is due to seasonal changes in the wind-forcing over the Weddell Gyre. The wind-controlled export of AABW from the Weddell Gyre has, through correlation studies, been linked to large-scale climate phenomena; the two largest within the Southern Ocean region being the Southern Annular Mode (SAM) and the El Niño Southern Oscillation (ENSO) (Jullion et al., 2010). Jullion et al. (2010) suggests that the positive tendency of the SAM in recent decades has a causal link with the warming trends of AABW, and show that spatial variation of the correlation between AABW temperature and the SAM index exhibits a "SAM-like" pattern in the Scotia Sea. A more recent study by Armitage et al. (2018) highlights a correlation between sea-surface-height (SSH) variability in the Southern Ocean and SAM. Since the Weddell Gyre is largely barotropic, the SSH provides an indication of the Weddell Gyre circulation, where changes in the Weddell Gyre circulation is strongly linked to month-to-month variability in the local wind stress curl (Armitage et al., 2018).

Wind forcing variability induced by SAM and ENSO has also been linked to the volume of High Salinity Shelf Water (HSSW) that can be formed, and is able to exit the continental shelf, in a study based on mooring observations by McKee et al., (2011). McKee et al. (2011) show that stronger winds push the sea ice away from the shelf edge, allowing for more sea ice and subsequently brine rejection to form on the continental shelf. This also links to the amount of AABW that is formed within the Weddell Gyre, since HSSW is a precursor to AABW formation (Foldvik et al., 2004).

Wind forcing is also important in the large-scale dynamics of the Weddell Gyre, owing to the open boundaries to the north and to the east. Fahrbach et al. (2011) show that the wind stress is not symmetric over the Weddell Gyre, i.e. the central axis of the Weddell Gyre circulation is centred over 60° S at the Prime Meridian, whereas the low air pressure system over the Weddell Gyre is centred at about 65° S. This means that the northern part of the westward flowing southern limb of the Weddell Gyre flows against the direction of the wind. Thus, when the easterly winds are strong, the southern limb of the gyre exhibits strong westward flow, and vice versa. When the westerly winds are weak, the eastward flowing northern limb of the Weddell Gyre is weak, and the northern part of the westward flowing southern limb is relatively strong. When the westerly winds are strong, the northern limb is also strong, but the northern part of the southern limb is weak, owing to its direction being against the direction of the wind

(Fig. 11 in Fahrbach et al. 2011). Owing to the open boundaries to the north and the east, the northern and southern limbs of the Weddell Gyre are unsynchronised, influencing the variability of the inflow of water masses into the southern limb from the east, and the outflow of water masses in the northern limb in the west (Fahrbach et al. 2011). The inflow controls how much heat is advected into the gyre, where it can potentially reach the Filchner-Ronne ice shelf cavities (Hellmer et al., 2012, 2017) and the outflow controls how much AABW is exported to the rest of the global ocean, resulting in the storage of heat in the extensive reservoir of the global abyss (Orsi et al., 1999; Johnson et al., 2008). Thus, the role of wind forcing in controlling the out-of-phase relationship of the Weddell Gyre circulation has important implications on the global ocean heat budget (Fahrbach et al., 2011).

1.3.3 Long-term changes in the Weddell Gyre

Like many other regions throughout the global ocean, the Weddell Gyre has been undergoing changes in recent decades. Large variability, sparsity of data, and a summer bias of data for a periodically sea-ice covered environment renders significant challenges in determining long-term trends due to anthropogenic forcing. Furthermore, the longest time-series exists for a section in a dynamically complex region, in close proximity to Maud Rise. Fahrbach et al., (2004) report significant levels of decadal variability in Weddell Gyre water masses, masking long-term trends. In a follow up paper, however, Fahrbach et al., (2011) shows that the mean temperature and salinity for the whole water column along the Prime Meridian displays a positive trend over 24 years, from 1996 to 2004. Despite this, long-term trends within the individual water masses are not clear in Fahrbach et al., (2011), and subject to significant variability. WDW shows decadal variability in both temperature and salinity, with no clear long-term warming trends. WSDW displays a warming trend between 1984 and 2005, but is cooler again in 2007. After an initial cooling from 1984 to 1992, WSBW is more or less warming until 2003, after which, no obvious change occurs in temperature (whereas salinity appears to begin a freshening trend after a positive trend from 1998 to 2005). The long-term temperature trends of the Weddell Gyre water masses are shown in Fig. 5 in Fahrbach et al., (2011). Fahrbach et al., (2011) suggest that the long-term trend of the whole water column may be the result of an accumulation of heat and salt that has been advected into the gyre during wind-driven “warm pulse” events, which is then

distributed into the deeper layers within the Weddell Gyre. The implications of this finding is that the Weddell Gyre plays a role in the Earth's climate system by bringing atmospheric heat into the deep ocean (Fahrbach et al., 2011; Heywood & Stevens, 2007). Naveira Garabato et al., (2016) and Jullion et al., (2014) show, through inverse modelling, that the Weddell Gyre indeed contributes towards closing the southern limb of the global overturning circulation. Naveira Garabato et al., (2016) highlights the existence of two interlinked overturning cells within the Weddell Gyre, where the deep overturning cell results in cooling-driven densification of deep and bottom waters. This deep overturning cell leads to the export of both locally and externally sourced AABW (also see Meredith et al., 2000) from the Weddell Gyre. In contrast to the cooling-driven deep overturning cell within the Weddell Gyre, an upper overturning cell exists, driven by freshening, which results in an increase in the buoyancy of the upper ocean, converting WDW into lighter upper ocean waters (Naveira Garabato et al., 2016).

The WW layer, found above WDW within the upper overturning cell, also exhibits decadal variation, which cannot be attributed to variations in sea-ice formation and entrainment of the underlying WDW alone (Behrendt et al. 2011). Behrendt et al. (2011) points out that the horizontal advection of both seawater and sea-ice also plays an important role in influencing WW variability. Thus, changing properties in WW might be expected to have occurred in the time period of 2016 onwards, due to the recent record-low in sea-ice cover in the Weddell Gyre in the Austral spring of 2016 (Turner et al. 2017). In November 2016, sea-ice loss in the Weddell Gyre was double the climatological change (Turner et al., 2017). Turner et al. (2017) show that the record sea-ice retreat coincided with record atmospheric circulation anomalies leading to northerly atmospheric flow in several regions throughout the Southern Ocean, indicating a role of wind-forcing in advecting sea-ice northwards out of the Weddell Gyre. They also speculate that ocean would have also played a role in sea-ice loss, while also acknowledging that this is difficult to quantify.

The most recent study of the temporal variability of water mass properties comes from Kerr et al. (2017), who analysed three decades of ship-based data collected within the Weddell Gyre, from 1984 to 2014. In fig. 5 of Kerr et al. (2017), WDW shows a warming from 1984 to 1996 along the Prime Meridian, and from 1988 to 1996 along the SR4 transect from Kapp Norvegia to Joineville Island. The WDW warming was followed by a cooling until 2011 along the SR4 transect, and a cooling until 2005 along

the Prime Meridian, after which a slight warming occurs up to 2014. Again, WDW exhibits strong decadal variability, and, if anything, suggests an overall cooling trend, at least after 1996. Long-term salinity trends in WDW are even less clear. However, the changes in temperature and salinity appear not to be density compensated, as neutral density suggests a lightening of WDW occurs along both transects until 1996-1998, after which, WDW undergoes some densification. The long-term trends in WSDW and WSBW are also exhibiting significant variability, though WSDW along section SR4 appears to be undergoing density-compensating increasing temperature and salinity. After 1992, WSDW along the Prime Meridian shows a generalised positive trend in temperature and salinity, though somewhat masked by the variability. Along the Prime Meridian, from 1984 to 1992, WSBW temperature and salinity initially both decrease, causing a lightening of the WSBW layer, after which, there is warming and increasing salinity. With the exception of a spike between 1990 and 1998, caused by a drop in temperature and salinity, WSBW appears to be undergoing a shift towards lighter waters, which, Kerr et al. (2017) suggest, is due to less WSBW being formed over time. This results in a reduction of WSBW volume observed until 2005, after which WSBW probably recovered. Kerr et al. (2017) also suggest that the increase in WSBW in the eastern Weddell Gyre, along the Prime Meridian, is likely driven by pulses of inflowing Dense Shelf Waters (DSW) and AABW sourced from the Indian sector of the Weddell Gyre. Regarding locally sourced WSBW, Kerr et al. (2017) show that WSBW is primarily composed of 71 ± 4 % modified WDW (mWDW), and 29 ± 4 % DSW, again highlighting the importance of WDW in transporting heat into the deeper layers of the Weddell Gyre (Fahrbach et al., 2011).

1.4 Research questions and project aim

While WSBW in the interior of the Weddell Gyre has been generally warming (Kerr et al., 2017, Fahrbach et al., 2011), the main source of locally formed WSBW, WDW, shows high decadal variability and no distinct long-term change. Furthermore, AABW throughout the global ocean has been displaying clear warming signals (Schmidtko et al., 2014; Purkey & Johnson, 2013; Meredith et al., 2011; Zenk et al., 2007; Kawano et al., 2006). To understand the role of the Weddell Gyre in the Earth's climate system, it is paramount to understand how heat might be distributed throughout the Weddell Gyre. Fahrbach et al. (2011) suggest that "warm pulse" events lead to an

accumulation of heat and salt within the Weddell Gyre, despite decadal variation of WDW (the main source of heat to the Weddell Gyre). They also suggest that the Weddell Gyre dynamics, controlled by a wind-forced, out of phase relationship between the northern and southern gyre limbs results in a redistribution of heat and salt to the deeper layers of the Weddell Gyre, which may account for some of the warming observed in WSBW. However, Fahrbach et al. (2011) and other similar studies base time-series analyses on observations from along the Prime Meridian. This leads to an important question: how representative are the observed changes along the Prime Meridian of the overall Weddell Gyre? The use of single transects across the Weddell Gyre leads to uncertainty about the circulation from a 3-dimensional perspective, especially when determining transports throughout the Weddell Gyre, which, to date, has led to a wide range of Weddell Gyre strength estimates in the literature. What is also not clear, is how the double-cell structure of the Weddell Gyre circulation (e.g. Beckmann et al., 1999 suggests a double cell structure from a numerical model study) responds to wind forcing variability, and how this may influence the transfer of heat into the global ocean interior.

The aim of this thesis is to use Argo float data as a tool to investigate the upper ocean dynamics and spatial distribution of water properties of the Weddell Gyre. This thesis was developed to answer the following three questions:

RQ 1. Is it possible to create gridded data sets of temperature and salinity throughout the entire Weddell Gyre, describing the spatial variation in the hydrography of the upper water column, which includes the WDW layer?

RQ 2. Can the large range in historical gyre strength estimates be reconciled with spatial inhomogeneity of the circulation of the Weddell Gyre?

RQ 3. In bringing together the outcomes from RQ.1 and RQ.2, what mechanisms contribute to distributing heat within the WDW layer of the Weddell Gyre?

1.5 Thesis outline

The remainder of the thesis is structured as follows. In the ensuing chapter, the Argo float array is presented, as the focal data source of the research presented herein. Chapter 3 presents the first of three publications, which delivers a detailed methodology of applying objective mapping to Argo float hydrographic data in order to provide basin-scale maps of the Weddell Gyre. As an assessment of validity, the results were compared to existing climatologies. This work corresponds to *RQ 1*, where the maps provide information about the spatial variation of temperature and salinity throughout the entire Weddell Gyre for the upper 50 to 2000 dbar, the pressure range in which WDW is found.

The second stage of the thesis involved fitting a stream function to the Argo float trajectory data of velocities at 800 dbar. This is combined with the gridded hydrographic fields to determine the circulation and volume transports of the upper 2000 m, the Warm Deep Water, and the full depth layers respectively. This work is presented in a manuscript in Chapter 4, which has been submitted to the journal, *Progress in Oceanography* and is currently under review. As a result, the Weddell Gyre circulation is assessed in the context of available literature, by assessing volume transports across ocean sections consistent with previous observations and estimates (*RQ 2*).

In answer to *RQ. 3*, the resulting fields lead to the determination of the heat budget of the upper Weddell Gyre, for a 1000 m thick layer encompassing the core of WDW, which is presented in Chapter 5 and forms the content of the third publication, currently in preparation. Ultimately, the aim is to advance current knowledge on the structure of the Weddell Gyre in terms of circulation (*RQ 2*) and heat distribution (*RQ 1*, *RQ 3*), in order to better ascertain the role the Weddell Gyre plays in a global climate perspective. The key findings and outlook of the overall thesis are summarised in Chapter 6.

1.6 List of own relevant Publications

Publication I:

Reeve, K.A., Boebel, O., Kanzow, T., Strass, V., Rohardt, G. and Fahrbach, E. (2016) 'A gridded data set of upper-ocean hydrographic properties in the Weddell Gyre obtained by objective mapping of Argo float measurements', Earth System Science Data, 8(1), pp. 15-40.

Publication II:

Reeve, K.A., Boebel, O., Kanzow, T., Strass, V., and Gerdes, R., Horizontal circulation and volume transports in the Weddell Gyre derived from Argo float data. Under review in Progress in Oceanography.

Publication III:

Reeve, K.A., Kanzow, T., Strass, V., Boebel, O and Gerdes, R., The Weddell Gyre heat budget associated with the Warm Deep Water circulation. In preparation.

Archived datasets:

Reeve, K.A., Boebel, O., Kanzow, T., Strass, V.H., Rohardt, G., Fahrbach, E (2016): Objective Mapping of Argo data in the Weddell Gyre: a gridded dataset of upper ocean water properties, link to data files in NetCDF format. PANGAEA, https://doi.org/10.1594/PANGAEA.842876.

2 Data: Argo floats, a tool for observing large-scale properties of the Polar Seas

Argo floats are free-drifting profiling floats that measure temperature, salinity and pressure of the upper 2000 m of the ocean (indeed there are further types of floats now available that measure to deeper depths and include other sensors such as bioptics). The floats drift at a parking depth, which is typically 1000 m. At the end of their assigned drifting period, the float descends to typically 2000 m, and then ascends to the surface while measuring temperature, salinity and pressure. Once at the surface, the floats drift for a period of time, during which they are programmed to establish connections to overpassing satellites, and transmit their position, time, and measured data. These data are transmitted to data centres around the world (DAC's), to be processed and ultimately made publicly available within hours after collection. Figure 3.1 shows a schematic of the Argo float profiling cycle, taken from the Argo project office website (www.argo.ucsd.edu).

The Argo array project is an international collaboration, with institutes around the world active in the deployment of Argo floats. As such, the Argo array has allowed for the continuous monitoring of the temperature, salinity and velocity of the global ice-free upper ocean. Deployments began in 2000; the target to establish global coverage at a density of 3º x 3º was achieved by the end of 2007. However, Argo floats were initially intended for the ice-free, open ocean. In areas of sea-ice cover, the floats would not be able to surface, and can get damaged in their attempt to surface. They can also become crushed in sea-ice forming or shifting while the floats are at the surface transmitting data to satellite. This problem was solved in 2007, through the development of a sea-ice-sensing algorithm (Klatt et al., 2007), which signals for the likely presence of sea-ice. In the event that sea-ice is predicted, the attempt of the float to surface is aborted, and the data are stored until the next opportunity for transmission arises.

A further improvement to the Argo array occurred in the improvement of data transmission. Originally, Argo float data were transmitted via the Argos System location and data transmission system, which requires that the floats spend 6 to 12 hours at the surface. Today, half of the floats in the Argo array are part of the Argos system. In addition, there are now floats that use positions from the Global Positioning System

(GPS) and data communication using Iridium satellites, which are able to provide more accurate position data and more rapid data transmission.

The Argo float array is unique in that it provides a uniform distribution of data throughout the global ocean, which is not dependant on shipping lanes or repeat ship-based surveys. There is no seasonal bias, as measurements continue every 10 days throughout the lifespan of a float. However, since Argo floats are rarely retrieved, sensors are not recalibrated after a period of deployment. DAC's therefore have the responsibility to scrutinise the data through the application of numerous quality control tests, and to assign data quality flags accordingly. This is implemented at two levels of data processing; at real-time, and to a more in-depth level during delayed-mode processing. During delayed mode processing, float profiles are evaluated by comparison with historical data (Owens & Wong, 2009); corrected "adjusted" values are then provided, which are each assigned a quality flag. The accuracy of Argo float measurements have been reported as follows: temperature measurements are accurate to ± 0.002 ºC, pressures are accurate to ± 2.4 dbar, and salinity measurements depend on the amount of sensor drift, but with a small sensor drift, uncorrected salinities are accurate to 0.1 (although the uncertainty increases with increasing sensor drift).

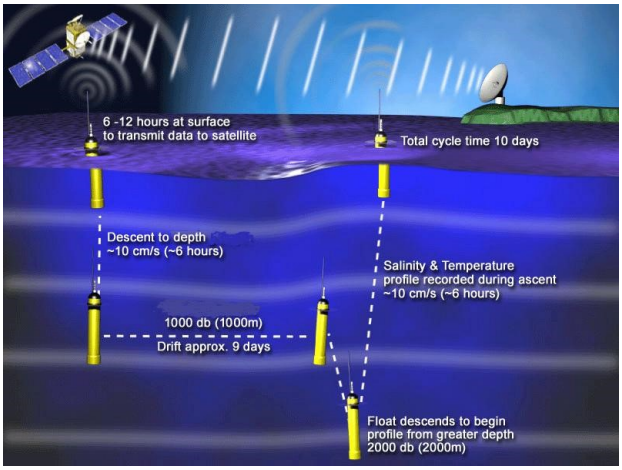

Fig. 2.1. A typical Argo profile cycle, where the duration of each cycle is 10 days. From the Argo project office website, www.argo.ucsd.edu.

In the Weddell Sea, the first Argo floats were deployed in December 2000, although due to damage from sea-ice, were unlikely to live to their full potential (the life expectancy of an Argo float is about 3-4 years). After the introduction of the sea-ice sensing algorithm to the floats, float deployment reached a peak in the austral summers of 2007/2008 and 2008/2009, after which, the number of deployments have continued,

but to a lesser extent (Fig. 3 in Chapter 4). As a result, there are now profile data providing full spatial coverage of the Weddell Gyre, over a period of 17 years. During the first 5 years, profile coverage was limited to regions close to the repeat ship-based surveys along the Prime Meridian and the WOCE transect from Kapp Norvegia to Joineville Island (see Fig. 2a in Chapter 4 for a map of the spatial distribution of float profile data during this time period).

While the sea-ice sensing algorithm has allowed for the measurement of the upper water column under sea-ice, complications occur due to the unknown position of the floats while they are under the sea-ice (the float position is established during data transmission at the surface). To date, the system currently in place provides position data for the under ice profiles by applying linear interpolation to the last known position of the float before it enters the sea-ice, and the first known position of the float after it leaves the region of sea-ice. Linearly interpolated profile positions are thus easy to identify on maps of profile distribution (such as those marked in red in Fig. 4 of Chapter 4). In order to improve the position data of Argo floats in the Weddell Gyre, a series of acoustic moorings have been deployed in strategic locations throughout the Weddell Gyre since 2002, with an approximate spacing of about 300 km (Klatt et al., 2007). Since then, RAFOS floats have been deployed within the Weddell Gyre, which are able to detect pings from the surrounding acoustic moorings. If pings are detected from three or more moorings, the position of the float can be triangulated. Therefore, the floats can be tracked while drifting at parking depth. To date, the processing of RAFOS data is still work in process, but presents a future improvement in our knowledge of the upper ocean velocity field.

In the following three chapters, Argo float data have been implemented in order to determine the large-scale structure of the Weddell Gyre. In Chapter 4, float profile data have been used to map the large-scale hydrographic properties of the Weddell Gyre. In Chapter 5, both float profile and trajectory data were used to determine the large-scale horizontal circulation of the Weddell Gyre. Both required a careful scrutinising of data, which are detailed in Section 2 of Chapter 3, and the appendix in Chapter 4. In the following chapter, the objective mapping of float profile data is described, and maps of the temperature and salinity fields are presented.

3 Publication I:

A gridded data set of upper-ocean hydrographic properties in the Weddell Gyre obtained by objective mapping of Argo float measurements

Published in Earth System Science Data, 8, 15-40, 2016

DOI: 10.5194/essd-8-15-2016

K.A. Reeve[1], O. Boebel[1], T. Kanzow [1], V. Strass[1], G. Rohardt[1], and E. Fahrbach[2]

1 Alfred-Wegener-Institut Helmholtz-Zentrum für Polar- und Meeresforschung, Bremerhaven, Germany

2 deceased

Abstract

The Weddell Gyre plays a crucial role in the modification of climate by advecting heat poleward to the Antarctic ice shelves and by regulating the density of water masses that feed the lowest limb of the global ocean overturning circulation. However, our understanding of Weddell Gyre water mass properties is limited to regions of data availability, primarily along the Prime Meridian. The aim of this paper is to provide a dataset of the upper water column properties of the entire Weddell Gyre. Objective mapping was applied to Argo float data in order to produce spatially gridded, time composite maps of temperature and salinity for fixed pressure levels ranging from 50 to 2000 dbar, as well as temperature, salinity and pressure at the level of the sub-surface temperature maximum. While the data are currently too limited to incorporate time into the gridded structure, the data are extensive enough to produce maps of the entire region across three time composite periods (2001-2005, 2006-2009 and 2010-2013), which can be used to determine how representative conclusions drawn from data collected along general *RV* transect lines are on a gyre scale perspective. The work presented here represents the technical prerequisite in addressing climatological research questions in forthcoming studies. These data sets are available in netCDF format at http://doi.pangaea.de/10.1594/PANGAEA.842876.

3.1 Introduction

The Weddell Gyre provides an important link between the upper ocean and the ocean interior through the formation of Weddell Sea Deep Water (WSDW) and Weddell Sea Bottom Water (WSBW). WSDW in particular contributes significantly to Antarctic Bottom Water; a prominent water mass present throughout much of the abyssal global ocean (Orsi et al., 1999; Johnson, 2008). As such, the Weddell Gyre potentially plays a key role in a changing climate through its role in regulating storage of heat in the deep ocean (Fahrbach et al., 2011). The main source water (and the main heat source) of the Weddell Gyre, Circumpolar Deep Water (CDW), enters at intermediate depths primarily from the east, although the open northern boundary permits intrusions of CDW to a lesser extent (Fahrbach et al., 2004; Klatt et al., 2005; Fahrbach et al., 2011; Cisewski et al., 2011). Upon entering the gyre, CDW becomes known as Warm Deep Water (WDW) and can be identified by its sub-surface potential temperature maximum of 0.6-1 °C (Fahrbach et al., 2011). WDW undergoes water mass transformation to form the underlying water masses. This process is controlled by (1) the transport and mixing of source waters into the gyre (Leach et al., 2011); (2) changes within the Weddell Gyre and on the adjacent shelves through influences from sea-ice and ice-shelves; and finally (3) the transport of modified water masses with the gyre outflow (Foster et al., 1987; Fahrbach et al., 1994; Fahrbach et al., 1995; Fahrbach et al., 2011). A schematic showing the basic Weddell Gyre circulation overlying a map of the bathymetry is shown in Fig. 3.1.

To date, the literature focusing on Weddell Gyre hydrography has been largely based on observations from repeat hydrographic sections – primarily collected during various cruises (see, e.g., Fahrbach et al., 2004, 2007, 2011), as well as data from moorings, deployed both along the Prime Meridian and strategically placed locations throughout the gyre (Klatt et al., 2005; Fahrbach and De Baar, 2010; Behrendt et al., 2011). These data are well-established (there are now 30 years of data collected from RV *Polarstern* alone). Historical measurements, however, date back to the early 1900's; for example, Brennecke (1918) combined the observations from Swedish (1901-03), Scottish (1902-04), French (1908-10) and German (1911-12) expeditions and provided sufficient evidence for proposing the cyclonic circulation of the Weddell Gyre. A review of historical research on the Weddell Gyre is provided by Deacon (1979). These data have provided us with a picture of the structure of the Weddell Gyre and have

provided insight into the role of the Weddell Gyre in a larger climate perspective; Fahrbach et al., (2011) provides an in-depth comprehensive analysis of the variations within the Weddell System. However, much of the analysis of long-term changes is based on data along the Prime Meridian only – a region of high variability due to its close proximity to Maud Rise – influencing the relatively high frequency fluctuations of observed WDW properties.

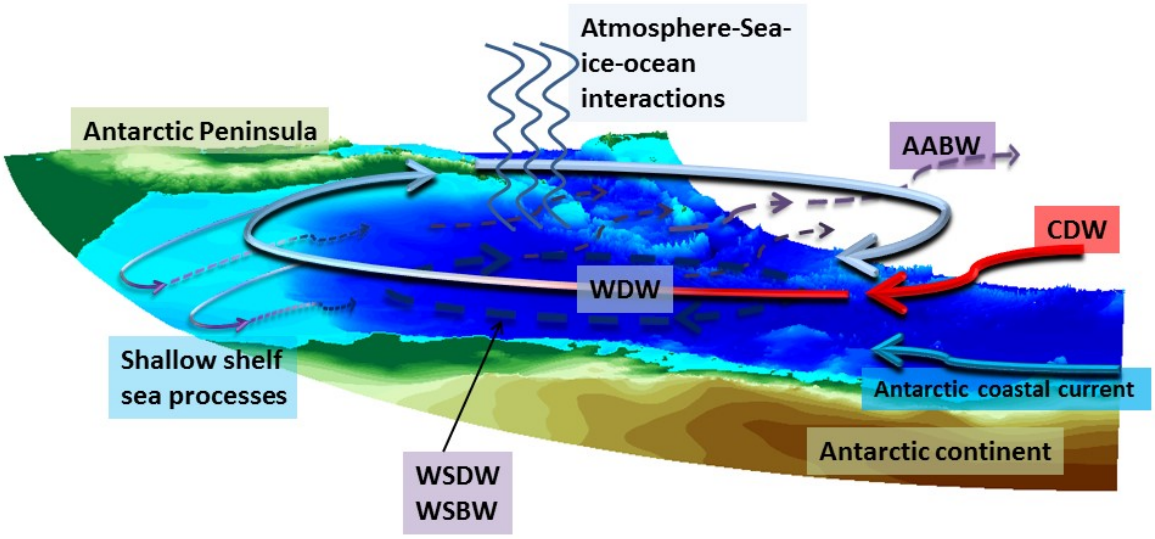

Figure 3.1. Schematic of Weddell Gyre circulation. The underlying 3D map shows ocean bottom depth (IOC, IHO and BODC, 2003). Relatively warm Circumpolar Deep Water (CDW) enters from the east, becoming Warm Deep Water (WDW) which circulates in a cyclonic direction throughout the gyre, cooling en route, due to mixing with surrounding waters and interaction with the atmosphere and sea-ice processes. Shallow shelf sea processes leads to the formation of cold, high-salinity water which, upon leaving the shelf, sinks below WDW to form Weddell Sea Deep and Bottom Waters (WSDW & WSBW); WSDW exits the gyre to the north to become Antarctic Bottom Water (AABW).

In addition to repeat hydrographic sections and moorings throughout the Weddell Gyre, there are also data from Argo floats, drifters and animal-borne sensors. These all combine to provide a multi-platform approach to observing the Weddell Gyre. Here, the authors focus on the Argo float data set, in order to provide an independent data set that can be compared to ship-based observations in the near-future. Moorings are excluded from the analysis as they provide vertically sparse data, while drifters only provide surface data, which is excluded from the analysis due to high surface variability, and animal-borne sensors require special treatment due to salinity and depth

sensor issues. Thus, delayed-mode adjusted Argo float data are the sole focus of this study.

The aim of this paper is to provide a spatially gridded data set of the upper water column properties with particular focus on the entire Weddell Gyre. We describe the method followed in order to objectively map the irregular Argo float profile data onto regularly gridded fields (on both pressure surfaces and onto the level of the sub-surface temperature maximum), excluding regions beyond the Weddell Gyre boundaries (50 to 80° S; 70° W to 40° E; however, the northern boundary is based on the position of the Weddell Front for the pressure surface maps: Section 3.3.1). Associated mapping errors are also provided. While spatially gridded, the resulting mapped fields represent time composites of three separate time periods (2001-2005, 2006-2009 and 2010-2013), since the data are currently too limited to incorporate both a spatial and temporal averaging scheme.

3.2 Source data description: Argo float profiles

Argo is a global array of over 3500 free-drifting profiling floats that measure the temperature and salinity of the upper 2000 m of the ocean, allowing for continuous monitoring of the global upper ocean. While in the major ocean basins the data are abundant enough to provide a relatively uniform distribution of data throughout, the deployment of Argo floats at high latitudes has been considerably more limited; this was especially the case prior to 2007. This is due to the risk of damage to floats resulting from the seasonal presence of sea ice, which prevents the float from surfacing or converges around the float while it is at the surface transmitting data to satellite, thus crushing and damaging the float. A sea-ice sensing algorithm was introduced to floats after 2007 (Klatt et al., 2007) whereby floats “sense” the likelihood of sea-ice at the surface, and can abort attempts to surface, storing the hydrographic data until the next opportunity to surface arises. There are now over 10 years of Argo float data available for the entire Weddell Gyre region, from December 2001 to present, which can be used to determine the spatial variation of upper water column properties throughout the gyre.

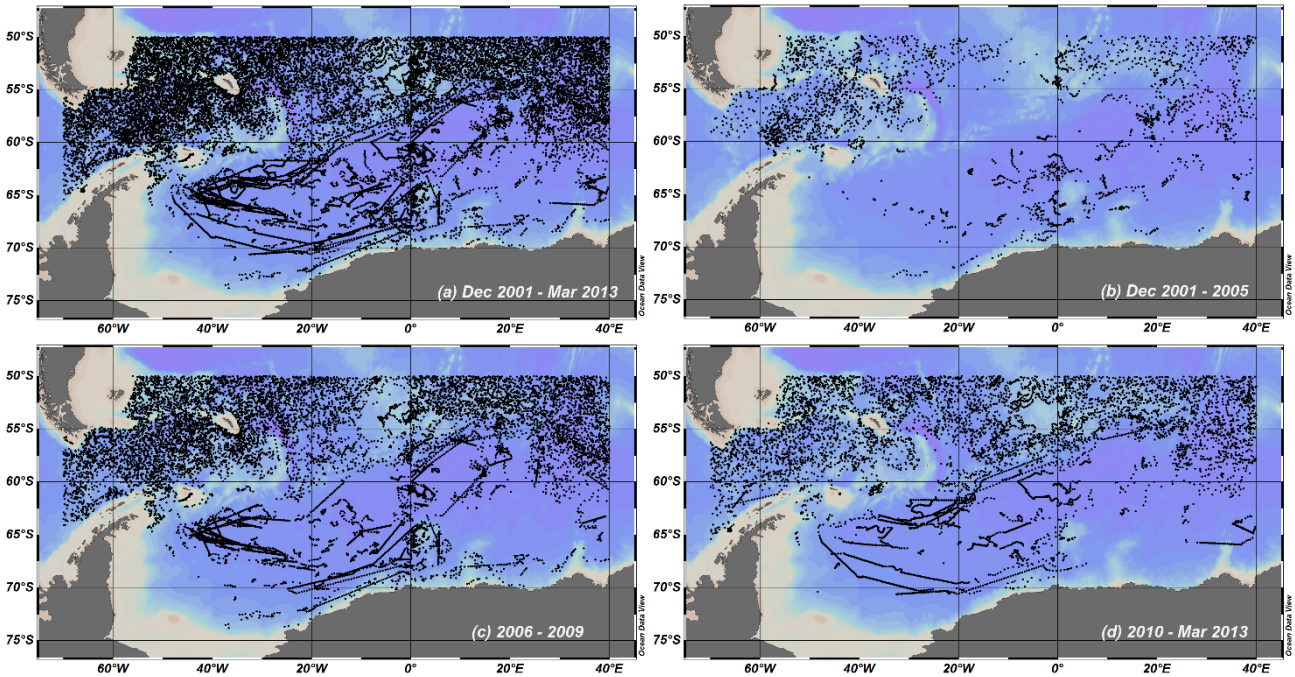

Figure 3.2. Argo float profile locations for **(a)** the entire time period, **(b)** time period (TP) 1, **(c)** TP2 and **(d)** TP3.

Float profile data were retrieved from the Coriolis website (www.coriolis.eu.org). All profiles from within the Weddell Gyre region (50 to 80° S; 70° W to 40° E) from December 2001 to March 2013 were selected. While there are 25,848 profiles, only profiles that have been subjected to delayed-mode quality control processing are used in this study, which leaves about 19,600. The profiles are checked for duplicates, which are subsequently removed (there were only three duplicate profiles from two floats overall). The profile distribution of the remaining profiles are shown in Fig. 3.2b-d. The majority of available delayed-mode profiles occurs in 2008 and 2009 (Fig. 3.3). There is a clear seasonal bias in the number of profiles in the first half of the time series, which reduces after 2007 due to improved float technology as mentioned above (Fig. 3.3). The majority of profiles have a vertical limit of 2000 dbar, although there are more than 1500 profiles that are limited to 1000 dbar (about 75 % of these profiles are actually located north of the Weddell Front; a frontal system which defines the northern boundary when mapping to pressure surfaces; see Section 3.3.1). These "shallow" float profiles most likely occur due to complex bottom bathymetry. Data are filtered according to their corresponding quality flags; only those with a quality flag of 1 are used, which indicates that the data have passed all quality control tests and that the "adjusted value is statistically consistent" (Wong et al., 2014; for more information about the quality control procedure of Argo floats, refer to the quality control manual at

www.argodatamgt.org). Additionally, any data points for which the corresponding adjusted pressure error exceeds 20 dbar are rejected. This is an extra precaution against pressure biases and is in accordance with the guidelines provided on the Argo website (www.argo.ucsd.edu). The temperatures in Argo are reported to be accurate to ± 0.002 °C while pressures are accurate to ± 2.4 dbar (Owens and Wong, 2009). For salinity, if there is a small sensor drift, uncorrected salinities are accurate to ± 0.1 PSU, although this value can increase with increasing sensor drift. Delayed-mode processing subjects all float profiles to detailed scrutiny by comparison with historical data (Owens and Wong, 2009), providing corrected adjusted values while assigning each value with a quality flag. In the delayed-mode adjusted salinity data (with a quality flag of 1) used in this study, the mean adjusted salinity error is 0.01, while the largest error does not exceed 0.1.

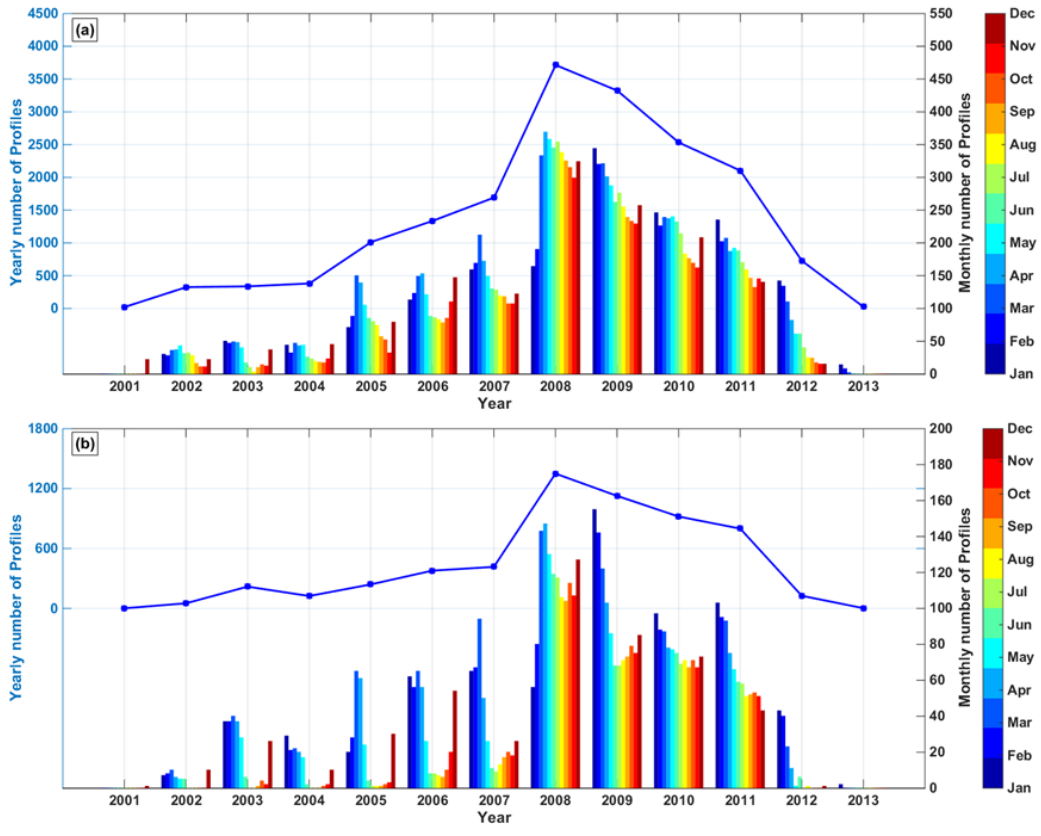

Figure 3.3. The number of profiles per year (line) and per month (bars) from (**a**) south of 50° S to the Antarctic continent and (**b**) south of 60° S to the Antarctic continent, between 70° W and 40° E.

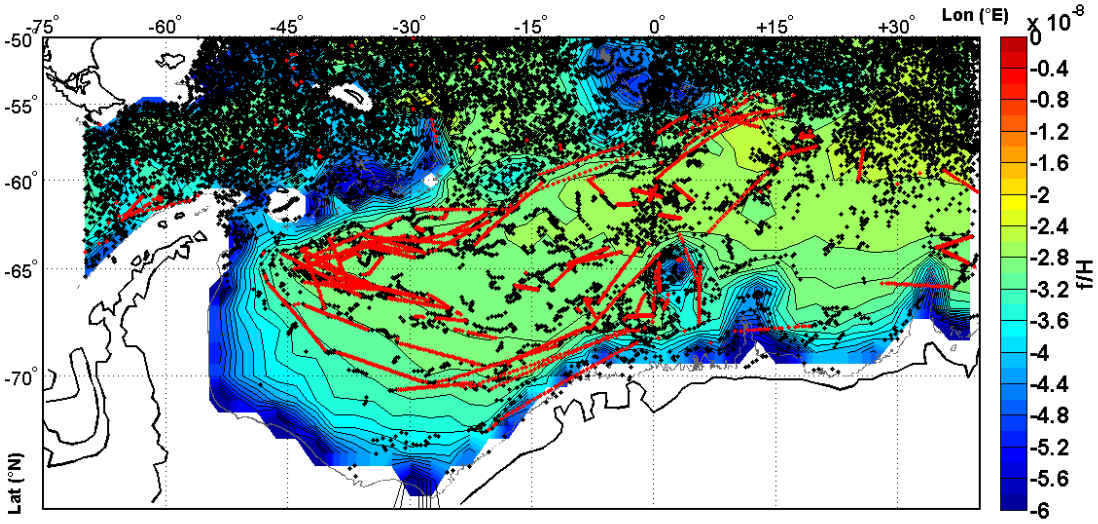

Figure 3.4. Argo float profile stations, with interpolated (under-ice) station locations marked in red. The filled contours show lines of constant planetary potential vorticity, *f/H*. The grey contour shows the 2000 m isobath.

Complications regarding position errors arise when the float enters the sea-ice zone. As already mentioned, new technology has allowed the floats to avoid surfacing in these regions. However, when a float profiles the water column under sea ice, it is not possible for the satellite to determine the float position. Thus, the position of an under-ice float profile is determined by linear interpolation between the last known profile position and the position of the first profile upon exiting the sea-ice zone, using the knowledge that floats perform on a 10-day cycle. Such profiles can be seen in particular in Fig. 3.4, where profiles with an interpolated location are marked in red. This situation will be improved as soon as RAFOS data (Klatt et al., 2007) collected by some of these floats have been analysed. RAFOS floats are fitted with signal receivers and so have the potential to triangulate their positions based on the arrival times of sound signals from moorings deployed in the region. About 13% of all profiles south of 50° S have an interpolated location (about 2600 profiles), although this increases to about 38% south of 60° S (about 2340 profiles). The mean distance between under-ice profiles and their nearest neighbor is about 27 km, although the largest distance is about 265 km. The mean number of days between under-ice profiles and their nearest neighbor is about 24, while the range of days is between 7 and 270. The influence of this uncertainty on the objective mapping will be discussed in Section 3.4 when assessing the robustness of the results.

Table 3.1. Standardized pressure levels (dbar) to which all profiles are linearly interpolated.

Standardized pressure levels (dbar)					
1	50	**15**	280	**29**	800
2	60	**16**	300	**30**	900
3	70	**17**	320	**31**	1000
4	80	**18**	340	**32**	1100
5	90	**19**	360	**33**	1200
6	100	**20**	380	**34**	1300
7	120	**21**	400	**35**	1400
8	140	**22**	450	**36**	1500
9	160	**23**	500	**37**	1600
10	180	**24**	550	**38**	1700
11	200	**25**	600	**39**	1800
12	220	**26**	650	**40**	1900
13	240	**27**	700	**41**	2000
14	260	**28**	750		

Conservative temperature, absolute salinity and potential density are determined from the in situ temperature, practical salinity and pressure variables in the profile data, in accordance with TEOS-10 (the international thermodynamic equation of seawater – 2010; IOC et al., 2010). Conservative temperature is more representative of the "heat content" of seawater than potential temperature (McDougall and Barker, 2011); however, because conservative temperature and absolute salinity have been introduced to oceanography comparatively recently, limiting comparison with historical climatologies and other hydrographic data sets, potential temperature and practical salinity are also provided. The profile data are linearly interpolated onto 41 dbar levels, ranging from 50 to 2000 dbar (Table 3.1). The upper 50 dbar are omitted from the data set due to strong seasonal variability and sea-ice interaction. The 41 levels are spread such that the intervals are smallest at 50 m (10 m) and increase to maximum of 100 m spacing below 800 m. The levels themselves were arbitrarily selected. Objective mapping is applied to the entire data set spanning from December 2001 to March 2013, as well as to three sub-sets, where the data are split according to the following time periods: (1) 2001-2005 (2) 2006-2009 and (3) 2010-2013 (hereafter TP1, TP2 and TP3 respectively). This splits the data set into roughly equal time spans. Note that the gridded fields of potential temperature and practical salinity include data up to 21 October 2014; however, with delayed-mode data availability at the time of data set creation, this provides only a small addition of about 47 profiles within the defined Weddell Gyre region, all of which are north of 62º N.

3.3 Methods

3.3.1 Sub-surface temperature maximum

In addition to temperature and salinity maps of the 41 pressure levels in Table 3.1, maps of temperature, salinity and pressure are also generated at the level of the sub-surface temperature maximum (hereafter Tmax). Examples of typical temperature-pressure profiles from Argo float data within the Weddell Gyre are shown in Fig. 3.5. The sub-surface temperature maxima are clearly marked. There are two reasons for providing the Tmax. Firstly, it represents the core of incoming Circumpolar Deep Water, which is the main source water (and heat source) feeding the Weddell Gyre. Secondly, it is used to define the northern boundary of the Weddell Gyre for the fields mapped onto pressure surfaces. The northern boundary is defined by the Weddell Front, which is controlled by the topography of the sub-surface ridges (e.g. the North Weddell ridge) but is not fixed in position due to strong interactions between the Antarctic Circumpolar Current to the north and the Weddell Gyre flow to the south. The Weddell Front can be located where the core of warm water from the Antarctic Circumpolar Current meets the relatively cold subsurface water of the Weddell Gyre (Fahrbach et al., 2011). Thus, the point at which the meridional gradient of the Tmax is largest is the latitude at which the Weddell Front is located. This boundary definition removes profiles from outside of the Weddell Gyre when mapping to fixed pressure levels, ensuring that profiles strictly within the gyre itself are selected for each grid point, which provides some security when using large length scales to determine the large-scale mean field of the gyre.

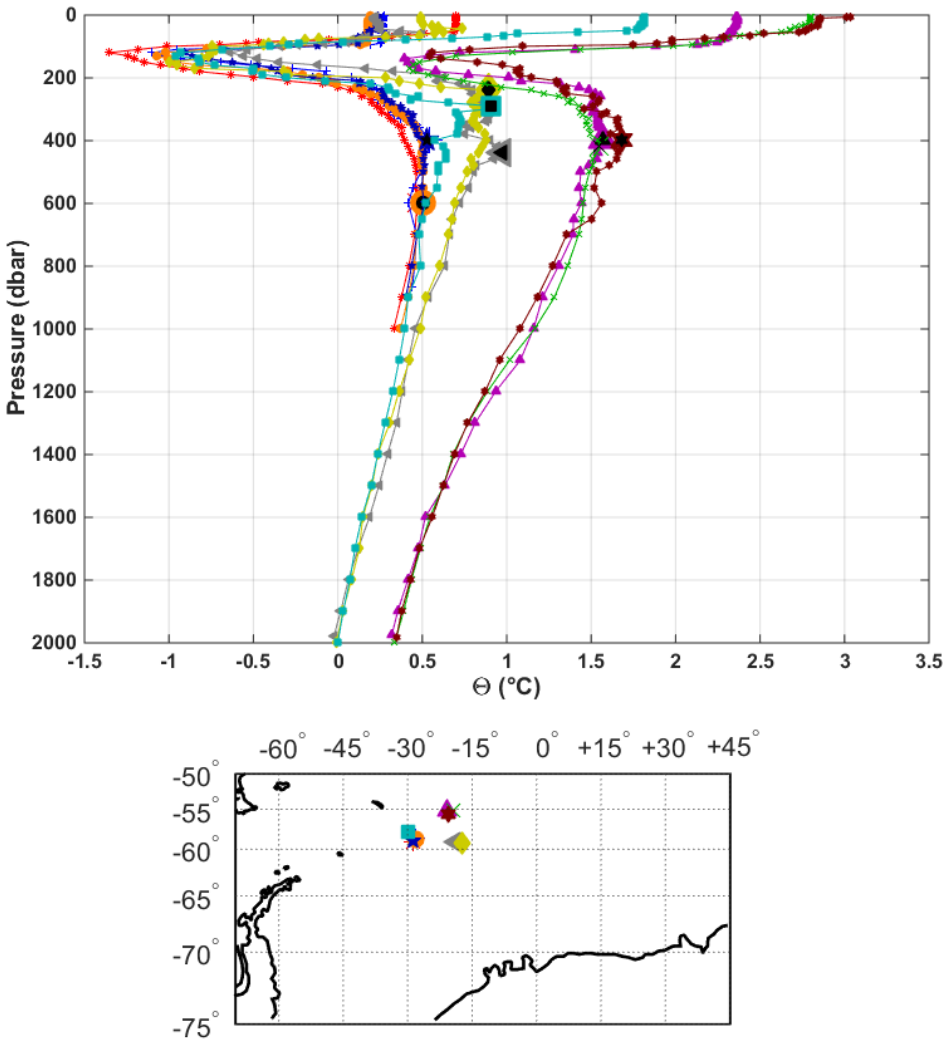

Figure 3.5. A random sample of pressure (dbar) – conservative temperature (°C) profiles from Argo floats within the region 15° to 30° W and 55° to 60° S **(a)** and the corresponding locations of the profiles **(b)**. The sub-surface temperature maximum of each profile is marked with an enlarged symbol.

The Tmax is determined by taking the sum of the *z* scores of temperature and pressure. The *z* score assigns "scores" to data points based on their deviation from the mean. Using *z* scores instead of the standard deviations (from which the *z* scores are calculated) allows for the direct consideration of standard deviations from two different variables: temperature and pressure. Above the Tmax is a sub-surface temperature minimum, which is representative of the water mass known as Winter Water (WW). This minimum is the coldest water at the shallowest depth (which will be at the surface during the winter and migrates to sub-surface level after summer warming at the surface), and can be located by finding the pressure at which point the sum of *z* scores is smallest. The maximum sub-surface temperature can then be determined as the maximum temperature below this temperature minimum. This statistical method finds

the deepest temperature maximum, thus taking into account seasonal surface warming and is particularly useful when dealing with large datasets with large seasonal surface variability. Computationally, the Tmax is determined as follows:

$$X = \text{sum}[z\ \text{score}(\text{tmp}), z\ \text{score}(\text{pressure})];$$

$$i = \text{find}\big(X == \min(X)\big)$$

$$\text{Tmax} = \max(\text{tmp}(i{:}\ \text{end}))$$

3.3.2 Objective Mapping

3.3.2.1 Approach

Due to the irregular nature of the free-drifting profiling float, both in a spatial and temporal context, there are significant challenges regarding the utilization of these data in the creation of statistically robust gridded data sets. One common method in dealing with profile data is the application of optimum interpolation, an adapted form of kriging first developed for application in oceanography by (Bretherton et al., 1976), though a similar method was previously applied in a meteorological context (Gandin, 1965). The technique is based on the Gauss-Markov theorem and provides a point-wise estimate of the interpolated field; this estimate is linear and unbiased and is based on the minimization of the expected interpolation error (i.e. is optimal in the least squares sense; Gandin, 1965; Mcintosh, 1990). The method also provides a map of error variance which takes into account the spatial distribution of the data used.

Objective mapping methods have been implemented in a number of studies, providing spatially averaged climatological data sets of observations as well as for more specific purposes. Wong et al., (2003) and Böhme and Send (2005) have applied the method in a two-stage procedure in order to calibrate float profile salinity data, while Rabe et al., (2011) mapped Arctic observation data in order to determine changes in freshwater content. On a global scale, objective mapping has been used to determine the warming of the global upper ocean, as well as other global ocean indicators (Lyman and Johnson, 2008; Lyman et al., 2010; Levitus et al., 2012). However, the limited volume of data at high latitudes is such that when objective mapping has been applied to float data on a global scale, regions south of ~50-60° S are poorly represented in the mapping process and are typically the primary cause of discrepancies (e.g. Roemmich and Gilson, 2009; Chang et al., 2009; von Schuckmann and Le Traon, 2011).

Objective mapping methods are typically used in the production of climatologies. The most prominent and recent are the WOA atlases (World Ocean Atlas; Locarcini et al., 2006, 2010, 2013; Antonov et al., 2006, 2010; Zweng et al., 2013), which use a three-pass successive correction method (with the exception of WOA98, which applies a one-pass successive correction; Cressman, 1959; Barnes, 1964; Barnes, 1994), and the WOCE atlases (World Ocean Circulation Experiment; Gouretski & Koltermann, 2004; Orsi et al; 2005), which follow the optimum interpolation technique described above. The successive correction method is used in WOA in order to avoid the use of second-order statistics due to the paucity of data (Locarcini et al., 2013), while WOCE justify the use of the Gauss-Markov technique by acknowledging that the Gaussian correlation function used is highly arbitrary and results in over-smoothing on small scales (McIntosh, 1990; Gouretski & Koltermann, 2004), but that the successive correction method may yield less consistent results (Sterl, 2001; Gouretski & Koltermann, 2004). Here, the optimum interpolation (or "Gauss-Markov technique") is used. The most notable differences between the mapping method described in the following section and the approach used in the climatologies above are discussed in Section 3.6.1.

In this study, the aim is to provide a broad outlook on the properties across the entire Weddell Gyre. Therefore the objective mapping omits temporal averaging resulting in maps that represent spatially gridded time composites of the field variables for these time periods. The mapping process is implemented in a two-step procedure, allowing for a step-by-step improvement of the mean field estimate. In the first stage, the first-guess field is the zonal mean, and the covariance is a function of large-scale separation. The resulting field estimate then becomes the first-guess field in the second stage of mapping, where the covariance is a function of small-scale separation, which gives extra weight to close-by data in regions where the data are abundant. In regions of sparse data density, the objective estimate reverts back to the mean guess field and the corresponding mapping error is large. This two-stage method approach reduces the possibility for errors by providing an improved estimate of the first-guess field, which leads to a general reduction in the magnitude of the signal variance, $<s^2>$, by which the covariance matrices are scaled.

3.3.2.2 Objective Mapping

For each pressure surface, the corresponding temperature and salinity data are extracted from the vertically linearly interpolated float profiles (for further details refer to Section 3.2). Thus, only vertically interpolated data at the pressure surface which they are to be mapped to are included in the mapping. The extracted data points are objectively mapped onto a regular 1° x (1°/cos(-65°)) grid. This results in grid cells of approximately 110 km x 110 km at 65 °S – roughly the central axis of the gyre. For each grid point, *N* representative profiles (*x*) are selected for the mapping procedure (for details regarding the selection procedure, refer to Section 3.3.2.3). The objective estimate of the variable, X_{g1}, at the grid point *g* is given by Eq. (1a) for stage 1 and Eq. (1b) for stage 2. The zonal mean, $\bar{x}_z$, is the first-guess field in stage 1 while the objective estimate from stage 1 becomes the first-guess field used in stage 2. The term ω denotes the weighting matrix (Wong et al., 2003).

$$X_{g1} = \bar{x}_z + \omega \cdot (x - \bar{x}_z) \tag{1a}$$

$$X_{g2} = X_{g1} + \omega \cdot \left(x - X_{g1}\right) \tag{1b}$$

Each profile *x* is weighted by the horizontal distance *D* and the fractional distance *F* in potential vorticity: (1) between the grid point location *g* and the profile location *i*, and (2) between the neighbouring N profile locations, *i* and *j*. Thus, the profiles are not just weighted according to their distance to the grid point but also to neighbouring profiles. As such, where three profiles may have the same distance to a grid point, the profile furthest away from the neighbouring profiles will be assigned the largest weight (for example, refer to Fig. 3.6). The fractional distance *F* (Eq. 2) accounts for the cross-isobath separation between two locations. This reflects the influence of potential vorticity, and thus bathymetry (Fig. 3.7) and the Coriolis force (and therefore changes in latitude); potential vorticity strongly influences the flow patterns of water masses, which is accounted for by the following equation (Böhme and Send, 2005):

$$F = \frac{|PV(a) - PV(b)|}{\sqrt{PV^2(a) + PV^2(b)}} \tag{2}$$

where *a* and *b* represent the locations of grid point *g* and profile *i* or the neighbouring *N* profile pairs, *i* and *j*. *PV* is the barotropic potential vorticity; $PV = \frac{f}{H}$, where *f* is the Coriolis parameter and *H* is the full ocean depth, based on the general bathymetric chart

of the oceans (GEBCO; IOC et al.,2003). The distances D and F are scaled by a horizontal length scale L ($L_{(stage\ 1)}$ = 1000 km and $L_{(stage\ 2)}$ = 500 km) and a cross-isobath scale ϕ ($\phi_{(stage\ 1)}$ = 0.5 and $\phi_{(stage\ 2)}$ = 0.25) respectively. See Section 3.3.2.3 for the reasoning behind the chosen values for L and ϕ.

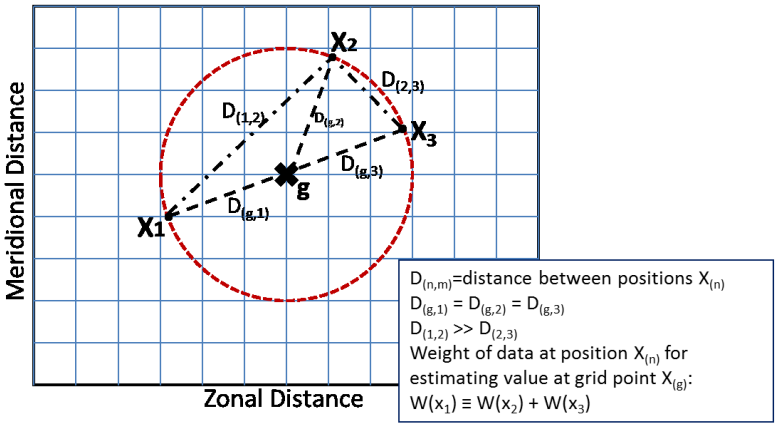

Figure 3.6. In objective mapping, the profile data are weighted based on their distance D to the grid point g, as well their distance to neighbouring profiles. Thus, while profiles x_1, x_2 and x_3 are all equally distanced from the grid point g, x_2 and x_3 are more closely spaced to each other than they are to x_1. Thus, the weight of x_1 would be equivalent to the sum of weights for x_2 and x_3 (i.e. $W(x_1) = W(x_2) + W(x_3)$).

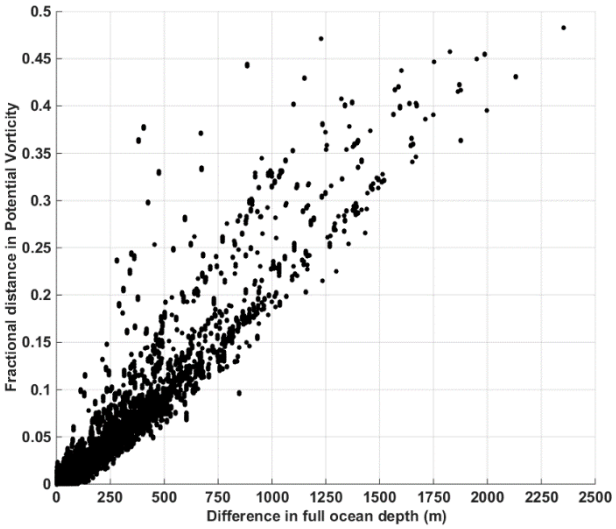

Figure 3.7. The fractional distance in potential vorticity (F) as a function of the difference in bottom ocean depth (H) between two locations. This is the generalised distance used in the decay scale of the covariance function in order to take into account cross-isobath separation (see text for explanation: Section 3.3.2.2).

The decay scales determined by the distances D and F and their associated length scales are applied in the form of covariance functions in order to determine the weight matrix, ω (Eq. 3). The data-grid covariance (C_{dg}; Eq. 4) is a function of the

distances between the grid point g and the profile location i while the data-data covariance (C_{dd}; Eq. 5) is a function of the distance between the N neighbouring profiles, i and j. Thus, for every grid point, while C_{dg} is a *1 x N* vector, C_{dd} is a *N x N* matrix. The covariance of the data is assumed to be Gaussian, following (Böhme and Send, 2005).

$$\omega = C_{dg} \cdot [C_{dd} + I \cdot \langle \eta^2 \rangle]^{-1} \tag{3}$$

$$C_{dg_i} = \langle s^2 \rangle \cdot \exp\left\{-\left[\frac{D_{ig}^2}{L^2} + \frac{F_{ig}^2}{\phi^2}\right]\right\} \tag{4}$$

$$C_{dd_{ij}} = \langle s^2 \rangle \cdot \exp\left\{-\left[\frac{D_{ij}^2}{L^2} + \frac{F_{ij}^2}{\phi^2}\right]\right\} \tag{5}$$

$$\langle s^2 \rangle = \left(\frac{1}{N}\right) \sum_i (x_i - \bar{X})^2 \tag{6}$$

$$\langle \eta^2 \rangle = \left(\frac{1}{2N}\right) \sum_i (x_i - x_n)^2 \tag{7}$$

The covariance functions are scaled by the signal variance, $<s^2>$ (Eq. 6). N is the number of profiles used to estimate the value at the grid point. The mean field $\bar{X}$, is the zonal mean in the first mapping stage, while the objective estimate from stage 1 becomes the mean field in the second mapping stage. A random noise signal (i.e. the noise variance), $<\eta^2>$ (Eq. 7), is added to the diagonal of the data-data covariance function, where x_n is the variable of the profile with the smallest distance to the profile location i. This term accounts for the variations between nearby data.

In addition to providing an estimate of the field at locations where there are no data, objective mapping also provides an error variance of the objective estimate. This is taken from the second stage of the mapping:

$$\sigma_g^2 = \langle s^2 \rangle - C_{dg} \cdot [C_{dd} + I \cdot \langle \eta^2 \rangle]^{-1} \cdot C_{dg}^T \tag{8}$$

where the superscript T signifies the transposition of the matrix C_{dg}.

3.3.2.3 Choosing appropriate length scales (L, F) and selecting N surrounding data points to a grid point

In stage 1 of the mapping, the length scales are L = 1000 km and ϕ = 0.5, while in the second mapping stage, in order to give extra weight to nearby data points, L = 500 km and ϕ = 0.25. Thus, a factor of 4 in the difference *f/H* is equivalent to a 500 km

horizontal separation on the separation parameter; the decay scale used in the covariance functions (Hadfield et al., 2007). The performance of the objective mapping is sensitive to the length scales used in the correlation function. For a successful and accurate mapping of the field of variables, the applied length scales need to be larger than the minimum distance between data points. Otherwise, the mapped estimate will revert to the mean first-guess field used in the mapping, and the resulting mapping error will be large. In order to estimate suitable length scales for the mapping, the percentage of grid points with at least 40 data points within certain distances are calculated in a similar manner to (Hadfield et al., 2007). The results are shown in Fig. 3.8. The minimum distance where 100 % of the grid points have at least 40 data points for the entire time series is 1000 km. However, while the percentage remains high (about 99%) for TP2 and TP3, the percentage decreases to about 95% for TP1. At 500 km, about 95 % of the grid points have 40 or more data points for the entire time period; about 75, 93 and 90% of the grid points have more than 40 data points within 500 km for the time periods TP1, TP2 and TP3 respectively. This value rapidly decreases for distances less than 500 km. Therefore, 1000 km is used for the large length scale in the first mapping stage and 500 km is the small length scale L used in the second mapping stage.

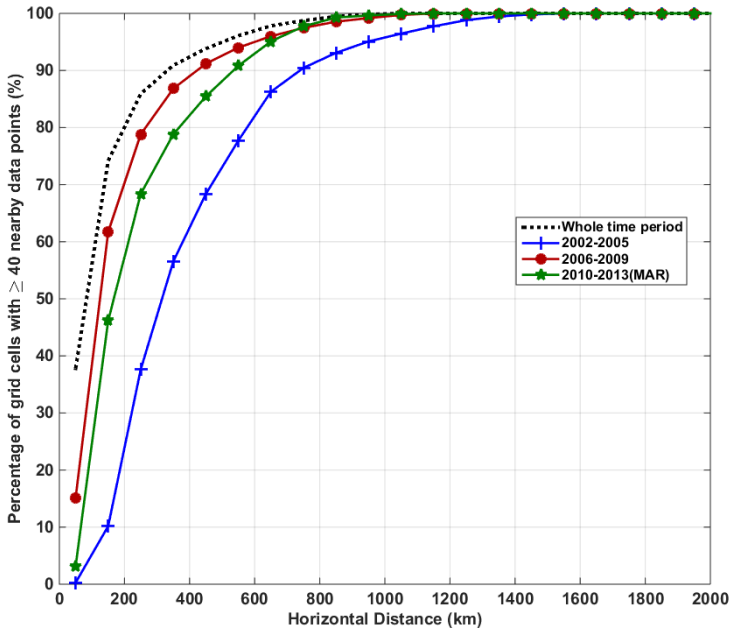

Figure 3.8. The percentage of grid cells with at least 40 profiles within an area of different radii, for different horizontal distances (km).

The number of data points (N) used in the calculation of the field estimate was set to 40, a necessary limitation to cope with constraints in computational power. The decay scale of the data-grid covariance function ($D_{ig}^2/L^2 + F_{ig}^2/\phi^2$) was applied to the data with the large length scales of stage 1 (L = 1000 km and ϕ = 0.5), and all corresponding data points where the decay scale was larger than 1 were filtered out (i.e. only data within the e-folding scale of the covariance function were selected; $D_{ig}^2/L^2 + F_{ig}^2/\phi^2 < 1$). Where more than 40 profiles were available within the decay scale limit, data were sub-selected by the shortest possible distance to the grid point (i.e. smallest decay scale values). Figure 3.9 demonstrates the influence of incorporating a cross-isobathic separation factor into the decay scale. The contours show the field of influence about a grid point at 71º S, 15º W (i.e. the e-folding scale); this field is circular when the decay scale is based purely on the horizontal separation between grid point and profile locations (Fig. 3.9a) and elongates along lines of constant potential vorticity when the cross-isobathic separation factor is incorporated (Fig. 3.9b). Figure 3.10 shows the influence of the cross-isobathic separation factor for a grid point close to the 2000 m contour line. Therefore, it is possible to use first principals of physical oceanography (as a water parcel is more likely to travel along lines of constant potential vorticity) to sensibly extrapolate to regions of sparse data coverage, so long as there is little variation in bottom bathymetry (the resulting mapping error will be large in areas of complex bathymetry, regions which consequently show dense contouring of potential vorticity).

At first, the mapping process was carried out for the Tmax. The resulting field of conservative temperature was used to determine the northern boundary of the gyre: for each longitudinal bin, the latitude where the sub-surface temperature is more than 2 °C is masked. Following this, the latitude at which the meridional sub-surface temperature gradient is largest is defined as the position of the Weddell Front. All grid cells north of this latitude are masked in the following objective mapping processes. This ensures the N profiles for any grid point are selected from within the Weddell Gyre. The mapping process is then carried out for 41 pressure surfaces, ranging from 50 to 2000 dbar.

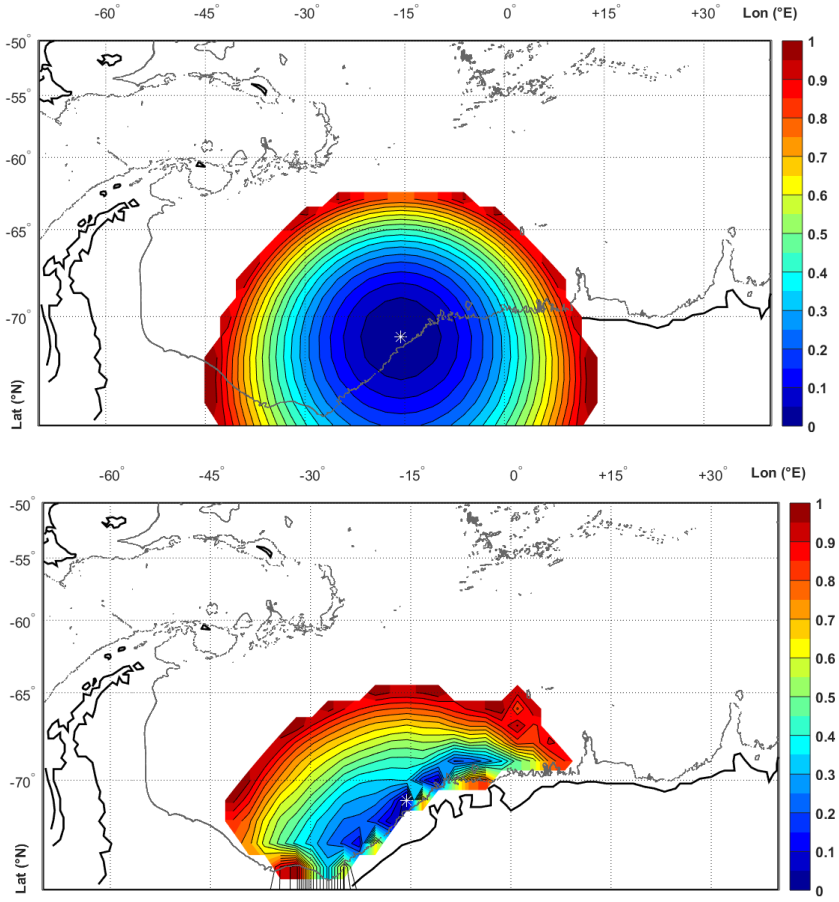

Figure 3.9. The e-folding decay scale for a grid point at ~15º E, 71º S with **(a)** only a horizontal component (i.e. $\exp\{-[D^2/L^2]\}$) and **(b)** with the cross-isobathic separation factor as the second component of the decay scale (i.e. $\exp\{-[D^2/L^2 + F^2/\Phi^2]\}$). See Section 3.3.2 for explanation. The grey contour shows the 2000 m isobath.

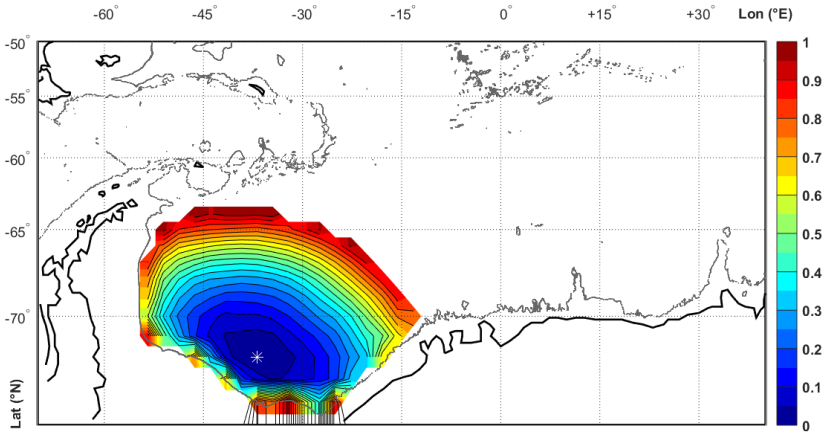

Figure 3.10. The e-folding decay scale for a grid point at~38º E, 72º S. The grey contour shows the 2000 m isobath.

3.4 Objective Mapping performance

3.4.1 Error sources

Interpolated fields of Argo profile data, such as conservative temperature and pressure at the level of the Tmax (Fig.3.11-12) and the maps presented in Section 3.5, may include several types of error one should be aware of. The first and most obvious is instrument error (Section 3.2); the second is the relative error of the objective interpolation (i.e. mapping error), which is the square root of the mapped error variance provided ($\varepsilon_g = \sigma_g^2$; Eq. 8). The mapped error takes into account the spatial distribution of the input data as well as its signal variance. The mapping error (e.g. Fig. 3.11c) is the quantitative error value provided and is representative of these factors but should only be taken to represent an estimate of error associated with the specific interpolation method. Indeed, this statistical error is sensitive to length scales used in the covariance functions within the mapping process. The error estimate is inaccurate because the "true" covariance function is unknown. The mapping errors are relatively small within regions of adequate data coverage, with small horizontal gradients of change within the variable to be mapped (so that the corresponding signal variance across the N data points is small), and where bathymetry is considerably constant (thus, leading to small variation in planetary potential vorticity). In the western sector of the gyre interior, the bathymetry is relatively flat and the horizontal gradients of change are relatively small. Therefore, the mapping errors in these regions are also small despite the sparsity of data, with the exception of areas where there are no data points nearby, such as in the far south-west region. In regions with dense data coverage, mapping errors can be high if bottom bathymetry is complex due to the increase in the cross-isobath separation between locations, regardless of horizontal distance. This can be seen along the northern gyre periphery, especially east of about 20º W: the data coverage is large and yet so are the mapping errors (west of 20º W there is a spatial gap over the northern submerged extension of the Antarctic Peninsula, which explains the large errors in this region). The bathymetry is complex due to the presence of submerged ridges and trenches. It is also at the very periphery of the gyre where complex interaction with the Antarctic Circumpolar Current takes place (e.g. Fahrbach et al., 2004; Klatt et al., 2005; Fahrbach et al., 2011). Thus, the objective mapping is poorly representative of these highly variable, complex regions. One way to improve the objective estimate of these regions is to incorporate more suitable correlation length scales as well as a temporal separation

factor into the decay scale in Eq. (4) and Eq. (5), such as in Böhme and Send (2005). The correlation length scales would need to match the scale of the true field in order to adequately map these regions. Since these regions typically only occur at the very periphery of the gyre, and due to data sparsity throughout the relatively invariant inner gyre, the correlation length scales are chosen to represent the large-scale field of the entire gyre. Thus, mapping error can be very low in regions of sparse data coverage if bathymetry is constant between the grid point and the station locations, and if the difference in water properties between the N neighbouring profiles are also small.

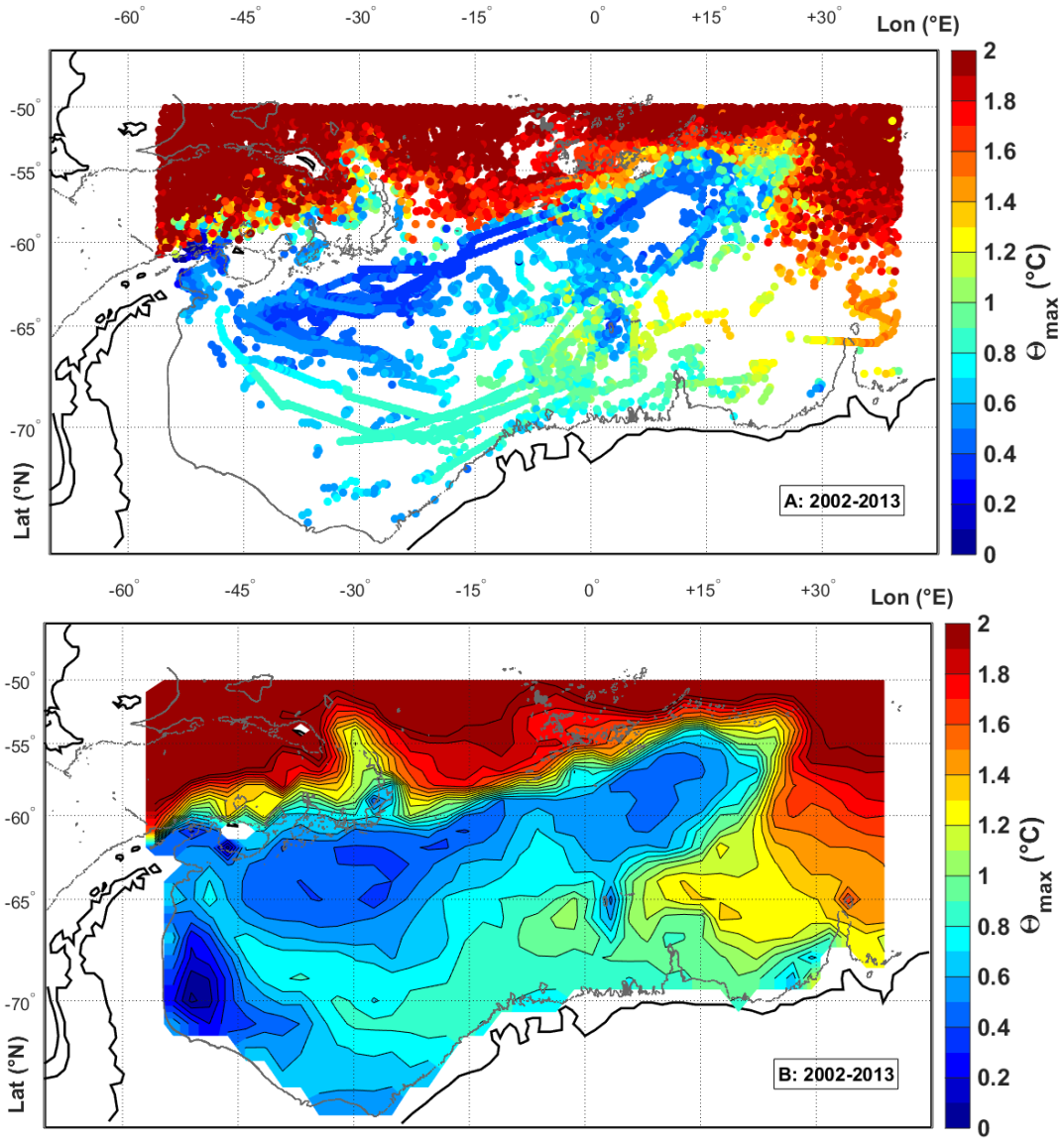

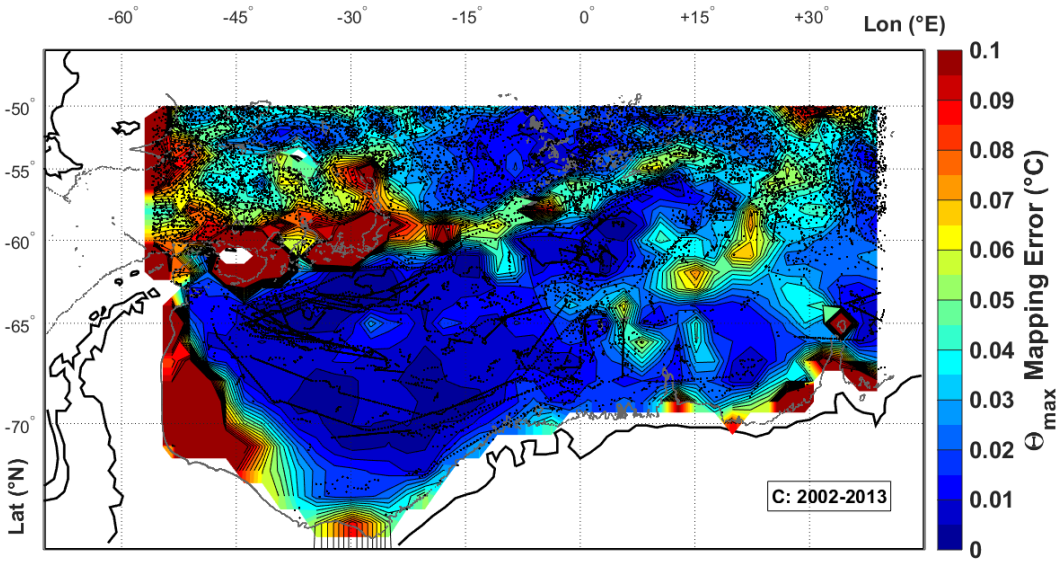

Figure 3.11. Conservative temperature (°C) at the sub-surface temperature maximum for the entire time period, where panel **(a)** shows the original float data, panel **(b)** shows the objectively mapped field and panel **(c)** shows the mapping error for the mapped field (profile locations are marked as black dots). The grey contour shows the 2000 m isobath.

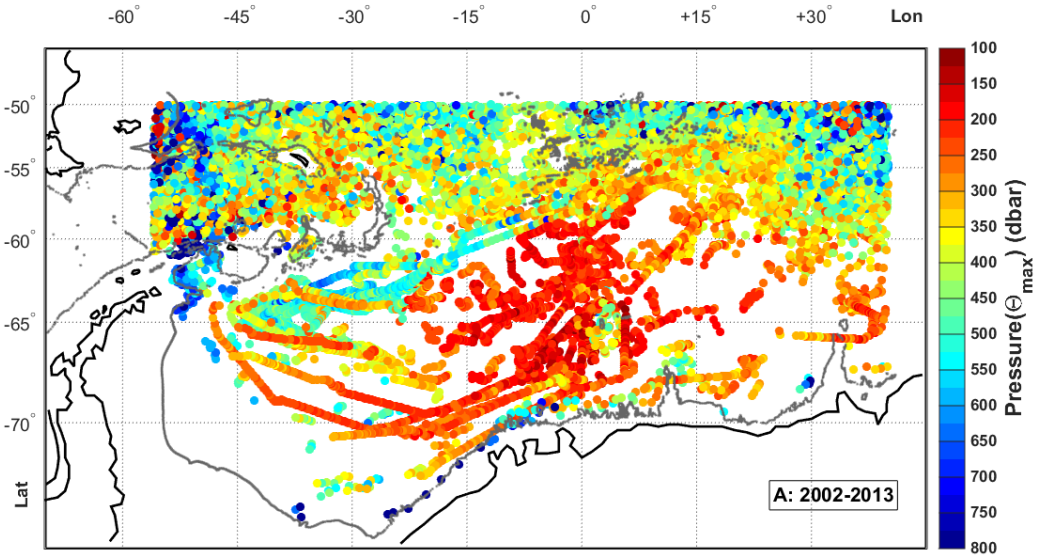

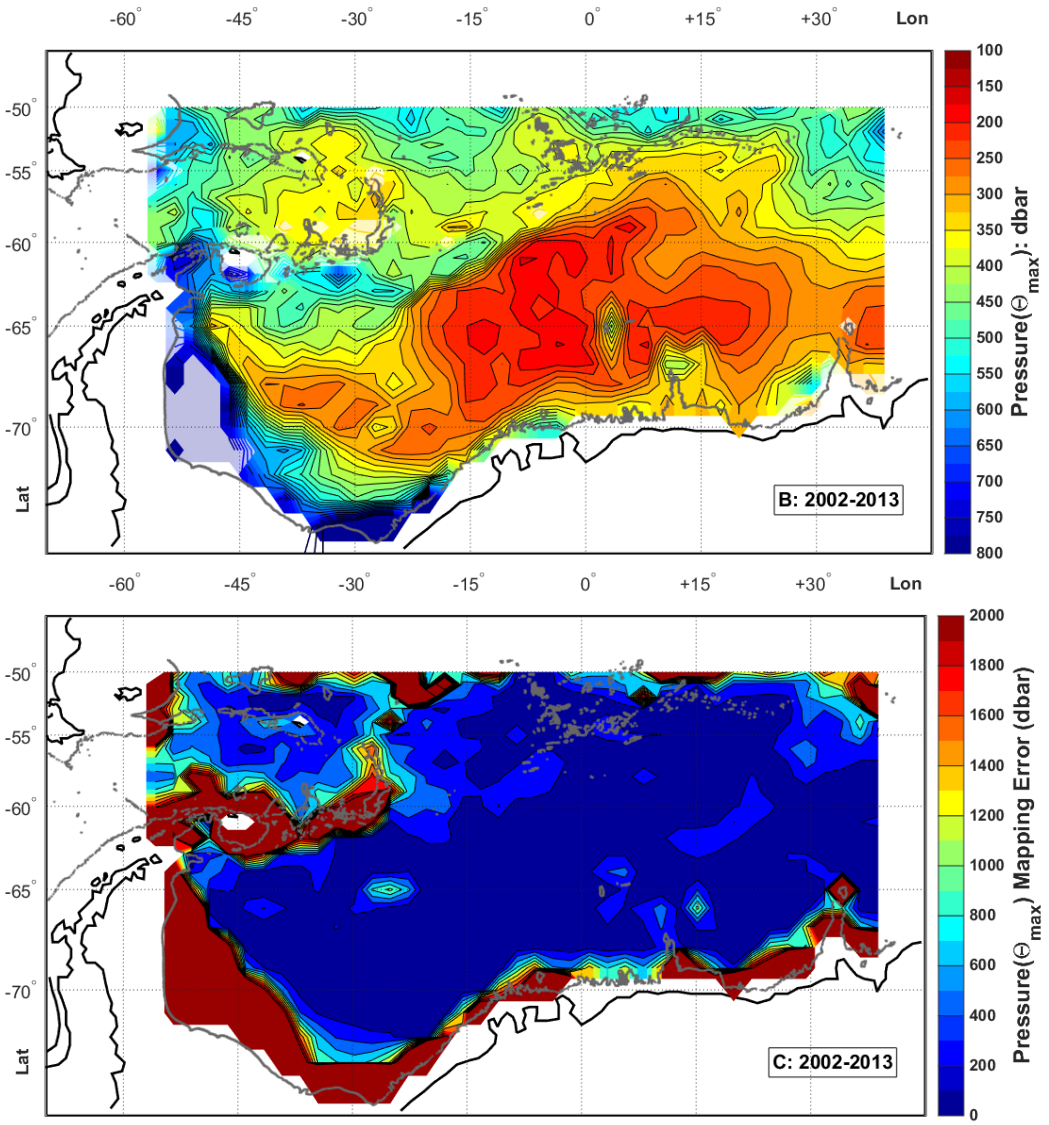

Figure 3.12. Pressure (dbar) at the sub-surface temperature maximum for the entire time period, where panel **(a)** shows the original float data, panel **(b)** shows the objectively mapped field and panel **(c)** shows the mapping error for the mapped field (profile locations are marked as black dots). The grey contour shows the 2000 m isobath.

Another source of error which must be taken into consideration concerns the under-ice profiles whose positions are linearly interpolated from the closest known positions of the float, as discussed in Section 3.2 (and shown in Fig. 3.4). The positions of these floats are clearly flawed, yet the question is, whether this impacts significantly on the estimated fields. We can make the assumption that floats follow contours of constant planetary potential vorticity (i.e. the *f/H* contour lines in Fig. 3.4) in order to maintain constant angular momentum. For the most part, we see that the linear interpolation of the float positions stay within regions of constant *f/H*; thus the position error can be assumed to be insignificant on the scales at which mapping is applied. The

exceptions are the southernmost floats closest to the 2000 m bathymetric contour (i.e. those that drift with the water that flows along the coastline), particularly at about 10 and 35ºE, where bathymetric features cause zonal variation in *f/H*. These are the regions along the Antarctic coastline where complex bathymetry, lack of available profiles, and interaction between the flow of the incoming Circumpolar Deep Water and the cold, westward Antarctic coastal current play a role in increasing error and result in relatively increased mapping errors.

A further potential factor influencing the mapped data output is linked to the selection process of N representative profiles for each grid point objective estimate. Many studies incorporate a decision process whereby one third of the profiles are randomly selected from within the e-folding scale of the covariance function in Eqs. (4) and (5), (i.e. $D_{ig}^2/L^2 + F_{ig}^2/\phi^2 < 1$), one third is selected on the basis of the smallest distance within the large correlation length scales, and the remaining third of profiles is selected on the basis of the shortest spatial and temporal separation distances (see, e.g., Böhme and Send, 2005; Rabe et al., 2011). This was done in order to remove potential bias by selecting nearby profiles, such as, for example, those from along repeat hydrographic sections, which are closely spaced in both distance and time. In this study, only data within the e-folding scale of stage 1 are selected, in accordance with the studies above. Where there are more than N (N=40) profiles available, the N profiles with the smallest spatial separations (based on both horizontal distance and planetary potential vorticity separation) are selected. This is justified because the only data utilized comes from Argo floats, which are independent of repeat-ocean transects. Furthermore, it is a necessary compensation due to limited data availability (and thus the necessity of large correlation scales).

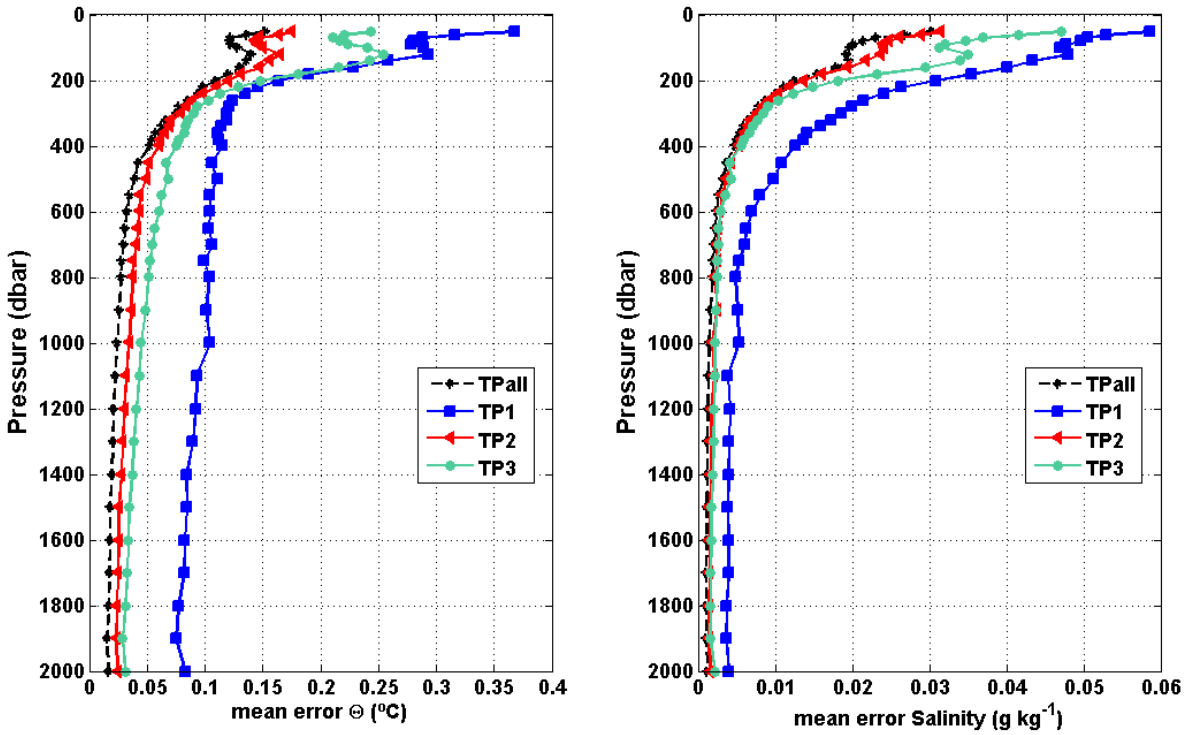

Figure 3.13. The vertical pressure profile of the area-weighted mean mapping error for **(a)** conservative temperature (°C) and **(b)** absolute salinity (g kg^{-1}); for the entire time period (black circles, dashed line), as well as TP1, TP2 and TP3 (the blue squares, red triangles and green circles respectively).

The mapping errors vary according to the corresponding pressure level. Figure 3.13a and b show the vertical variation of the area-weighted mean mapping error for conservative temperature and absolute salinity respectively. While the error limits are relatively invariant below 400 dbar, there is a considerable change in shallower waters. For all time periods, there is a small peak in mean error at about 120 dbar and a small minimum at about 70-90 dbar for temperature. The features are also present in salinity but to a much lesser extent, where the peaks are less clearly defined. This coincides with the region of Winter Water, where the maximum peak occurs at the approximate depth of the lower boundary (see, e.g., Fig. 3 in Behrendt et al., 2011). Thus, seasonal signals may have led to the increase in the mapping errors in the shallower mapped surfaces, which should be taken into account when interpreting the mapped surfaces above 200 dbar.

3.4.2 *Mapping the sub-surface temperature maximum: two approaches compared*

When mapping to the level of the Tmax, there are two approaches one can take. One approach is to extract the corresponding pressure, temperature and salinity values at the Tmax for every float profile in the dataset and map each variable independently. This is the approach outlined in Sect. 3.3.1. Another approach is to extract the pressure of the Tmax for each float profile and apply objective mapping to the pressure variable alone in order to determine a regular gridded data set of pressure at the level of the Tmax. For each grid point, one then selects the *N* closest profiles, from which the temperature and salinity values are extracted at the pressure level provided by the mapped field previously determined. Thus, the resulting mapped fields of temperature and salinity are dependent on the mapped pressure of the Tmax rather than the individual profiles themselves. Both approaches were investigated and compared for the entire time period. The resulting mapped field of temperature and the corresponding mapping error are shown in Fig. 3.11b, c for the first approach and in Fig. 3.14 for the second approach. The mapped temperature fields for the two approaches are similar. The differences between the two temperature maps is less than 0.15° C throughout the Weddell Gyre, with the exception of regions at the gyre periphery where the differences can be as high as 0.4° C (Fig. 3.15). The first approach typically yields warmer values than the second approach throughout most of the region (hence the map in Fig. 3.15 is largely negative (blue), as it shows temperature from approach 2 with regard to temperature from approach 1). The second approach leads to slightly larger mapping errors, in particular along the Antarctic coastline. Thus, the first approach, where the temperature, salinity and pressure of the Tmax are independently mapped, is the approach followed in this study. Taking temperature as an example, for the first approach, at any one grid point, the mapped temperature is mapped from the temperature of the Tmax of individual profiles, and thus the *N* data points could all have differing pressures, but all represent that same Tmax value. Thus the individual pressures are a deviation from the objectively weighted mean pressure. The second approach however, by taking the temperature values of the *N* profiles at the level of the mapped Tmax pressure, all have the same pressure; however, they are not necessarily at the actual Tmax of their corresponding profiles but rather represent a deviation from the objectively weighted mean temperature of all *N* profiles. Thus, while the mapping error is largely based on both horizontal length scales and planetary potential vorticity

separation, the differences between the methods described above (Fig. 3.15) could be interpreted as an error estimate of the variability in the vertical range of the Tmax that can be attributed to small-scale processes (e.g. to internal waves, tides, temporal uncertainties) that are ultimately smoothed out in the mapping process. If this interpretation were to hold true, the mapping error due to large-scale smoothing would be 0.15 ºC or less for the majority of the Weddell Gyre and would increase to as much as 0.4 ºC in regions of high variability such as north of the western periphery or in regions of no data such as in the far west of the gyre for temperature at the level of the Tmax. We can assume that this estimate would increase for pressure levels above the Tmax and significantly decrease below the Tmax based on Fig. 3.13. As these error estimates are open to interpretation, they are not included in the final mapped error estimates. Furthermore, these errors also apply to the field variables mapped onto standard pressure levels. However, the errors would be reduced as the input data are interpolated to standardized pressure levels prior to interpolation, which removes small-scale instabilities.

The mapping error of pressure at the level of the Tmax (Fig. 3.12c) has the largest corresponding mapping errors of all mapped surfaces, ranging from 5 m within the gyre interior to an excess of 50 m at the coast and in the north-west gyre periphery, directly over sub-merged mountain ridges that extend from the Antarctic Peninsula. This is because it is subjective to allocate a specific point at which the temperature has reached its maximum in many of the profiles, while the temperature values themselves differ only slightly. Although a statistical method is employed here (see Sect. 3.3.1), the processes that influence the position of the Tmax are too complex for the method to be extremely accurate, and the number of profiles are too numerous to identify each peak manually. Some profiles do not have a pronounced Tmax. The peak temperature then occurs with a small vertical gradient, so a small change in temperature could shift the peak temperature by hundreds of meters. Thus, while the mapping of the Tmax is relatively successful, caution needs to be exercised when considering the pressure at the level of the Tmax. It is primarily for this reason that the second approach described above was not used in the mapping process.

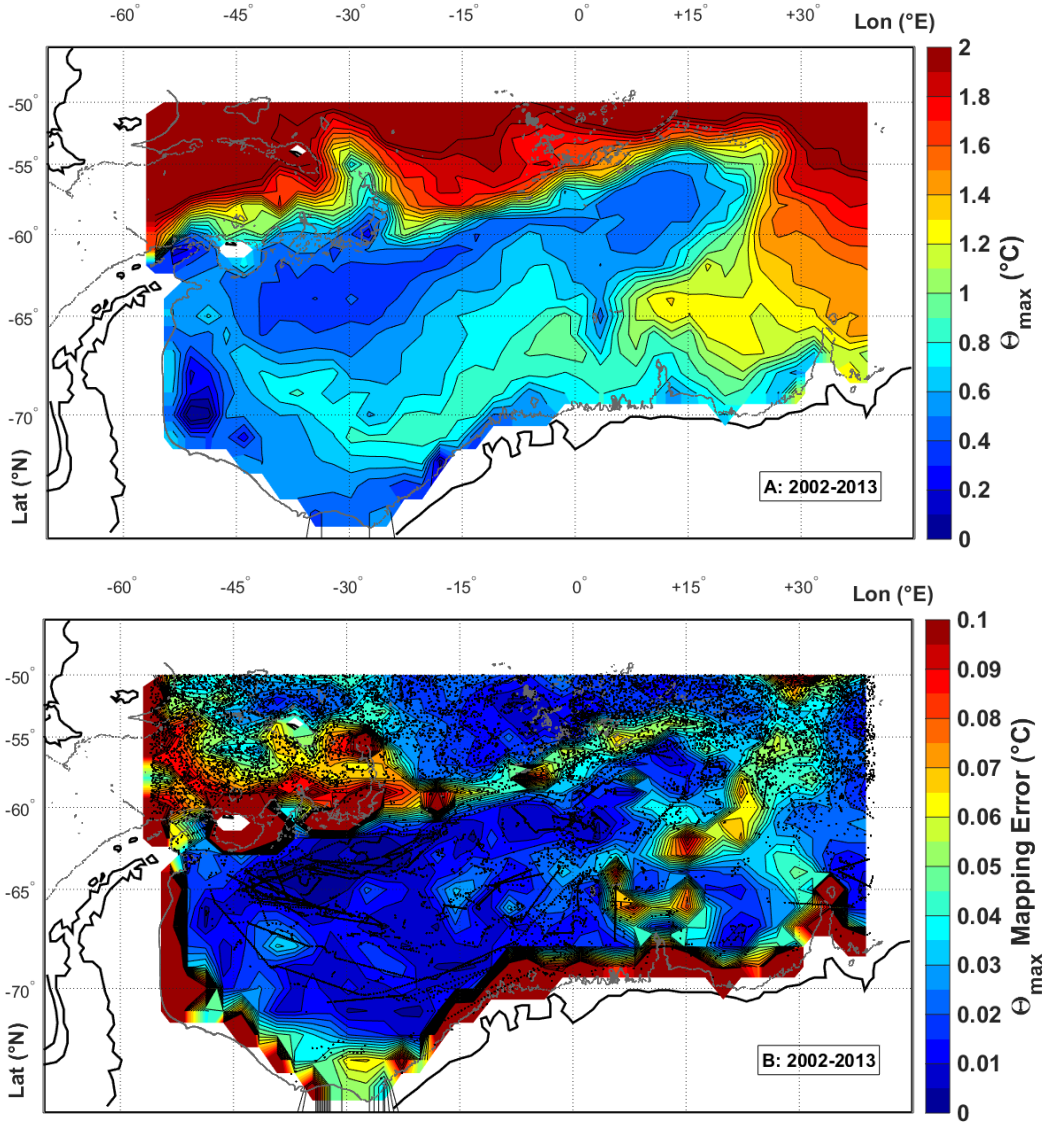

Figure 3.14. Conservative temperature (°C) at the sub-surface temperature maximum for the entire time period, where panel **(a)** shows the objectively mapped field based on the second approach (i.e. using the mapped pressure of the sub-surface temperature maximum to extract the temperature data points). The mapping error is shown in panel **(b)**; profile locations are marked as black dots. For more details, refer to Sect. 3.4.2. The grey contour shows the 2000 m isobath.

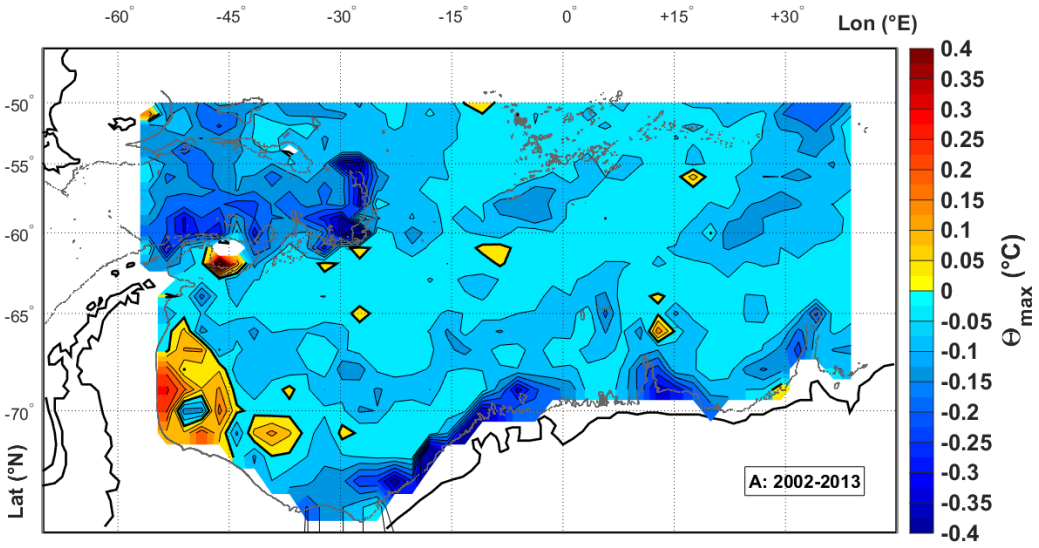

Figure 3.15. Comparing methods of mapping the sub-surface temperature maximum: this map shows the temperature difference (°C) where the output in the first approach in Fig. 3.11b is subtracted from the output of the second approach in Fig. 3.14a. Bold contour lines at 0 °C. The grey contour shows the 2000 m isobath.

3.4.3 Objective Mapping to float profile locations

In addition to objectively mapping Argo float data to a grid to create a spatially regular field of data variables, the profile data were also objectively mapped to the locations of the profiles themselves, in order to assess the performance of the objective mapping procedure. It is important to note that the resulting maps are not expected to precisely match the profile data, due to the assumption of noise in the dataset ($<\eta^2>$; Eq. 7). While the objective mapping was carried out at the level of the Tmax as well as at 800 dbar, only the latter is presented here. Figure 3.16a shows the original profile data of conservative temperature at 800 dbar for the entire time period. Figure 3.16b shows the objectively mapped field estimate, mapped to the profile locations, while Fig. 3.16c shows the difference, where the mapped profile data has been subtracted from the original data (i.e. Fig. 3.16a minus Fig. 3.16b). The mapping process performs well particularly within the gyre centre, where the differences for the profile locations within the gyre are less than ± 0.2 °C, most often less than 0.1 ºC. The differences are larger north of the gyre (mostly north of 60° S), especially in the bathymetrically complex region west of 15° W (i.e. approaching the Scotia Sea). This is outside of the Weddell Gyre region, but may influence the accuracy of the northern boundary of the gyre. Taking into account all data points shown in Fig. 3.16c, 87% of the data points have differences between the original data and the mapped data that are within ± 0.2 °C (Fig.

3.17a). Furthermore, by considering only profiles within the gyre itself (using the northern boundary definition described in Sect. 3.2.2), 89% of the mapped data points differ from the original data points by ± 0.2 °C (Fig. 3.17b; 83% are within ± 0.15 °C). Regarding temperature at the Tmax (Fig. 3.18), 82% of the mapped data points differ from the original data by ± 0.2 °C at most for the entire data set (84 % when looking at profiles within the Weddell Gyre only; Fig. 3.18b). Within the gyre, the 84% of those max data points differ by ± 0.15 °C at most. Lastly, for pressure at the Tmax, 77% of the mapped data points differ from the original data points by ± 100 m (Fig. 3.19a); this value increases to 84% when considering only those profiles within the Weddell Gyre (Fig. 3.19b). These values could be interpreted as an estimation of small-scale noise smoothed out through the mapping process, which is generally less than 0.2 ºC and indeed within 0.15 ºC for over 80% of the data points. This is also the general temperature difference between the two methods of mapping temperature at the Tmax (Section 3.4.2). Again, as these values are interpreted values, they are excluded from the mapping error, but are discussed here to emphasise caution regarding possible interpolation errors.

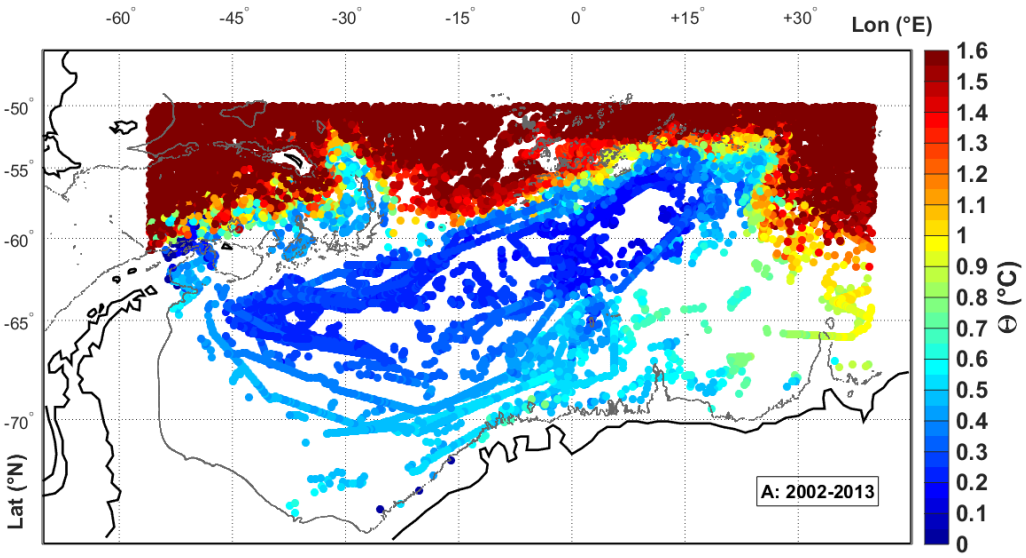

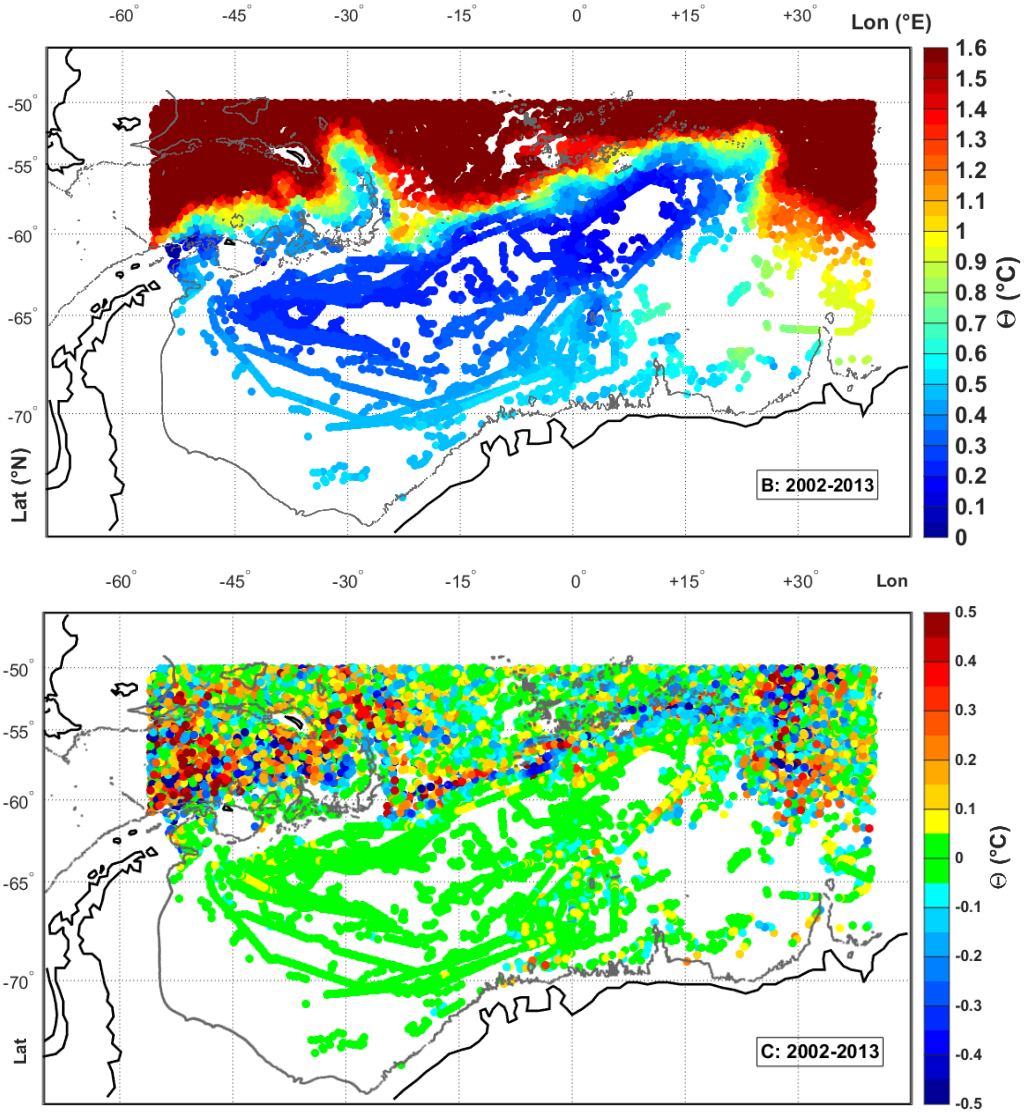

Figure 3.16. Conservative temperature (°C) at 800 dbar for the entire time period, where panel **(a)** shows the original float data, panel **(b)** shows the float data objectively mapped to the profile locations and panel **(c)** shows the difference where the output in panel **(b)** is subtracted from the original data in panel **(a)**. The grey contour shows the 2000 m isobath.

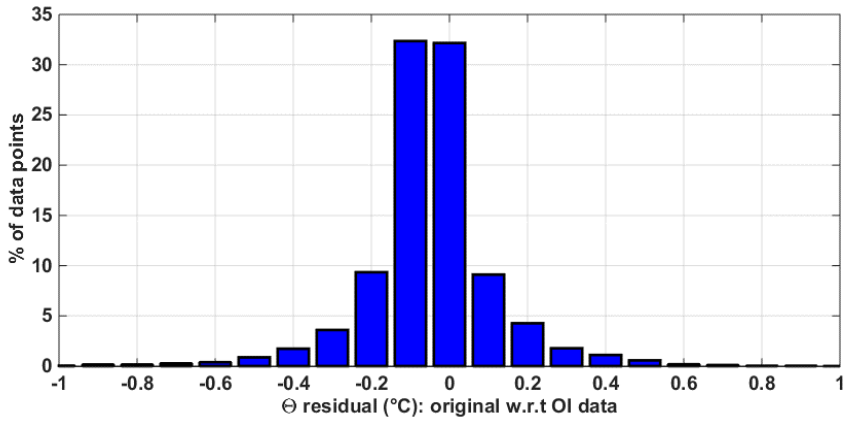

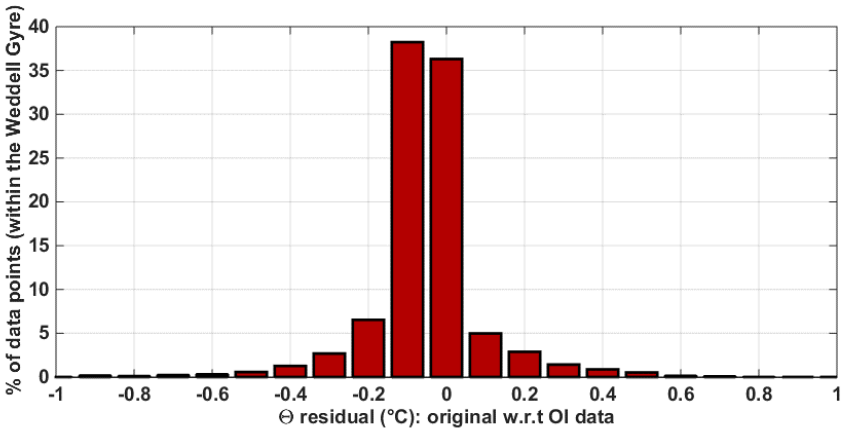

Figure 3.17. A histogram showing the percentage of data points binned by temperature residuals (°C) at 800 dbar, where the float data objectively mapped to the profile locations (i.e. Fig. 3.16b) are subtracted from the original profile data points (i.e. Fig. 3.16a), for **(a)** the entire dataset and **(b)** for those data points within the "defined" Weddell Gyre region only.

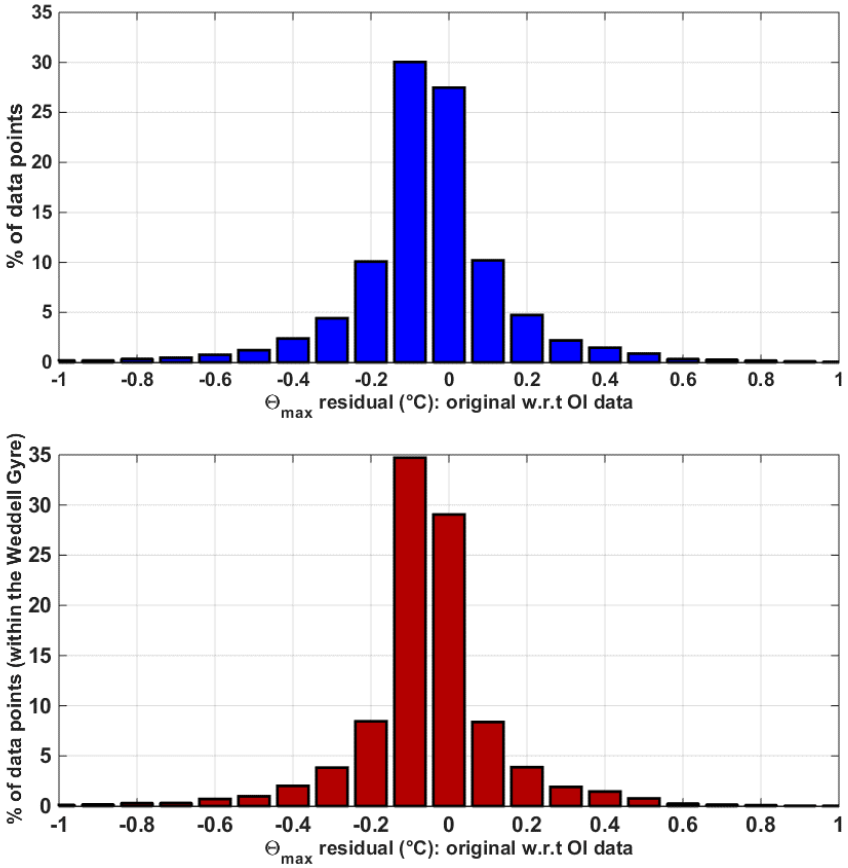

Figure 3.18. The percentage of data points binned by temperature residuals (°C) at the sub-surface temperature maximum, where the float data objectively mapped to the profile locations are subtracted from the original profile data points, for **(a)** the entire dataset and **(b)** for those data points within the defined Weddell Gyre region only.

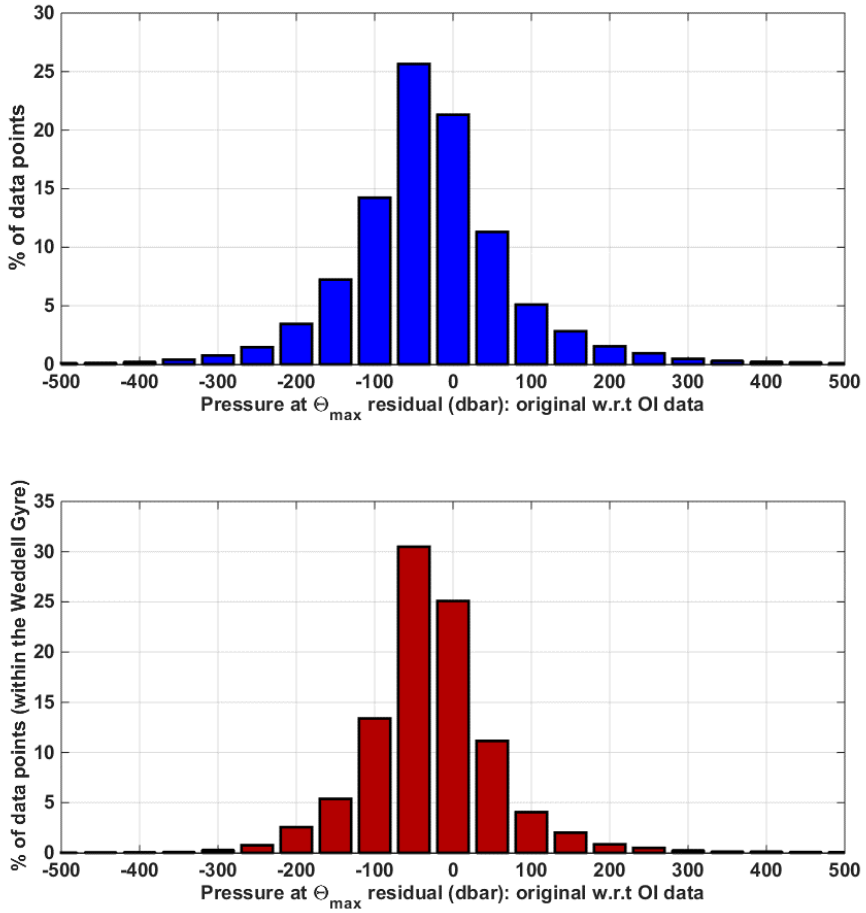

Figure 3.19. The percentage of data points binned by pressure residuals (dbar) at the level of the sub-surface temperature maximum, where the float data objectively mapped to the profile locations are subtracted from the original profile data points, for **(a)** the entire dataset and **(b)** for those data points within the defined Weddell Gyre region only.

3.5 Results

The following section presents the main features of the gridded fields of data through mapped surfaces at the Tmax and of the isobaric surface of 800 dbar, which is the depth at which the Argo floats drift, a level generally understood to be fully within the source water mass of WDW (Fahrbach et al., 2011). Further results extracted from the gridded data are presented in Section 3.6.

3.5.1 Sub-surface conservative temperature maximum

A typical feature in the hydrography of polar regions is the presence of a sub-surface temperature maximum, as displayed in Fig. 3.5, which results from influx of warmer waters from lower latitudes. The maps in Fig. 3.11 present conservative temperature, Θ, at the level of the Tmax, for the entire time series. The boundary of the gyre to the north is clear as a sharp transition between warmer temperatures above 2 °C to the north and cooler temperatures of the gyre below 1 °C to the south. This boundary reflects the bathymetry of the region, including the northern extension of the gyre at the South Sandwich Trench (just east of 30° W, 53 to 60° S). The incoming source water of the Circumpolar Deep Water is shown as a core of warm water entering the gyre in the east, in the southern limb of the gyre (at about 65° S, 30° E, although caution should be exercised regarding data sparsity in this region; Fig. 3.11a, c). This warm water cools from about 1.2 °C to 0.6 °C as it circulates westwards through the southern limb of the gyre. A double-gyre structure is also suggested, where the secondary gyre occurs in the north-east sector, splitting from the main gyre at about 5° W; this is in agreement with the literature which commonly refers to the Weddell Gyre as a double-cell structure (e.g. Beckmann et al., 1999; Klatt et al., 2005). The largest mapping errors (Fig. 3.11c) occur at the gyre boundary in regions of complex bathymetry and to a lesser extent over the eastern sector of the gyre, east of the Prime Meridian where there are considerable spatial gaps in the data distribution. The error is small in the gyre interior, even in regions of especially sparse data density, so long as the bathymetry is unchanging (with the exception of 45-55^{o} W, 64-72^{o} S, where no profile floats are located). This is because the temperature field is relatively uniform, which results in a small signal variance field, and the bathymetry is constant, which results in minimal change in planetary potential vorticity (Fig. 3.4). Conversely, pressure at the sub-surface temperature maximum ($Pr_{(\Theta max)}$, Fig. 3.12) is less stable; hence the large errors (Fig. 3.12c) at the gyre periphery and along the Antarctic coast. There is a considerable

deepening of the sub-surface temperature maximum at about 65° S, just east of the Prime Meridian, from about 200 m in the surrounding region to roughly 400 m, which occurs directly over Maud Rise (note the mapping error is relatively small in this region due to the large availability of profiles despite the large change in bathymetry). This is in agreement with literature, which shows the presence of trapped water in a Taylor column over Maud Rise, identifiable by a localised cooler sub-surface temperature maximum in comparison to surrounding regions (Bersch et al., 1992; Muench et al., 2001 and Leach et al., 2011). The sub-surface temperature maximum is shallowest within the gyre centre, and deepest towards the gyre peripheries, demonstrating the domed structure associated with the cyclonicity of the gyre.

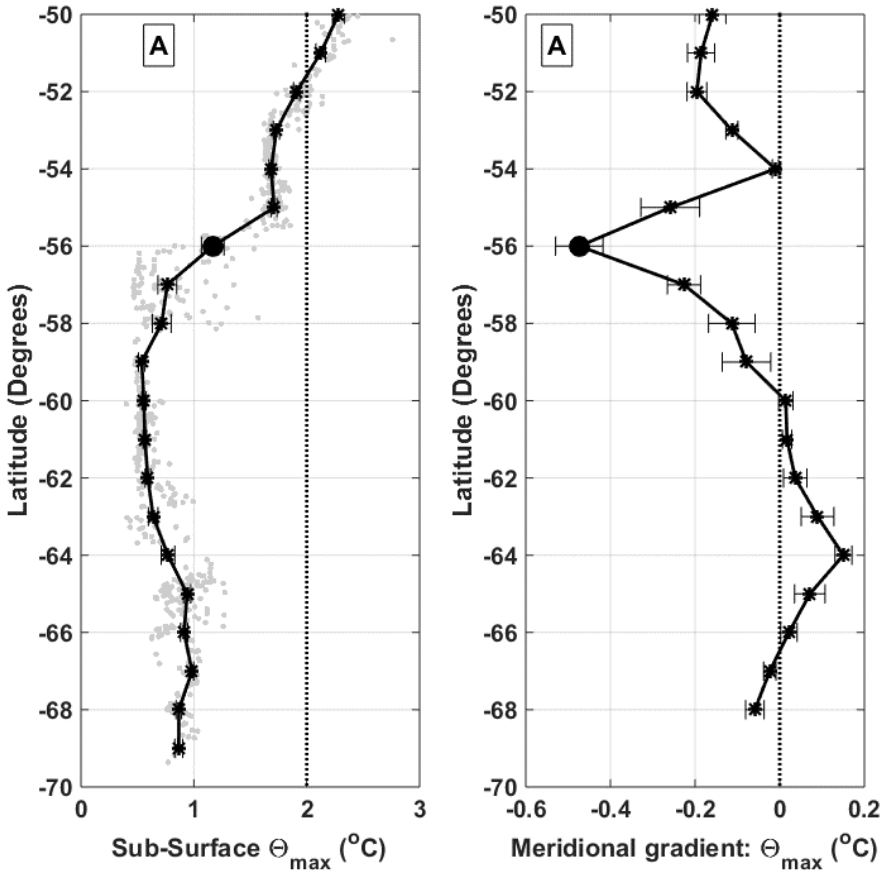

Figure 3.20. Panel **(a)**: mean meridional temperature distribution (°C) at the sub-surface temperature maximum extracted from the mapped field in Fig. 3.11b, for longitude bins encompassing the Prime Meridian. The meridional gradient of the temperature maximum is shown in panel **(b)**. The large, solid, circular symbols mark where the magnitude of the gradient is largest – this marks the latitude of the northern boundary of the gyre for this longitude. The error bars both in panel **(a)** and **(b)** represent the propagation of the mapped errors from each grid cell used in the calculation (i.e. two grid cells, immediately to the east and west of the Prime Meridian). The original profiles within 1° of the Prime Meridian are shown in grey in the background in panel **(a)**.

The mean meridional sub-surface temperature, $\Theta_{(\Theta max)}$ along the Prime Meridian (as extracted from the gridded data set) is given in Fig. 3.20a along with the resultant meridional temperature gradient in Fig. 3.20b. The large dots show the latitude at which the gradient is largest, which occurs at 56° S (note: the gradient is negative due to the south-north direction). This is the latitude used to define the northern boundary at the Prime Meridian, which corresponds with the northern boundary used in the long-term analysis of properties at the Prime Meridian in (Fahrbach et al., 2011). All grid points north of this latitude are masked from the mapping process for the subsequent isobaric mapped surfaces.

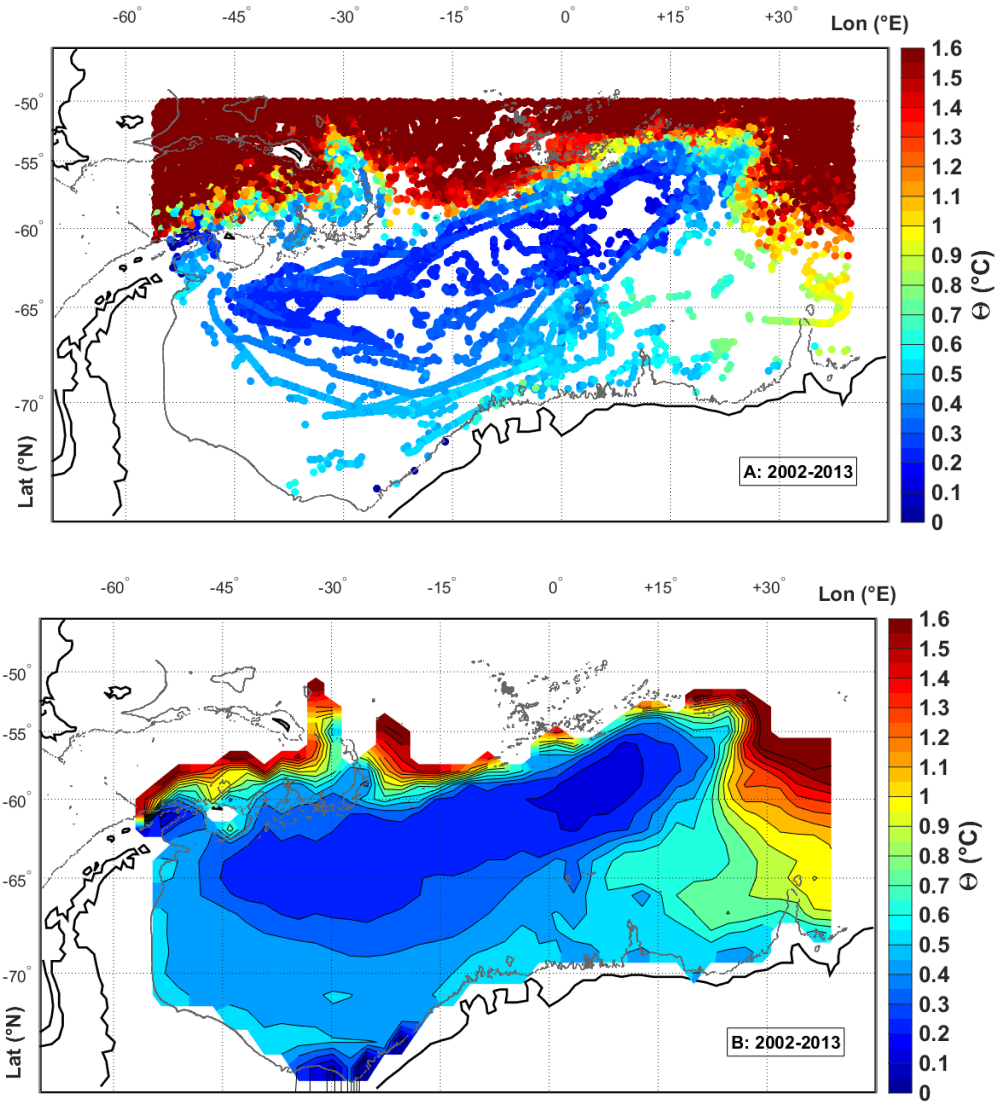

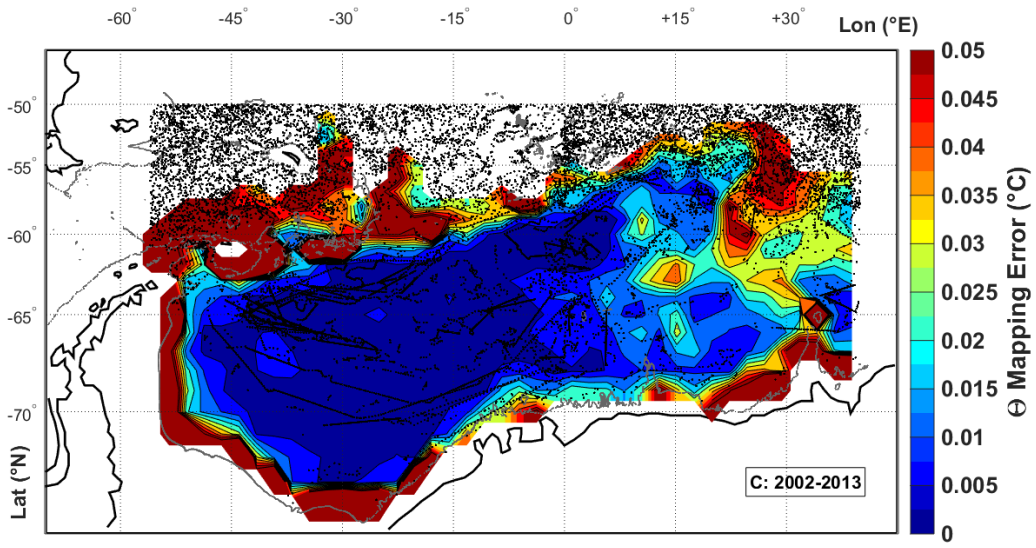

Figure 3.21. Conservative temperature (°C) at 800 dbar for the entire time period, where panel **(a)** shows the original float data, panel **(b)** shows the objectively mapped field and panel **(c)** shows the mapping error for the mapped field (profile locations are marked as black dots). The grey contour shows the 2000 m isobath.

3.5.2 Conservative temperature and absolute salinity at 800 dbar

Figure 3.21a, b and c show the original profile data, the mapped field and the associated mapping errors, respectively, of conservative temperature at 800 dbar, for the entire time period. Figure 3.22 shows the same but for absolute salinity, S_A. Both fields show the structure of the gyre, where relatively warm, salty water from the north enters the gyre in the southern limb (south of 60° S) at about 30° E and gradually cools as it circulates in a clockwise direction throughout the gyre. Note that while the data is sparse in this entry zone, the available stations in Figs. 3.21a and 3.22a also show the incoming warm, salty source water. There is a gradual transition from relatively warm, salty water in the south-east sector of the gyre, to cooler, fresher water in the western southern limb of the gyre, to even cooler, fresher water in the northern limb of the gyre. The coolest, freshest water at 800 dbar occurs in the east within the northern limb of the gyre. The associated mapping errors for both temperature and salinity are small, in particular at the centre of the gyre, and larger in regions of complex bathymetry at the gyre boundaries. The mapping errors represent the large-scale field (i.e. the assumption is that the resulting fields have been considerably over-smoothed).

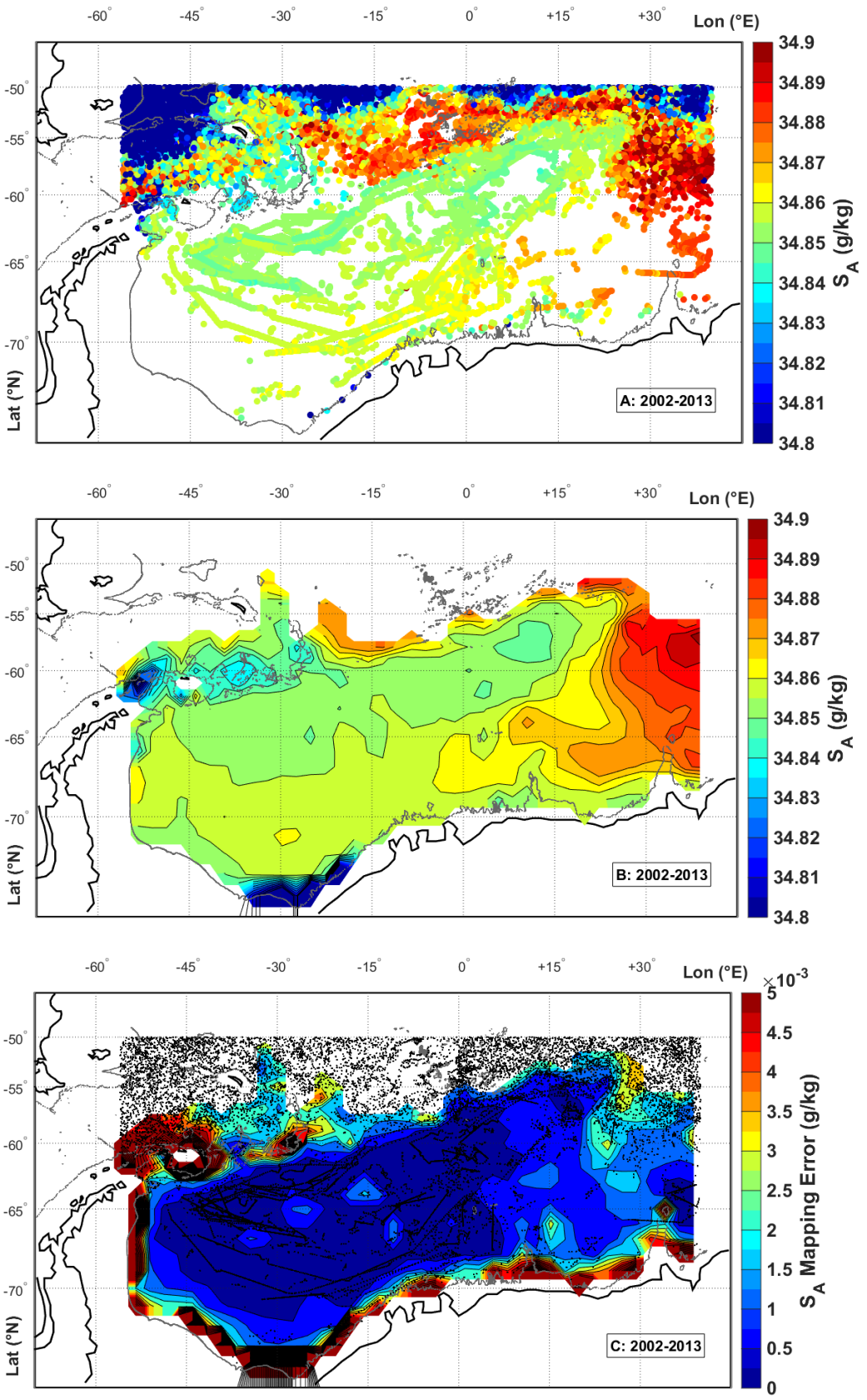

Figure 3.22. Absolute salinity (g kg^{-1}) at 800 dbar for the entire time period, where panel **(a)** shows the original float data, panel **(b)** shows the objectively mapped field and panel **(c)** shows the mapping error for the mapped field (profile locations are marked as black dots). The grey contour shows the 2000 m isobath.

3.6 Discussion

The objective mapping performance was investigated in Section 3.4. Here, we expand on performance by (1) comparing the mapping approach to global and major-ocean basin climatologies and (2) assessing the resulting gridded fields in the context of what is already known about Weddell Gyre hydrography (an interpretation of data is avoided, as it is beyond the scope of this data paper).

3.6.1 Approach to objective mapping – comparison to climatologies

Table 3.2. List of climatologlies discussed in Section 3.6, along with their corresponding grid resolutions, number of interpolation passes, the first-guess fields and radii of influence for each interpolation pass.

CODE	Climatology	Grid resolution	No. passes	Pass 1: first-guess field	Pass 1: radius of influence	Pass 2: radius of influence	Pass 3: radius of influence
HA_SO	Hydrographic Atlas of the SO (Olbers et al., 1992)	1° × 1°					
WOA94	World Ocean Atlas (Levitus et al., 1994)	1° × 1°	1	Zonal mean	555 km		
WOA98	WOA (Antonov et al., 1998)	1° × 1°	3	Zonal mean	892 km	669 km	446 km
WOA01	Stephens et al. (2001)	1° × 1°	3	Zonal mean	892 km	669 km	446 km
WOA05	Locarnini et al. (2005)	1° × 1°	3	Zonal mean	892 km	669 km	446 km
WOA09	Locarnini et al. (2010)	1° × 1°	3	Zonal mean	892 km	669 km	446 km
WOA13	Locarnini et al. (2013)	1° × 1°	3	Zonal mean	892 km	669 km	446 km
WOA13	Locarnini et al. (2013)	$\frac{1}{4}° \times \frac{1}{4}°$	3	Zonal mean	321 km	267 km	214 km
WOCE_global	Locarnini et al. (2013)	1° × 1°	1	Mean subdomain within radius of 750 km	$R = 450$ km (open ocean; > 500 km from coast)		
WOCE_SO	Orsi and Whitworth (2005)	24 × 24 km	1		$R = 666 \times 333$ km (open ocean > 4000 m depth)		
WG		*1° ×(1/cos(−65))°	2	Zonal mean	$R = 1000$ km, $\Phi = 0.5$	$R = 500$ km, $\Phi = 0.25$	

* Approximately 110 km × 110 km along the central gyre axis at 65° S.

Climatologies are generally constructed as mean oceanographic fields that represent a reference dataset for a given period, which can then be used to derive temporal or spatial change across different scales or periods. Figure 3.23 shows the different time periods of a group of climatologies, as well as the gridded datasets provided here (hereafter WG_all, WG_TP1, WG_TP2 and WG_TP3 where "all" denotes the entire time period analysis and "TP" denotes the time period subsets). Table 3.2 provides the full name, regional boundary definitions and citations for each of the climatologies listed in Fig. 3.23. The closest matching time period to WG_all is WOA13, with a time span of 2005 to 2012 ("WOA13_0512" in Fig. 3.23); indeed WOA13 is the only climatology that will have incorporated the high-latitude float data of the Weddell Gyre, which provides improved spatial coverage of the upper 2000 m. The WG datasets are representative of smaller time periods, which may be helpful in the cross comparison with ship data and analysis of variability over smaller time periods (although users should take caution in the larger errors associated with WG13_TP1 due

to data sparsity). The data source for the climatologies listed consists of historical data and more modern, higher quality data (e.g. WOCE), combining different data types (e.g. ship conductivity-temperature-depth (CTD) measurements, ship water sample, moorings, buoys, drifters and gliders). The WG data sets provide Argo-only gridded fields, which are therefore independent data sets which may be useful in comparison studies. Furthermore, these data sets demonstrate the potential of Argo in providing upper ocean reduced-time-span gridded fields, which can only improve in the future as more data becomes available. By using all (or most) available observations, the climatologies listed have to apply strict and numerous levels of quality control procedures in order to remove poor-quality data. Since such a large amount of data is available for the global ocean as well as for the Southern Ocean, a procedure to reduce the amount of data that goes into the mapping method has to be carried out for every climatology. For example, in WOCE_global, the data are binned into 55 km^2 boxes; if more than 4 data points are available, a box-average of all binned data points is calculated on density surfaces. Therefore, the input data are a combination of observed data points and box-average data points (Gouretski & Koltermann, 2004). In the WG data sets, data sparsity is the largest limitation, and therefore the input data are the original observed values which have been vertical interpolated onto standard pressure levels.

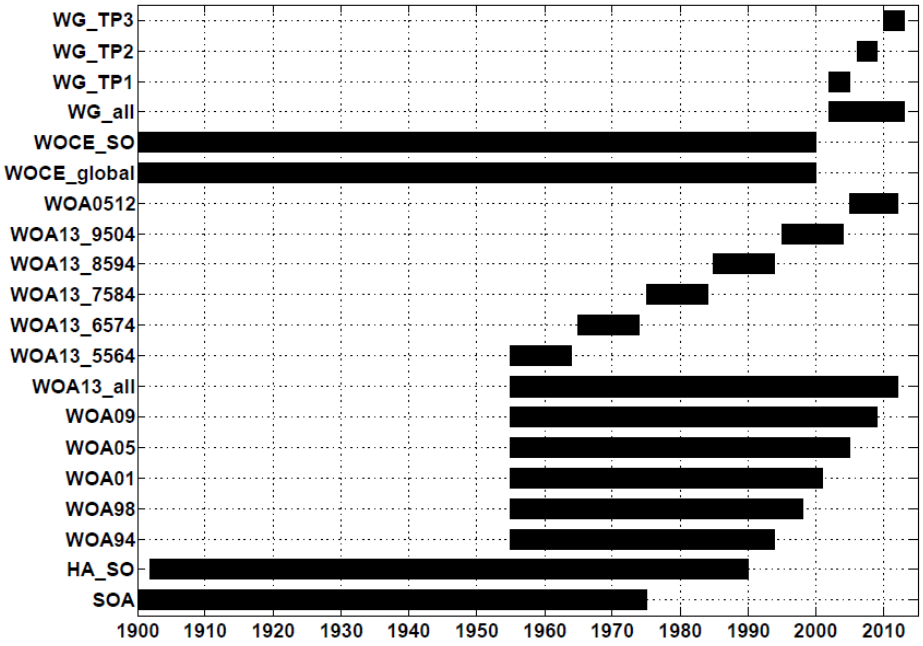

Figure 3.23. A plot showing the time spans of a list of climatologies, including the time spans of the data set provided here; WG_all represents the gridded fields of the entire time span, while WG_TP1, WG_TP2 and WG_TP3 represent the time spans of the gridded fields for TP1, TP2 and TP3 respectively.

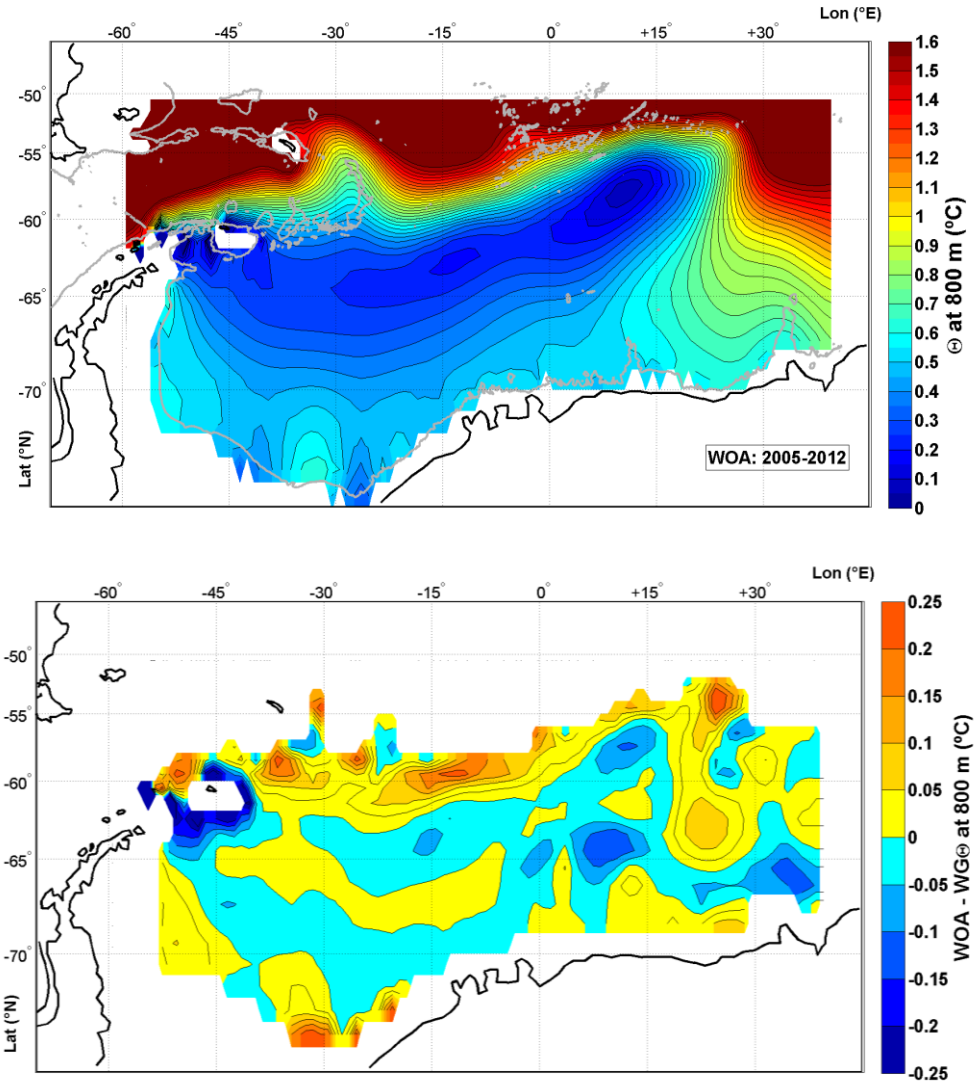

Figure 3.24. Panel **(a)**: Conservative temperature (ºC) at 800 m from the WOA13 climatology during 2005 to 2012 (i.e. WOA0512 in Fig. 3.23). Panel **(b)** shows the difference with the entire time span of the data set provided, i.e. WOA0512 minus WG_all. The grey contour shows the 2000 m isobath.

The most prominent differences between the climatologies listed, and the WG data sets are the objective mapping method and corresponding weight function. As discussed in Section 3.3.2.1, the WOA climatologies use a successive correction method while WOCE climatologies use the optimal interpolation method, the same method as applied for the WG data sets. The weight function is dependent on a radius of influence, where data beyond the radius of influence of a grid point have zero weighting. For the WOA climatologies, the mapping method is applied three times, each time with a reduced radius of influence, of 892, 669, and 446 km for the 1º x 1º grid (the exception is WOA94, which uses a single-pass successive correction with a radius of 555 km). This allows for increased weighting to nearby data points. Note that this applies to the

entire global ocean. The WOCE climatologies use the same optimum interpolation method as the WG data sets, and the same Gaussian model of the autocorrelation function, but with a key difference based on how the influence of bathymetry is incorporated into the correlation function. In the WOCE algorithm, the function, $\exp\{-[r^2/R^2]\}$, where r is the horizontal distance and R is the radius of influence, is the same as the first component of the decay scale in Eqs. (4) and (5). Bathymetry is incorporated into the weighting function by setting the condition that if the grid point is more than 500 km from the coast, R = 450 km, otherwise R decreases as a function of distance to the coastline. A map of the resulting length scales can be seen in Gouretski & Koltermann (2004; Fig. 13). For the WOCE_SO climatology (Orsi and Whitworth, 2005), the radius of influence is elliptical rather than circular, to take into account the fact that currents in the Southern Ocean are dominantly zonal. Furthermore, bathymetry is incorporated by having different radii of influence according to bottom depth. So for example, R is an ellipse of 666 km x 333 km in the zonal/meridional direction where the bottom depth is larger than 4000 m. In comparison, the WG method incorporates an additional component into the decay scale, which is the cross-isobath separation factor (F^2/Φ^2 in Eqs. 4 and 5), which accounts for changes in planetary potential vorticity and thus provides a more detailed inclusion of bathymetry (and latitude, consequently taking into account the zonal dominated flow). The way this impacts the radius of influence is illustrated in Figs. 3.9 and 3.10, while the level of detail of the bathymetry factor is seen by looking at the f/H contours in Fig. 3.4. Another key difference between the WOCE climatologies and the WG data is the first-guess field and pass number (Table 3.2). The WOCE climatology takes the first-guess field as the mean of the subdomain in which the radius of influence is 750 km, and then the N closest observations are selected for the mapping (N=150). The mapping is carried out once. In the WG maps, a two-pass optimal interpolation is applied, where the zonal mean is the first-guess field of the first pass and the length scales D and Φ are 1000 km and 0.5 respectively, while the output becomes the first-guess field for the second pass, in which the length scales are reduced to 500 km and 0.25 in order to place extra weighting on the closest data points.

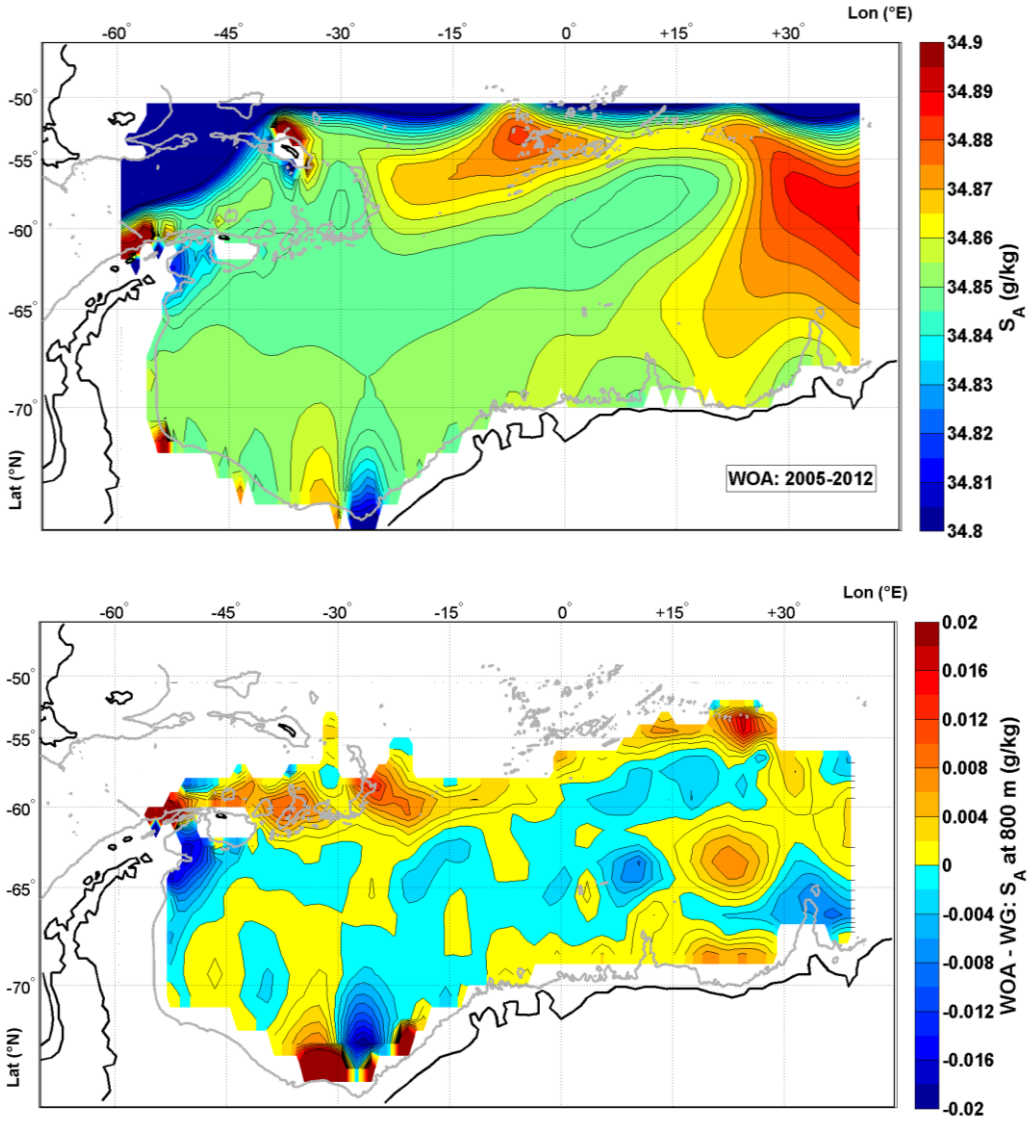

Figure 3.25. Absolute salinity (g kg^{-1}) at 800 m from the WOA13 climatology during 2005 to 2012 (i.e. WOA0512 in Fig. 3.23). Panel **(b)** shows the difference with the entire time span of the dataset provided, i.e. WOA0512 minus WG_all. The grey contour shows the 2000 m isobath.

To summarise, all climatologies incorporate a large amount of varying data sources over long periods of time, whereas the WG data constitute an independent Argo-only data set over relatively shorter time periods. The input data for the climatologies listed are typically a combination of observed data in sparse-data-coverage regions and box-averaged data elsewhere, whereas the WG input data consist of vertically interpolated observed values only. While the climatologies listed contribute to incorporating the influence of bathymetry on the radius of influence by adjusting the radius based on distance to coastline (WOCE), or bottom depth and radius shape (WOCE_SO), the WG mapping incorporates cross-isobathic separation and thus accounts for bathymetry in a detailed manner. While all climatologies provide maps on

standardized depth levels (and neutral density surfaces in WOCE), the WG data sets also provide maps of the level of the sub-surface temperature maximum. This is the level representing the core of incoming source water. While fields of potential temperature and practical salinity are provided, gridded fields of conservative temperature and absolute salinity are also provided; conservative temperature is deemed more representative of the "heat content" of seawater than potential temperature (McDougall and Barker, 2011).

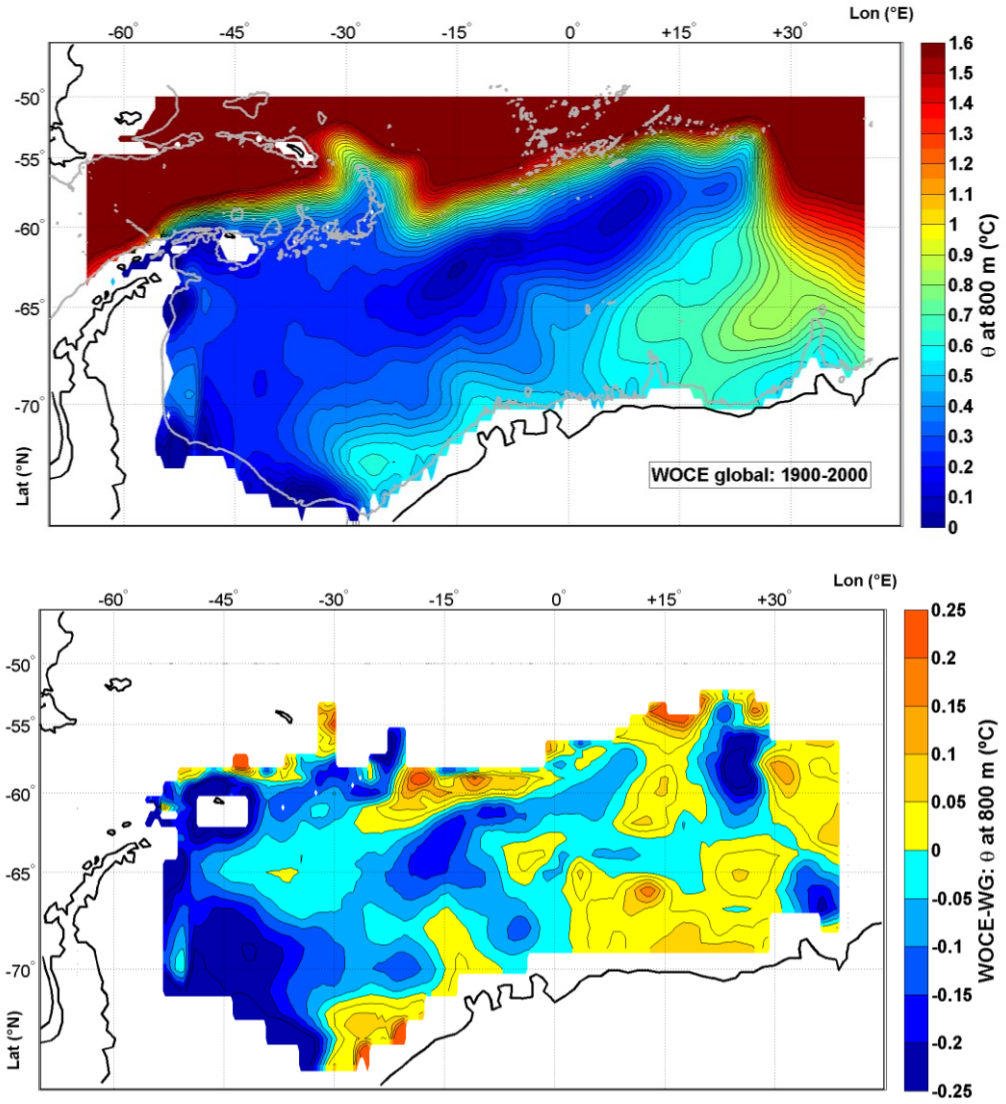

Figure 3.26. Conservative temperature (ºC) at 800 m from the global WOCE climatology during 1900 to 2000 (i.e. WOCE_global in Fig. 3.23). Panel **(b)** shows the difference with the entire time span of the data set provided, i.e. WOCE_global minus WG_all. The grey contour shows the 2000 m isobath.

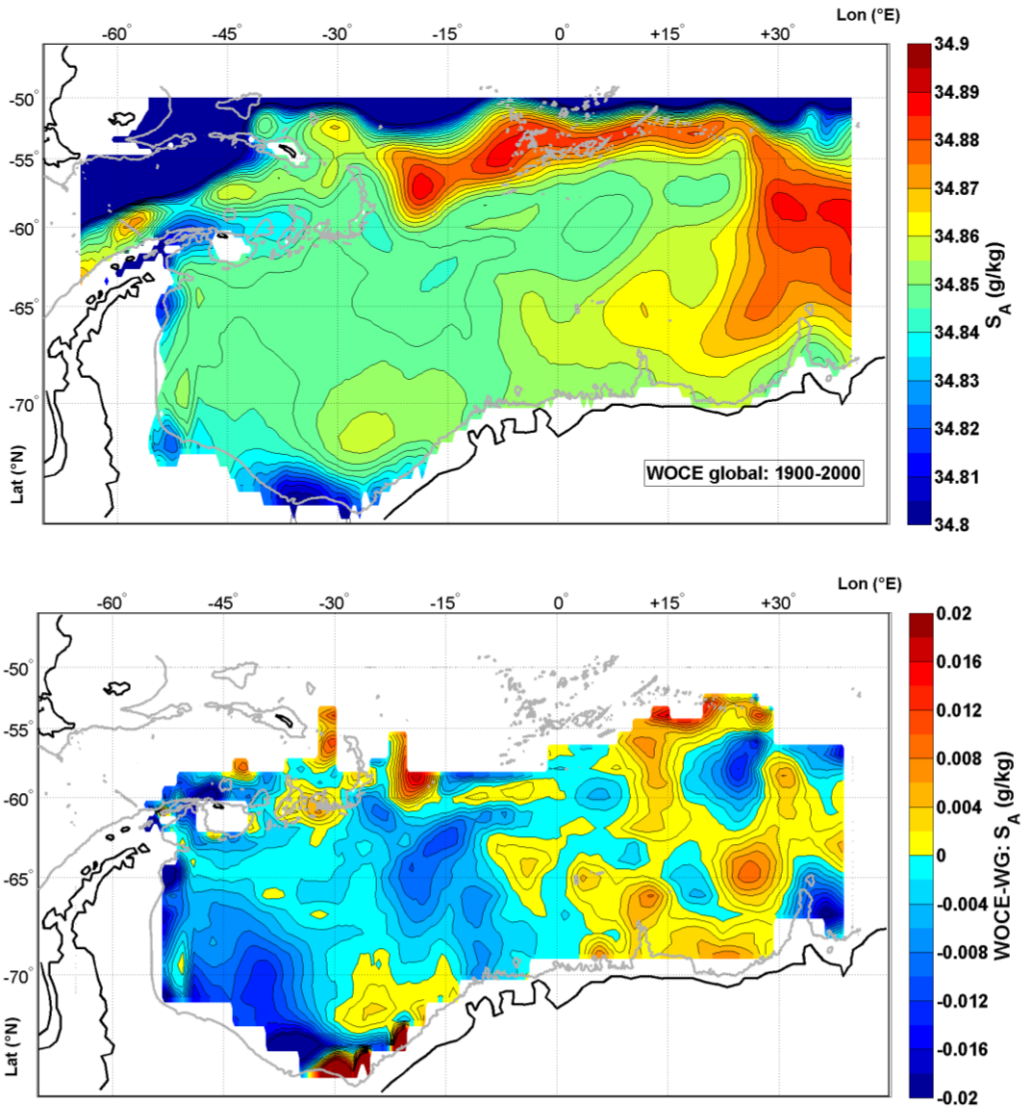

Figure 3.27. Absolute salinity (g kg^{-1}) at 800 m from the global WOCE climatology during 2005 to 2012 (i.e. WOCE_global in Fig. 3.23). Panel **(b)** shows the difference with the entire time span of the data set provided, i.e. WOCE_global minus WG_all. The grey contour shows the 2000 m isobath.

Figure 3.24 shows (a) the conservative temperature at 800 m from WOA13 (time span 2005 to 2012; Locarnini et al., 2013), and (b) the corresponding difference between WOA13 and WG_all. Figure 3.25 shows the same for absolute salinity (Zweng et al., 2013), and Figs. 3.26 and 3.27 are the same as Figs. 3.24 and 3.25 but using the WOCE_global atlas (1900-2000; Gouretski and Koltermann, 2004). Note temperature and salinity from WOA13 and WOCE_global are used to calculate conservative temperature and absolute salinity, WG_all is on a pressure surface of 800 dbar, and the WG grid had to be interpolated to match the WOA13 grid for this rough comparison. WOA13 is considerably smoother than WG_all (Figs. 3.21 and 3.22). In particular, the Taylor column over Maud Rise as discussed in Section 3.5 is not visible nor is the warm

and salty tongue that emerges to the south and west of Maud Rise, half way between Maud Rise and the coast that appears to be curving around Maud Rise. This warm and salty tongue of water is a small feature and yet it is present in the longer-time-period-composite of WOCE in Fig. 3.26, although the Taylor column is not. This may be because the WOA13 is from the 1º x 1º grid, whereas the WOCE grid is ¼º x ¼º grid; however, the WG grid succeeds in representing these features, possibly a result of incorporating the cross-isobath separation component into the decay scale, which is discussed above. A potential reason why WOA13 omits the smaller-scale details is that the mapped fields were also smoothed with a median filter and a five-point smoother (Locarcini et al., 2013). The far south along the 2000 m contour between 15º and 45º W is unique across all three maps. WOCE displays this region as a particularly cold and fresh stretch parallel to the 2000 m isobaths. WOA13 displays an alternation between cold and fresh and warm and salty water, which extends northwards from the 2000 m isobath. This region is marked as an area of relatively large mapping error (in excess of 0.05 ºC and 0.005 g kg^{-1} for temperature and salinity in Figs. 3.21 and 3.22, i.e. at the upper range in error for the region), and therefore caution should be made in interpreting the results in this area. The maps show a slightly warmer region in comparison to the region just north (of about 72º S). The difference between WOA13 and WG is relatively small in general (less than 0.05 ºC for temperature and 0.004 for salinity; Figs. 3.24b and 3.25b), which increases in regions where the WG map shows more complex features. In general the WOA map appears to show slightly warmer and saltier values than the WG map (i.e. more blue than yellow or orange), although roughly 30-40 % is slightly cooler and fresher. The WOCE maps show greater differences in general, as the majority of the gyre interior is warmer and saltier (Figs. 3.26b and 3.27b). There appears to be a zonal pattern in the differences, in that for about 80% of the region west of 0º E, WOCE is warmer than WG_all, and for about 60-70% of the region west of 0º E, it is cooler. This zonal pattern is even stronger in salinity. The outstanding question is whether these differences are the result of methodical differences (such as data source and interpolation methods), or a result of representing different time periods and thus indicative of long term change.

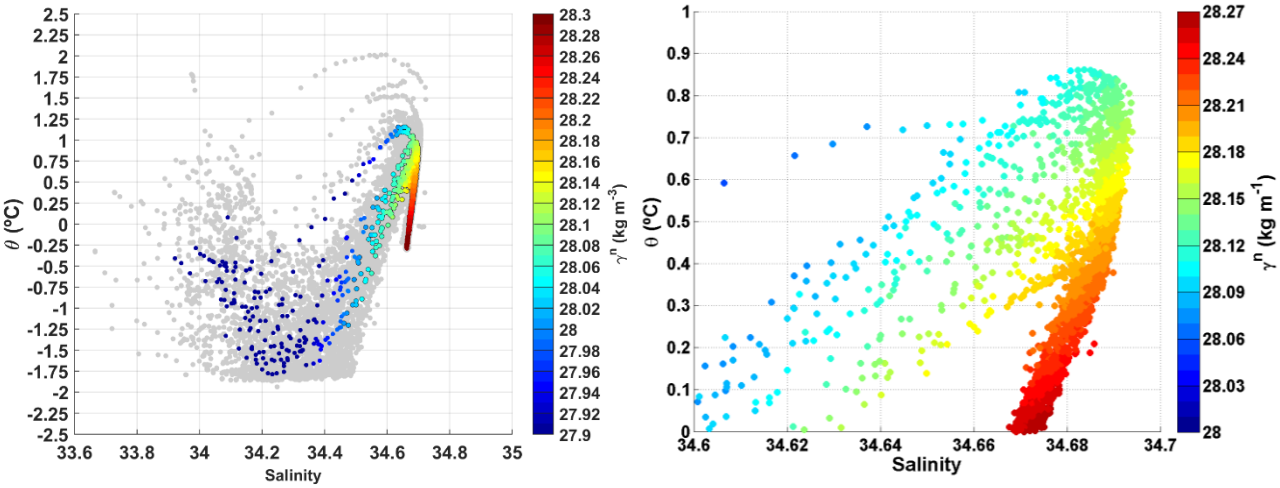

Figure 3.28. Potential temperature (ºC) - salinity diagram of **(a)** data extracted from the entire time span data set (WG_all) from along the Prime Meridian. The colour bar shows the corresponding neutral density (kg m^{-3}). The original float profile data extracted from within 1.5º of the Prime Meridian are shown in the background in grey. Panel **(b)** shows the potential temperature (ºC) – salinity diagram of gridded data extracted from the entire time period (WG_all), from a region south of 60º S between 10º and 25º W. The axis limits match the boundary definitions of WDW, and the colour bar shows neutral density, for direct comparison of WDW with Fig. 4b in Heywood and King (2002).

3.6.2 Water Mass Properties of the Weddell Gyre: along the Prime Meridian

In order to assess the resulting water mass properties of the WG data sets, a section of the Prime Meridian is presented. This is because a large proportion of literature focusing on long term change in the Weddell Gyre focuses on this region, due to data availability (see, e.g., Fahrbach et al. 2011). As there are no grid cell centres falling directly over the Prime Meridian, in order to create the sections in Figs. 3.29 to 3.31, the mean of the two nearest grid cells (the immediate grid cells to the east and west of the Prime Meridian) is created for each variable. Note the following figures show potential temperature and practical salinity for the purpose of comparison to the literature. Figure 3.28a shows a T-S diagram for all grid cells along the Prime Meridian, where the colour indicates the corresponding neutral density. All original Argo float profiles within 1.5º of 0º E are shown in the background in grey. The sub-surface temperature maximum is shown mostly at about 1º C although the two northernmost grid cells show a Tmax of about 1.1 to 1.2ºC. The surface values spread out considerably and are colder and fresher than the underlying water column. Argo floats are ideally suited to investigating WDW properties as WDW is fully encompassed within the top 2000 m, the depth limit of Argo floats. This is illustrated in Fig. 3.28, which captures the full range of WDW. WDW is characterized as having a potential temperature of more than 0ºC and salinity of more than 34.6 (Carmack and Foster,

1975), or, taking a more conservative approach, neutral density limits of 28 to 28.27 kg m^{-3} (Fahrbach et al., 2011). Figure 3.28a shows good general agreement with the T-S diagram of Fig. 2 in Schroeder and Fahrbach (1999), which comprises data from 6 hydrographic surveys, in which most stations are located on the Prime Meridian (note that these stations record information on the entire water column from the surface to the sea floor). Figure 3.28b, which focuses on WDW within a sample region south of 60º S and between 25º and 10º W, agrees well with Fig. 4b in Heywood and King (2002) which focuses on WDW in the Weddell Gyre at about 20º E.

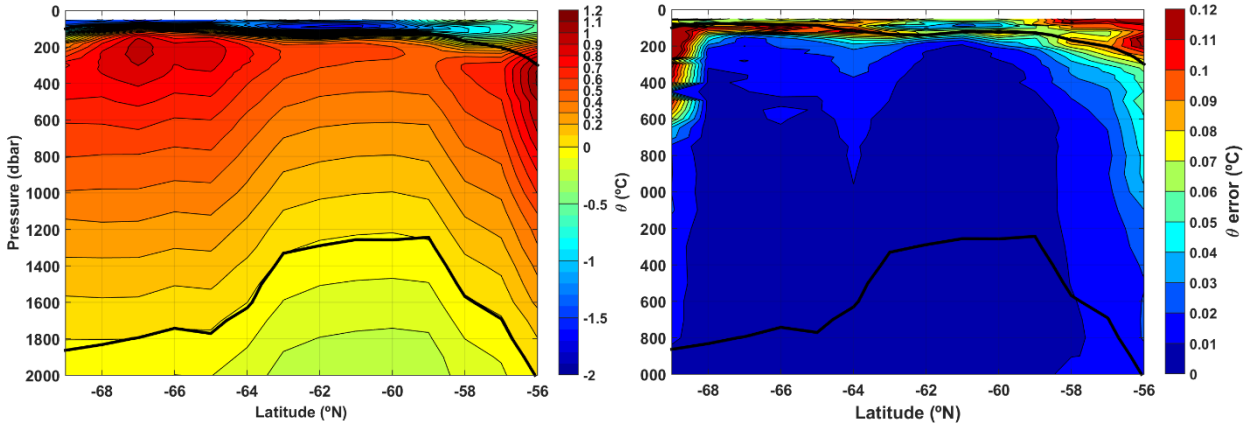

Figure 3.29. **(a)** Potential temperature (ºC) and mapping error (ºC) **(b)** for a section from 56º S to the coast along the Prime Meridian. The sections consist of the mean of the two grid cell sections adjacent to 0º E. The thick black lines show the upper and lower boundaries of WDW, i.e. the neutral densities of 28.0 and 28.27 kg m^{-3} respectively.

Figures 3.29, 3.30 and 3.31 show the cross section along the prime meridian of (a) potential temperature, salinity and neutral density respectively along with the corresponding mapping errors (b). Similar figures can be found in Fahrbach et al. (2011) for potential temperature and neutral density from 1992 (Figs. 4a-b) and 2008 (Figs. 4c-d) and in Klatt et al., (2005) for mean potential temperature and mean salinity for the period 1992 to 2000 (Fig. 4). Note the depth range differences and the direction from north to south along the x-axis. In particular, the domed structure of the gyre can be seen, with the contours shoaling towards the centre and with the central axis at about 61º S. The incoming Lower Circumpolar Deep Water can be identified as a temperature maximum of about 1.1-1.2 ºC in Fig. 3.29 at about 67º S, with its core at about 200 m, in agreement with Fahrbach et al., (2011) and Klatt et al., (2005), although in the latter, the Tmax is further south at about 68.5º S. Across all three sources, the deeper 0º C contour, which generally agrees with the 28.27 kg m^{-3} γ^n contour (i.e. the deep WDW boundary definition; shown as the thick black contour in Figs. 3.29-31a), is in

agreement. At its shallowest, the deep WDW boundary occurs at about 1200 m at ~60º S (in Fahrbach et al., 2011, this occurs slightly to either side of 60º S for the 1992 cruise), and deepens slightly to about 1300 m at 63º S, before deepening at a steeper gradient to about 1750 m at 64-5º S. Klatt et al. (2005) show agreement with Fig. 3.30, where the salinity contour of more than 36.68 "bulges out" south of about 63º S, from a minimum at 59-60º S (~700 m) to a maximum at 67º S (~1300 m). The bulge coincides with the core of incoming Circumpolar Deep Water previously discussed. The general similarities are remarkable considering the different sources and time periods (the literature uses CTD data from research vessel expeditions), although the features highlighted do not allow comparison of the shallow regions, where the corresponding mapping errors are largest (especially north of the upper boundary of WDW marked by the thick black contour in Figs. 3.29 to 3.31; 28.0 kg m^{-3} γ^n). Figure 3.32 shows potential temperature and salinity extracted from WOA13 (2005 to 2012). The gradients of the contours are considerably smoother than both in the literature and the sections in Figs. 3.29 and 3.30; the 0º C contour is shallowest at 61º S at 800 m (in comparison to 1200 m in Fig. 3.29a). There is no discernable steepening of the meridional gradient between 63º and 64-65º S, and the contour is about 1300 m at 65º S (in comparison to ~1750 m of the mapped data in Fig. 3.29a).

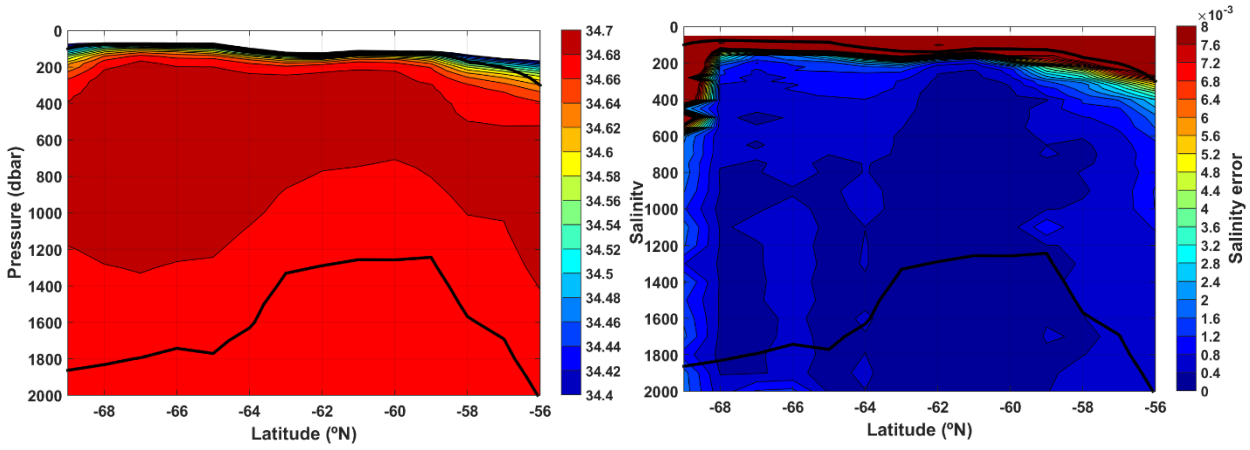

Figure 3.30. Salinity **(a)** and mapping error **(b)** for a section from 56º S to the coast along the Prime Meridian. The sections consist of the mean of the two grid cell sections adjacent to 0º E. The thick black lines show the upper and lower boundaries of WDW, i.e. the neutral densities of 28.0 and 28.27 kg m^{-3} respectively.

The WG datasets perform generally well in the context of current literature on the Weddell Gyre water mass properties. The main way in which the new datasets provided could be further improved is the inclusion of additional data. As more data become available, it may be possible to reduce the length scales used and to incorporate

a temporal separation component into the second-pass decay scale, both of which would lead to resolving the gridded fields to smaller scales (both spatially and temporally). Another key improvement (and indeed priority in the field of Argo floats) of any future gridded data sets is the improvement of the position estimates of under-ice floats (see Section 3.2). However, the aim is to provide an Argo-only dataset, of relatively small time spans, looking at the large-scale mean field. In general, the resulting gridded hydrographic fields show good agreement with other climatologies and current knowledge of the water masses drawn from ship data. The main question that remains is whether the differences noted, in particular between climatologies and the data set presented in this paper, are the result of methodology, or are suggestive of changes in the Weddell Sea climatic system.

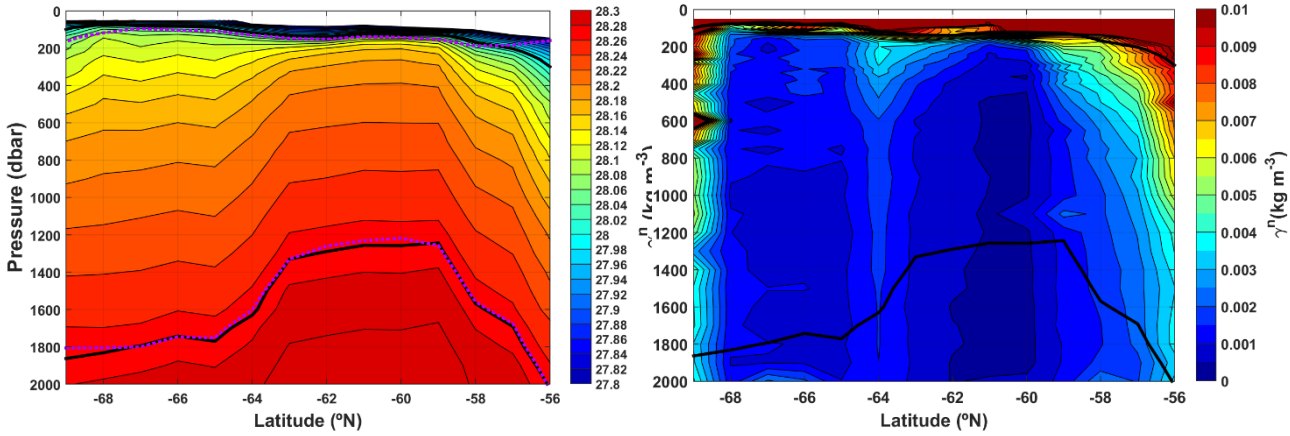

Figure 3.31. Neutral density (kg m^{-3}) **(a)** and mapping error (kg m^{-3}) **(b)** for a section from 56º S to the coast along the Prime Meridian. The sections consist of the mean of the two grid cell sections adjacent to 0º E. The solid black lines show the upper and lower boundaries of WDW, i.e. the neutral densities of 28.0 and 28.27 kg m^{-3} respectively. The dashed magenta line in panel **(a)** shows the 0 ºC contour; another definition of the WDW boundaries.

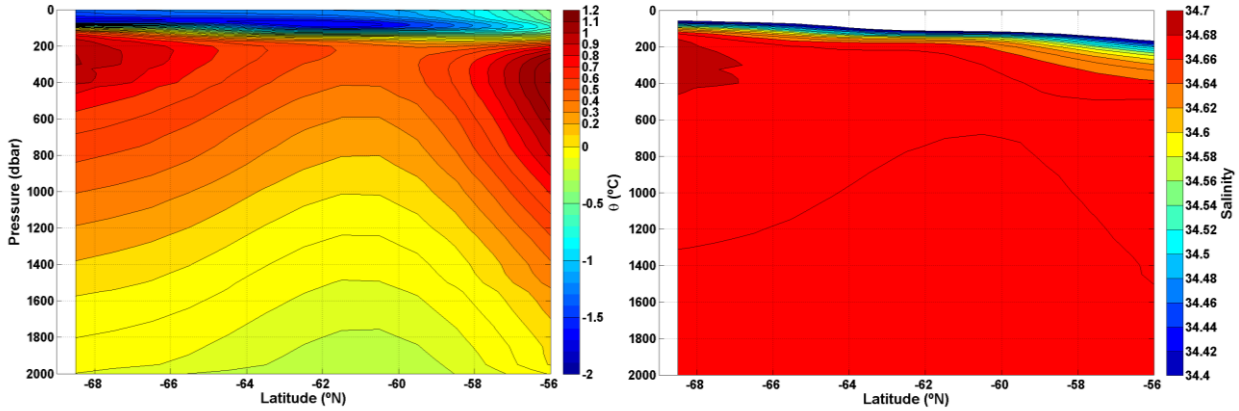

Figure 3.32. Potential temperature (ºC) **(a)** and salinity **(b)** for a section from 56º S to the coast along the Prime Meridian from the WOA13 climatology; time span 2005 to 2012.

3.7 Concluding Remarks

The objective of this paper was to provide a spatially gridded dataset of the upper 2000 m of the water column properties of the entire Weddell Gyre region. Objective Mapping was applied in a two-step process to Argo float profile data spanning December 2001 to March 2013 and to subsets of the float data for the 2002-2005, 2006-2009 and 2010-March 2013 periods. Maps of pressure, conservative temperature and absolute salinity are provided at the level of the sub-surface temperature maximum, and maps of conservative temperature and absolute salinity are provided at 41 standardized pressure levels ranging from 50 to 2000 dbar (along with additional fields of potential temperature and practical salinity). The corresponding mapping errors are also provided. The resulting mapped fields provide a complete, detailed view of the large-scale pertinent features of the Weddell Gyre, such as the doming of the gyre centre owing to its cyclonic rotation and the associated relatively cool gyre interior. The relatively warm incoming source water at the eastern sector of the southern limb is also visible, although considerable data gaps in this region require caution when interpreting the data, along with the variability of water properties owing to bathymetric features such as Maud Rise, which is not clearly visible in the climatologies investigated in Section 3.6.1. The mapping errors corresponding to the mapped field variables are relatively small, with the exception of regions where the bathymetry is complex or where data coverage is limited. The mapping errors vary with pressure, where the overall largest mapping errors coincide with the layer of the Winter Water, particularly within the vicinity of its lower boundary (about 120-180 dbar). In order to gauge the performance of the mapping procedure, objective mapping was also applied to the location of the float profiles themselves. The objective mapping successfully represents the Weddell Gyre in its entirety, whereby 89% of mapped profiles within the Weddell Gyre differ from the original profile values (for temperature at 800 dbar) by less than 0.2 °C. Comparison of the gridded fields of data with both climatologies and the literature show good agreement, which also suggests the mapping procedure has been successful in representing Weddell Gyre hydrography. Caution should be exercised when considering the increased mapping error at the gyre periphery, in regions of limited data coverage, and due to the fact that all mapped fields are spatially gridded temporal composites. The work presented here provides the prerequisite technical component of investigations into the variability of Weddell Gyre

water mass properties, providing further insight into the role of the Weddell Gyre in a changing climate.

3.8 Appendix 1: Data format: gridded fields of upper Weddell Gyre water properties

The time-composite data sets of mapped field variables are provided as netCDF files, with one file for each available time period. The filenames and corresponding variables provided in each netCDF file are listed in Tables 3.A1 and 3.A2 respectively. Mapped fields of conservative temperature (° C), absolute salinity (g kg^{-1}), potential temperature (ºC), practical salinity and potential density (kg m^{-3}) as well as corresponding mapping errors are provided for 41 vertical pressure levels (listed in Table 3.1). Additionally, conservative temperature, absolute salinity and pressure (dbar) at the level of the subsurface temperature maximum are provided. The coordinates represent the centre of each grid cell. The missing value is defined by *NaN*. Further details found in the global attributes of the netCDF files are described throughout the main paper.

Table 3.A1. List of netCDF filenames where the mapped field variables for the different time-composite periods are found.

Name of netCDF files
WeddellGyre_OM_Period2001to2013.nc
WeddellGyre_OM_Period2001to2005.nc
WeddellGyre_OM_Period2006to2009.nc
WeddellGyre_OM_Period2010to2013.nc
WeddellGyre_OM_Period2001to2014_potTpSal.nc
WeddellGyre_OM_Period2001to2005_potTpSal.nc
WeddellGyre_OM_Period2006to2009_potTpSal.nc
WeddellGyre_OM_Period2010to2014_potTpSal.nc

Table 3.A2. List of variable names in the accompanying netCDF file. The mapped variables listed are provided in the form of grids structured by latitude x longitude x pressure level, where fill values are NaNs. The asterisk (*) indicates variables which are not found in the netCdf file of the entire 11-year time period, *WeddellGyre_OM_Period2001to2013.nc*.

Variables provided in the netCDF files
Pressure Levels (dbar)
Latitude (DegN)
Longitude (DegE)
Tmax Conservative Temperature (DegC)
Tmax Absolute Salinity (gPERkg)
Tmax Pressure (dbar)
Tmax RHO (kgPERm3)
Tmax Conservative Temperature mapping error (DegC)
Tmax Absolute Salinity mapping error (gPERkg)
Tmax Pressure mapping error (dbar)
Tmax RHO mapping error (kgPERm3)
Conservative Temperature (DegC)
Absolute Salinity (gPERkg)
RHO (kgPERm3)
Conservative Temperature mapping error (DegC)
Absolute Salinity mapping error (gPERkg)
RHO mapping error (kgPERm3)
Tmax Conservative Temperature mask based on Period2002to2013
Tmax Absolute Salinity mask based on Period2002to2013
Conservative Temperature mask based on Period2002to2013
Absolute Salinity mask based on Period2002to2013
Tmax Conservative Temperature mask based on Period of file*
Tmax Absolute Salinity mask based on Period of file*
Conservative Temperature mask based on Period of file*
Absolute Salinity mask based on Period of file*

Acknowledgements

These data were collected and made freely available by the International Argo Program and the national programs that contribute to it (http://www.argo.ucsd.edu, http://argo.jcommops.org). The Argo Program is part of the Global Ocean Observing System. The GEBCO Digital Atlas is published by the British Oceanographic Data Centre on behalf of IOC and IHO, 2003. This work is dedicated to the memory of Eberhard Fahrbach (who passed away on the 21th April 2013), a great Polar Oceanographer who championed the observation of the Polar Oceans and was an inspiration to us all. The authors would like to thank the anonymous reviewers for their invaluable feedback.

4 Publication II

Horizontal circulation and volume transports in the Weddell Gyre derived from Argo float data

Under review in Progress in Oceanography, 2017

K.A. Reeve[1,2], O. Boebel[1], V. Strass[1], T. Kanzow [1,3], and R. Gerdes[1,2]

1 Alfred-Wegener-Institut Helmholtz-Zentrum für Polar- und Meeresforschung, Bremerhaven, Germany

2 Physics and Earth Sciences, Jacobs University, Bremen, Germany

3 Bremen University, Physics and Electrical Engineering, Bremen, Germany

Abstract

Argo floats provide both hydrographic and trajectory data, affording the opportunity to investigate surface to mid-depth ocean dynamics. Here, Argo float data are used to determine the absolute geostrophic velocity field of the upper 50 to 2000 m of the Weddell Gyre, from which the overall circulation pattern is investigated. The Weddell Gyre plays a pivotal role in the modification of climate by advecting heat towards the Antarctic ice shelves and by modifying the water masses that feed into the lowest limb of the global ocean overturning circulation. Warm Deep Water, the source water mass that delivers heat to the Weddell Gyre, is conveniently located within the upper 2000 m domain covered by the floats; we investigate its volume transport as it circulates the gyre. Full depth volume transports are estimated by applying a quadratic function to extrapolate the relative dynamic height field component to the full ocean depth, using CTD profiles from ship-based surveys to determine an extrapolation error. Major new insights are provided by this study. There is an established double-gyre structure to the circulation, with a strong eastern cell and a weaker western cell. Regional variation of the baroclinic component of the flow field is revealed, indicating a northeast-to-southwest reduction in the baroclinic flow, along with a strong meridional gradient of baroclinic flow along the northern limb of the gyre, especially east of ~25º W. The zonal mean gyre strength away from the shelf edge is 32 ± 5 Sv (1 Sv = 1 x 10^6 m^3 s^{-1}), of which 13 ± 3 Sv are associated with the advection of Warm Deep Water. There is a considerable amount of recirculation within the gyre interior, where water does not traverse the full zonal extent of the gyre. The recirculation is stronger in the eastern cell of the observed double-gyre structure. The interior circulation cells partly explain the large variations in previous gyre strength estimates. We provide an extensive review of previous estimates in context of the new results obtained.

4.1 Introduction

The formation and equatorward export of Antarctic Bottom Water (AABW) feeds the lower limb of the overturning circulation and accounts for deep ocean ventilation (Jullion et al., 2014, Talley, 2013, Orsi et al., 2002). As such, AABW is a prominent water mass present throughout most of the deep basins of the world ocean (Orsi et al., 1999; Johnson, 2008). AABW properties are changing as a result of a rapidly changing climate (Anilkumar et al., 2015, Johnson & Doney, 2006, Purkey & Johnson, 2012, 2013). The Weddell Gyre plays a key role in the global ocean overturning circulation, by supplying source water masses for the formation of Weddell Sea Deep and Bottom Water (WSDW and WSBW, respectively), through the modification of Warm Deep Water (WDW) over the shelf and during periods of open ocean convection (Fahrbach et al., 1991, Fahrbach et al., 1995, Garabato et al., 2002, Meredith et al., 2000). The subsequent northward export of WSDW, which feeds into AABW, and the transport of AABW originating from the Indian sector of the Southern Ocean, contributes towards the closure of the southern limb of the overturning circulation (Jullion et al., 2014; Couldrey et al., 2013, Hoppema et al., 2001, Meredith et al., 2000).

The Weddell gyre is a predominantly wind-driven gyre where relatively warm, salty Circumpolar Deep Water (CDW) enters from the open eastern boundary and to a lesser extent the open northern boundary (Fahrbach et al., 2004, Fahrbach et al., 2011, Klatt et al., 2005, Cisewski et al., 2011, Donnelly et al., 2017). A simplified schematic of the gyre circulation is provided in Fig. 4.1. The CDW that has entered the gyre is commonly referred to as WDW. WDW is established by a subsurface temperature and salinity maximum (Fig.2 and Fahrbach et al., 2004, Fahrbach et al., 2011, Klatt et al., 2005).

The gyre has long been recognized as cyclonic, characterized by a central doming of its isopycnals, a view that was established as early as the early 1900s (Brennecke, 1918). The description of the Weddell Gyre as an elongated, cyclonic system constrained by the Antarctic Peninsula to the west with a more complex and less well defined eastern boundary was then provided by Deacon (1979), through the provision of maps of the sub-surface temperature maximum and its depth in the water column. Gordon et al. (1981) showed that the Weddell Gyre is wind-driven, comparing the Sverdrup transport of the wind data over the Weddell Gyre with baroclinic dynamic

topography derived from hydrography data. The comparison yielded a similarity in the general circulation patterns west of 30º E, but highlighted the poor alignment of the cyclonic troughs between the Sverdrup Transport and dynamic topography patterns. Orsi et al. (1993) further investigated the Weddell Gyre circulation by providing maps of dynamic height surfaces and tracer distributions, and used patterns of geostrophic shear to demonstrate that the northeastern extent of the Weddell Gyre occurs at ~30º E, and inferred a "two-gyre cyclonic system" in the WSDW layer, but not in the sub-surface layer. Since these early studies in the Weddell Gyre, numerous ship campaigns have allowed for a more complete description of the gyre structure, and volume transports have been estimated for various cross-sections throughout the Weddell Gyre. The cross-sections for which estimates exist in the literature differ in both time and space, and provide a wide range of volume transport estimates. Most studies indicate a general disproportion between the volume transports of the eastward flowing northern and the westward flowing southern limbs of the gyre, suggesting that the inflow versus outflow regimes must be imbalanced, due to export of water masses from the open northwest boundary as well as water mass transformation within the Weddell Sea (Klatt et al., 2005; Fahrbach et al., 2011). Water-mass transformation plays a prominent role in the thermodynamics of the Weddell Gyre, which exhibits an asymmetric double-celled overturning circulation (Jullion et al., 2014), where the lower cell involves densification of deep and bottom waters at the south and western margins, and the upper cell involves lightening of WDW into upper ocean waters within the centre of the gyre (Jullion et al., 2014; Naveira Garabato et al., 2016). While volume transports derived from observations vary zonally throughout the gyre, where, for example, transports are larger in the east at the Prime Meridian (Klatt et al., 2005) than in the west at 30º W (Heywood & King, 2002), it is not clear whether this is an artifact of different time periods being examined, or if it truly reflects zonal differences in gyre structure.

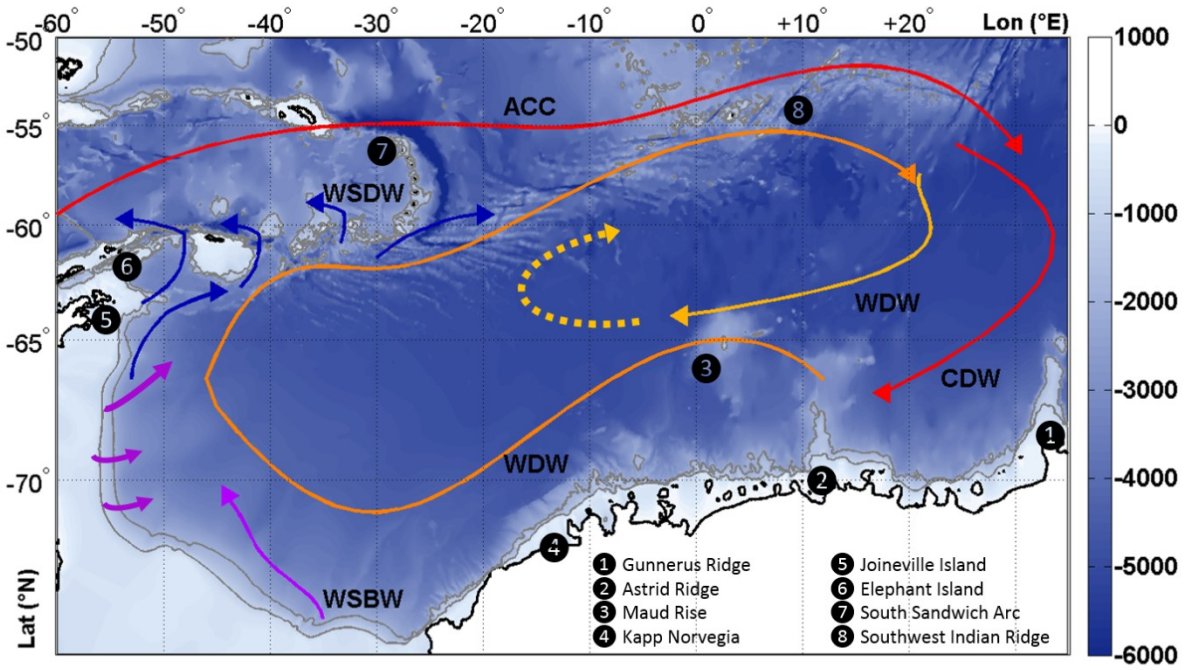

Figure 4.1. Schematic of the Weddell Gyre circulation overlying bathymetry (IOC, IHO and BODC, 2003), adapted from Ryan et al. (2016). The red arrows indicates the relatively warm and salty Circumpolar Deep Water, which enters the Weddell Gyre to the east from the ACC. As CDW enters the gyre, where it is named WDW (orange), it undergoes modification as it circulates the gyre (light orange arrow). WSBW spills into the Weddell Gyre basin from underneath the ice shelves in the southwestern Weddell Sea (purple arrows). The dark blue arrows indicate the export routes of WSDW. The legend provides the names of prominent bathymetric features. The grey contours provide the 1000 and 2000 m isobaths.

Since the implementation of the Argo float program, the amount of data available for the Weddell Gyre has increased significantly, albeit down to a depth of 2000 dbar or approximately 2000 m (Fig. 4.2a). Conveniently, WDW is fully contained within this pressure range (Fig. 4.2b). This provides an opportunity to assess the complete, large scale circulation of the upper 2000 dbar of the Weddell Gyre, by combining both Argo float trajectory and profile data to obtain a 3-dimensional grid of the absolute geostrophic circulation. Gray & Riser (2014) implemented such a procedure on a global scale, to calculate gridded dynamic height fields referenced to a level of known absolute velocity derived from Argo trajectories. However, the Weddell Gyre was mostly omitted due to insufficient data coverage at the time.

In this paper, Argo trajectory and profile data are gridded with special focus and consideration to the Weddell Gyre in order to describe the offshore, full gyre circulation and more specifically the volume transport of WDW throughout the gyre. The analysis excludes the coastal currents and associated frontal transports, such as the Antarctic Slope Front (ASF), since Argo floats are not able to resolve these narrow coastal features, and thus focuses on the offshore circulation, where the bottom depth is deeper

than 2000 m. The inability to resolve the ASF and narrow frontal coastal jets is a major limitation of the study, since as much as 50 % of the transport can be concentrated within these small-scale features above the continental shelf edge (Thompson & Heywood, 2008). The paper commences by outlining the processes involved in determining a gridded non-divergent absolute velocity field for 41 pressure levels spanning 50 to 2000 dbar in the methods section. In the results section, maps of the stream function describing the circulation will be presented along with estimates of volume transports. Finally, the discussion provides a comparison to previous Weddell Gyre volume transports given in the literature. Profile and trajectory Argo data are described in the Appendix. The procedure for deriving velocity from the trajectory data is also provided in the Appendix.

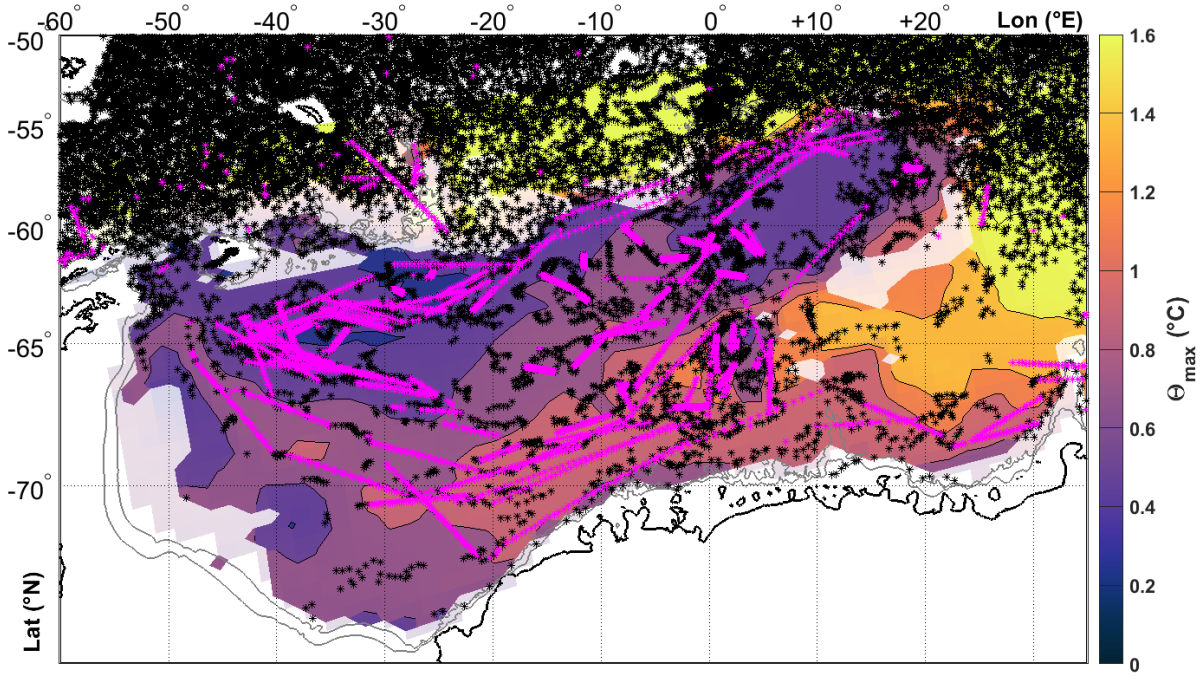

(4.2a)

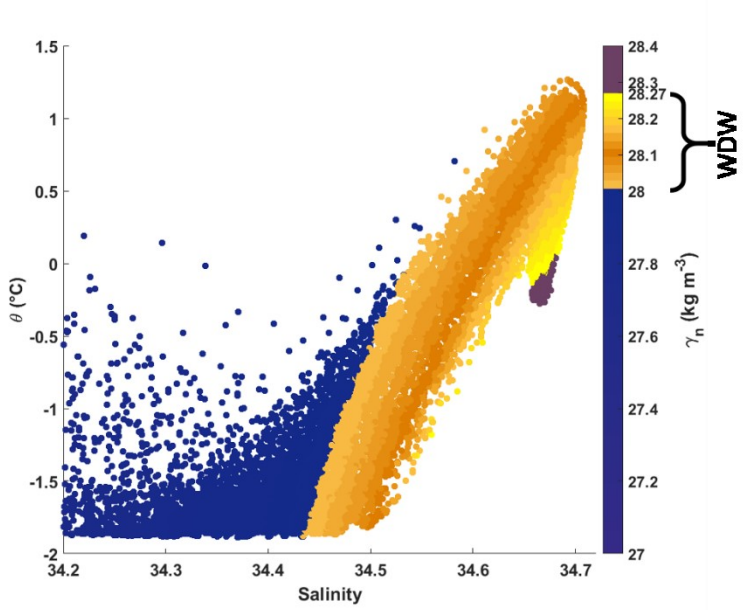

(4.2b)

Figure 4.2 **(a)**. Map of sub-surface temperature maximum (ºC), with Argo float profile positions between 2002 and 2016 (*). Profiles with interpolated positions under the sea-ice are marked in magenta (*). The grey contours provide the 1000 and 2000 m isobaths. Panel **(2b)**: potential temperature - salinity diagram of a random selection of Argo float profiles within the Weddell Gyre, showing the upper 2000 dbar of the water column. The colour scale shows the neutral density of the water column (kg m^{-3}), where water within the WDW layer (with neutral density limits 28.0 and 28.27 kg m^{-3}) is emphasized by the yellow/orange colour range.

4.2 Methods

4.2.1 Argo float data

All available floats within the region bounded by 40° S to the Antarctic coast, and 90° W to 60° E were downloaded from ftp.ifremer.fr. Since few delayed-mode trajectory data are available for this region, all available trajectory data including real-time mode were included in this study. Data from 603 floats were downloaded. All floats where no trajectories entered the region 50° to 80° S, 60° W to 40° E were removed. For a float trajectory to be used, it had to have at least 5 cycles. All cycles where position accuracy is 0 or 4 were discarded (including cycles with interpolated positions under the sea-ice; highlighted in magenta in Fig. 4.2a), likewise if the float has drifted at the surface for more than a day. A cycle required a minimum of 4 satellite fixes if it was to be used. After the application of quality control checks (for details refer to Appendix), the number of floats was reduced to 341 from 603 (note only for trajectories). The remaining floats span 20/02/2002 to 06/09/2016, where most trajectories south of 60º S have been obtained from summer months (Fig. 4.3a). At

parking depth, there are 9169 data points (where the peak number of data points occurs both in 2012 and 2008, Fig. 4.3b), with just 1496 data points south of 60º S; about 39% of which are from 2006-2007 (Fig. 4.3c). After quality control processes were applied, a total of 28,424 delayed-mode hydrographic profiles from 460 floats were used in this study, spanning from 12/12/2001 to 14/05/2016 (for profile positions, see Fig. 4.2a, and for further details, see Appendix). Profile data includes those profiles with an interpolated position under the sea-ice (i.e. the profiles marked in magenta in Fig. 4.2a).

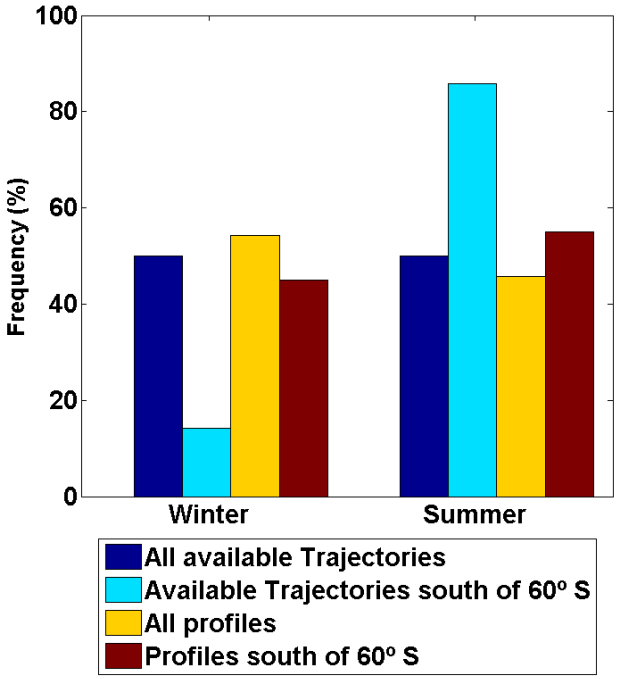

(4.3a)

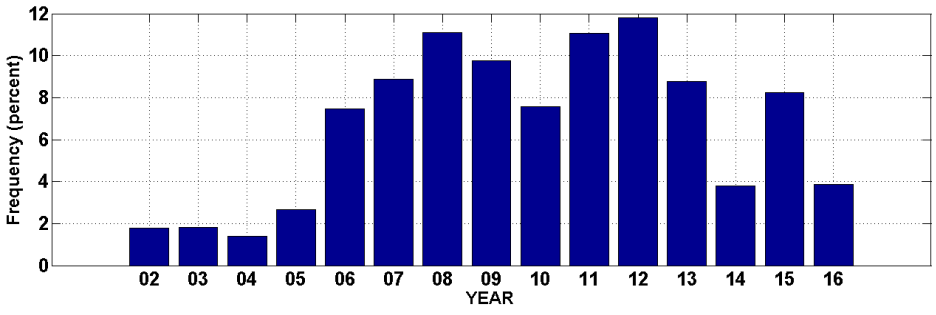

(4.3b)

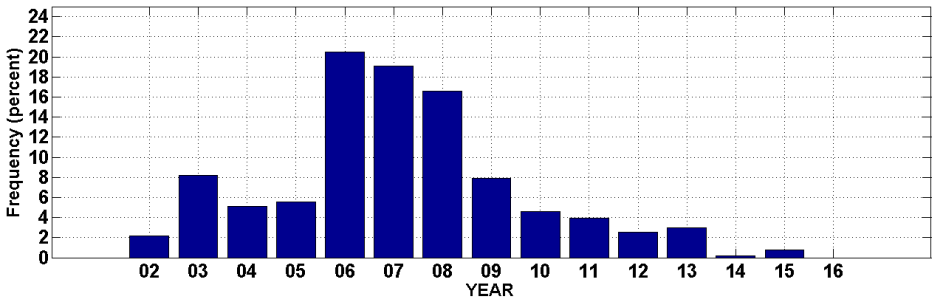

(4.3c)

Figure 4.3. **(a)** Percentage of profile and trajectory data taking place in summer months (December to April) versus winter months (May to November) for all data and data south of 60º S. Panel **(b)**: the yearly percentage of total float trajectory data used in this study between 2002 and 2016 for the whole domain and for south of 60º S in panel **(c)**. The trajectory data exclude interpolated positions where the float is under sea-ice, and includes only the trajectories that passed all conditions detailed in the appendix.

4.2.2 Baroclinic geostrophic velocity relative to 800 dbar from hydrographic profile data

The method described in the following section is an extension of the work presented in Reeve et al. (2016), which applies objective mapping to Argo float data to provide gridded maps of temperature and salinity for the entire Weddell Gyre. For further information than is provided here, refer to Reeve et al. (2016). The analysis proceeded along 41 pressure levels. For a given fixed pressure level, the absolute salinity (S_A) and conservative temperature (Θ), derived using the TEOS-10 Matlab toolbox (the international thermodynamic equation of seawater; IOC et al., 2010), were objectively mapped onto a grid, rotated at a +14^o angle to the zonal (x) axis. A rotated grid is used to better capture the full elliptical-shaped gyre, whose central axis gradually displaced from ~64^o S in the western sector to ~58^o S in the eastern sector of the gyre (Fig. 4.4). The average grid cell resolution is about 80 x 60 km (or ~1.7 x 0.5º), although each grid cell area varies due to the influence of latitude on the x-axis (the grid cell length varies from ~60 km to ~102 km; the y-component varies by just over 1 km). The objective mapping method is the same as that outlined in Reeve et al (2016). The only differences are a dataset that includes more recent data up to 2016, the use of a 14º-rotated grid, and different length scales for the objective mapping procedure. The length scales in Reeve et al. (2016) are comprised of the horizontal distance (L) and fractional distance in potential vorticity (φ), in the e-folding decay scale, $D^2_{ig}/L^2 + F^2_{ig}/\varphi^2 < 1$; where D is the horizontal separation (distance) and the fractional distance F accounts for the difference in potential vorticity between the grid cell g and data point i. L and φ are

the length scales of components D and F respectively. Here, the length scales used were L = 800 km and φ = 0.5 in stage 1 and L = 400 km and φ = 0.25 in stage 2 of the objective mapping procedure. This two-stage method described in Reeve et al. (2016), which incorporates the fractional distance in potential vorticity as a length scale, was originally adapted from Bretherton et al. (1976) by Boehme & Send (2005). The method works particularly well in the Weddell Gyre due to the nature of the gyre circulation and water properties, and indeed Argo float trajectory paths, as revealed by LaCasce (2000), who demonstrated that floats typically flow along contours of constant potential planetary vorticity, *f/H*, where *f* is the Coriolis parameter and *H* the water depth. Bathymetry data for determination of *H* is based on the general bathymetric chart of the oceans (GEBCO; IOC et al., 2003). For further details regarding the objective mapping of profile data, refer to Reeve et al. (2016).

Gridded temperature and salinity fields were used to compute gridded dynamic height anomaly, Ψ_{dh}, relative to the parking depth pressure, p_{ref}, 800 dbar, of floats. Dynamic height anomaly is the pressure integral of the specific volume anomaly $\delta(S_A,\Theta,p) = 1/\rho_{(S_A,\Theta,P)} - 1/\rho_{(Sref,0°C,Pref)}$, where S_A, Θ and P are Absolute Salinity, Conservative Temperature and pressure respectively, implemented using the Gibbs Sea Water package (McDougall & Barker, 2011). This is a geostrophic stream function of the difference between horizontal velocity at pressure P, and the horizontal velocity at P_{ref}. The two-dimensional horizontal gradient (i.e. in both x and y directions of the grid) of the stream function on a given pressure surface, $\nabla_P \Psi_{dh}$, is related to the difference in the geostrophic velocity between P and P_{ref}, thus providing the baroclinic component of geostrophic velocity relative to 800 dbar (IOC, SCOR and IAPSO, 2010):

$$\boldsymbol{k} \times \nabla_P \Psi_{dh} = f\boldsymbol{v} - f\boldsymbol{v_{ref}} \qquad \text{(Eq. 1)}$$

where $\boldsymbol{k}$ is the unit vertical vector, $\boldsymbol{v}$ is the velocity vector and $\boldsymbol{v_{ref}}$ is the velocity vector at the reference (parking depth) pressure level. We used a reference level of 800 dbar as this is the pressure level at which we know absolute velocity from the trajectory data, which is detailed in the following section.

4.2.3 *Objective mapping of parking depth velocity derived from trajectory data*

From the floats we can obtain two fields of absolute velocity at parking depth: the uncorrected velocity, and the surface-horizontal-drift corrected velocity (from now

on we will refer to this as SD corrected velocity), as detailed in the Appendix. Objective mapping was applied to both fields in order to obtain gridded absolute velocity fields at 800 dbar. The method followed is the same as applied to the profile data, with few differences. In the method described in Reeve et al. (2016), the number of data points used to determine a grid point value, N, was 40, which is also the criterion used for dealing with the hydrographic profiles in the previous section. Grid points were neglected if less than 40 data points were available within the decay scale criteria (i.e. e-folding decay scale < 1). When gridding the velocity data with the same criterion, significant areas were being omitted from the interpolation despite numerous velocity data points close to the grid point in question, leading to implausible features in the stream function that would be fitted to the data. Therefore we adjusted our criteria, so that if less than 40 data points passed the decay scale criteria, a new decay scale would be calculated using a smaller length scale and larger φ, of L = 220 km and φ = 0.5. This creates a smaller, less elliptical radius of influence (this condition is applied to 23 grid cells along the shelf edge in the southwestern Weddell Sea, south of 66º S, which had no influence on the resulting fitted stream function). If there were more than 2 velocity data points available, these were used (this applied to 5 grid cells in the southernmost part of the grid between 30 and 40º W, and 9 grid cells along the shelf edge between 20 and 0º W). If there was only one velocity available, it would only be used to represent the grid point if the data point was less than 110 km from the grid point in question, and passed manual inspection (this applied to three grid points). The grid points that influenced the fitted stream function are those grid points close to the Antarctic coast east of 15º W, where the meridional gradient of bathymetry (and therefore the gradient in background potential vorticity, f/H) is large. Upon inspection of all grid points listed above, the available velocity data points appeared to follow the bathymetry closely. Including these data points greatly improved the resulting stream function derived from the gridded velocity field, described below. Lastly, we changed the way we estimate the first guess field in stage one of the mapping of velocity data from the mapping of profile data. When mapping profile data in Reeve et al. (2016) and in Section 4.2.2, the first guess field was estimated by taking a zonal mean of profile data binned into latitudinal bands, which works well as a first guess due to the dominant meridional gradient of the hydrographic field in the Southern Ocean. However, this is not appropriate for estimating the first guess velocity field within a gyre. Therefore, the first guess field of any grid point was the median of all data points within a 600 km radius of the grid

point. The median was used instead of the mean in order to avoid skewing the data to anomalously large values. The first guess field of stage one of the two-step mapping procedure provides a large scale mean field which is then "corrected" using stages one and two of the mapping method, as with, for example, Böhme & Send (2005) and Reeve et al. (2016).

4.2.4 *Determination of a reference dynamic height field from absolute velocity at 800 dbar*

For both the uncorrected and SD corrected gridded velocity data (see Appendix for further details on SD corrected velocity), a horizontal stream function, Ψ, was fitted to approximate a non-divergent, geostrophic velocity field, following Pollard & Regier (1992) and Allen & Smeed (1996). The stream function relates to the horizontal velocity components of $\boldsymbol{u}$ (Eq.2), and is obtained by solving Eq. 3 using Neumann boundary conditions (Eq. 4):

$$u = -\frac{\partial \Psi}{\partial y}, \quad v = \frac{\partial \Psi}{\partial x} \qquad \text{(Eq. 2)}$$

$$\nabla^2 \Psi = \nabla \times \boldsymbol{u} \qquad \text{(Eq. 3)}$$

$$\frac{\partial \Psi}{\partial n} = \boldsymbol{n} \times \boldsymbol{k} \cdot \boldsymbol{u} \qquad \text{(Eq. 4)}$$

where **n** is the unit vector perpendicular to the boundary and **k** is the unit vertical vector. In Eq. 4, Neumann boundary conditions ensure that the horizontal gradient of the stream function perpendicular to the boundary is forced to be equal to the component of the velocity along the boundary (e.g. Allen and Smeed, 1996). The resulting stream functions were then multiplied by the Coriolis parameter field in order to arrive at a stream function of the reference dynamic height at 800 dbar. This was then added to each pressure level of the relative dynamic height field calculated from the profile data at each pressure level.

4.2.5 *Calculating volume transports: gyre-scale means and cross-sections for WDW, the upper 2000 m and the full-ocean depth*

The resulting 3-dimensional grid of the horizontal geostrophic stream function was used to estimate the gyre-scale mean volume transport, as well as the volume transports across various cross-sections throughout the gyre. The volume transport is

determined by the vertical integral of the horizontal gradient of the stream function. A water mass specific volume transport was calculated for the WDW; the vertical limits at each grid point were taken from the pressure of the upper and lower limits of WDW. We define WDW as the mass of water with a neutral density range of 28 to 28.27 kg m^{-3}, in accordance with Fahrbach et al (2011).

The volume transports for the full depth were also determined, although with an additional degree of uncertainty: since Argo floats provide only measurements of the upper 2000 dbar, the relative dynamic height field for below 2000 dbar was extrapolated. The extrapolation was implemented by using a least squares approach to fit a quadratic function to the vertical profiles of relative dynamic height, from 1000 to 2000 dbar. This was carried out individually for the vertical profile of each grid cell. A quadratic function was found to represent the best fit by comparison with full depth dynamic height profiles derived from ship-based CTD data (for an example. See Fig. 4.A4), which was subsequently used to calculate an error estimate for extrapolating to the full ocean depth. The error calculation is detailed in the following Section, 4.2.6. A flow chart outlining the full procedure in arriving at a 3-Dimensional grid of the gyre circulation and resulting volume transport estimates is provided in the Appendix (Fig. 4.A5).

Since the grid domain includes part of the ACC (a rotated grid helps to keep out most of the ACC from the domain but cannot remove it completely), a definition of the northern Weddell Gyre boundary becomes necessary for volume transport calculations. Fahrbach et al. (2011) define the northern boundary as the position of the Weddell Front, which is located at the position where the core of CDW of the ACC meets the relatively cold subsurface water of the Weddell Gyre. In Reeve et al. (2016) a simple method is outlined which locates the northern boundary by finding the latitude at which the meridional gradient of the sub-surface temperature maximum is greatest. By this method, the northern boundary at the Prime Meridian was found to be at 56º S, in agreement with Fahrbach et al, (2011). For the volume transports presented in Section 4.3.2, the streamline that marks the boundary is the most peripheral streamline that is encompassed by the gyre at the reference level, 800 dbar (-0.35×10^4 $m^2 s^{-1}$; in Figs 6-8, the domain within the streamline boundary is in colour). In the south, the streamline boundary sits as close to the coast as possible, but still excludes parts of the coastal region of the gyre. The position of this streamline boundary is applied to each depth

level, fixing the total area of the gyre for all depth levels. This streamline shows good agreement with the northern boundary based on the sub-surface temperature maximum distribution defined in Reeve et al. (2016) and also resides between 55 and 56º S at the Prime Meridian, in agreement with Fahrbach et al. (2011). Since both the Weddell Gyre and the ACC are considered largely barotropic (e.g. Fahrbach et al. 1994, Gille, 2003), we make the assumption that the northern boundary is uniform with depth.

4.2.6 Estimating uncertainty through perturbation of the flow field

Before presenting the stream functions and the resulting volume transports of the Weddell Gyre, it is important to establish the sources of potential error, and the approach to estimating error for the volume transport estimates. There are many sources of error in this approach, each of which will be detailed subsequently hereinafter. Estimation of uncertainty in the volume transports will be presented later in Discussion Section 4.4.1, when comparing the new results with those given in the literature.

4.2.6.1 Sources of error

We have four main sources of error to consider: the calculation of velocity at 800 dbar based on float positions at the surface, instrumental errors, and errors associated with interpolation of observations covering a long period of time (from 2002 to 2016). The final source of error concerns only the full depth transports, which use a data set that has been extrapolated below 2000 dbar. We discuss the first three of these below while the latter will be discussed in 4.2.6.2:

I. Absolute velocity field at 800 dbar:

We use float position data in order to determine velocity at 800 dbar. Since Argo floats have a cycle period of typically 10 days, it is assumed that they provide good estimates of time-averaged geostrophic reference velocities at their parking depth level, averaging over tidal and internal wave cycles (Gille, 2003). However, the velocities are dependent on the quality of the position data. We apply quality control procedures as described in Section 4.2.1 and the Appendix, where all data with quality flags of 0 or 4 are removed, and a single float has to have at least 5 cycles in order to be used (5 cycles is also the criterion used in Grey & Riser, 2014). This results in the removal of all under-ice trajectories, where the position of the float is estimated from linear interpolation of the time and start and end positions before/after the float enters the sea-ice covered area (such profiles are marked in

magenta in Fig. 4.2a, and the resulting seasonal bias in trajectory data is provided in Fig. 4.3a). We also apply a surface drift (SD) correction for the time delay between the float surfacing (descending) and the first (last) satellite fix, using a cost function as a function of the position accuracy (Eq. 4.A3; the cost function is described in the Appendix). We do not, however, account for any horizontal drift while the float is ascending/descending and subjected to variable currents, such as geostrophic shear, Ekman velocity and inertial oscillations (Park et al., 2004, Park et al., 2005). For the SD correction, we have a mean position accuracy of 0.1 km for the position of the float after surfacing, and of 1 km for the position of the float when leaving the surface (this is provided by the cost function; Appendix Section 4.A1). Over 10 days, 1 km amounts to an uncertainty in velocity of 0.0012 m s^{-1}, negligible in context of the other sources of uncertainty incorporated into this work. Therefore, we can assume that the uncertainty resulting from applying no correction for horizontal drift during ascent/descent will be less than 1 km, (as the strongest velocities are typically observed at the surface and time at the surface is longer than the typical ascent time). Park et al. (2005) show that the total error associated with SD corrected subsurface velocity estimates leads to an uncertainty of 0.002 m s^{-1}, while Lebedev et al. (2007) calculate parking depth velocity without using a SD correction procedure, and find a mean velocity error of 0.0053 m s^{-1} (although they note a most probable value of 0.0025 m s^{-1}).

II. Instrument sensor error:

A principal problem of Argo floats is that it is impossible to service and recalibrate the sensors after deployment, or to calibrate floats to one another. While data quality control aims to improve the quality of data by the best means possible, we still have a source of error to consider. Pressure data from Argo floats are accurate to ±2.4 dbar while temperature data are reported as accurate to ±0.002 ºC, (Owens and Wong, 2009). For salinity data, with a small sensor drift, uncorrected salinities are accurate to ±0.1, although this value can increase with increasing sensor drift. Float profiles are subject to detailed scrutiny during delayed-mode processing by comparison with historical data (Owens and Wong, 2009), which provides corrected adjusted values as well as corresponding quality flags. In the delayed-mode adjusted salinity data (with a quality flag of 1) as used in this study, the mean adjusted salinity error is 0.01, while the largest error does not exceed 0.1

(Further information is provided in Reeve et al., 2016). It is assumed that uncertainty due to instrumental errors is insignificant, as it is considerably smaller than uncertainty introduced by noise from time and spatial – dependent variations owing to the large scales used in the objective mapping, and the composite nature of the final gridded data set.

III. Objective mapping:

The major source of error is associated with the application of optimal interpolation to the velocity vector field (Section 4.2.3), as well as to the hydrography data (Section 4.2.2). The advantage of the objective mapping method is that it provides a statistical error estimate; however, this estimate is sensitive to the choice of length scales in the covariance functions used for mapping, and is inaccurate as the "true" covariance function is unknown. The mapping error takes into account the spatial distribution (Sections 4.2.2 and 4.2.3 and Reeve et al. 2016) of the data as well as its signal variance; thus errors are relatively small in regions where bottom bathymetry is flat, horizontal gradients are small, and where data density is adequate. Reeve et al. (2016) show that this results in relatively small errors within the Weddell gyre interior, but larger errors at the gyre periphery. Due to the lack of data, and the fact that we are mapping a dataset spanning a large time period as a time composite dataset, it is necessary to ensure that the spatial length scale used is large enough to avoid skewing different regions to data from different time periods. Thus, the large spatial scales and the lack of a time scale potentially results in a large source of error as the data span 14 years. However, by incorporating an f/H component in the decay scale, we try to improve the decorrelation scales by allowing the radius of influence about a grid point to skew in favor of f/H contours (Section 4.2.2, and in more detail in Section 3.2.3 in Reeve et al., 2016). Reeve et al (2016) show that the mapping error is largest above 200 dbar, within the domain of Winter Water, and decreases with increasing pressure (note pressure surfaces above 50 dbar are not provided due to strong seasonal variability).

4.2.6.2 Estimate of uncertainty of volume transports through "perturbed scenarios"

We combine the gridded absolute velocity field at 800 dbar with the gridded hydrographic data through the derivation of the dynamic height field; the absolute

dynamic height field at 800 dbar becomes the reference level for the relative dynamic height field computed as geostrophic shear from the hydrographic gridded data. Due to the presumed largely barotropic nature of the gyre, we expect that the uncertainty is likely dominated by the determination of the reference velocity field. Therefore, in order to estimate uncertainty when evaluating volume transports, we provide a series of "perturbations" to the geostrophic stream function. We consider the best estimate of the flow field to be the sum of the non-divergent stream function from the SD corrected velocity field at 800 dbar, and the stream function derived from hydrography data relative to 800 dbar. The following describes the perturbations from which we estimate error for the derived volume transports:

i. Stream function of the SD *corrected* velocity field, plus the stream function of the objectively mapped hydrographic field plus mapping error
ii. Stream function of the SD *corrected* velocity field, plus the stream function of the objectively mapped hydrographic field minus mapping error
iii. Stream function of the SD *uncorrected* velocity field, plus the stream function of the objectively mapped hydrographic field
iv. Stream function of the SD *uncorrected* velocity field, plus the stream function of the objectively mapped hydrographic field plus mapping error
v. Stream function of the SD *uncorrected* velocity field, plus the stream function of the objectively mapped hydrographic field minus mapping error

When calculating the volume transport, the volume transports of all "perturbed" fields are calculated, and the difference between these "perturbed" field estimates and the "correct" estimate is evaluated. The volume transport error estimate is assessed as the root mean square deviation (RMSD) between the true field and the perturbations; RMSD is a measure of accuracy that can be used to assess forecasting errors of different models (or in this case, perturbations) of the same dataset, by accumulating the magnitudes of the errors of the various predictions. Therefore the error estimate is not confined to a statistical error as it represents the general uncertainty, pointing to a range of possible values determined by the propagation of mapping errors. By creating

perturbations of the geostrophic velocity field, we simulate the potential possible outcomes owing to uncertainty prescribed by the complex method involved in arriving at volume transport estimates from a time composite dataset.

Regarding full depth volume transport, we incorporate an additional error due to extrapolating below 2000 dbar to the full ocean depth. This error is determined using CTD profiles collected from 15 ship-based surveys in the Weddell Gyre from 1983 to 2016. At each grid cell of the gridded Argo float data set, all CTD profiles within an arbitrarily defined 100 km radius were selected for comparison to the grid cell vertical profile of dynamic height. If there was more than one profile available, the RMS of the differences between relative dynamic height of the grid cell profile and the CTD profiles were determined, and the CTD profile with the smallest RMS (hence, most similar vertical profile to the gridded profile) was selected. Only grid cells where a CTD profile is available within 100 km radius of the grid cell are used for the error calculation. The CTD profiles were linearly interpolated onto the same pressure levels as the gridded float data set to allow for direct comparison. The error estimate of extrapolation is defined as the square root sum-squared of two components (Eq. 6): the first component, RMS_{CTD}, is the performance of a quadratic function determined from data between 1000 and 2000 dbar in predicting the true dynamic height field below 2000 dbar, which is defined as the RMS between the original CTD profile and the fitted CTD profile. The second component, RMS_{ARGO}, is the difference between the extrapolated Argo profile and the fitted CTD profile, in order to determine the error of extrapolating Argo data beyond the depth of data coverage. Thus, we estimate the error related to the quadratic function, but also the error of not knowing how representative the CTD profile is of the gridded Argo profile, which is a mapped product of objective interpolation from an independent data source. The above procedure results in a series of error estimates for grid cells where a comparable CTD profile is available. The final error estimate is the RMS of all N errors (Eq. 7), which results in a dynamic height error estimate of 0.1585 $m^2 s^{-2}$. This finally results in a volume transport error estimate that is dependent on the latitude, ϕ (due to the Coriolis force, f) and bottom depth, H (Eq. 8). For example, at 65º S, with a bottom depth of 5000 m, the error in extrapolating below 2000 m is 3.6 Sv. The median error for the entire Weddell Gyre, where bottom depth is deeper than 2000 m, is 3 Sv. It should be noted that the time period or season of the

ship-based profile is not taken into account in this error analysis, and that the available ship-based CTD profiles are mostly from summer months only.

$$\varepsilon_{Extrap} = \sqrt{RMS_{CTD}{}^2 + RMS_{ARGO}{}^2} \quad \text{(Eq. 6)}$$

$$\varepsilon_{ExtrapTotal} = \sqrt{\sum_n \frac{\varepsilon_{Extrap}{}^2}{N}} = 0.1585\ m^2 s^{-2} \quad \text{(Eq. 7)}$$

$$\varepsilon_{Extrap\_Transport} = \left(\frac{\varepsilon_{ExtrapTotal}}{f(\phi)}\right)(H - 2000) \div 1x10^6\ (Sv) \quad \text{(Eq. 8)}$$

This error estimate is added in quadrature to the RMS of the error perturbations outlined at the beginning of this section, to estimate a total propagation of error for full depth volume transports.

4.3 Results

4.3.1 Weddell Gyre circulation in the upper 50-2000 dbar

We present the stream functions for 6 pressure surfaces at 50, 800, 1600, 2000, 3000 and 4000 dbar respectively (Fig. 4.4). Figure panels 4.4a-d (50 to 2000 dbar) show an elongated cyclonic gyre structure, whose central axis exhibits a general northward displacement from west to east, from ~65ºS at 45ºW to ~58ºS at 10ºE, which remains virtually the same for all pressure levels (it is also apparent in Figs 4.4e-f, at 3000 and 4000 dbar respectively, although the gyre structure is less well defined). The flow is considerably broader in the southern limb of the gyre, especially west of 10º W, although it must be noted the mapped domain does not extend to the southern continental shelf edge where one can assume the flow would be intensified due to the Antarctic Slope Front (ASF), and the fast, narrow Antarctic Coastal Current (ACoC), typically observed along the coast (e.g. Gill, 1973, Fahrbach et al., 1992, Heywood et al., 1998). The general circulation east of 10º W is stronger (Figs. 4.4a-f) than to the west. Between ~ 20° and 25º E, the streamlines of the Weddell Gyre curve towards the coast, leading to an inflow associated with its southern limb, south of 60ºS.

The most striking difference between the pressure levels occurs north of the Weddell Gyre, in the ACC, where the flow decreases markedly with depth. While the strongest velocities at 50 and 200 dbar are clearly occurring in the ACC, where contours

indicate a strong west-east flow field, this pronounced west-east contouring is replaced with a less distinct flow field at pressure levels larger than 1200 dbar, particularly west of the Prime Meridian. The curvature of the northern boundary streamline around the South Sandwich Arc at ~27ºW reduces with increasing depth; at 50 and 200 dbar, the contours exhibit intense curvature, showing an almost directly southward flow along the South Sandwich Trench before transitioning into the eastward flow at the northern boundary at ~22ºW, while at 800 dbar the fairly broad contours extend south-east before curving into an eastwards direction as part of the northern boundary at ~15ºW. At 1200 dbar (not shown), there is a very slight indication of a northward flow which becomes increasingly well-defined with increasing depth (this outflow is most pronounced at 4000 dbar, although caution is warranted when interpreting flow at this depth; Fig. 4.4f).

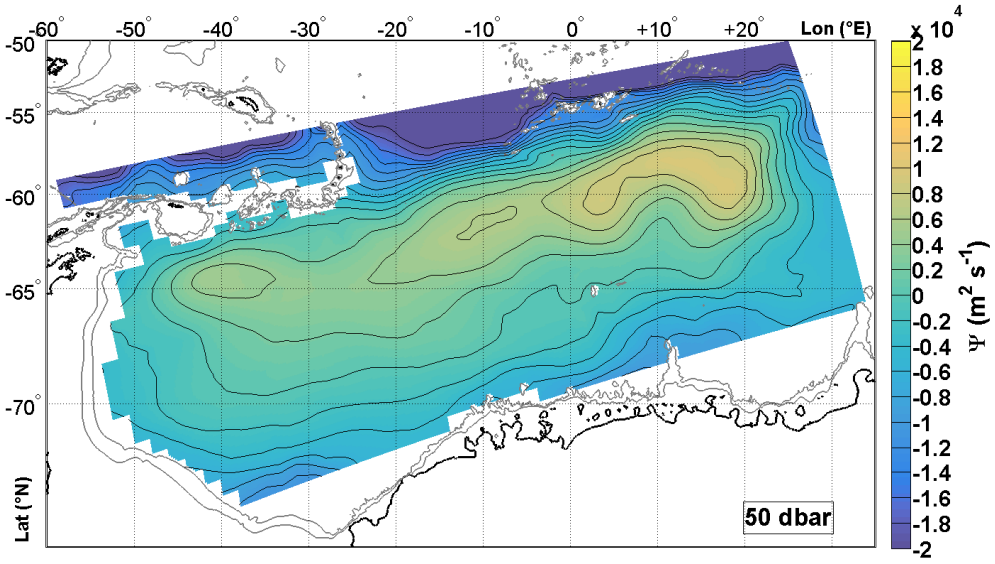

(4.4a)

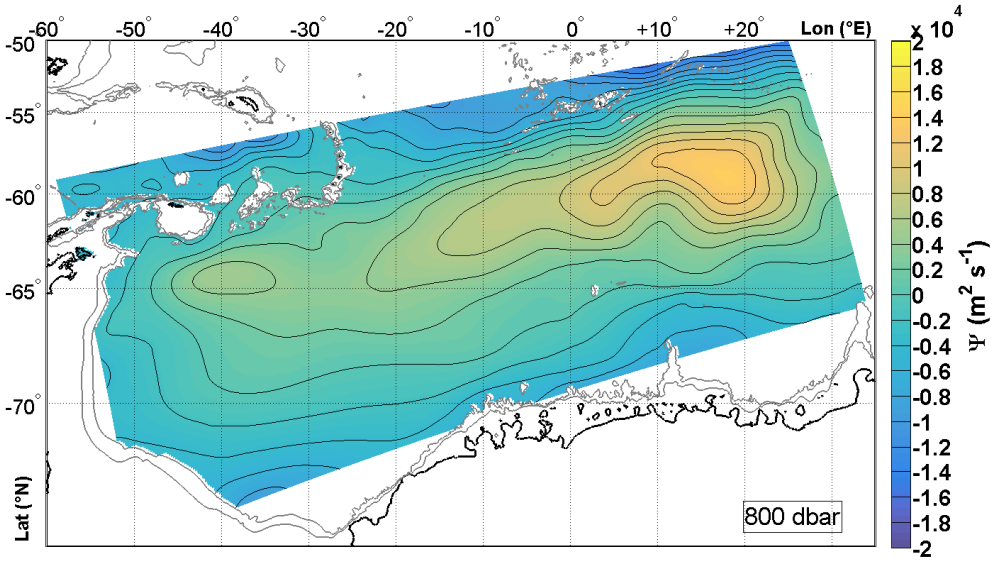
Lon (°E)
Lat (°N)
800 dbar
x 10^4
Ψ (m^2 s^-1)

(4.4b)

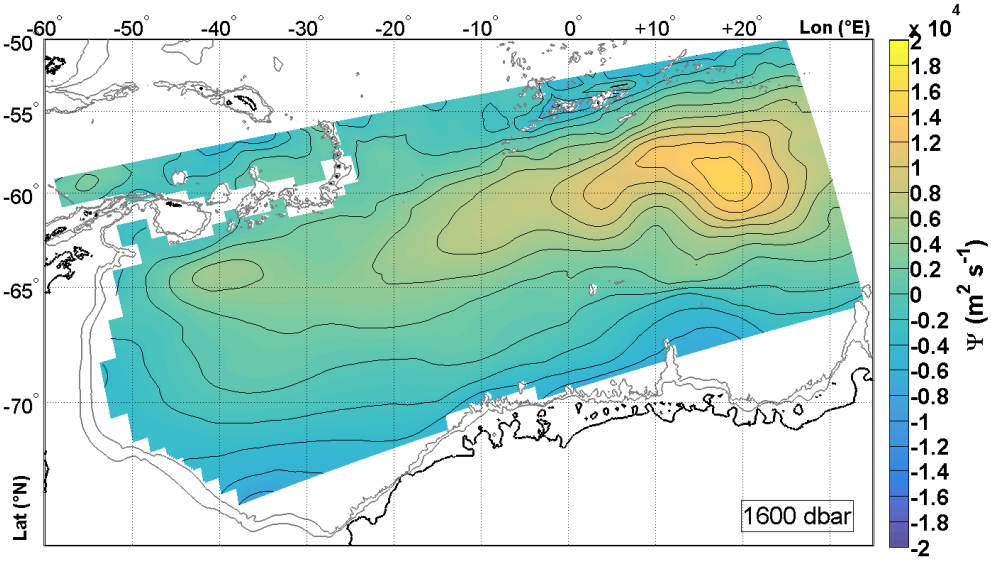
Lon (°E)
Lat (°N)
1600 dbar
x 10^4
Ψ (m^2 s^-1)

(4.4c)

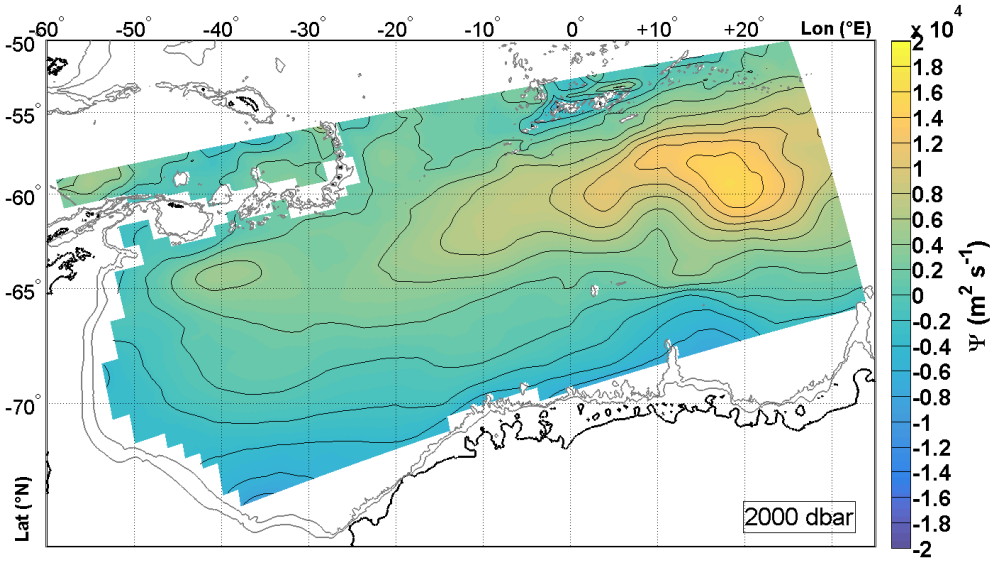
Lon (°E)
Lat (°N)
2000 dbar
x 10^4
Ψ (m^2 s^-1)

(4.4d)

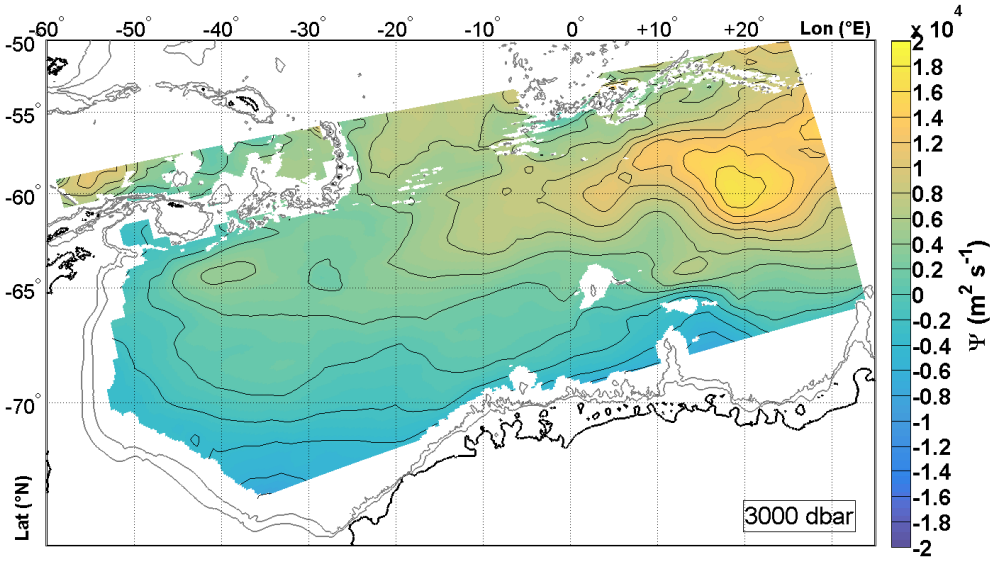

(4.4e)

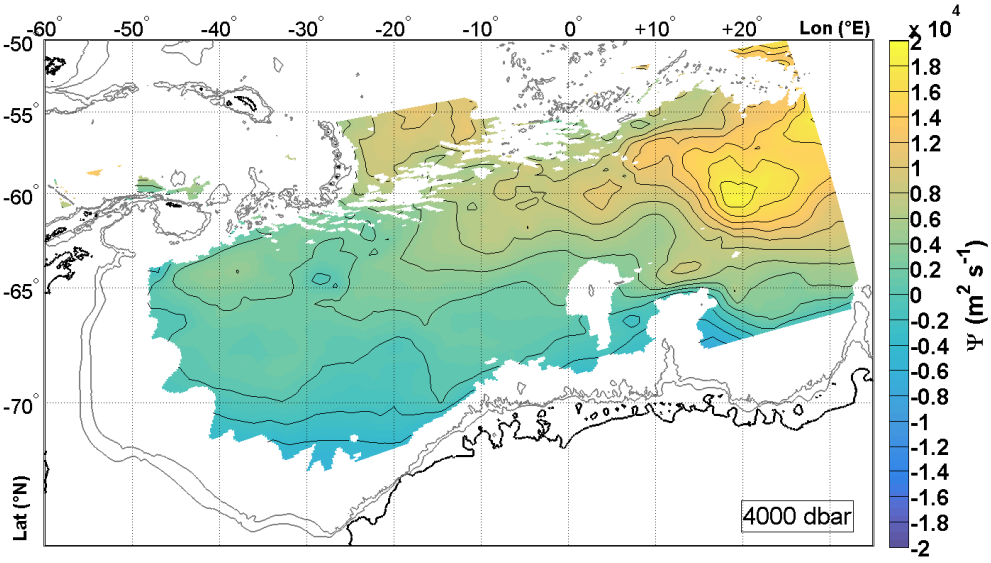

(4.4f)

Figure 4.4a-f. The stream function (Ψ; m^2 s^{-1}) of the absolute non-divergent horizontal velocity for **(a)** 50 dbar, **(b)** 800 dbar, **(c)** 1600 dbar, **(d)** 2000 dbar, **(e)** 3000 dbar and **(f)** 4000 dbar. The direction of flow is parallel to the streamlines, and the spacing between contours describes the magnitude of velocity. Where the contour spacing is tight, the magnitude of velocity is stronger, and vice versa. The contour interval is 2000 m^2 s^{-1}. The black contours show the 2000 m and 1000 m isobars. Regions where bottom depth is less than 2000 m are masked.

The Weddell Gyre exhibits a double cell structure, with two interior cells at about 18º E and 40º W (visible in all panels in Fig. 4.4). The separation between the eastern and western cells occurs at ~27º W. The circulation of the eastern cell varies with depth, whereas the circulation of the western cell is almost barotropic. The western cell is also associated with a weaker circulation (Fig. 4.4, all panels). The separation between the two cells is most clearly defined at 2000 dbar.

Below 2000 dbar, where the data are extrapolated (Fig. 4.4e-f), the southern limb and the western sector (below 60º S) remain to a large degree unchanged when compared to 2000 dbar. The northern limb of the eastern cell (i.e. east of ~27º W) varies with depth, and the west to east return flow becomes less coherent. Some of the deep inflow below 2000 dbar flows northwest between ~15°W and 15°E, some of which flows eastwards as a return flow in the northern limb, while the remainder results in a northward outflow from the gyre at the South Sandwich Trench (Fig. 4.4f-g).

Figure 4.5 shows the difference, dψ, between 2000 and 50 dbar, (i.e. $\psi_{2000dbar}$ - ψ_{50dbar}) and demonstrates that the interior of the gyre is largely barotropic over this depth range. The baroclinic component of geostrophic velocity is largest north of the Weddell Gyre, along the ACC. At the eastern boundary of the gyre, this component gradually decreases as the water circulates southwards towards the inflow region. Within the gyre itself, there is a general east to west gradient of decreasing dψ, indicating that the baroclinic component is larger in the east than in the west.

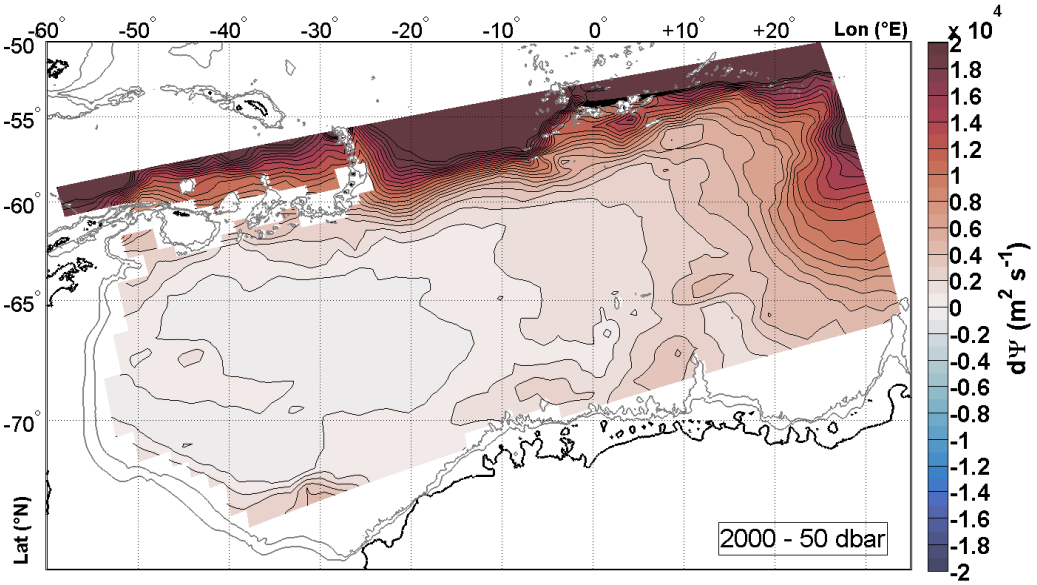

Figure 4.5. The difference between the stream function at 2000 dbar and the stream function at 50 dbar (i.e. $\Psi_{2000} - \Psi_{50}$). The grey contours are the same as in Fig. 4.1.

4.3.2 Volume transports of WDW throughout the Weddell Gyre

The volume transports were determined for three different layer thicknesses: the WDW layer (defined as the layer with neutral density limits: 28.0 kg m^{-3} < WDW < 28.27 kg m^{-3}), the 0-2000 dbar layer and the full ocean depth (from now on, referred to as FD). The cumulative transports were calculated across the central gyre axis (i.e. the thick blue line in Fig. 4.6-4.8a), which was extended outwards from both the eastern and western cells of the double gyre-structure to cover the full grid domain. The cumulative transport calculation starts at the southeast of the grid domain, at the northern tip of Gunnerus Ridge (~33º E, 66º S, Fig. 4.6a). From the western circulation cell, the transect line extends northwestwards to just north of the tip of the Antarctic Peninsula at ~50º W, 62º S (Fig. 4.6). These outward segments of the cross-section are chosen because the streamline boundary for the volume transport calculation thus lies within these transects. The resulting transports are presented in Figs. 4.6-4.8, for the WDW, 0-2000 dbar and FD layers respectively. South of the eastern cell we find westward flow, and west of the western cell the flow turns northeastward. The interface between the two cells (E-W dividing line) occurs at the point where the cumulative volume transport (cVT) exhibits a weak local maximum between the cells, at ~27º W. From the centre of the eastern cell (17º E) to the E-W divide (27º W), cVT is increasing, indicating a northward flow. West of the East-West divide (27º W) to the centre of the western core, cVT is decreasing, indicating a southward flow. The overall shape of the cVT in panel b of Figs. 4.6-4.8 is the same for the WDW, 2000 dbar and FD layers, respectively.

(4.6a)

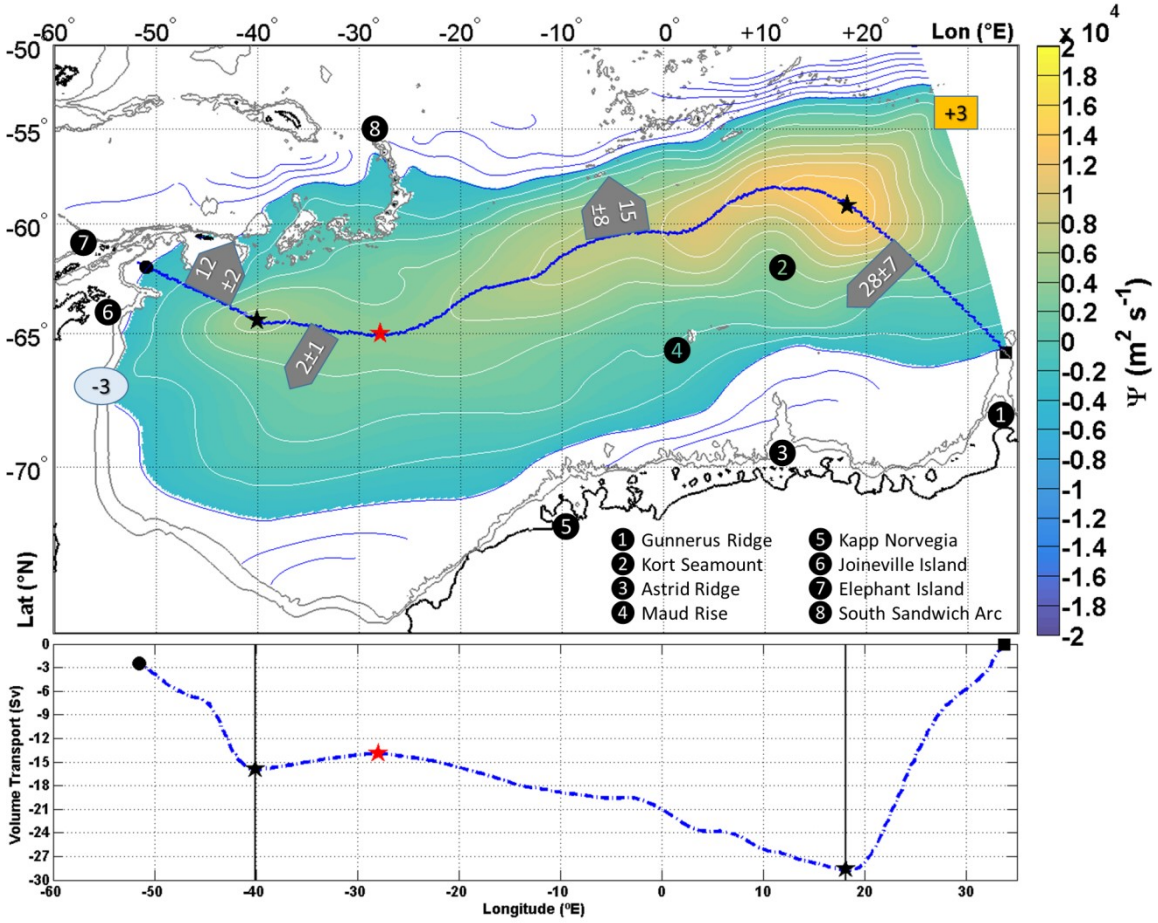

(4.6b)

Figure 4.6. **(a)** The stream function at 800 dbar with WDW volume transport estimates. The grey contours show the 2000 m and 1000 m isobars. Regions shallower than 2000 m are masked. The contour interval is 2000 m^2 s^{-1}. Areas outside the streamline boundary are not filled with colour (see text for further details; Section 4.2.5). The blue thick line indicates the central gyre axis, i.e. section along which cumulative WDW volume transports are estimated. The black square and circle indicates the start and end-points of the cross-section respectively. The black stars indicate the centres of the eastern and western circulation cells, whereas the red star indicates the mid-point between the eastern and western cells. The grey, arrow-shaped boxes provide the volume transport (in Sv; 1 Sv = $1x10^6$ m^3 s^{-1}) across a sub-section and the direction of flow. The legend provides the names of bathymetric features. The square yellow box and pale blue circular box provide the imbalance of the volume transport section. For example, 3 Sv surplus volume transport enters the southern limb of the gyre than leaves it. Panel **(b)**: the cumulative volume transport (Sv) integrated along the section in panel **(a)**. The thick black lines correspond to the locations of the east and west circulation cells, and the black and red symbols along the section correspond to those same symbols in panel **(a)**.

The WDW transport in Fig. 4.6a is characterized by an inflow of 28 ± 7 Sv (where 1 Sverdrup, Sv, is $1x10^6$ m^3 s^{-1}) into the southern limb from the east, of which 15 ± 8 Sv flows northwards to circulate the eastern cell of the gyre, leaving 13 Sv to continue westwards of the E-W divide at ~27º W. Here, it joins the 2 ± 1 Sv that are

recirculated southwards from the western cell. The outflow from the southern limb of the gyre west of the western cell is 12 ± 2 Sv.

(4.7a)

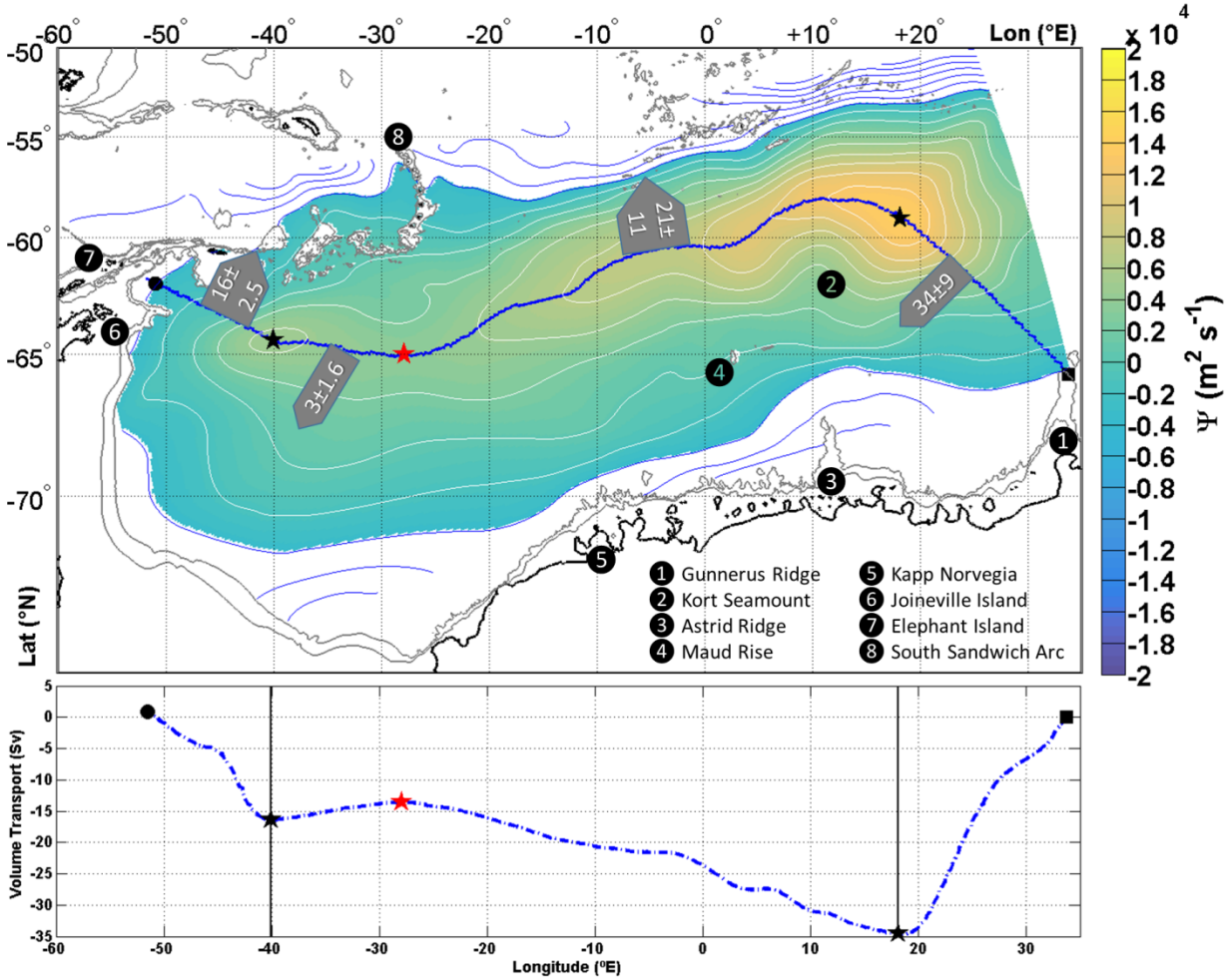

(4.7b)

Figure 4.7. The same as Fig. 6 for the 0-2000 dbar layer.

For the 0-2000 dbar layer in Fig. 4.7a, the inflow into the southern limb of the gyre is 34 ± 9 Sv; of this, 21 ± 11 Sv flows northwards east of the E-W divide (i.e. east of 27º W), leaving 13 Sv to continue westwards into the western sector of the gyre, where it is joined by a southward recirculation of 3 ± 1.6 Sv. The outflow from the southern limb into the northern limb in the western sector of the gyre is 16 ± 2.5 Sv. The total inflow is balanced with the total outflow in upper 2000 dbar layer (i.e. the sum of the cVT is 0 Sv). In Fig. 4.8, of the 83 ± 22 Sv that enters the southern limb from the east, a large volume (71 ± 28 Sv) is transported northwards east of ~27º W (i.e. the divide between the eastern and western circulation cells), leaving 12 Sv to enter the western part of the southern limb (note this is 1 Sv less than the amount inferred for

WDW and the 2000 dbar layer, although with large uncertainty). Here it is joined by 11 ± 5 Sv of recirculated water from the north, which has circulated around the western cell. 27 ± 5 Sv flows into the northern limb of the gyre west of the western cell.

(4.8a)

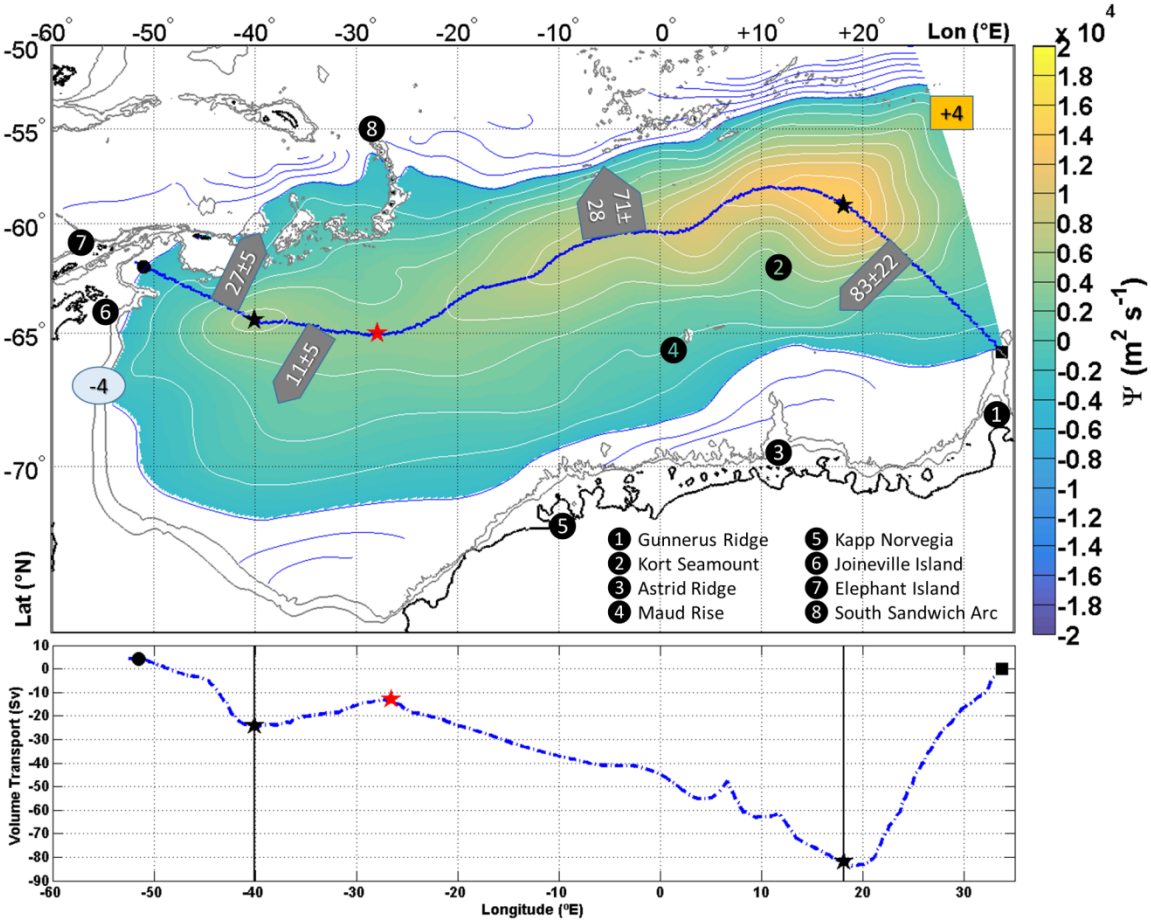

(4.8b)

Figure 4.8. The same as Fig. 4.6 for the full depth (FD) layer. There is an insignificant imbalance between the inflows and outflows to and from the southern limb of the Weddell Gyre, of 4 Sv (the yellow box and blue circle), well within the range of errors in this analysis.

Mean volume transports were also determined for the Weddell Gyre and the different sectors within the gyre. Given that the Weddell Gyre has a double-cell structure, it is not straightforward to determine the overall strength of the gyre. Here, we take the central axis of the gyre, and a line extending from north to south of the grid, crossing the east-west divide between the eastern and western cells, and divide the grid into quadrants, to determine the mean volume transport of each quadrant in Fig. 4.9. These transport calculations describe the quasi-westward flow in the southern limb (SL) of the gyre and the quasi-eastward flow in the northern limb (NL) of the gyre. We also provide the mean volume transport of the eastern quadrants and the western quadrants

in Fig. 4.9. The mean of all four quadrants is then used to determine the mean volume transport for the entire gyre. The resulting mean volume transports are provided in Table 4.1. The mean volume transport of the Weddell Gyre is 32 ± 5 Sv, of which 17 ± 4 Sv is from the upper 2000 dbar, and 12.5 ± 3 Sv (36% of the volume of the Weddell Gyre is WDW, while 39% of the volume transport occurs within the WDW density range) is WDW (WDW provides the main component of the upper 2000 dbar; 73 %). The mean flow is strongest in the SL and weaker in the NL, with a difference of 13 ± 10 Sv in the FD. We find a difference between the NL and SL of 2 ± 6 Sv and 3 ± 5 Sv in the upper 2000 dbar and WDW respectively (note the associated error estimates are larger than the differences). The mean transport is larger in the east than in the west by 14 ± 7 Sv, 7 ± 4.5 SV and 4 ± 4.5 Sv (for FD, 2000 dbar and WDW respectively). The difference is partly due to more intense recirculation occurring east of the Prime Meridian (Fig. 4.8), but also likely influenced by flow becoming topographically constricted in the east, where water is forced to flow faster between topographic features such as Maud Rise and Astrid Ridge (e.g. Cisewski et al, 2011).

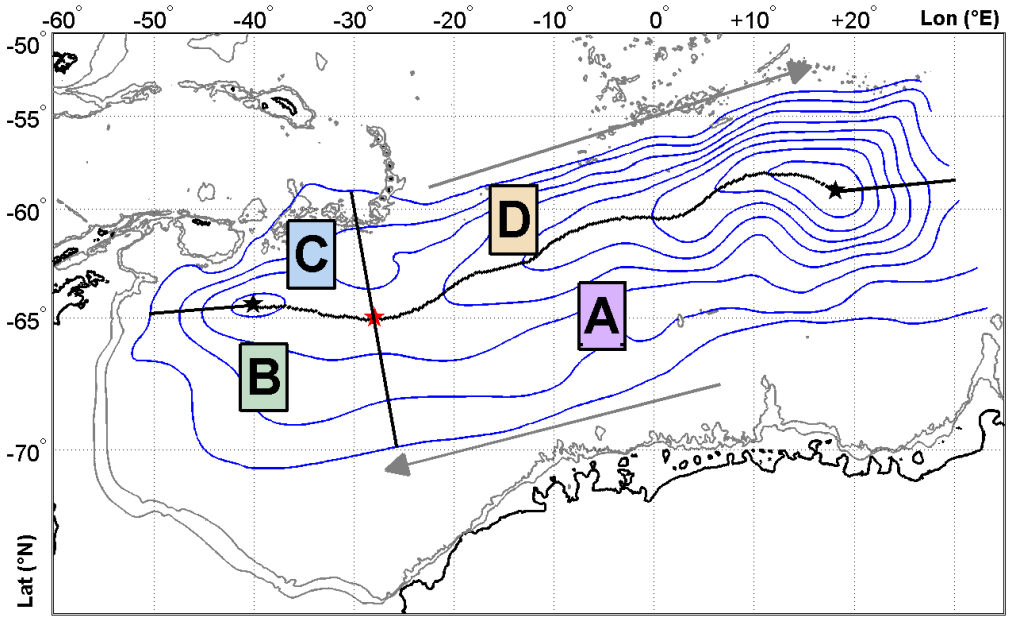

Figure 4.9. Stream lines for 800 dbar (the contour spacing is 2000 m^2 s^{-1}). The dark grey line across the centre marks the central gyre axis and separates the northern quadrants (C and D) from the southern quadrants (A and B) for the calculation of the mean volume transports in Table 4.1. The red star at 27º W indicates the mid-point between the eastern and western circulation cells (i.e. to the east of the point, the flow direction is northward across the axis, and to the west of this point, the flow direction is southwards across the axis). The black line that passes through the red star from north to south separates the eastern (A and D) and western (B and C) quadrants to calculate the mean volume transports in Table 4.1. The grey arrows provide the general flow direction of the gyre. The black stars mark the centre of the eastern and western cells. The grey contours provide the 1000 and 2000 m isobaths, as in Fig. 4.1. The mean volume transports for each quadrant, and for combinations of quadrants (e.g. the mean of A and B provides the mean volume transport of the southern limb of the Weddell Gyre), are provided in Table 4.1.

Table 4.1. Mean volume transport estimates for the Weddell Gyre for full depth and for WDW. The mean volume transports were estimated for each quadrant of the Weddell Gyre, labelled A to D, in Fig. 4.9. For example, we calculate the mean all four quadrants to estimate an overall mean volume transport for the Weddell Gyre. The method for estimating the root mean square error is described in Section 4.2.6.2.

Gyre region	Mean of quadrant (Fig. 9)	Volume transport (Sv):		
		Full Depth	0-2000 dbar	WDW
Gyre	A + B + C + D	32 ± 5	17 ± 4	12.5± 3
Southern limb	A + B	38 ± 7	18 ± 4	14 ± 4
Northern limb	C + D	25 ± 7	16 ± 4	11 ± 3
West (of 27° W)	B + C	23 ± 3	13 ± 2	10 ± 2
East (of 27° W)	D + A	37 ± 6	20 ± 4	14 ± 4
Southeast	A	44 ± 6	21 ± 4	15 ± 4
Northeast	D	30 ± 6	19 ± 4	13 ± 3
Mean percentage of VT as WDW (FD & 0-2000 dbar)		35.7 %	73 %	

4.4 Discussion

The results in Section 4.3.1 provide a gyre scale perspective of the long-term mean circulation of the Weddell Gyre, for different depth layers throughout the water column. This has enabled us to identify the pertinent features of the Weddell Gyre, namely:

I. The Weddell Gyre exhibits a cyclonic circulation, with a double cell structure, which is in agreement with previous estimates (e.g. Gordon et al., 1981; Beckmann et al., 1999), but provided in more detail.
II. The western cell is barotropic (although this is possibly due to lack of float data south of the cell region).
III. The eastern cell varies with increasing depth (although again this is in a region with little data available, Fig. 4.2a).
IV. The general elongated central axis of the gyre is tilted from ~65° S at ~30-35° W to ~57° S at ~15° E.
V. The baroclinic component of the gyre circulation in the 50 to 2000 dbar layer varies spatially: it is virtually absent in the gyre interior but increases towards the inflow region in the east and particularly towards the ACC in the north.
VI. In the northern limb, some of the return eastward flow takes place within the Weddell-Scotia Confluence. After flowing northwards at the tip of the Antarctic Peninsula, and westwards through the Scotia Sea, it can re-enter the gyre east of the South Sandwich Arc in the upper 1200 dbar. Deep water (below 1200 dbar) appears to exit northwards from the gyre along the South Sandwich Trench.

Before discussing the implications of the results, we investigate how our volume transport results in Section 4.3.2 compare to previous VT estimates available in the literature.

4.4.1 Volume transport of the Weddell Gyre: comparison to previous transport estimates

Previous estimates for the strength of the Weddell Gyre range from approximately 30 to 100 Sv. Early volume transport estimates include 97 Sv from adjusted geostrophic transports by Carmack & Foster (1975), while 76 Sv is suggested by Gordon et al. (1981), from the Sverdrup transport estimate. Lower estimates are

provided by studies such as from moorings and ship data by Fahrbach et al. (1991), in the range of 20-56 Sv, and by Yaremchuk et al. (1998), of 30 Sv. However, it is not immediately clear whether the large range in available volume transport estimates is due to positioning, time, instrumentation, or method applied. In this section, we provide a detailed comparison of Argo-derived volume transport estimates with those from the literature listed in Table 4.2, to ascertain how the transport estimates within this study sit in the context of previous research, and aim at explaining the wide range in previous estimates. Cross-sections are extracted from the gridded dataset to best match the coordinates of cross-sections provided in the literature (dashed lines in Figs. 4.10a, which are assigned numbers that correspond to the x-axis in Fig. 4.10b-c and Table 4.2), from which volume transports are estimated for WDW (Fig. 4.10b) and the FD (Fig. 4.10c). The southern boundary we define by the streamline -6000 m^2 s^{-1} at 800 dbar (Fig. 4.4c), which lies closest to the shelf edge, yet omits the flow in shallower water where data are lacking). Direct comparisons between the volume transports and the estimates from the literature are provided in Figs. 4.10b-c, where the new estimates (black) are shown directly alongside the estimates from the literature (grey).

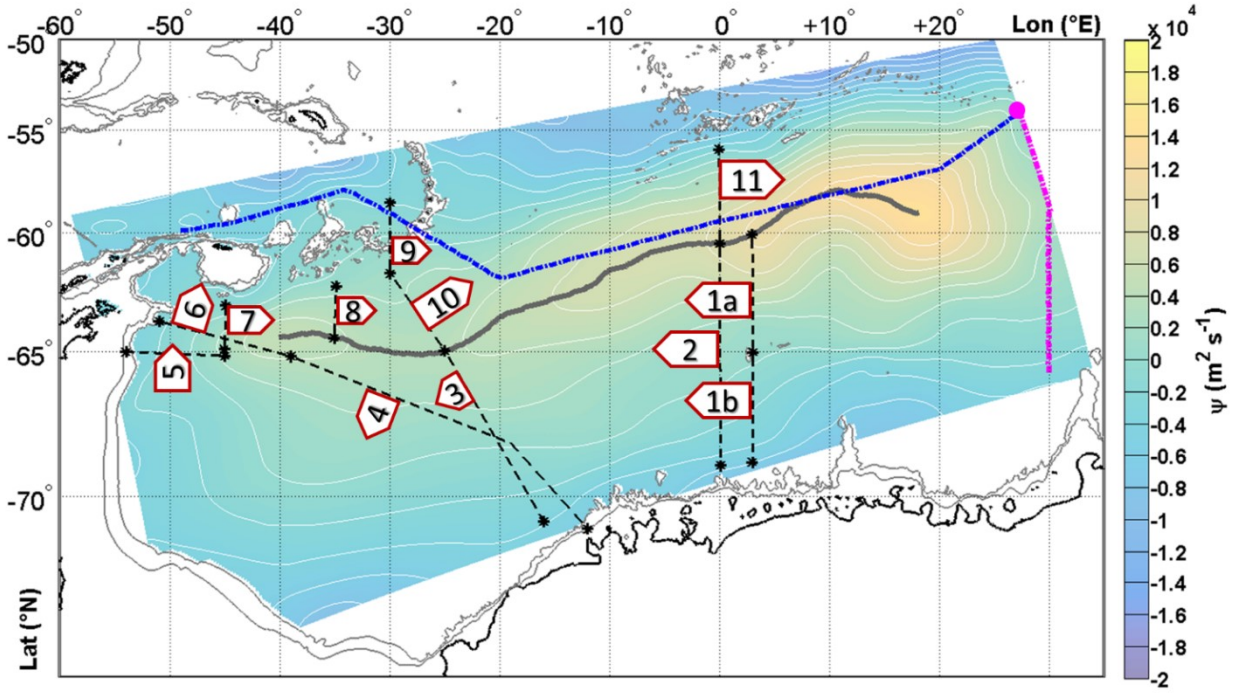

(4.10a)

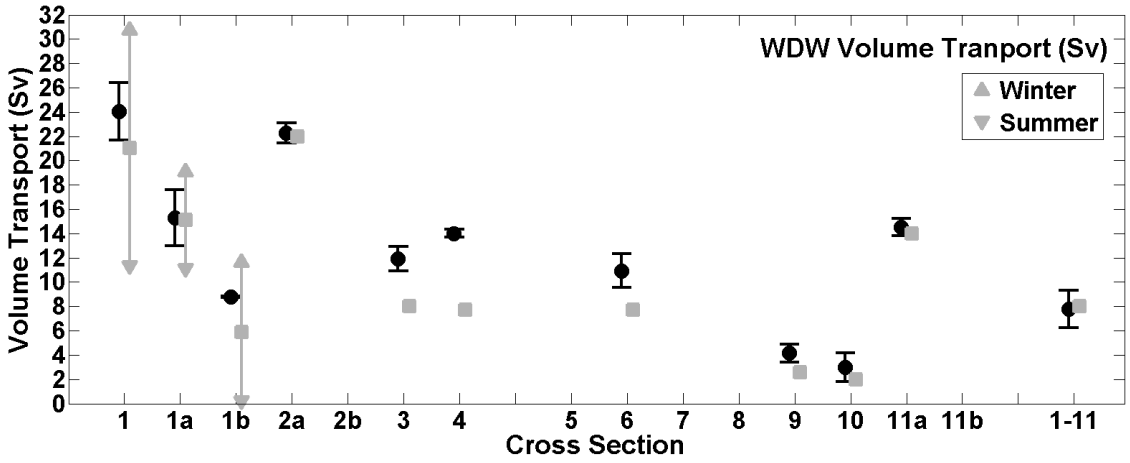

(4.10b)

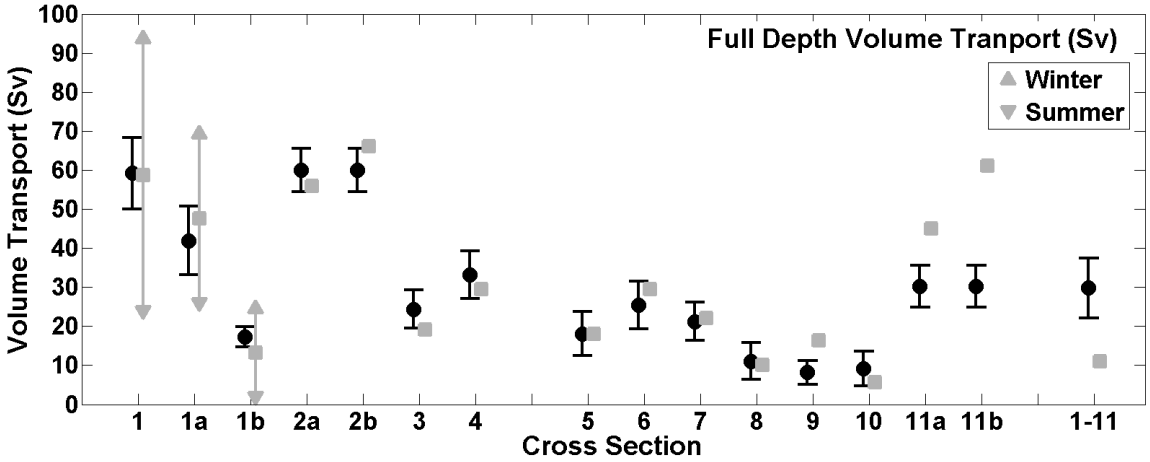

(4.10c)

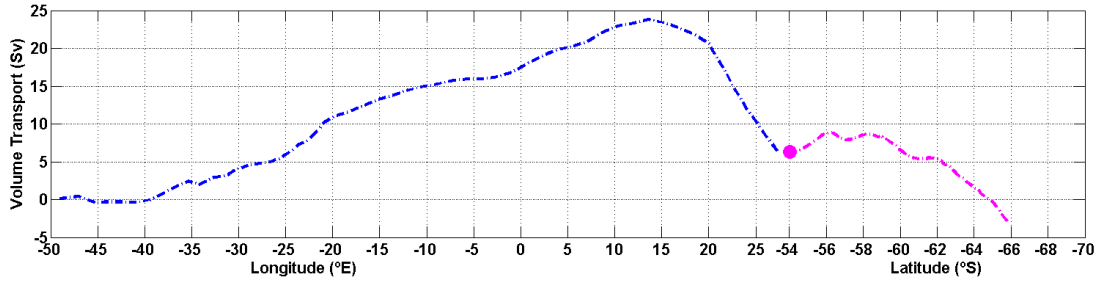

(4.10d)

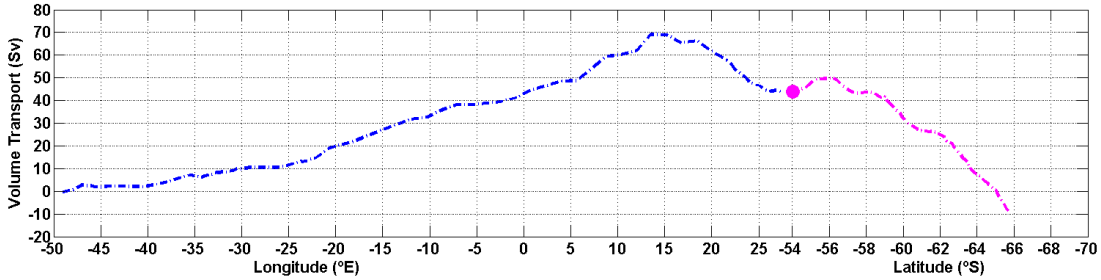

(4.10e)

Figure 4.10 **(a):** The stream function at 800 dbar (m^2 s^{-1}), as in Fig. 4.4b. The grey central line marks the central axis of the gyre. The black dashed lines show cross-sections which match the positions of cross-sections in the literature. The arrow shaped boxes attached to each section indicates direction of flow, and provides a key, which corresponds to the x-axis in panels **(b)** and **(c)**, and to the literature citations and data information provided in Table 4.2. The blue and magenta dashed line matches the position of the cross-section in Jullion et al. (2014), also listed in Table 4.2 under a pink and blue asterisks symbol. Panels **(b)** and **(c)**: WDW and FD Volume transport estimates respectively (Sv, where 1 Sv = 10^6 m^3 s^{-1}). Estimates provided in the literature (grey) are compared to Argo-derived transports (black). The numbers correspond to the various sections in panel **(a)**, with further details of the literature estimate in Table 4.2. For sections 1a-b, Cisewski et al. (2011) provide volume transport estimates for both winter and summer. The mean of the winter and summer volume transports are provided for sections 1 and 1a-b as a grey square between the triangles, which mark the summer and winter range in volume transport estimates.

Panels **(d)** and **(e)**: The cVT from west to east of the WDW and FD volume transport respectively, for the cross-section matching the position of the cross-section of the ANDREX cruise in Jullion et al. (2014). This cross-section is marked in blue and magenta in panel **(a)**, the position of which corresponds to the blue and magenta lines in panels **(d)** and **(e)**. The magenta circle marks the point where the cross-section changes from longitude to latitude in panels **(a)**, **(d)** and **(e)**. Note in the ANDREX cruise, the magenta section spans from 55º S to the shelf edge at the Prime Meridian, which is not possible here due to the prescribed grid domain. Thus the magenta line follows the eastern edge of the grid until it reaches the Prime Meridian at 58º S (panel **a**).

Table 4.2. The citation, position, instrumentation and time period of volume transport estimates in the literature. The numbers in the first column correspond to the numbers in Fig. 4.10a, and the literature estimates shown as grey symbols in Fig. 4.10b-c. The numbers marked with (*) are sections for which there is no WDW volume transport estimate in Fig. 4.10b. For Cisewski et al. (2011), volume transport estimates for both winter and summer are provided (triangle symbols and error bars marked with triangles in Fig. 4.10b-c). Jullion et al. (2014) is marked with a blue and magenta (**), to indicate the dashed blue and magenta lines in Fig. 4.10a, and the cumulative volume transports in Fig. 4.10d-e, which show the position matching the cruise track of the ANDREX cruise in Jullion et al., (2014).

	Citation	Position	Instrument(s)	Period
1	Cisewski et al., 2011	3ºE, 60-70ºS	SHIP CTD & ADCP	Summer▼ & Winter▲ 2005/6
1a	Cisewski et al., 2011	3ºE, 60-65ºS	SHIP CTD & ADCP	Summer▼ & Winter▲ 2005/6
1b	Cisewski et al., 2011	3ºE, 65-70ºS	SHIP CTD & ADCP	Summer▼ & Winter▲ 2005/6
2a	Klatt et al., 2005	0º S	Moorings (57-69.5ºS) & SHIP CTD	1996-2001 (Ship months: 12-01, 03-08)
2b*	Schröder & Fahrbach, 1999	~0º S	SHIP CTD & ADCP	1989-1996 (Ship months: 12-07, 09-10)
3	Heywood & King, 2002	16ºW at coast to 25ºW at 65ºS	SHIP CTD & ADCP	1995 (Ship months: 03-05)
4	Fahrbach et al., 1994	KN to JI	Moorings & SHIP CTD	1989-1993 (Ship months: 09-01, 05-08)
5	Fahrbach et al., 1994	KN to JI	Moorings & SHIP CTD	1989-1993 (Ship months: 09-01, 05-08)
6*	Matano et al., 2002	53-47º W, 65º S	Model Simulation	
7*	Matano et al., 2002	45º W, 62-65º S	Model Simulation	
8*	Matano et al., 2002	35º W, 62-65º S	Model Simulation	
9	Heywood & King, 2002	WSC	SHIP CTD & ADCP	1995 (Ship months: 03-05)
10	Heywood & King, 2002	25ºW,65ºS to 30ºS at NB	SHIP CTD & ADCP	1995 (Ship months: 03-05)
11a	Klatt et al., 2005	0º S	Moorings (57-69.5ºS) & SHIP CTD	1996-2001 (Ship months: 12-01, 03-08)
11b*	Schröder & Fahrbach, 1999	~0º S	SHIP CTD & ADCP	1989-1996 (Ship months: 12-07, 09-10)
**	Jullion et al., 2014	~50ºW-30ºE, ~60ºS	Inverse Model	2005-2010 (Ship months: 01-04)
1,11	Klatt et al., 2005	0º S	Moorings (57-69.5ºS) & SHIP CTD	1996-2001 (Ship months: 12-01, 03-08)

Cross-section 1 (hereon cross-section is written as CS) compares with Cisewski et al., (2011), who provide both summer and winter estimates (see CS 1 in Table 4.2) for the southern limb of the gyre at 3º E (CS 1), also split into sections north (CS 1a) and south (CS 1b) of Maud Rise. Cisewski et al. (2011) report a large difference between seasons, with a full-depth westward transport for the whole section of 23.9 ± 19.9 Sv and 93.6 ± 20.1 Sv for austral summer and winter respectively (Fig. 4.10c), which they attribute to differences in forcing by the wind stress curl. The Argo-derived

long-term mean transports for WDW in Fig. 4.10b are in good agreement with the mean of the seasons provided by Cisewski et al. (2011), especially the section north of Maud Rise (CS 1a in Fig. 4.10b). South of Maud Rise, and by extension to the whole transect (CS 1b and CS 1 respectively in Fig. 4.10b), the VT estimates tend toward the stronger winter estimate. This is despite the southerly limit of the section in Fig. 4.10a, which is 1º north of the southerly limit in Cisewski et al. (2011) in Table 4.2, and therefore likely excludes the strongest flow at the shelf edge. The FD transport for CS 1 (Fig. 4.10c) agrees with the mean VT in Cisewski et al. (2011), due to counteracting estimates for the sub-sections: north of Maud Rise the VT tends toward the weaker summer VT and south of Maud Rise the VT tends towards the stronger winter estimate, although both estimates are within the range indicated by the seasonal differences in Cisewski et al. (2011).

Despite the large range in transport estimates in the literature, one commonality of available estimates is the lower transport in the narrow, northern limb with respect to the broader southern limb of the Gyre. About 140 km to the west of the section discussed above, Schröder & Fahrbach (1999) evaluated the transport across the Prime Meridian (PM) during a ship campaign in 1996. They estimated a full-depth volume transport of 66 Sv in the southern limb (SL, CS 2b), and 61 Sv in the northern limb (NL, CS 11b, Fig. 4.10c). Klatt et al. (2005) combined CTD data and moorings along the same transect for 1996-2001, and estimated 56 Sv and 45 Sv in the SL and NL respectively (CS 2a and CS 11a in Fig. 4.10c). A remarkable agreement exists for the SL of our Argo-based transport of 60 ± 5 Sv with both Schröder & Fahrbach (1999) and Klatt et al. (2005) in Fig. 4.10c. Klatt et al. (2005) observe a 6 Sv reverse flow due to the presence of a Taylor Column over Maud Rise, a local feature that is not resolved in the Argo-derived stream function (Fig. 4.4) due the grid-cell resolution and length-scales applied in the objective mapping (Section 4.2.2). This unresolved feature in the Argo-derived stream function possibly explains the difference in transport estimates. However, our NL transport in Fig. 4.10c (30 ± 5 Sv) is just half the transport estimated by Schröder & Fahrbach (1999) in CS 11b, and about 15 Sv weaker than the NL VT in Klatt et al. (2005) in CS 11a. There is excellent agreement of WDW VT with Klatt et al. (2005) for both the SL (22 Sv in the literature compared to 22.3 ± 0.8 Sv in CS 2a, Fig. 4.10b), and the NL (14 Sv in comparison to 14.5 ± 0.7 Sv in CS 11a, Fig. 4.10b). The difference between the WDW NL and SL VTs at the Prime Meridian in Fig. 4.10b

provides a deficit of 7.8 ± 1.5 Sv that has been lost on transit between the SL at 0ºE and the NL at 0ºE (CS 1-11, Fig. 4.10b). Klatt et al. show that an 11 Sv deficit in the full depth NL VT is dominated by an 8 Sv difference in WDW between the NL and SL at the Prime Meridian. The excellent agreement of the NL and SL transports for WDW suggests that the placement of the northern boundary is not the cause of the difference between the FD estimate for the NL presented here and those of Klatt et al. (2005).

Using the CTD profiles in the NL at the Prime Meridian that were used in the determination of an extrapolation error, we find that the quadratic function used to extrapolate to the full ocean depth below 2000 dbar works well, resulting in an extrapolation error of 4.5 Sv and a total error of 5 Sv. It is possible that the difference in transport estimates is due to the definition of the northern boundary. Schröder and Fahrbach (1999) interpreted the Weddell Front and southern boundary of the Antarctic Circumpolar Current as part of the Weddell Gyre NL flow, which may be why their estimates are larger than both ours and those provided in Klatt et al. (2005). The largest uncertainty in Klatt et al. (2005) is the unknown position of transition between the eastward flowing northern limb and the westward flowing southern limb of the gyre – a shift north or south of just 55 km results in an error of 5 Sv. Klatt et al. (2005) observed the NL deficit mostly in WDW, but also to a lesser amount in the surface waters and WSDW; whereas WSBW gains 3 Sv, which they interpret as the amount of WSBW formation in the gyre interior. This suggests that our FD estimates do not adequately represent the contribution of WSBW to the overall volume transports, in the deep gyre interior where WSBW is bathymetrically constrained, due to poor representation of the near-bottom flow.

FD transports in the northwestern Weddell Sea compare reasonably well with previous estimates (CS 5-8 and CS 10, Fig. 4.10c). Matano et al. (2002) used an eddy-permitting model to investigate the northwestern Weddell gyre circulation. We reproduce three of the cross-sections presented in Matano et al. (2002), which show excellent agreement. The off-shelf western boundary current at 65º S (CS 5, Fig. 4.10a) differs by less than 1 Sv, within the range of uncertainty (Fig. 4.10c). At 45º W (CS 7), Matano et al. (2002) estimate an eastward transport of 22 Sv, with 18 Sv coming from the western boundary current, 3 Sv coming from the gyre interior, and 1 Sv entering the gyre from the Powell basin. Here, our total VT (Fig. 4.10c) is 1 Sv smaller (21 ± 5 Sv). At 35º W (CS 8, Fig. 4.10a,c), an eastward VT of 11 ± 5 Sv compares well with 10 Sv

in Matano et al. (2002). In contrast to earlier studies, who assume that the preferred escape route of the WSDW is along the South Sandwich Trench (just east of about 25 ºE), Matano et al. (2002) found that some of the flow is recirculated to the south, and that the net flux near the tip of the trench is southward. Our findings agree with this, although the associated volume transports are not provided as they have large uncertainties. This is also in agreement with Locarnini et al. (1993), who observed that the northward transit is inhibited by the ACC in this region. While the stream functions in Fig. 4.4 indicate a net southward flow over the trench in the upper depth levels, strongest at 50 dbar (Fig. 4.4a), below 1200 dbar (not shown) the picture is less clear, and may indicate a net northward flow (most evident at 4000 dbar in Fig. 4.4f, but also visible at 1600 and 2000 dbar in Figs. 4.4c-d). This is consistent with the trench being an outflow pathway for WSDW, as indicated by Meredith et al. (2008), although we cannot argue with any degree of certainty due to inadequate gridding resolution and mapping length scales applied in Section 4.4.2.

The most notable differences between the WDW transports in Fig. 4.10b and the literature occur in the western Weddell gyre, i.e. the sections aligned with that of Heywood & King (2002) as part of WOCE in 1995 (CS 3, 9 and 10 in Table 4.2 and Fig. 4.10b), and Fahrbach et al. (1994), as part of the "Weddell Gyre Study" between 1989 and 1993 (CS 4 and 6 in Table 2 and Fig. 4.10b). Our WDW transport for the SL of the WOCE section is 11.9 ± 1 Sv (CS 3, Fig. 4.10b). This is ~4 Sv larger than in Heywood & King (2002), yet the southern limit of the cross-section in Fig. 4.10b is at ~71º S, rather than extending to the shelf edge. There is better agreement between the estimates for the NL (CS 10, Fig. 4.10b), where the difference is less than 1 Sv, within the range of uncertainty. For the FD, our estimates are larger than in Heywood & King (2002), by ~5 Sv and ~3 Sv in the SL and NL respectively (CS 3 and 10, Fig. 4.10c). Heywood & King (2002) suggest that they underestimate the NL transport, due to an inappropriate reference layer. Furthermore, in agreement to the streamlines in Fig 4.4, they note that some of the return eastward flow in the NL actually occurs within the Weddell-Scotia confluence to the north of the Weddell Front. Heywood & King (1995) estimate that 2.6 Sv of WDW passes through the Weddell Scotia Confluence (CS 9, Fig. 4.10b), which is 1.6 Sv smaller than the Argo-derived estimate in Fig. 4.10b. The Argo-derived FD flow through the Weddell-Scotia Confluence is 50 % smaller than that estimated by Heywood & King (2002) in Fig. 4.10c. We assume that the grid resolution

in this study (~80 x 60 km) is too coarse to resolve the flow through this bathymetrically complex region, whereas Heywood & King use CTD profiles with a station spacing of 5-10 km over regions of steep bathymetry and across fronts (though station spacing was wider across the central Weddell Gyre: ~110 km).

The "Weddell Gyre Study" of Fahrbach et al. (1994) covers the southwest corner of the gyre, from Kapp Norvegia to Joineville Island (CS 4 & 6). In a numerical model study, Beckmann et al. (1999) suggested that the section does not cut fully through the Weddell Gyre axis and thus only a part of the transport is captured. The stream function in Fig. 4.10a shows agreement to this statement, where the section intersects the western circulation cell south of the central axis (marked by the western end of the thick grey line in Fig. 4.10a). The new estimates for WDW VT (CS 4 & 6) are larger than those provided in Fahrbach et al. (1994), by ~6 Sv and ~3 Sv for the SL and NL respectively. The estimate from Fahrbach et al. (1994), however, is estimated indirectly. The authors do not provide a VT for WDW, but state that 26 % of the section is occupied by WDW, which allows us to approximate that WDW contributes 7.7 Sv to the total volume transport (from a FD transport of 29.5 Sv). It is possible that the WDW transport is larger than the approximated 7.7 Sv, due to a stronger flow field in the WDW layer. Fahrbach et al. (1994) adjust the current field for the full water column so that the net volume transport across the whole section is zero, hence the equivalent transports for both the NL and SL. We do not apply the same adjustment here, instead we directly determine the transport for WDW and the FD. The Argo-derived FD VT is 3.5 Sv larger in the SL (CS 4, Fig. 4.10c) and 4.5 Sv smaller in the NL (CS 6, Fig. 4.10c) than the 29.5 Sv estimated by Fahrbach et al. (1994). The authors provide an error estimate of 9 Sv, which brings the estimates within the range of uncertainty. The section in Fig. 4.10a omits a substantial part of the section in Fahrbach et al. (1994), on the shelf approaching the Antarctic Peninsula, and to a lesser extent the shelf approaching Kapp Norvegia in the south. Thus, we can assume our results are underestimating the total flow, especially at the northern tip of the section. Yaremchuk et al. (1998) used the same data in a dynamically constrained inverse model to arrive at a volume transport of 34 ± 2 Sv across the same section (CS 4 & 6), which compares remarkably well to our SL VT (CS 4 in Fig. 4.10a), suggesting that, in the NL, by omitting the shelf transport at the broad northern tip of the section in Fig. 4.10a results in potentially 9 Sv weaker transport (i.e. the NL transport is 25 Sv, 9 Sv weaker than the

estimate by Yaremchuk et al., 1998). However, the section used for transport calculation in Yaremchuk et al (1998) began west of 17º W, omitting the 350 km closest to the coast at the southern end of the section. Thus, we can assume that the flow would be larger if the coastal flow to the south of the section was also included. Indeed, Klatt et al. (2005) calculate a volume transport for the Antarctic Coastal Current (albeit at the Prime Meridian) of 26 ± 4 Sv. The limitations of this study concerning the shelf edge boundary currents will be further addressed in Section 4.4.2.1.

A further comparison is carried out with results from an inverse model in Jullion et al. (2014) by extracting from our gridded data-set sections corresponding to the ANDREX and I6S sections (Fig. 1 of Jullion et al., 2014 and the blue and magenta line in Fig. 4.10a. Note the northern part of the I6S section has a westward slant due to the limitations of the eastern extent of the grid domain, thus omitting the intersection with the ACC, and the westward limit of the section is at 50º W and does not extend to Elephant Island as in Jullion et al., 2014). In Jullion et al. (2014), an "inner" FD transport of 42 ± 8 Sv is estimated for the same cross-section as the "Weddell Gyre Study" (from Kapp Norvegia to Joineville Island, CS 4 & 6, Fig. 4.10a). This is larger than the 33 ± 6 Sv in Fig. 4.10c (CS 4). However, in our work, the shelf edge where the strong inflow associated with the ASF is not resolved, and therefore a smaller estimate is to be expected. An "outer" FD transport between ~57º W and the Prime Meridian (along the ANDREX section, i.e. the blue line in Fig. 4.10a) is estimated as 54 ± 15 Sv. In Fig. 4.10e, between 50º W and the Prime Meridian, we estimate a FD VT of 44 Sv. We exclude the 50-57º W part of the section, where the bottom depth is typically less than 1000 m. Our dataset is unable to resolve the highly varying bathymetry in the region, and therefore artificially smooths narrow frontal regions associated with large transports, as can be seen in Jullion et al. (2014). An interior recirculation of about 20 Sv between 10º W and 20º E is suggested in Jullion et al. (2014). This is similar to our own estimates; in Fig. 4.10e, we see a recirculation where about 26 Sv flows northwards between the Prime Meridian and ~12º E, and recirculates southwards between ~12º E and ~25º E. However, when determining the VT along the central gyre axis (Fig. 4.8), a much larger recirculation is estimated, with 71 ± 28 Sv flowing northwards between ~18º E and ~27º W (i.e. at the E—W transition between the two sub-gyres). The majority of the recirculation occurs east of the Prime Meridian (39 Sv). These results will be further discussed shortly.

The results above indicate that the wide range in values for the strength of the Weddell Gyre is mainly due to variations in the positioning of the cross-sections throughout the Weddell Gyre. This is due to the elongated, double-cell structure of the Weddell Gyre, with a weak barotropic cell west of 27º W, and a stronger, elongated eastern cell which varies with changing depth. Estimates from the literature are thus placed in the context of a single map of the Weddell Gyre circulation in Fig. 4.10a, despite the differing time periods of the observations, and the instrumentation and methodology in deriving volume transport estimates. We will expand upon these findings in Section 4.4.3, after describing some of the major limitations of the study in the subsequent section.

4.4.2 Weddell Gyre circulation: a gyre scale perspective

There are of course some general shortcomings one should be aware of when interpreting the results. The sources of error stemming from the methodology applied in this work are detailed in Section 4.2.6.1. Due to the many possible sources of error, the implementation of a detailed comparison to the literature is an important component of this work, as it delivers an additional check that provides certainty beyond the statistical representation of error. There is in general good agreement between the literature and the transports provided in Section 4.4.1, despite the different time periods, data sources and methods employed. The differences appear to be a result of two main issues:

I. Lack of float data on and at the shelf edge for resolving coastal flow and frontal jets such as the ASF
II. The deep baroclinic flow in the NL of the eastern sector of the gyre: despite good agreement for the WDW transports, poor agreement for the FD suggests that the near-bottom flow becomes important in this region.

In the following, the two issues above will be examined in further detail. In Section 4.2.3, the importance of seasonal and inter-annual variability will be addressed, which is not included in this study but has some important consequences for the strength of the Weddell Gyre circulation.

4.4.2.1 The shelf-edge and coastal flow

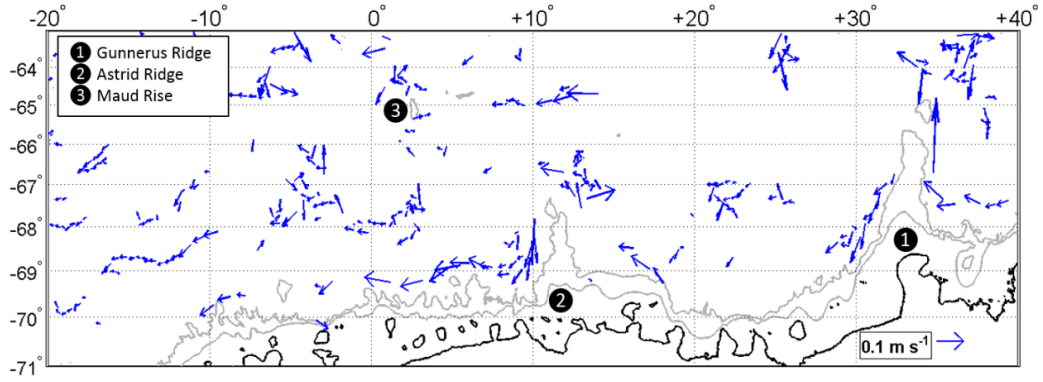

Figure 4.11. SD corrected parking depth velocities of Argo floats in the lower southeastern sector of the gyre. The grey contours show the 2000 m and 1000 m isobars. The two extensions from the coastlines are Astrid Ridge (~12° E) and Gunnerus Ridge (~35° E). The length of the arrows are scaled to 0.1 m s^{-1} in the lower right-hand corner of the map. The legend provides the names of the bathymetric features discussed in Section 4.4.

Frontal jets, associated for instance with the continental slope, account for a substantial contribution of the transport within the Weddell Gyre. Resolving the frontal jets can lead to a 50 % increase in the mass transports at the tip of the Antarctic Peninsula (Thompson & Heywood, 2008), and account for 85% of the Weddell Gyre transport according to Jullion et al. (2014). In Jullion et al. (2014), the ASF (the collective term for the Antarctic Slope Front) provides an inflow at 30° E of 24 ± 4 Sv, which then increases to 37 ± 9 Sv at the northwestern edge of the gyre, at 64° S. Dong et al. (2016) provide transport estimates of the Antarctic Slope Current (ASC) at 30-35° E, of 9.6 ± 2.3 Sv. Two branches of the ASC were identified in Dong et al. (2016): a shallow coastal branch that flows over topography and an outer offshore branch that flows around topography. The outer branch may help to explain the strong barotropic eastern flow along the southern domain of the grid east of the Prime Meridian, in the stream functions in Fig. 4.4. Although our grid domain excludes the region around Gunnerus Ridge (the bathymetric feature at ~33° E, believed to be responsible for splitting the ASC into the two branches; Fig. 4.11), it may be that the southernmost streamlines in the area between 30° E and the Prime Meridian in Fig. 4.2a-f are partly capturing an eastward, topographically steered flow along the shelf edge associated with the ASC. Indeed, there are some float data available in the region south of the grid domain east of- and between- Gunnerus Ridge and Astrid Ridge, the trajectories of which are tightly hugging the 2000 m contour line, circulating around both Gunnerus Ridge and Astrid Ridge (Fig. 4.11). The parking depth velocities are larger than those

further north, away from the coast. Due to the presumed tendency of water to flow along *f*/*H* contours (LaCasce, 2000), at a parking depth of 800 dbar, there are virtually no data available over the shelf edge region. Since it has been observed that the shelf-edge currents contribute substantially to the gyre transport, we can assume that the transports provided in Sections 4.3.2 and 4.4.1 are underestimating the total transport, which is a major limitation of this study. In particular, the southern boundary of the grid domain stops short of the shelf edge by a considerable distance, east of the Prime Meridian and west of about 15º W. Thus, we are most likely to predominantly capture the inflow to the gyre between the 0-15º W, where the southern edge of the grid is in closest contact with the coastline. Our transports agree very closely to previous estimates at the Prime Meridian and at 3º E (CS 1-2, Fig. 4.10a-c). However, further west we find our estimates are larger than those provided by Fahrbach et al. (1994) and Heywood & King (2002), but 9 Sv smaller than the estimate derived from an inverse modelling study in Jullion et al. (2014) across CS 4 in Fig. 4.10a. This suggests that Fahrbach et al. (1994) did not fully capture the shelf-edge flow, to a larger degree than the Argo-derived estimates in Fig. 4.10c.

In the western sector of the gyre, adjacent to the Antarctic Peninsula, again the outflow from the gyre is unlikely to be fully captured due to lack of data on the shelves, and we are unable to resolve transports associated with fronts due to the grid cell resolution, mapping length scales, and lack of available data on the shelf edge. Thompson & Heywood (2008) provide high resolution transport estimates for the shelf and shelf edge at the tip of the Antarctic Peninsula, and find that the coastal current, Antarctic Slope Front and Weddell Front provide 1.3 Sv, 3.9 Sv and 16.8 Sv respectively. The total transport where bottom depth is less than 2000 m amounts to about 7 Sv (Fig. 4.11 in Thompson & Heywood, 2008), whereas the full transport for the section is 46 Sv. With the exclusion of the Weddell Front transport, the transport in water deeper than 2000 m amounts to about 22 Sv, which agrees with the 18 ± 6 Sv shown in CS 5 (Fig. 4.10a,c).

4.4.2.2 Deep baroclinic flow

We also provide a basin-scale, measurements-based analysis of the spatial distribution of the baroclinic component of the entire Weddell Gyre circulation (for the 50-2000 dbar layer; Fig. 4.5). To our knowledge, this is the first time such a map has

been produced. Thus, it represents a major scientific advancement, in comparison to analyses in the literature that are rather localized to mooring locations and ship routes. In Fig. 4.3, we show that the interior of the Weddell Gyre is more barotropic relative to the ACC to the north and to the east, for the upper 2000 dbar. There is spatial variation in the baroclinic components of the gyre, where the comparatively larger baroclinic component of flow of the ACC intrudes inwards towards the Weddell Gyre at the east (~15-30º E). Looking carefully at Fig. 4.5, this intrusion starts in the lee of the South Sandwich Arc, ~25º W (i.e. where the horizontal gradients are largest in Fig. 4.5), and continues eastwards along the open northern boundary. While it has been widely acknowledged that the Weddell Gyre is largely barotropic, the ACC is in general viewed as a topographically steered equivalent barotropic flow, which describes a situation where flow is unidirectional with depth, but with varying magnitude of velocity (e.g Gille, 2003). In context of Figs. 4.4 and 4.5, our results show consistency with the literature.

The near-bottom baroclinic component of flow may play an important role in the circulation of the eastward flowing northern limb of the Weddell Gyre. This is also suggested by the favourable agreement between the literature and the Argo-derived estimates for the WDW transports in the northern limb at the Prime Meridian, whereas the FD estimates are considerably smaller (by as much as 50%). This is in contrast to the southern limb of this section, where the transports are in excellent agreement for both the WDW layer and the FD. Additionally, there is good agreement in the northern limb of the western sector of the gyre, where the baroclinic component of flow does not intrude as far into the gyre interior (Fig. 4.5). This may explain the lack of a distinct eastward flowing northern limb of the gyre circulation at 3000 and 4000 dbar in Figs. 4.4e-f. Here, the water that flows into the Weddell Gyre from the east, south of 60º S, transitions into a mostly northwestward flow across the gyre, some of which does not recirculate eastwards in the northern gyre limb. This may also explain why volume transports presented in Section 4.4.1 and in the literature generally show a larger westward transport in the southern limb of the gyre in comparison to the eastward flow in the northern limb of the gyre. If we were able to truly resolve the deep baroclinic flow in the northeast, then perhaps we would better capture the deep cyclonic circulation, whereas currently we appear to be significantly underestimating the eastward flow. Klatt et al. (2005) find a deficit in the northern limb of the gyre at 0º E

relative to the southern limb, for both WDW (in agreement with the float-derived transports in Fig. 4.10b, CS 1-11) and WSDW. In contrast, the authors find that WSBW had gained 3 Sv, which would require a stronger eastward flow component in the NL relative to the westward flow in the SL for this bottom water mass layer. Klatt et al. (2005) use a combination of full depth CTD profiles and moorings to arrive at transport estimates and are therefore able to better estimate the full depth baroclinic component of flow, than the full-depth extrapolation method applied here (Section 4.2.5). Thus, we conclude that, in the northeastern sector of the Weddell Gyre, the deep baroclinic component of flow is an important factor that is not represented by the Argo float-derived estimate of full depth volume transports presented in this study.

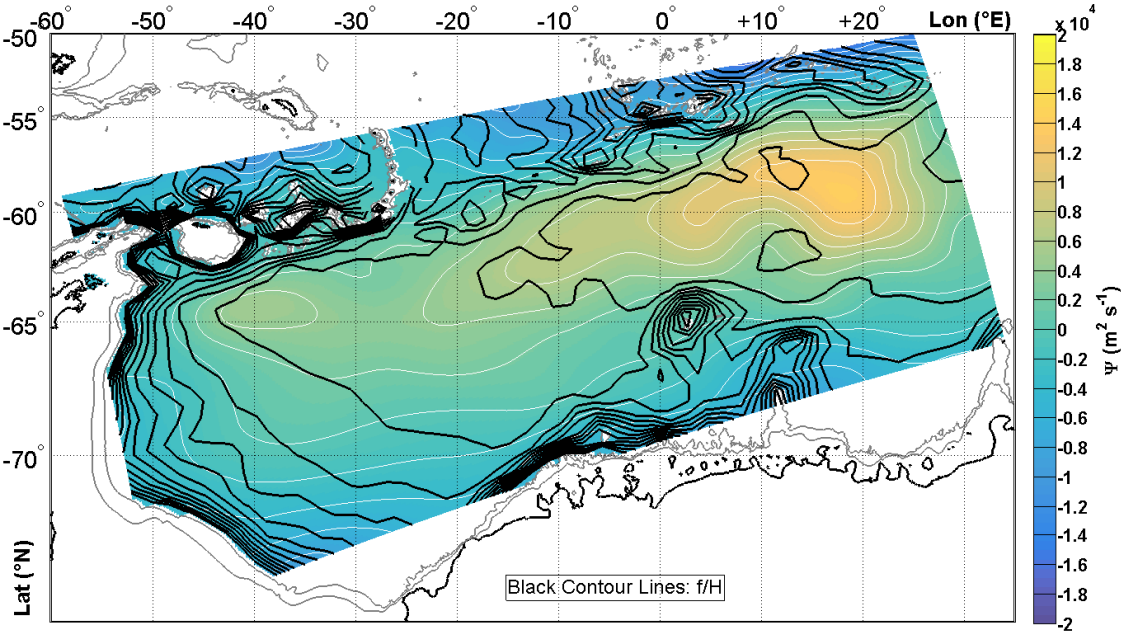

Figure 4.12. Planetary potential vorticity (*f/H;* black contour lines, where *H* is full ocean depth) and the absolute geostrophic stream function at 800 dbar. The grey contours show the 2000 m and 1000 m isobars. Regions shallower than 2000 m are masked. The colour bar interval is 2000 m^2 s^{-1}.

Another suggestion that the deep baroclinic component of flow is mainly important in the northeast sector of the gyre can be demonstrated by assessing the relationship between planetary potential vorticity (i.e. *f/H* contours) and the stream function (Fig. 4.12). In the western sector of the gyre, the *f/H* contouring exhibits a simple structure with more or less parallel contouring, reflecting the curvature of the basin adjacent to the continental shelves, with a relatively invariant interior west of ~20º W. The stream function displays similar characteristics, where the western circulation cell is found at the inner corner (~40º W, ~64º S). Here, the *f/H* contours turn sharply inwards along the southern edge of the submersed mountain chain (~50-20º W, ~60º S).

The broad westward flow south of the western cell in contrast to the narrow, intensified eastward flow in the north are also reflective of the *f/H* contours in Fig. 4.12. The structure of the western cell is prominent throughout the full water column, indicative of a barotropic, topographically steered flow. The situation is less straightforward in the eastern sector of the gyre and to the north, where complex bathymetry interferes with the circulation. In the southern limb east of about 15º W, there are two features in the circulation that stand out in context of the *f/H* contours. First, the flow appears to be intensified due to topographic constriction between Astrid Ridge and Maud Rise (Figs. 4.4 and 4.12). The second and perhaps most pertinent feature present throughout the whole water column, is a strong "meandering" of the circulation found upstream of and to the north of Maud Rise, over the Kort seamount at ~14ºE, 62ºS (Figs. 4.4a-f & Fig. 4.12). Kort Seamount is a considerably smaller bathymetric feature than Maud Rise, and therefore the meandering of the circulation is assumed to be more a result of the interaction between interior recirculating waters and the inflow from further east, although it is possible that it is an artifact of the time composite dataset. To the east and to the north of Kort seamount, there is no clear relationship between *f/H* contours and the stream function in Fig. 4.12.

4.4.2.3 Seasonal and inter-annual variability in the Weddell Gyre circulation

Another limitation of this study is the lack of estimates of the temporal variability of the gyre's strength and structure. We provide a composite data set, which incorporates Argo float profile and trajectory data between 2002 and 2016 in this study, but omit the upper 50 dbar due to challenges in resolving the seasonal variability. The resulting dataset represents a long-term mean of the horizontal circulation of the Weddell Gyre. However, while the hydrography data are relatively balanced between winter and summer months, about 85 % of the trajectory data south of 60º S are from summer months (Fig. 4.3a). This may have contributed to the good agreement between the Argo-derived volume transports and previous estimates in Section 4.4.1, since most previous estimates are also biased towards summer months (not completely, due to the use of mooring data). The largest seasonal variability of the Weddell Gyre circulation is found in the shelf edge and coastal boundary currents, where the ASF speeds up to twice as fast in autumn (e.g. Armitage et al., 2018; Cisewski et al., 2011; Nunez-Riboni & Fahrbach, 2009). However, we are not able to resolve the shelf-edge boundary

currents as discussed in Section 4.4.2.1. Thus, since the analysis in this study is biased towards summer months south of 60º S, and Armitage et al. (2018) show stronger circulation during autumn months, we conclude that the volume transports provided in Sections 4.3.2 and 4.4.1 are underestimated.

Armitage et al. (2018) demonstrate month-to-month variability in the gyre depth, derived from sea-level anomaly from satellites, which is correlated with the local wind curl. Additionally, the authors show there is a weak correlation between gyre depth and the change in westerly winds related to the Southern Annular Mode index (SAM). Given that the correlation mostly stems from intraseasonal variability, we would expect a mostly barotropic response of the flow field to the wind forcing. However, it is not possible to infer from their study (owing to the short time period considered), how observed decadal strengthening and southward migration of the westerly winds over the Southern Ocean (i.e. a shift to a more positive SAM) might have affected the long-term circulation of the Weddell Gyre. Fahrbach et al. (2011) proposed that there is an asymmetric response to the wind field associated with positive SAM, since the Weddell Gyre has open-ended limbs. Thus, the eastward flowing northern limb of the gyre would be expected to strengthen, and the westward flowing southern limb may actually weaken (especially towards the northern part of the southern limb where flow direction opposes the direction of the wind field, Fahrbach et al., 2011). This suggests that the relationship between SAM and the gyre strength is not straightforward, and further research is required to establish the long-term effect of the wind field on the circulation of the Weddell Gyre.

4.4.3 How consistent are the current estimates of the Weddell Gyre Circulation?

The new Argo-based volume transports are within the range of previous assessments, especially for WDW (Fig. 4.10a-b). The fact that estimates spanning the 1980's to 2008, covering different cross-sections throughout the Weddell Gyre, using different data sources and methods, can show good general agreement with a time composite dataset encompassing all cross-sections in one single figure, is testament to the robustness of the provided volume transport estimates, and to the long-term stability of the Weddell Gyre circulation (during this period) itself. The estimates show excellent agreement for the WDW transports, considerably better than for the full depth, which is

to be expected due to the extrapolation that was applied to extend the dynamic height field to the full ocean depth. Regarding the full depth volume transport, in comparison to the literature, more consistency is observed for the southern limb than for the northern limb estimates. The least agreement occurs in the northern limb at the Prime Meridian, despite best agreement for the corresponding WDW estimates. This may be due to a missing deep baroclinic component of flow (Fig. 4.5). There is a general underestimate of the total transport, both in the results presented here as well as in much of the literature, due to the omission of fast-flowing, narrow frontal currents, both on the shallow shelf and at the shelf edge, where data is rarely available, and yet can be responsible for as much as 50 to 85 % of the overall flow (Thompson & Heywood, 2008; Jullion et al., 2014). This is likely the reason why the transport estimates generally concur with the literature, whereas overall mean gyre flow is considerably weaker than that of the inverse model based estimate in Jullion et al., (2014), which includes the frontal currents. We assume the good agreement with the literature is also in part due to a summer bias in most estimates.

By visually comparing the stream function at 50 dbar in Fig. 4.4a to the 6-year mean dynamic topography in Fig. 5a in Armitage et al. (2018), there is a clear agreement between satellite-derived circulation of the Weddell Gyre and the Argo-derived circulation in this study. There is the multi-cell structure along the elongated, central gyre axis, an intensification of the flow field up-stream of Maud Rise, the influence of the South-Sandwich Island chain in the northwest of the gyre, and even a similarity in the shape of the contours at the eastern end of the Weddell Gyre. Since our data is representative of a long-term mean, and provides the baroclinic component of flow in the Weddell Gyre for the upper 50-2000 dbar, this study complements the work of Armitage et al. (2018), who is able to provide an in-depth seasonal analysis of the barotropic circulation strength, which is shown to vary on a month-to-month basis.

While error estimates are provided for the volume transports in Sections 4.3.2 and 4.4.1, the issue of data density will always be an important factor when deriving large-scale estimates from objectively mapped in-situ observations. We assume that we are working with the absolute minimum amount of data required to carry out such an analysis of the Weddell Gyre circulation. However, a future study that would be useful to the scientific community would be to determine a baseline level of required data to resolve the circulation, which could be achieved by applying a bootstrap error analysis

in a numerical model study (e.g. Lumpkin & Elipot, 2010; Koszalka et al., 2009; Toole et al., 1994).

A question remains regarding the stationarity of the circulation cells of the interior Weddell Gyre (we estimate interior recirculation of 15 ± 8 Sv and 2 ± 1 Sv of WDW and 71 ± 28 Sv and 11 ± 5 Sv for the full water column for the eastern and western cells respectively). How fixed are these features? It has long been suggested that the gyre consists of two sub-gyres (Beckmann et al., 1999). Matano et al. (2002) suggested that the cause is topographic steering of the northern limb east of the Prime Meridian, where the South-West Indian Ridge bathymetrically constrains the flow. Orsi et al. (1993) observed that the double-cell structure is more prominent in deeper layers, which appears to agree with the maps in Figs. 4.4a-f, particularly for the eastern cell. However, what is unknown is: (1) how stationary are these observed (both here and in the literature) circulation cells, for example, with changing wind forcing (or is the double cell structure an artifact from aliasing flow over a 14-year time composite dataset?), and (2) how do they influence mechanisms of water mass transformation, entrainment and mixing within the gyre? Changing wind forcing is particularly relevant given the sensitivity of the inter-annual variability of the Weddell Gyre circulation strength to local variability in the wind curl (Armitage et al., 2018). Studies of Weddell Gyre physical oceanography mostly stem from individual hydrographic sections spanning across the gyre. The resulting estimates of the circulation highly depend on the placement of these sections, i.e. at which point they intersect the gyre axis influences the amount of recirculation incorporated into the transport estimates. For example, a cross-section at 15º E in Fig. 4.10a would result in larger volume transports than across the Prime Meridian, due to crossing through closer to the innermost cell of the eastern circulation cell. If a study is based on a single ship-based transect, as often is, it will not be clear to what extent the associated transports are representative of the zonal strength, or of the interior recirculation of the gyre, which may account for the large variation in volume transport estimates, particularly in older studies. Here, we demonstrate the usefulness in having a synoptic, gyre scale view of the circulation. The influence of the small-scale recirculation is why the mean volume transport in the east is stronger than in the west (Table 4.1). The eastern cell is in an important region for the inflow of CDW into the Weddell Gyre, since strong or variable recirculation in this region may lead to varied mixing of new WDW and modified recirculated WDW. If, for example, the

strength of this eastern sub-gyre is highly sensitive to wind-forcing, we may observe a change in WDW properties that may be attributed to differing ratios of WDW components.

4.5 Conclusions

Argo floats deployed in the Weddell Sea since 2002 have allowed for us to obtain a new Weddell Gyre wide representation of its circulation. This was possible through combining the stream function fitted to the absolute velocity field at 800 dbar (i.e. the float parking depth) with a grid of the relative geostrophic field from hydrographic profile data provided from the same Argo floats. In addition to the upper 2000 dbar and the WDW layers, full depth volume transports were provided by extrapolating the relative dynamic height field to the full ocean depth using a quadratic fit; CTD data from ship-based hydrographic surveys provided an extrapolation error estimate. Perturbations of the flow field using the mapping error and uncorrected parking depth velocity field resulted in an estimation of uncertainty, while an in-depth comparison of the volume transports to those provided by the literature provides an additional assessment of uncertainty.

We provide a full gyre scale view of the Weddell Gyre's circulation from a purely observation-based dataset, whose pertinent features include the double-cell structure, with a stronger eastern cell that varies with depth, and a weaker barotropic western cell. Regional variation of the baroclinic flow field reveals a northeast to southwest reduction in the baroclinic component of flow, while a strong meridional gradient of baroclinic flow is found along the northern limb of the gyre extending southwards from the ACC. Given that the streamlines representing the total flow (Fig. 4.4) are continuous around the Weddell Gyre, we conclude that the southwestern part of the gyre is almost purely barotropic. To our knowledge, this is the first time such a representation of the baroclinic flow field is provided. The zonal mean gyre strength away from the shelf edge is 32 ± 5 Sv, of which 13 ± 3 Sv is WDW. The transport is characteristically larger in the southern limb than the northern limb of the Weddell Gyre for the full depth, upper 2000 dbar and WDW layers, both in the literature and in the results presented here, which may be due to export of water masses from the northwest of the gyre, and as a result of an unresolved deep baroclinic component of flow in the northern limb of the gyre, whereas the southern limb is found to be comparatively barotropic.

A deep baroclinic component of flow may be important and unresolved for in the eastern sector of the northern limb of the gyre; this might be a useful location for mooring deployments in the future, as well as carefully located CTD stations, in order to fully resolve the eastward transport, and to understand the vertical variation on the northern boundary of the Weddell Gyre, something that, to date, is not clearly established or considered. Considerable recirculation occurs within the gyre interior about the eastern cell, before the water is able to fully traverse the full zonal extent of the gyre, which causes considerable uncertainty when determining the gyre strength using single transects as is typical with ship-based surveys. A significant seasonally varying contribution to the Weddell Gyre circulation from shelf-edge boundary currents is not resolved here, nor is the month-to-month variability of the gyre strength resulting from local changes in the wind curl (Armitage et al., 2018; Cisewski et al., 2011). Further investigation of the causes, temporal stability and the physical consequences of the circulation cells along the central gyre axis, is required if we are to fully identify and understand the ways in which the Weddell Gyre may be changing in a rapidly changing climate.

4.6 Appendix:

4.6.1 Data acquisition and processing

4.6.1.1 Argo float trajectory data

All available floats within the region bounded by 40° S to the Antarctic coast, and 90° W to 60° E were downloaded from ftp.ifremer.fr. Since few delayed-mode trajectory data are available for this region, all available data including real-time mode were included in this study. Data from 603 floats were downloaded. All floats where no trajectories entered the region 50° to 80° S, 60° W to 40° E were removed. For a float to be used, it had to have at least 5 cycles. All cycles where position accuracy is 0 or 4 were discarded, likewise if the float has drifted at the surface for more than a day. A cycle required a minimum of 4 satellite fixes if it was to be used.

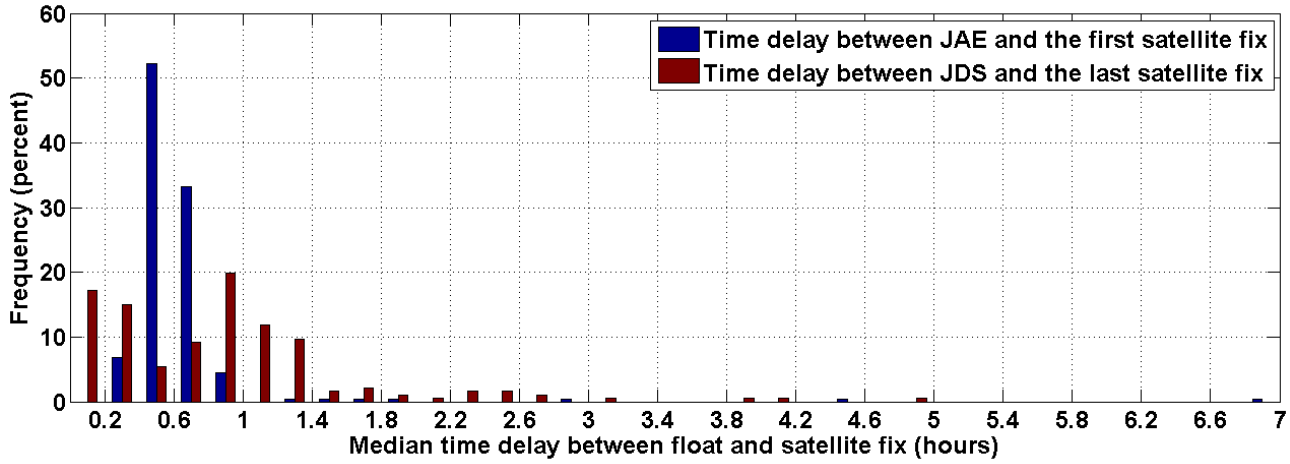

Figure 4.A1. Percentage histogram of the median time delay (in hours) between (1) JAE (i.e. the moment the float reaches the surface) and the first satellite fix (where the first position is recorded), in blue, and (2) the last satellite fix (the last known position of the float before it dives) and the JDS (the float dive time, i.e. the moment the float leaves the surface, in red.

The most straightforward approach in determining the velocity at parking depth, $\boldsymbol{U}_{\text{park}}$, is simply by taking the time and displacement of the float from when it first leaves the surface ($\boldsymbol{\tau_D}$ and $\boldsymbol{x_D}$ respectively) during cycle $\boldsymbol{n}$ (i.e. the last satellite fix of cycle $\boldsymbol{n}$), to when it first arrives at the surface for cycle $\boldsymbol{n}$+1 ($\boldsymbol{\tau_A}$ and $\boldsymbol{x_A}$; i.e. the first satellite fix of cycle $\boldsymbol{n}$+1):

$$\boldsymbol{U}_{park} = \frac{\boldsymbol{x_A} - \boldsymbol{x_D}}{\boldsymbol{\tau_A} - \boldsymbol{\tau_D}} \qquad \text{(Eq. A1)}$$

However, a potential source of error results from the time delay between the float first arriving at the surface (JAE: Julian day Ascent End), and its first satellite fix ($\boldsymbol{\tau_A}$), whereby position $\boldsymbol{x}_{\mathbf{A}}$, is recorded. The median time delay of all float cycles here for JAE is about half an hour (Fig. 4.A1; blue bars). The same can be said of the time delay between the last satellite fix (τ_D) and the time at which the float leaves the surface (JDS: Julian Day Descent Start); the median time delay associated with JDS is about an hour north of 57° S, but reduces to about 20 minutes south of 57° S (Fig. A1: red bars). Since velocity magnitude typically reduces with increasing depth, the horizontal drift can lead to substantially overestimating the magnitude of flow at the parking depth level. However, we can assume that since the baroclinic component of flow is very small in the Weddell Gyre (Heywood and King, 2002, Klatt et al., 2005), and also that the time delays are smaller at high latitudes due to the convergence of polar orbiting satellites, this error would not be significant in the Weddell Gyre. We determine velocity both with and without a surface horizontal drift correction in order to investigate the sensitivity of fitting a stream function to changing velocities, and thus to estimate error for the resulting volume transport estimates. This is discussed in more detail in the methods Section 4.2.6. Since the positions of JAE and JDS ($\boldsymbol{x_{AE}}$ and $\boldsymbol{x_{DS}}$ respectively) are typically unavailable, we followed the method by Park et al. (2005) in order to predict the positions $\boldsymbol{x_{AE}}$ and $\boldsymbol{x_{DS}}$, and determine a "surface horizontal-drift corrected" velocity as well as the "observed uncorrected" velocity in Eq. A1 (which is the approach followed by Lebedev et al., 2007). To determine the "horizontal-drift corrected" velocity, the satellite fixes of a float cycle were used in a least-squares cost function to iteratively adjust the input parameters of a trajectory equation (equations 1-3 in Park et al. (2004)), where the trajectory $\boldsymbol{x(t)}$ is defined as the sum of linear ($\boldsymbol{U}_L$) and inertial ($\boldsymbol{U}_I$) components of velocity:

$$\tilde{x}(t) = x(t_0) + \boldsymbol{U}_L \times (t - t_0) + \int_{t_0}^{t} \boldsymbol{U}_I(t)dt \qquad \text{(Eq. A2)}$$

where $\tilde{x}$(t) is the fitted position at time t, and $x(t_0)$ is an origin position at time t_0. Inertial velocity is defined as Ωf x **r**, where Ωf is the angular velocity of the earth's rotation and **r** is the inertial radius. The input parameters of Eq. A2 are realized when the cost function, J, is minimized:

$$J = \sum_{k}^{N} \frac{\left(\tilde{x}_k - x_k^{obs}\right)^2 + \left(\tilde{y}_k - y_k^{obs}\right)^2}{2\sigma_k^2}, \frac{\partial J}{\partial(u_L, v_L, x_o, y_o, x_i, y_i)} = 0 \qquad \text{(Eq. A3)}$$

where $(\tilde{x}_k, \tilde{y}_k)$ and (x_k^{obs}, y_k^{obs}) are the fitted and observed positions of satellite fix k respectively. (u_L, v_L) is the linear background velocity, (x_o, y_o) is the origin position and (x_i, y_i) is the centre of inertial motion. Each satellite fix is weighted by its position accuracy (i.e. standard deviation, σ_k), provided by the ARGOS quality flags of 3, 2 and 1 (accuracies 150 m, 350 m and 1000 m respectively).

We then extrapolate the fitted trajectory to the time stamps JAE and JDS in order to determine the positions $\boldsymbol{x_{AE}}$ and $\boldsymbol{x_{DS}}$. Figure 4.A2 shows an example trajectory of an Argo float, with the satellite fixed positions and the extrapolated positions, along with the resulting surface velocity vectors. Figure 4.A3 shows (a) the distance between the satellite-fixed positions and the fitted trajectory positions, and (b) the resulting difference in velocity. Where the observed surface velocities are larger than 2 m s^{-1}, the corresponding data point is discarded. A model position error is provided for both $\boldsymbol{x_{AE}}$ & $\boldsymbol{x_{DS}}$ (i.e. from the cost function $\boldsymbol{J}$, $\left(J/\sum dt\right) \times \boldsymbol{d\tau_{AE}}$ **km**). This provides the best estimate of model position accuracy, and any data where the model position error for $\boldsymbol{x_{AE}}$ is larger than 2 km or for $\boldsymbol{x_{DS}}$ is larger than 5 km are removed. The model position error (i.e. the cost function) is larger for JDS than JAE, due to the larger time delay associated with JDS; the means are less than 0.1 km and 1 km for JAE and JDS respectively.

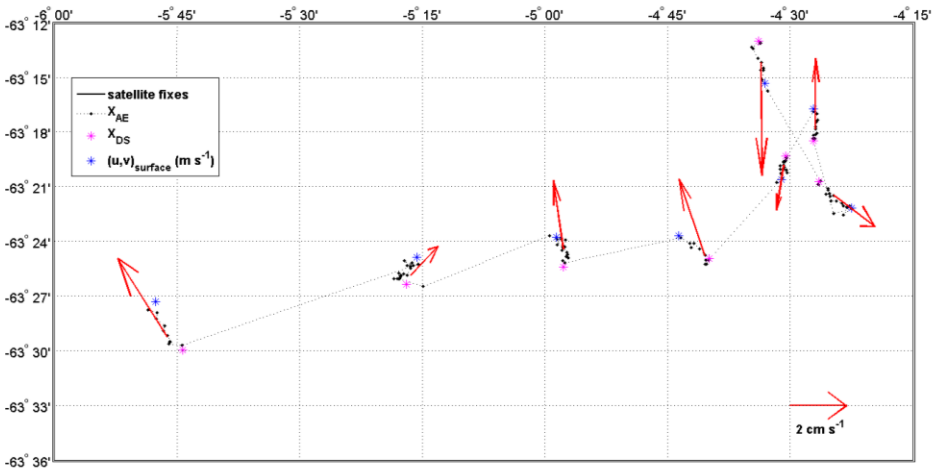

Figure 4.A2. An example Argo float trajectory (float 3900073), with the satellite fixed positions (black dotted line) and the extrapolated positions for JAE (magenta *) and JDS (blue *), along with the resulting SD corrected surface velocity vectors (red arrows).

Lastly, not all floats and float cycles have a corresponding JAE or JDS; for these floats we then flag the cycle and take a mean time delay of all cycles for that float; if the float has no JAE (JDS) at all, then a median time delay of all nearby float cycles within an ellipse of radius arbitrarily defined by ± 5° N and ± 15° E is used. This is also the approach taken by Gray & Riser, (2014), when determining global velocity field estimates. Less than 23% of data points required an estimated JAE and 36 % of data points required an estimated JDS. The position accuracy for these data points is 1000 m, which then results in a larger cost function (i.e. error).

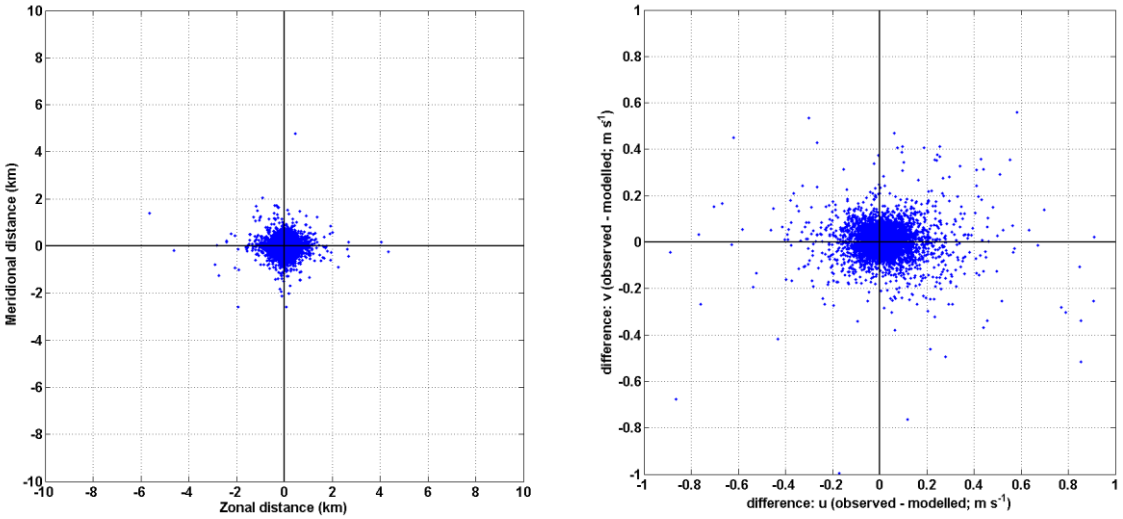

Figure 4.A3. (a) Distance between first (last) satellite fix and the predicted positions for JAE (JDS) and b) the difference in surface velocity between the satellite-fixed positions and the predicted positions (i.e. SD corrected surface velocity).

After the application of quality control checks, the number of floats was reduced to 341 from 603. The remaining floats span 20/02/2002 to 06/09/2016. At parking depth, there are 9169 data points (where the peak number of data points occurs both in 2012 and 2008), with just 1496 data points south of 60º S; about 39% of which are from 2006-2007 (Fig. 4.3c).

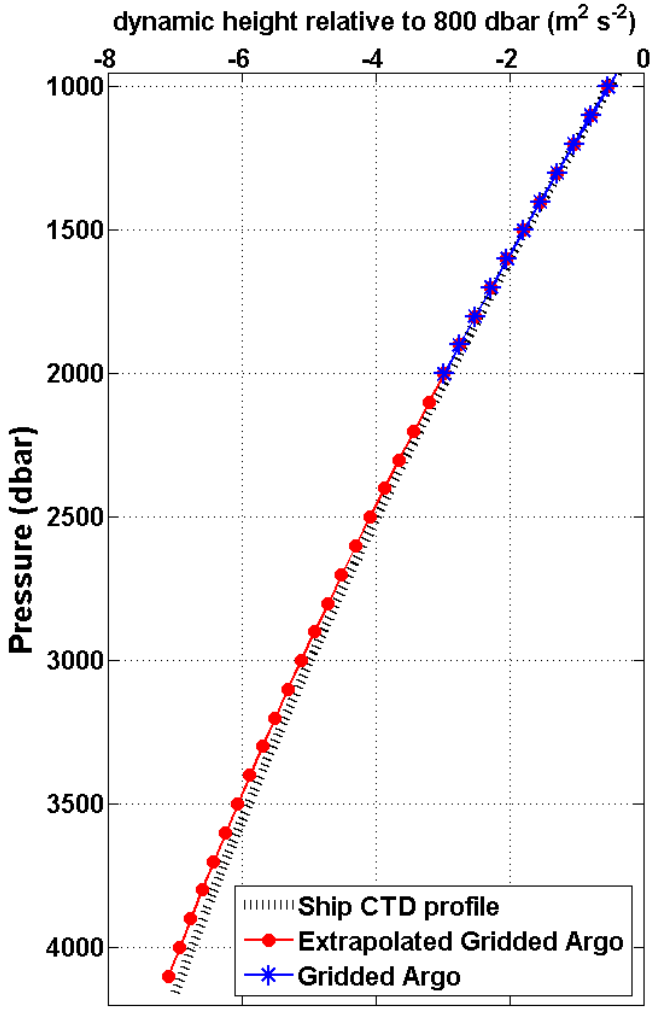

Figure 4.A4. Example profile of dynamic height relative to 800 dbar. The blue profile is from the gridded Argo float data, the black dashed line is from the closest available ship CTD profile, and the red line shows the extrapolated profile derived from the Argo float data, which is extrapolated by fitting a quadratic function to the profile below 1000 dbar. The difference between the profiles are used to determine the extrapolation error (refer to Section 4.2.6.2).

4.6.1.2 Argo float profile data

The same quality control criterion were applied as in Reeve et al. (2016). The only difference is that this study updates the float data set used to incorporate more recent data. Each profile was quality control approved, and then linearly interpolated onto 41 fixed pressure levels spanning 50 dbar to 2000 dbar (the upper 50 dbar were omitted due to high seasonal variability). The spacing of the pressure levels increases with increasing depth. Profile data includes those profiles with an interpolated position under the sea-ice (i.e. the profiles marked in magenta in Fig. 4.2a). For further

information on why it is assumed acceptable to include under-ice profiles in the objective mapping of float profile data, refer to Reeve et al. (2016).

In Section 4.2.5, we describe the method of extrapolating to the full ocean by fitting a quadratic function to the gridded Argo profile based on ship CTD data. In Fig. 4.A4, we provide an example of the vertical profile of dynamic height relative to 800 dbar for the following: (1) for the upper 2000 dbar extracted from the gridded Argo dataset (blue, Section 4.2.2), (2) derived from a CTD-profile from the Polarstern cruise ANT_IX_3 (1991, black dotted line), and (3) the extrapolated gridded Argo profile (red). The grid point of the example Argo profile is located at 24.6º W, 71.6º S, and the ship-based CTD profile is located at 24.9º W, 71.75º S.

4.6.2 Methods Flow Chart

The methods section details how we arrive at a full-depth grid of stream-functions, which is then used to describe the Weddell Gyre circulation and estimate volume transports. Figure 4.A5 shows a flow chart which summaries the processes detailed in Section 4.2.

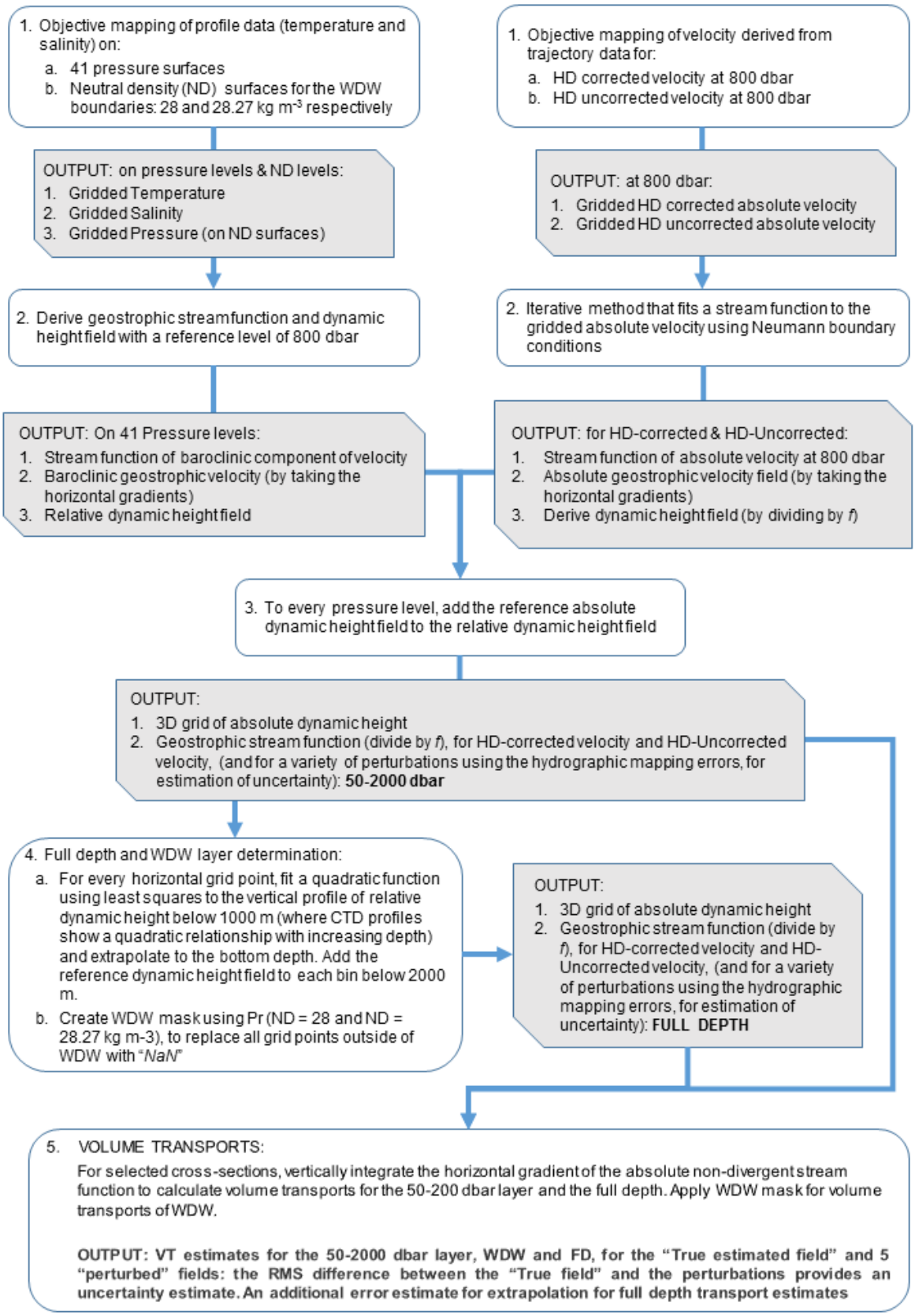

Figure 4.A5. Flow chart outlining and summarising the method for arriving at stream functions and volume transport estimates as detailed in Section 4.2.

4.7 Acknowledgements

These data were collected and made freely available by the International Argo Program and the national programs that contribute to it (http://www.argo.ucsd.edu, http://argo.jcommops.org). The Argo Program is part of the Global Ocean Observing System. The GEBCO Digital Atlas is published by the British Oceanographic Data Centre on behalf of IOC and IHO, 2003. A special thank you goes to J.T. Allen for his invaluable support with correctly fitting a stream function to the velocity data. We would like to express our gratitude to the three anonymous reviewers, whose feedback was both constructive and interesting while also helping to greatly improve the manuscript. This work is dedicated in memory of Eberhard Fahrbach (who passed away on the 21th April 2013), a pioneering Polar Oceanographer who's dedication to the observation of the Polar Oceans was an inspiration to us all.

5 Publication III:

The Weddell Gyre heat budget associated with the Warm Deep Water circulation

In preparation,

K.A. Reeve[1,2], T. Kanzow [1,3], V. Strass[1], O. Boebel[1] and R. Gerdes[1,2]

1 Alfred-Wegener-Institut Helmholtz-Zentrum für Polar- und Meeresforschung, Bremerhaven, Germany

2 Physics and Earth Sciences, Jacobs University, Bremen, Germany

3 Bremen University, Physics and Electrical Engineering, Bremen, Germany

Abstract

The Weddell Gyre plays an important role in the global climate system by supplying heat to underneath the ice shelves, and to the formation of deep and bottom water masses, which ultimately feed heat into the global abyssal oceans. In this study, we investigate the distribution of heat throughout the Weddell Gyre by diagnosing the heat budget for a 1000 m thick layer of water encompassing the core of Warm Deep Water. The heat budget is derived from gridded climatologies of temperature and velocity, obtained from Argo floats in the Weddell Gyre from 2002 to 2016. While the heat budget is somewhat noisy on a local scale, it nearly closes when integrated over the southern limb and the interior circulation cell of the Weddell Gyre, within the range of uncertainty provided by a range of values for horizontal and vertical diffusivity. There is an overall balance between the mean horizontal advection and horizontal turbulent diffusion of heat, whereas the vertical terms contribute comparatively little to the heat budget. Heat convergence due to mean horizontal advection balances with divergence due to horizontal turbulent diffusion in the southern limb of the Weddell Gyre. In contrast, heat divergence due to mean horizontal advection balances with convergence due to horizontal turbulent diffusion in the interior circulation cell of the Weddell Gyre. Heat is advected into the Weddell Gyre along the southern limb, some of which is diffused northwards into the interior circulation cell, while some is diffused southwards towards the shelf seas. This suggests that horizontal turbulent diffusion plays a role in transporting heat towards the ice shelves. Horizontal turbulent diffusion is also a mechanism by which heat can be transported into the Weddell Gyre across the open northern boundary. The sum of the heat budget terms provides mean temperature trends over the 14 year time period for the southern limb of the gyre and the central circulation cell, of 0.0095 ± 0.035 °C/year and 0.006±0.032 °C/year respectively. These trends, while insignificant due to the assumptions involved, are similar to estimates in previous studies, which calculate temperature trends directly from long-term time series of temperature of Warm Deep Water within the Weddell Gyre.

5.1 Introduction

Understanding the drivers and pathways of large-scale ocean circulation is a fundamental component of climate science (Rhein et al., 2013). To comprehend the regulatory role of the oceans in the climate system one can determine the ocean heat budget, which describes the distribution of heat throughout the ocean by means of horizontal and vertical advection, turbulent diffusion, and surface heat fluxes to the atmosphere (e.g. Tamsitt et al., 2016; an adapted form of the heat budget equation is given in Eq. 1).

The Weddell Gyre is located south of 50° S in the Atlantic sector of the Southern Ocean, where Circumpolar Deep Water (CDW) predominantly enters the gyre's southern limb in the east at about 30° E. The CDW that enters the Weddell Gyre is commonly referred to as Warm Deep Water (WDW). WDW circulates the cyclonic gyre, undergoing cooling and freshening on-route, through interaction with the underlying and overlying water masses (e.g. Fahrbach et al., 2004; Klatt et al., 2005; Fahrbach et al., 2011; Leach et al., 2011). The core of WDW is identified as the sub-surface temperature maximum (Fig. 5.1; hereafter referred to as Θ_{max}), which feeds heat into the Weddell Gyre (Fahrbach et al., 2004, 2011; Cisewski et al., 2011; Ryan et al., 2016). The Weddell Gyre has been ascribed the role of a heat buffer (Fahrbach et al., 2011), in that it acts to store and redistribute heat and salt in the water column, effectively transferring heat to the deeper layers where it is ultimately exported northwards, spreading throughout the abyssal global ocean (e.g. Foster et al., 1987; Naveira Garabato et al., 2002, 2016; Fahrbach et al., 2011).

WSDW and WSBW (Weddell Sea Bottom Water), have exhibited warming trends over recent decades (Fahrbach et al., 2011; Meredith et al., 2011). However, their primary source of heat, WDW, exhibits pronounced decadal variations and shows no significant long-term warming trend (Fahrbach et al., 2011; Kerr et al., 2017). To understand how the circulation redistributes heat throughout the Weddell Gyre, we combine observations of the velocity field with the temperature field, both derived primarily from Argo floats, to diagnose components of the heat budget of a fixed volume of water fully encompassing the core of WDW within the Weddell Gyre. The upper 50 dbar is omitted from the analysis due to its high seasonal variability. By analysing the heat budget for a fixed volume encompassing the core of WDW, we can

determine the ways in which heat from WDW is redistributed throughout the Weddell Gyre, and indirectly estimate the change in mean temperature of that layer of water over the time period covered by the Argo float data (from 2002 to 2016).

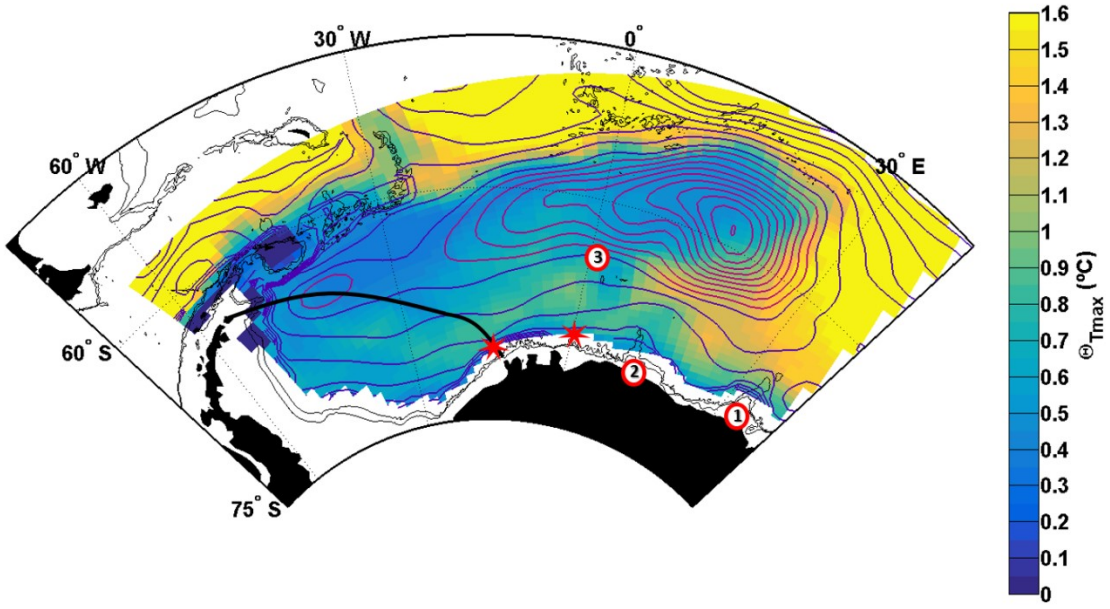

Figure. 5.1. Sub-surface conservative temperature maximum (Θ_{max}) with streamlines of the vertically integrated stream function for 50-2000 dbar. Blue contours are spaced by 5 Sv and red contours have 3 Sv spacing. Red stars show mooring positions used in velocity field. The circles labelled 1-3 show Gunnerus Ridge, Astrid Ridge and Maud Rise respectively. The thick black line shows the repeat ship-based transect from Kapp Norvegiaa to Joineville Island. The grey contours show the 1000 and 2000 m isobaths, from the general bathymetric chart of the oceans (GEBCO, IOC et al., 2003).

5.2 The heat budget

The heat budget integrated for a volume of water not in contact with the atmosphere is defined as:

$$\frac{d\Theta}{dt}dz = -\nabla_H(U\cdot\Theta) - w_E\frac{d\Theta}{dz} + \kappa_H\nabla_H^2\Theta + \kappa_V\frac{d^2\Theta}{dz^2} \qquad \text{Eq. 1.1}$$

$$\rho C_p\int_{mT-1000}^{mT}\frac{d\Theta}{dt}dz = \rho C_p\left\{\int_{mT-1000}^{mT}(-\nabla_H(U\cdot\Theta) + \kappa_H\nabla_H^2\Theta)\,dz - w_E(\Theta_{mT} - \Theta_{mT-1000}) + \kappa_V\left(\frac{\partial\Theta}{\partial z}\Big|_{mT} - \frac{\partial\Theta}{\partial z}\Big|_{mT-1000}\right)\right\} \qquad \text{Eq. 1.2}$$

↑ ***Mean horizontal geostrophic advection*** ↑ ***Horizontal turbulent diffusion*** ↑ ***Mean vertical advection*** ↑ ***Vertical turbulent diffusion***

where ∇_H is the horizontal divergence operator, U is the horizontal geostrophic velocity, Θ is the conservative temperature, z is depth and κ_H and κ_V are the horizontal and vertical diffusivity in m^2s^{-1} respectively (adapted from Tamsitt et al., 2016). For the vertical integration in Eq. 1.2, the subscript *mT* describes the mid-point of the thermocline, which provides the upper boundary, while *mT+1000* describes the lower boundary (explanation of the vertical boundaries is provided in Section 5.2.1). Each term is multiplied by the specific heat capacity of seawater, C_p (~4000 J K^{-1} Kg^{-1}), and seawater density, (ρ_0 = 1027 kg m^{-3}), and integrated for a 1000 m thick layer so that units of each component are given in W m^{-2}. The first term on the right-hand side in Eq. 1.1 describes the mean horizontal geostrophic heat advection, where U is derived from horizontal differentiation of the geostrophic stream function derived from Argo float data (i.e. where $u = \partial\psi/\partial y$ and $v = -\partial\psi/\partial x$; see Section 5.3.1 and Reeve et al., in review). Since we derive velocity from a non-divergent stream function, we assume geostrophic flow conditions and omit ageostrophic advection from the first term. This is a pertinent assumption given that the Ekman Layer is excluded from the analysis. The second term on the right-hand side in Eq. 1.1 describes the mean vertical heat advection, where vertical velocity is defined as the Ekman pumping velocity (Section 5.3.2). The third and fourth terms in Eq. 1.1 (or, the second part of the first term and the third term, labelled in Eq. 1.2 respectively) describe the horizontal and vertical turbulent heat diffusion components respectively. The sum of these terms results in an estimate of heat tendency over time ($d\Theta/dt$), which can be used to determine mean temperature change for a column of water. Maps of the different components are provided in the results section.

There are two unknowns in Eq. 1. These are the horizontal and vertical diffusivities, κ_H and κ_V respectively. Based on the varying values provided in the literature, such as in Donnelly et al. (2017), we define κ_H as 400 ± 200 m^2s^{-1}, and κ_V as 2.6 x 10^{-5} ± 2.4x10^{-5} m^2s^{-1}. The error ranges are to provide a range of reasonable estimates while acknowledging lack of consensus of appropriate values for the diffusivities. While κ_v is similar to Donnelly et al's estimate of 2.4 x 10^{-5} m^2 s^{-1}, our horizontal diffusivity is slightly larger than the 247 m^2 s^{-1} provided by Donnelly et al. (2017; though within range of our values provided by the uncertainty range). This is

because we focus on larger length-scales, since the resolution of our grid is of the order of ~80 x 60 km. The implications of these decisions are discussed in Section 5.5.

In part 2 of the results (Section 5.4.2), the heat budget terms are horizontally integrated, to provide an analysis of the zonal variation in the heat budget for (1) the southern limb and (2) the interior circulation cell of the Weddell Gyre, of which the cumulative sum of the heat budget terms are provided in Tables 5.2 and 5.3 respectively. The errors provided in Tables 5.2 and 5.3 are calculated based on a method in calculating volume transport errors in Reeve et al. (in review). We extend the error analysis here as follows. A perturbation to the heat budget terms is provided. The heat budget is calculated primarily from gridded temperature, and velocity (see Section 5.3.1 for details on how these fields were derived from Argo float profile and trajectory data). For the perturbation, the heat budget is calculated for adjusted temperature and horizontal velocity fields. The adjusted temperature is the objectively mapped temperature field described in Section 5.3.1, plus its corresponding objective mapping error. The adjusted velocity field is defined as the sum of an adjusted reference field at 800 dbar and an adjusted baroclinic component of flow, derived from density. The adjusted reference level is derived from Argo float trajectories, which are not corrected for surface horizontal drift (the unperturbed velocity field applies a surface drift correction to the Argo float trajectories, see Section 5.3.1), and the adjusted baroclinic component of flow, which is used to extend the horizontal velocity field to different depths from 50 to 2000 dbar, is calculated using the gridded temperature and salinity plus their corresponding mapping errors to calculate density. This results in a heat budget that is perturbed from the original, using a combination of mapping errors and a non-surface-drift corrected velocity field. The differences between the original heat budget terms and the perturbed terms are used as an estimate of uncertainty in Section 5.4.2. For the diffusion terms, an additional uncertainty is provided based on the range of diffusivity values (described in the previous paragraph). The uncertainty from the range in diffusivity and the uncertainty from the perturbation are then summed in quadrature to provide a total error estimate for the diffusion terms. Lastly, for the heat tendency (i.e. the sum of all terms), the combined error is defined as the summation in quadrature of the errors of the mean advection and turbulent diffusion terms.

5.2.1 Vertical boundary conditions for heat budget integrals:

Before describing the data resources in Section 5.3, some explanation is required regarding the vertical boundaries applied to the heat budget calculations of this paper. Since we are unable to integrate for the full ocean depth (Argo floats profile the upper 2000 dbar), and most importantly, to the surface of the ocean, due to the high seasonal variability at the surface (Section 5.3.1), we need to decide on suitable vertical boundaries for the heat budget integrals. However, if we simply select uniform depths for the vertical boundaries, we may include certain features in the T-S profile (e.g. such as the temperature minimum) in some areas of the Weddell Gyre, while excluding them in other regions. This is particularly true with regards to defining the upper boundary. Hence we need to ensure the upper boundary is defined such that Θ_{max} (i.e. the core of WDW) is always fully included in the vertical layer, given that the core of WDW is the primary source of heat to the Weddell Gyre. At the same time, we need to avoid incorporating seasonally variable Surface Water and Winter Water (a surface water mass characterised by a sub-surface temperature minimum, e.g. Behrendt et al., 2011) within the layer, since the depths at which Winter Water are found varies spatially throughout the gyre (for example, fixing the depth of the upper boundary may result in the presence of Winter Water in some grid cells but not others). Otherwise, in regions of the gyre where the profile includes the temperature minimum layer, the vertical advection component will be stronger due to a larger vertical temperature gradient, in contrast to regions where the Winter Water is altogether omitted. This will result in bias in the spatial distribution of the heat budget terms. It is also necessary to ensure the same thickness of water is analysed throughout the Weddell Gyre, again to avoid including bias in the heat budget terms. We resolve this by defining the upper boundary as the mid-point of the thermocline, and the lower boundary as 1000 m below the thermocline mid-point (Fig. 5.2a). That way, regardless of location, we exclude Winter Water, but always include the core of WDW, and maintain equal layer thickness throughout. Maps of the upper boundary depth and the difference in temperature between the upper and lower boundaries are shown in Fig. 5.2b-c, along with an example vertical profile (Fig. 5.2a) to illustrate the vertical boundary conditions.

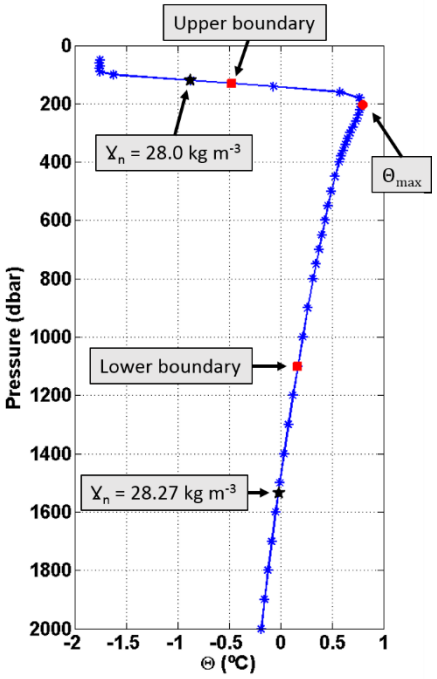
Upper boundary
γ^n = 28.0 kg m^{-3}
Θ_{max}
Lower boundary
γ^n = 28.27 kg m^{-3}
Pressure (dbar)
Θ (°C)
0
200
400
600
800
1000
1200
1400
1600
1800
2000
-2
-1.5
-1
-0.5
0
0.5
1

(5.2a)

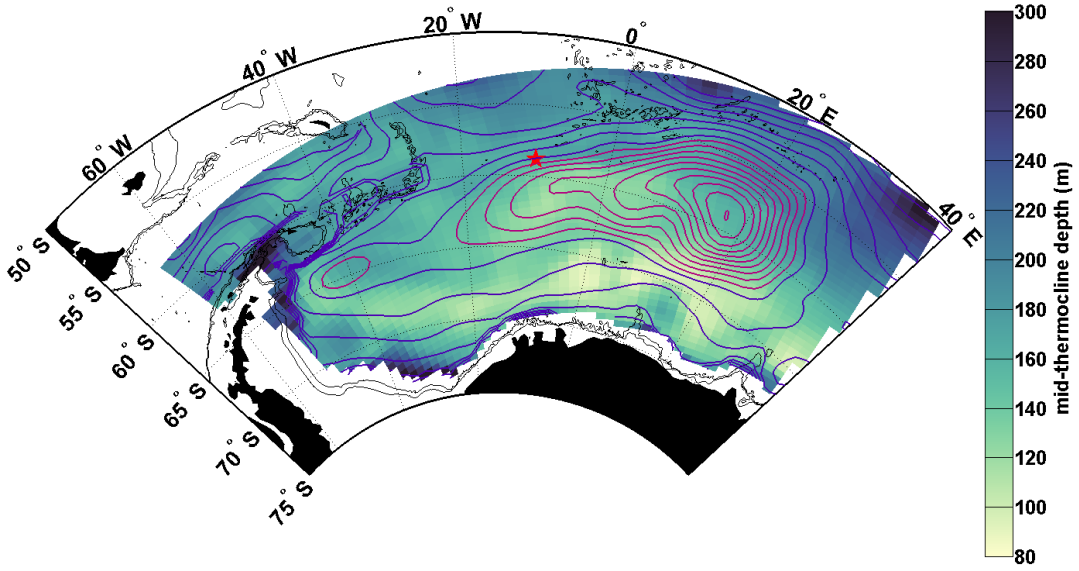
20° W
0°
40° W
60° W
20° E
40° E
50° S
55° S
60° S
65° S
70° S
75° S
mid-thermocline depth (m)
300
280
260
240
220
200
180
160
140
120
100
80

(5.2b)

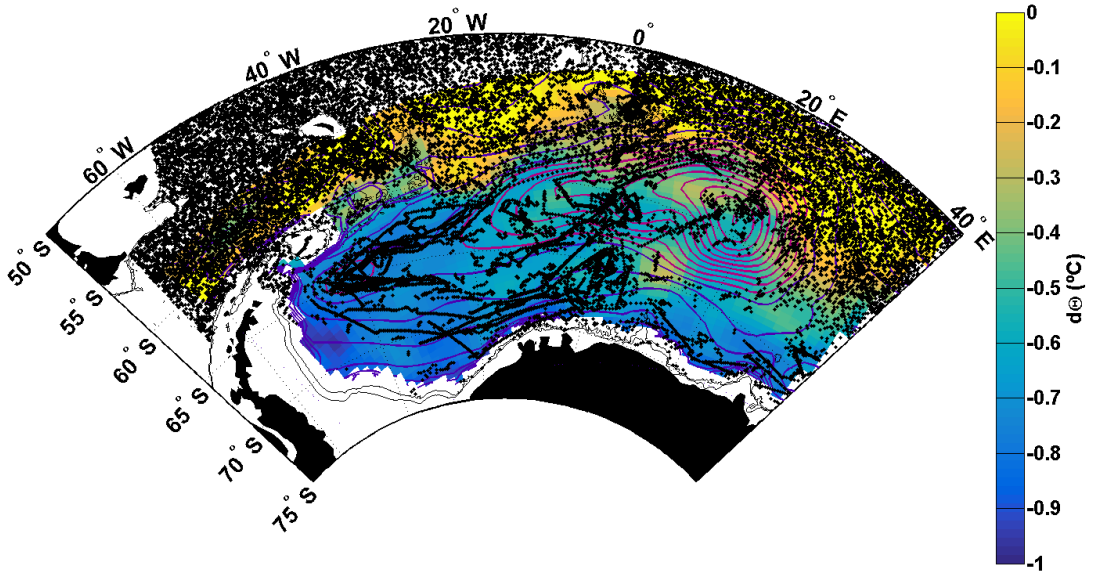

(5.2c)

Figure 5.2. **(a)** A vertical profile of conservative temperature (the position of the profile is marked by a red star in panel **b**), where Θ_{max} is marked by a red circle, the upper boundary (i.e. mid-thermocline) and the lower boundary (mid-thermocline + 1000) are marked by red squares, and the upper and lower WDW boundaries (defined by a neutral density range of 28 to 28.27 kg m^{-3}) are marked by black stars. This is to highlight that our method for the vertical boundary limits allows for the full inclusion of the core of WDW while also excluding Winter Water. **(b)** Upper boundary depth (m), defined at the mid-thermocline and **(c)** the conservative temperature difference between the upper and lower boundaries ($\Theta_{up} - \Theta_{dn}$), with black dots showing the positions of the original Argo float profile positions. Contours as in Fig. 5.1.

In the following section, we will provide information of the data resources used for this analysis, in particular the Argo float gridded data that provide temperature and horizontal velocity, and wind stress data, which provide for an estimate of vertical Ekman pumping velocity (Section 5.3).

5.3 Data resources

5.3.1 Gridded velocity and temperature fields derived from Argo floats:

All Argo float data available for the Weddell Gyre region between 2002 and 2016 were used in this study, where objective mapping of the profile data resulted in a climatology of gridded conservative temperature on 41 pressure levels between 50 and 2000 dbar, where conservative temperature was derived using the TEOS-10 program in Matlab (McDougall et al., 2011). This method followed, and is an extension of that

provided in, Reeve et al., (2016), and the reader is referred to that study for further details on the data quality control and mapping method used in this study. The absolute velocity field was derived from Argo float trajectory data at the depth of the float drift (800 dbar in the Weddell Gyre). This process required careful quality control assessments and surface drift corrections following Park et al., (2005), and, given that under-ice profiles have no geo-located position, all such interpolated trajectories were omitted from the study. Thus, the derived velocity field exhibits considerable bias to summer conditions. The velocities were objectively mapped to provide a grid of absolute velocity at 800 dbar. This process is detailed in Reeve et al., (in review).

Following Reeve et al., (in review), a stream function was fitted to the velocity field at 800 dbar through the application of a cost function. By applying a cost function, the resulting stream function provides a best fit for the entire Weddell Gyre, providing a good representation of the large-scale circulation of the Weddell Gyre, despite regions where float data availability is sparse or lacking (such as in the southwestern Weddell Gyre), as opposed to directly deriving the stream function during the objective mapping process. The stream function at 800 dbar provides the reference level for the relative geostrophic velocity, derived from the gridded density field from Reeve et al., (2016), above. For full details on this methodology, refer to Reeve et al., (in review), which, in addition to Reeve et al., 2016, is the prelude to this study. In Reeve et al., (in review), a careful error analysis and a detailed comparison of volume transports to available estimates in the literature justify the method as a reasonable solution to obtaining a large-scale observation-based estimate of the Weddell Gyre circulation.

There are, however, some differences between the stream function provided in Reeve et al., (in review), and the stream function used in this study. The cost function was adapted to allow for a variable coastline, so that the stream function provides a solution which includes the southern ice shelf edge east of the Prime Meridian (though not the shelf edge currents, such as the Antarctic Slope Front, which are not resolved in this study), which is excluded in Reeve et al., (in review). To better estimate the velocity field along the southern coast of the Weddell Gyre, a few minor adjustments were made to the gridded velocity field prior to fitting a stream function. Firstly, long-term average velocities derived from mooring data were included at the coast at the Prime Meridian and Kapp Norvegia, to better resolve the flow which follows the coastline as it curves southwards towards the Filchner-Ronne ice shelves (the mooring

positions are marked in Fig. 5.1). Secondly, the velocity field at Gunnerus Ridge (also marked in Fig. 5.1) required special treatment. The trajectories of Argo floats show a tight, bathymetrically steered flow around Gunnerus Ridge, which is lost during the objective mapping process due to larger length scales. Also, while the potential vorticity values to either side of the ridge are the same, the direction of the flow is opposing (i.e. primarily northwards on the eastern flank of Gunnerus Ridge and southwards to the west of Gunnerus Ridge; see Fig. 11 in Reeve et al., in review). This opposing direction is averaged out in the objective mapping. Therefore, after the objective mapping, the closest grid cells to Gunnerus Ridge are replaced with direct velocity measurements derived from the three Argo floats that drift along the ridge (the Argo floats have WMO numbers: 7900164, 7900166 and 7900168). There are caveats to this decision, in that these are data points from three floats with a limited time span (from February-May 2007, and then December 2007 until April 2008), during a period when the area is ice-free. However, by making this adjustment, we improve the performance of the cost function in providing a stream function representative of the large-scale circulation, which includes a more complete inflow (in comparison to Fig. 4, Reeve et al., under review). The resulting stream function for the vertically integrated flow from 50-2000 dbar is shown in Fig. 4.1, where the streamlines curve around Gunnerus Ridge, indicating the main inflow into the southern limb of the Weddell Gyre.

5.3.2 *Vertical Ekman pumping velocity derived from the wind stress field: Era-interim*:

Outside of surface and bottom boundary layers we assume the velocity to be geostrophic. Therefore we define the vertical advection term (the second term on the right-hand side of Eq. 1.1) as the vertical temperature gradient multiplied with Ekman vertical pumping velocity, w_E. Since the system is assumed geostrophic, vertical velocity is assumed constant with changing depth (outside of the turbulent surface and bottom boundary layers, which are excluded in this study, see Section 5.2.1). The Ekman pumping velocity, w_E, was derived from a mean of the wind stress field for the period 2002-2016:

$$\tau_w = \rho_{air} C_{DW} \left(\underline{U_{10}^2}\right) \qquad \text{Eq. 2.1}$$

$$w_E = \frac{1}{\rho_0 f}\left(\frac{d\tau_y}{dx} - \frac{d\tau_x}{dy}\right) \qquad \text{Eq. 2.2}$$

where τ_w is wind stress, x and y describe the zonal and meridional directions along the grid respectively, ρ_{air} is the density of air (1.29 kg m^{-3}), C_{DW} is the wind drag coefficient ($1.5x10^{-3}$), U_{10} is the wind velocity at 10 m above sea level, ρ_0 is seawater density (1027 kg m^{-3}) and f is the Coriolis parameter.

The wind stress field (Fig. 5.3a) was taken from ERA-interim reanalysis, based on previous convictions that it provides one of the most reliable estimates for the Southern Ocean (Jones et al., 2016). The resulting Ekman pumping velocity averaged over 2002-2016 (Fig. 5.3b) is positive throughout the Weddell Gyre (indicative of upwelling) and the only region of downwelling is on the shelf in the south-west, which is excluded from this study since Argo float data are sparse for the shelf seas. Since w_E is assumed to be constant with depth below the Ekman layer, and the surface mixed layer is omitted from the objectively mapped grids of velocity and temperature, w_E is a suitable estimate of the vertical velocity within the scope of this study. The resulting w_E was re-gridded to the same grid as the Argo data, using a simple distance-weighted mean.

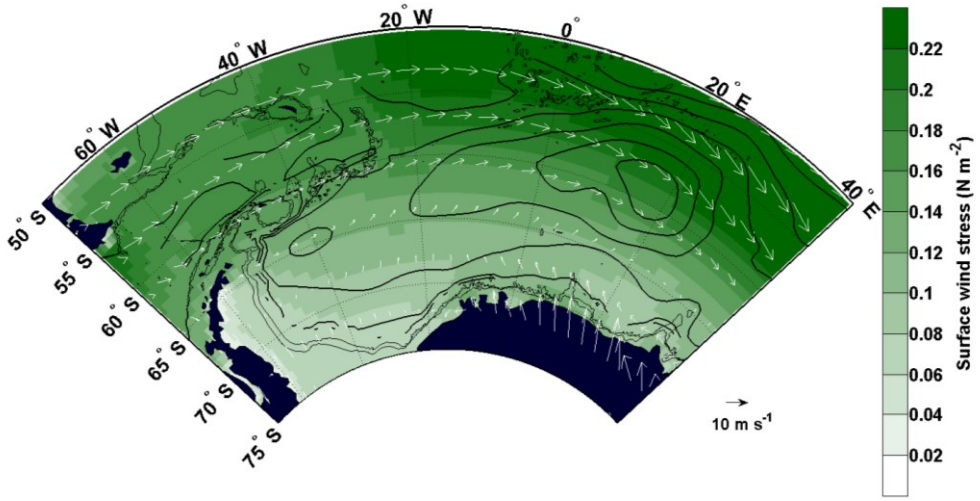

(5.3a)

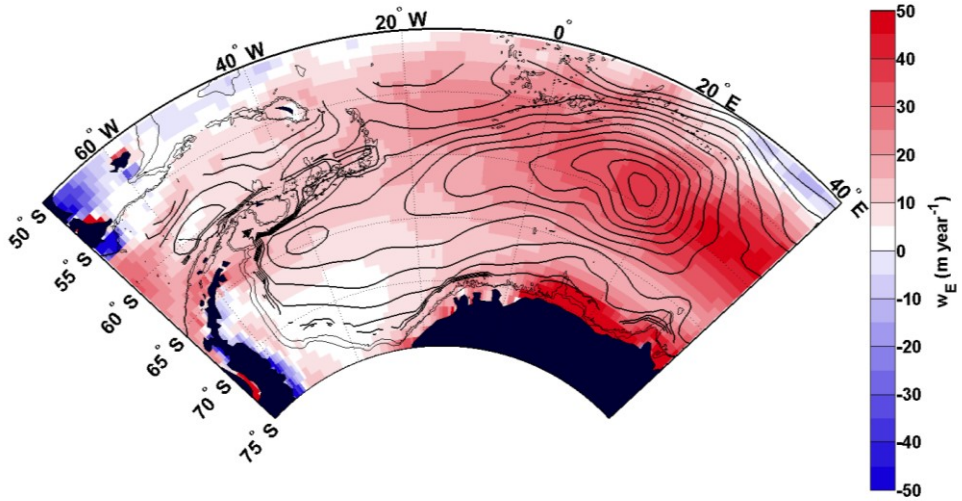

(5.3b)

Figure 5.3 **(a)** Surface wind stress (N m^{-2}): mean from 2002 to 2016 from Era-interim ECMWF reanalysis, with the wind velocity at 10 m above sea level (the legend provides the scaling for the vector arrows of 10 m s^{-1}). Black streamlines have a spacing of 10 Sv, integrated from 50 to 2000 dbar. Panel **(b):** vertical Ekman pumping velocity (w_E: m/year), where positive values indicate upwelling. Black streamlines have a contour spacing of 5 Sv integrated from 50 to 2000 dbar.

5.3.3 *Air-sea-heat fluxes*:

The net air-sea heat flux is the sum of the following components: shortwave solar radiation, longwave thermal radiation, latent heat flux and sensible heat flux. The air-sea heat fluxes are not directly relevant in the calculation of the heat budget in this study, since the heat budget calculations are restricted to depths exceeding 80 m (i.e. the minimum depth of the mid-thermocline below 50 m, Fig. 5.2b), and downward shortwave radiation decreases exponentially with depth (only 1% of the radiation reaches past 75 m; Tamsitt et al., 2016). However, gaining perspective on where we expect heat loss through the surface of the ocean may help to understand the mechanisms through which WDW loses its heat as it circulates the Weddell Gyre. Long-term means between 2002 and 2016 of surface heat fluxes are derived from ERA-interim, as above.

5.4 Results

The following section is presented in two parts. In part one, we provide maps of the net surface heat flux, vertically integrated heat budget terms (from Eq. 1.2), and vertically averaged temperature, to obtain an overview of the large-scale heat field of the Weddell Gyre. Part 2 considers the zonal variation of the heat budget, for both the southern limb and the interior circulation cell (i.e. where streamlines form a closed circuit) of the Weddell Gyre. The northern limb is mostly included within the interior circulation cell analysis, and is not analysed on its own due to the applied grid cell resolution, which is not high enough to apply double differential analysis to the narrow northern limb of the Weddell Gyre.

5.4.1 Part 1: the large-scale investigation of heat within the Weddell Gyre

The net air-sea heat flux into the ocean in Fig. 5.4 (here on referred to as Q_{net}) is positive along the northern limb of the gyre and negative over the southern limb, creating a north-south divide parallel to the central gyre axis (indicated by the thick black line in Fig. 5.4).There is, however, some offset between Q_{net} and the central axis of the depth-integrated circulation, as indicated by the offset between the thick black line and the thick dashed black line in Fig. 5.4. Thus, the Weddell Gyre interior (i.e. the red streamlines in Fig. 5.4) is dominated by positive Q_{net} fluxes (Fig. 5.4), and the zero contour in Q_{net} (thick black line in Fig. 5.4) appears south of the central gyre axis, roughly between the interior circulation cell (where streamlines form a closed circuit within the gyre) and the open inflow zone in the southern limb (i.e. the blue streamlines south of the central cell), instead of directly along the central axis of the oceanic gyre. Within the vicinity of the zero line separating positive and negative Q_{net}, the general flow direction is opposite to the direction of the prevailing winds in Fig. 5.3a, which is also shown in Fahrbach et al. (2011). An exception to the north-south divide is found east of the Prime Meridian at about 20-30°E, 60°S, where there exists a patch of negative air-sea heat flux just east of the eastern circulation core (as indicated by the northward displacement of the thick black line between 0 and 30° E).

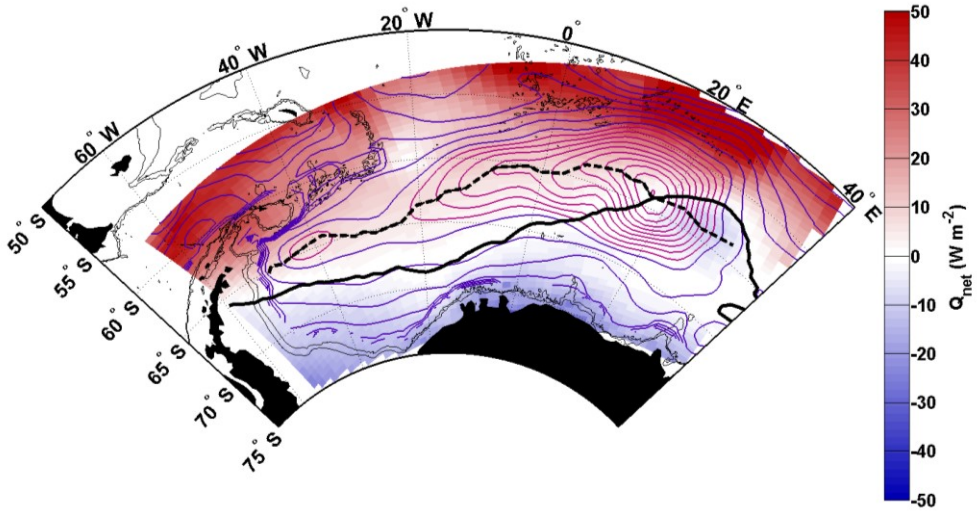

Figure 5.4. Net air-sea heat flux (i.e. the sum of long/short-wave radiation, latent and sensible heat flues, in W m^{-2}): long-term mean from 2002 to 2016, from ERA-interim reanalysis data. The thick black line indicates the 0 Wm^{-2} contour line for Q_{net}. The central gyre axis is the thick dashed black line, defined as the meridional maximum stream function value. South of the dashed line the flow of the water column is westward and flow north of the dashed line is eastward. The blue and red contours are as in Fig. 5.1. Positive values indicates heat flux into the ocean.

The heat budget contributions from the different terms in Eq. 1 (including the signs of each term, e.g.$-\nabla_H U\Theta$ and $+\kappa_H\nabla^2\Theta$) are provided in Fig. 5.5. While the mean horizontal geostrophic heat advection (Fig. 5.5a) shows a patchwork display of heat transport convergence (positive) and divergence (negative), the southern limb of the gyre is generally dominated by heat transport convergence, of about +20 W m^{-2} west of the Prime Meridian. A small patch of divergence is found over the western cell of about -10 to -20 Wm^{-2} (~35-45°W, ~65°S), and over Maud Rise of about -20 to -30 Wm^{-2} (~3°W, 65°S). The whole region east of the Prime Meridian is dominated by particularly strong patches of positive and negative values in excess of ±80 W m^{-2}. Along the northern limb of the gyre, the pattern is dominated by alternating positive and negative values, of about ±60-80 W m^{-2}, which are aligned in a manner that appears to follow the complex bathymetry in the region.

The heat flux due to mean vertical advection ($-w_E(\Theta_{mT} - \Theta_{mT\text{-}1000})$, Fig. 5.5b) is positive throughout, and considerably weaker than that due to mean horizontal advection, in the range of ~0-4 W m^{-2}. Vertical advection is weakest in the southwest of the Weddell Gyre, where sea-ice cover is a more prominent feature regardless of season, and strongest along the coast between 0 and 30° E. That the entire region shows positive vertical fluxes results from two factors: (1) the mean Ekman pumping velocity is

positive (indicating upwelling) throughout the Weddell Gyre (Fig. 5.2b), and (2) the upper boundary is colder than the lower boundary (Fig. 5.2b), which is a consequence of the vertical boundaries applied in this analysis. Positive vertical advection implies that more heat is entering the grid cell from below than is leaving the grid cell through the top, implying a convergence of heat within that layer, unless it is removed through other mechanisms such as mean horizontal advection or turbulent diffusion.

Horizontal turbulent diffusion (Fig. 5.5c) is characterised by a positive signal of about 0-40 Wm^{-2} within the interior circulation cell (i.e. within the red streamlines in Fig. 5.5c), and a negative signal along the southern limb of the gyre in the range of 20 - 60 Wm^{-2}, with the exception of local patches of heat flux convergence such as over Maud Rise and just north of Astrid Ridge at ~10°E (topographic features are marked in Fig. 5.1). The northern limb of the Weddell Gyre is mostly positive, (40-80 Wm^{-2}), though a strip of heat flux divergence sits directly north to this, in the northern boundary zone between the Weddell Gyre and the Antarctic Circumpolar Current.

As with mean vertical advection, vertical turbulent diffusion (Fig. 5.5d) exhibits a uniform sign throughout the Weddell Gyre, with negative values in the range of -2 to -7 Wm^{-2}. The strongest values are found in the southern limb, east of the Prime Meridian (~ -7 Wm^{-2}), as well as just west of Maud Rise. There also appears to be slightly enhanced vertical turbulent diffusion along the gyre axis between about 10°E and 20°W, in comparison to the two circulation cells.

The heat tendency resulting from the sum of the heat budget terms is provided in Fig. 5.5e. There is a patchwork of negative (cooling) and positive (warming) values throughout, spatially similar to the heat flux due to mean horizontal advection in Fig. 5.5a.

The depth-averaged temperature, Θ_{ave}, for the layer corresponding to the heat budget terms in Fig. 5.5 is provided in Fig. 5.6. The spatial distribution of temperature is very similar to Θ_{max} in Fig. 5.1, with lower over-all magnitudes, as is to be expected since this is the mean temperature over a layer thickness of 1000 m. There is a gradual decrease in temperature from east to west in the southern limb, and there appears to be a northward spreading of warmer waters west of the eastern circulation core, and west of the western circulation core, indicative of mean advective pathways of heat.

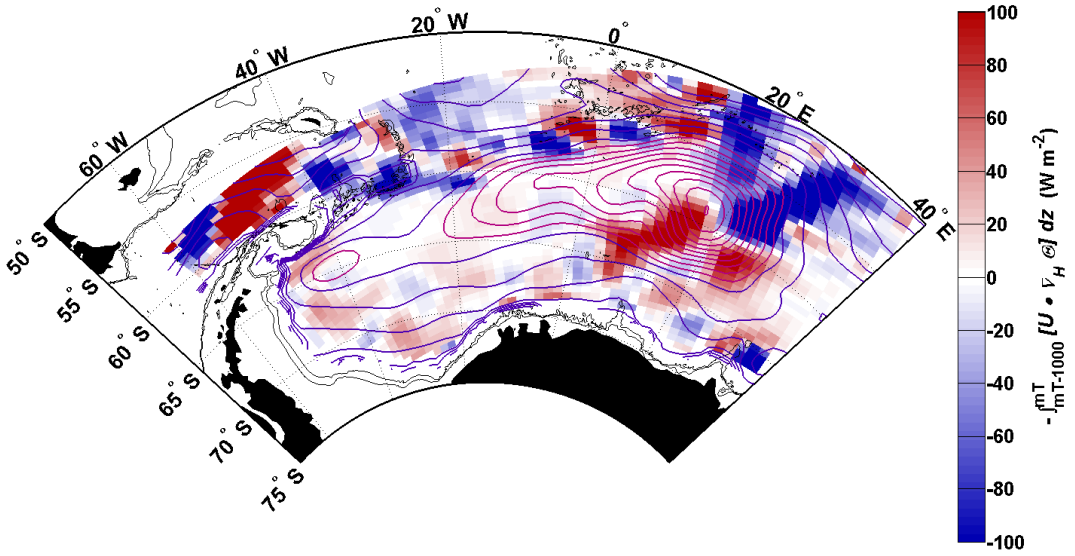
20° W
0°
40° W
20° E
60° W
40° E
50° S
55° S
60° S
65° S
70° S
75° S
100
80
60
40
20
0
-20
-40
-60
-80
-100
$-\int_{mT-1000}^{mT} [U \bullet \nabla_H \Theta] dz$ (W m^{-2})

(5.5a)

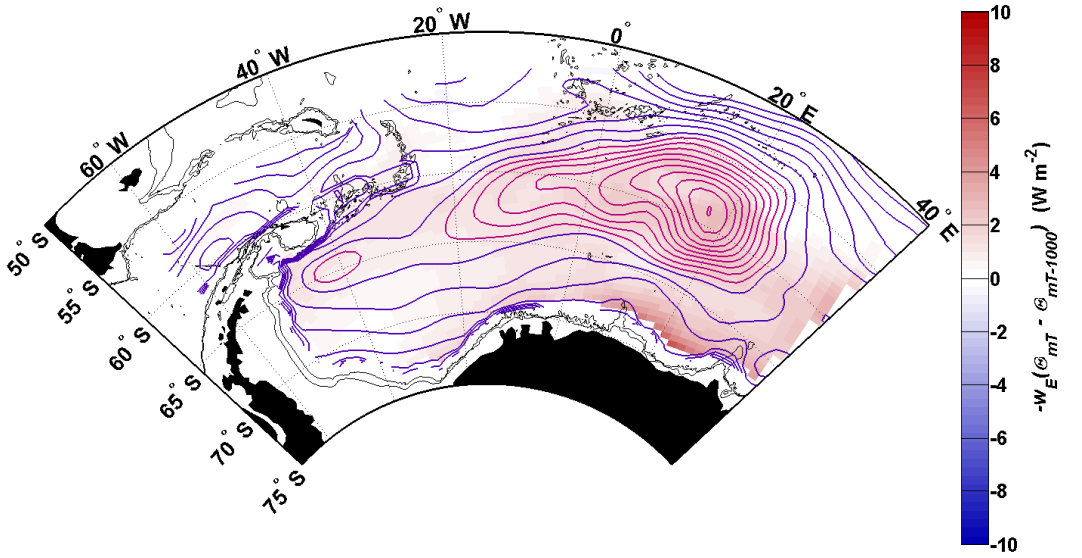
20° W
0°
40° W
20° E
60° W
40° E
50° S
55° S
60° S
65° S
70° S
75° S
10
8
6
4
2
0
-2
-4
-6
-8
-10
$-w_E(\Theta_{mT} - \Theta_{mT-1000})$ (W m^{-2})

(5.5b)

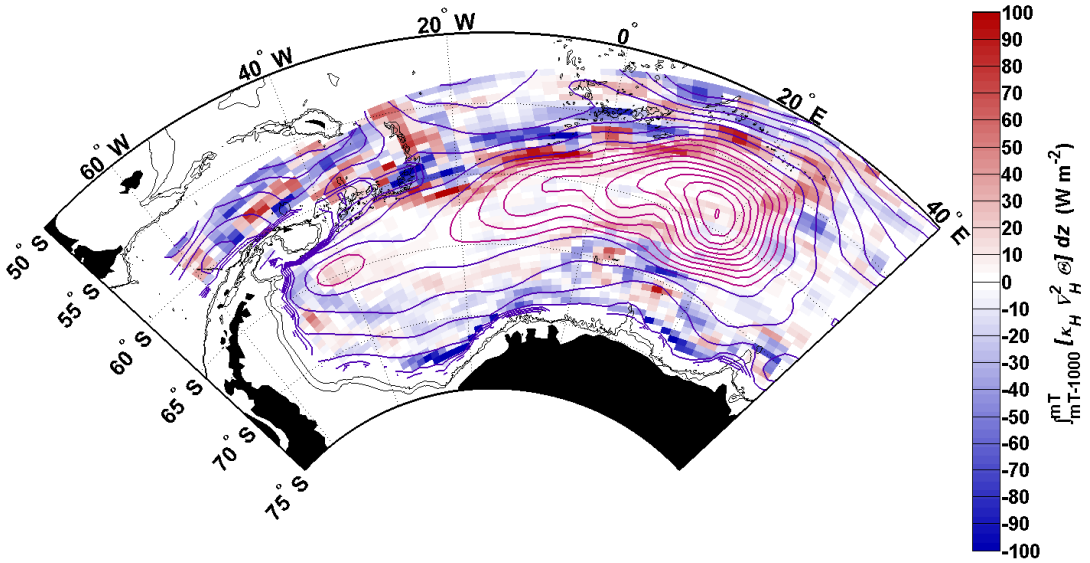
20° W
0°
40° W
20° E
60° W
40° E
50° S
55° S
60° S
65° S
70° S
75° S
100
90
80
70
60
50
40
30
20
10
0
-10
-20
-30
-40
-50
-60
-70
-80
-90
-100
$\int_{mT-1000}^{mT} [\kappa_H \nabla_H^2 \Theta] dz$ (W m^{-2})

(5.5c)

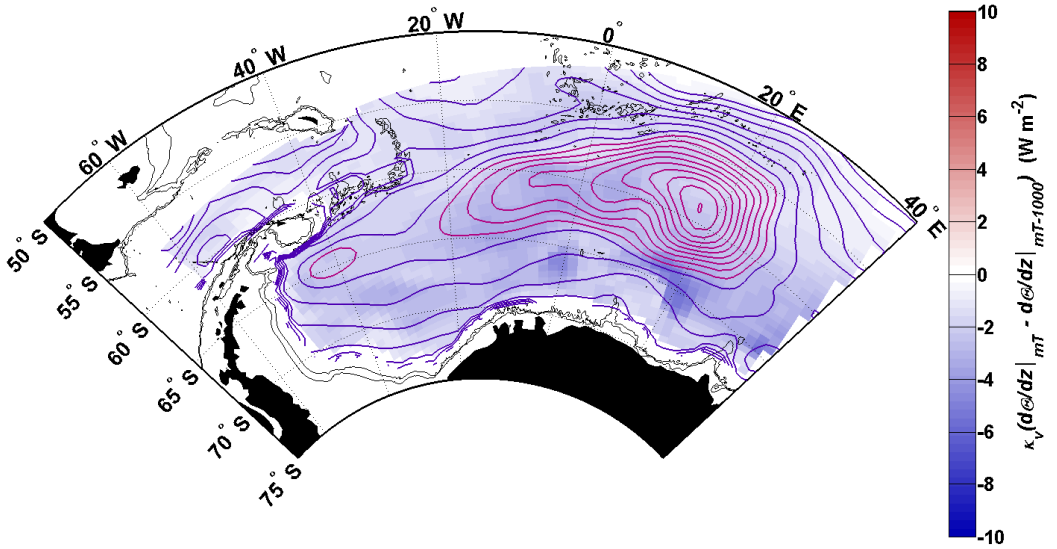

(5.5d)

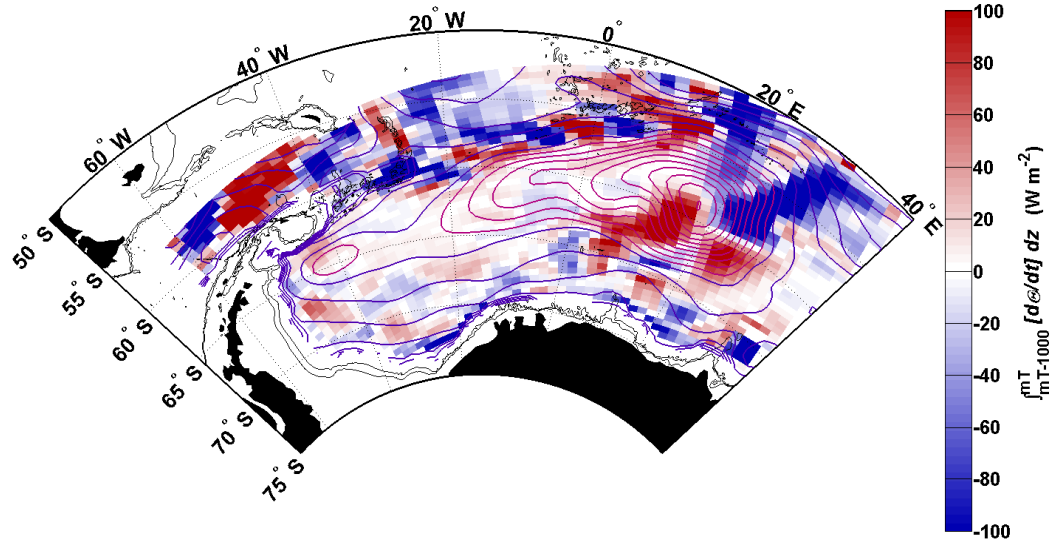

(5.5e)

Figure 5.5. The heat budget terms from Eq. 1, for a volume of water 1000 m thick from the depth of the mid-thermocline: **(a)** mean horizontal geostrophic heat advection, **(b)** mean vertical advection, **(c)** horizontal turbulent diffusion **(d)** vertical turbulent diffusion and **(e)** the heat tendency, which is the sum of the terms in a-d. The contours are as in Fig. 5.1. Positive values indicate warming, i.e. heat transport convergence, where more heat is entering the grid cell than is leaving it.

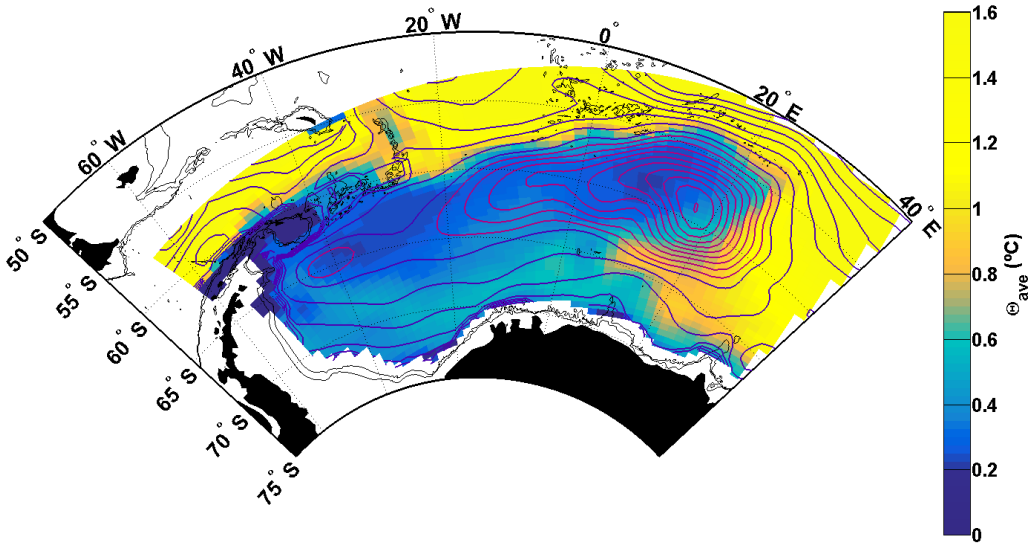

Figure 5.6. Depth averaged temperature for the same vertical limits in Fig. 5.5. The contours are as in Fig. 5.1.

5.4.2 Part 2: zonal variation in the heat budget and temperature

In this section, we provide an analysis of the zonal variation of the heat budget in the Weddell Gyre. We first focus on the southern limb of the gyre, with the northern boundary being the streamline that separates the southern limb of the gyre from the interior circulation zone and the southern boundary being the southernmost streamline that does not break into the coastline (the southern limb region is filled with colour in Fig. 5.7a). This enables us to focus on the water that circulates the entire zonal extent of the gyre, thus reaching into the south-western interior (Fig. 5.7a). Table 5.1 provides a list of the abbreviations for the terms presented in Figs. 5.7 to 5.10.

The area- weighted mean (i.e. the mean of each x-column of data) of the sub-surface temperature maximum (Θ_{max}), depth-averaged temperature from mT to mT-1000 (hereon referred to as Θ_{ave}), and the depth-averaged temperature for WDW (Θ_{WDW}, defined by neutral density limits 28.0 and 28.27 kg m^{-3}) were calculated to show the zonal variation in mean temperature for the southern limb of the gyre (Fig 5.7b). There is a gradual decrease in temperature from east to west, with a drop in the temperature of about 0.3 °C over Maud Rise at ~3° E (Fig. 5.7b). Downstream of Maud Rise, the temperature rises slightly, by ~0.15 at 0° E, before continuing to decrease westwards. A patch of relatively cold water is also found over Maud Rise in Fig. 5.1.

West of 30° W, there is no obvious change in temperature. While the changes in temperature are strongest at Θ_{max}, the pattern of temperature change is mirrored in both Θ_{ave}, and Θ_{WDW}. There is an overall decrease from east to west of 0.7, 0.5 and 0.25 °C for Θ_{max}, Θ_{ave} and Θ_{WDW} respectively.

The zonal variation of the heat budget terms along the southern limb of the Weddell Gyre are presented in Fig. 5.7c (Wm^{-2}), while the cumulative sum from east to west of the heat budget terms are provided in Fig. 5.7d (in Terrawatts, 1 TW = $1x10^{12}$ Watts). The presence of Maud Rise appears to result in a spike in mean horizontal advection, and to a lesser extent, horizontal turbulent diffusion. In Fig. 5.7c, mean horizontal advection increases by ~50 Wm^{-2} just east of the Maud Rise seamount (from 10° to 7° E), and then sharply decreases by 80 Wm^{-2} from 7° E to the Prime Meridian. This regional pattern strongly dominates the heat tendency (i.e. the sum of the heat budget terms) in Fig. 5.7c. The effect of Maud Rise is also visible in Fig. 5.7d, where it results in an increase in mean horizontal advection of 10 TW from 10° to 5° E, after which a small decrease of ~3 TW occurs from 5° E to the Prime Meridian. This influences the heat tendency (sum of the heat budget terms), which increases from 0 to ~8 TW, and then decreases to ~4 TW over the same longitudinal range. West of the Prime Meridian, mean horizontal advection steadily increases throughout, resulting in a total contribution of +26 ± 1 TW to the heat budget (Table 5.2). Mean vertical advection and vertical turbulent diffusion appear relatively small and invariant throughout, and seem to cancel each other out by 50 %, contributing to the heat budget by +3.4 ± 0.2 and -7.2 ± 6.7 TW respectively, where the uncertainty provided is described in Section 5.2. Horizontal turbulent diffusion shows some zonal variation in Fig. 5.7c, albeit to a lesser extent than mean horizontal advection. Overall, the horizontal turbulent diffusion nearly balances with mean horizontal advection, especially when taking into account the range of possible values the diffusivity parameter may take, i.e. the heat tendency is +3.1 ± 12 TW (see Table 5.2).

Table 5.1. Explanations of the abbreviations used in Fig. 5.7-5.8.

Term	Description
$\mathbf{A_H}$	Mean horizontal geostrophic heat advection
$\mathbf{A_V}$	Mean vertical heat advection
$\mathbf{D_H}$	Horizontal turbulent diffusion
$\mathbf{D_V}$	Vertical turbulent diffusion
$\overline{\mathbf{d\Theta/dt}}$	Heat tendency (i.e. the sum of the heat budget terms in Eq. 1).
Θ_{max}	Area-weighted mean of sub-surface temperature maximum for the filled (i.e. coloured surface plot) region in Fig. 5.7-5.9(a).
Θ_{ave}	Area-weighted mean of depth-averaged temperature for the filled (i.e. coloured surface plot) region in Fig. 5.7-5.9(a).
Θ_{WDW}	Area-weighted mean of WDW temperature for the filled (i.e. coloured surface plot) region in Fig. 5.7-5.9(a).

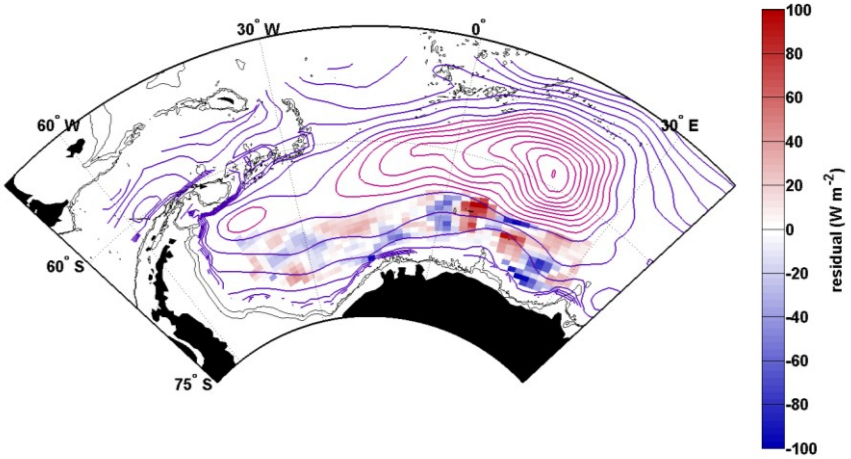

(5.7a)

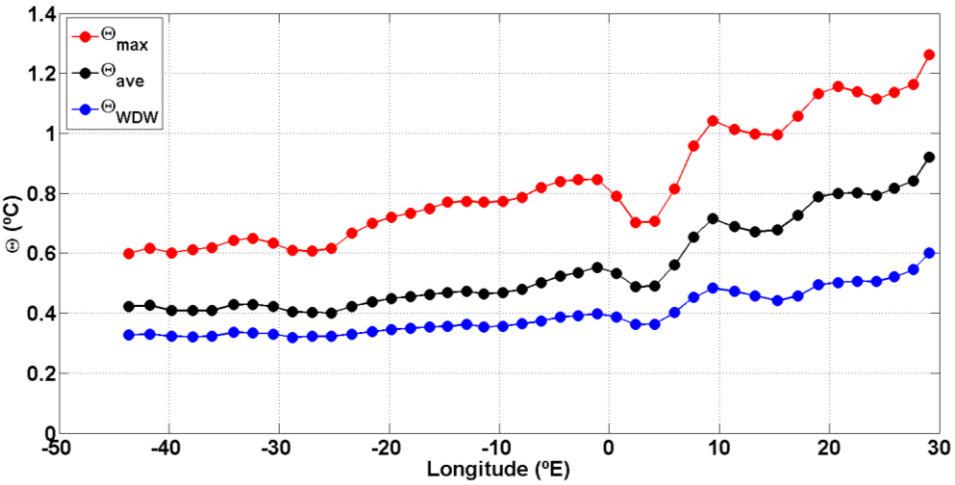

(5.7b)

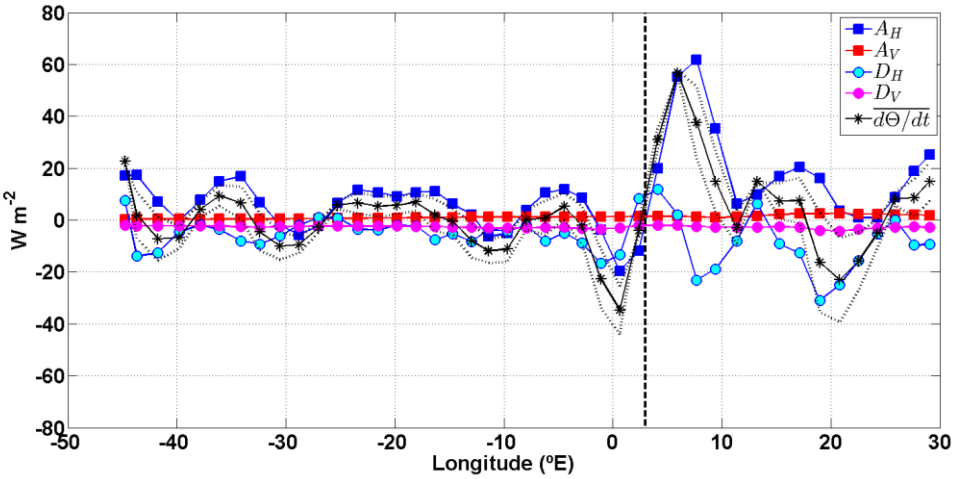

(5.7c)

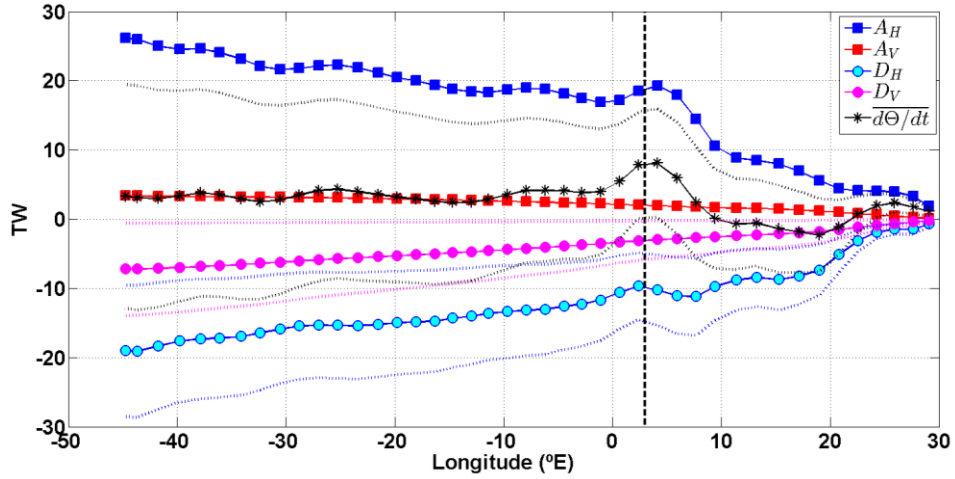

(5.7d)

Figure 5.7. **(a)** map of heat tendency, showing only the southern limb of the gyre, the region for which the following is estimated: **(b)** the zonal variation of the depth-averaged, meridional-averaged temperature, **(c)** the heat budget terms in Wm^{-2} and **(d)** the cumulative heat budget terms in Terawatts (TW; d). In panel **(b)**, Θ_{max} (red), Θ_{ave} (black) and Θ_{WDW} (blue) are provided. For panels **(c)** and **(d)**, the key for the legend is listed in Table 5.1.The dashed vertical line marks the approximate longitude of Maud Rise, at 3º E.

Table 5.2. Total heat budget contribution (TW) of the different terms in Eq. 1 for the southern limb of the Weddell Gyre (Fig. 5.7a), and an estimate of temperature change (dT/dt), using a timescale of 14 years, and the change in Θ_{ave} from east to west. The uncertainties for the turbulent diffusion terms provide a range of estimates based on a range of values for the diffusivity terms, κ_H and κ_v.

Heat Budget Term (southern limb)	**Wm^{-2}**	**Total (TW) (temperature: °C)**
Mean Air-Sea flux	-1.7	-4.6
Mean horizontal advection	+9.8 ± 0.35	+26 ± 1
Mean vertical advection	+1.3 ± 0.07	+3.4 ± 0.2
Horizontal turbulent diffusion	-7.1 ± 3.8	-19.1 ± 10.2
Vertical turbulent diffusion	-2.7 ± 2.5	-7.2 ± 6.7
Heat tendency (sum of the heat budget terms)	+1.2 ± 4.6	+3.1 ± 12
Temperature tendency over 14 years		+ 0.13 ± 0.5 °C or +0.0095 ± 0.035 °C/yr
Depth-averaged zonal temperature decrease (Θ_{ave})		0.5 ± 0.01 °C

We next shift our attention to the interior circulation cell of the Weddell Gyre, which is defined as the region in which the streamlines form a closed circuit, as indicated by the coloured region in Fig. 5.8a. Regarding the zonal variation in mean temperature (Fig. 5.8b), there is an initial sharp decrease from 30 to 20° E, from 1.6 to 0.8 °C for Θ_{max}, from 1.3 to 0.6 °C for Θ_{ave}, and from 0.9 to 0.4 °C for Θ_{WDW}. West of 20 °E, the temperature decreases further, from ~0.8 to ~0.4 °C at 30° W for Θ_{max}. West of 30° W, there is a slight increase in Θ_{max}, Θ_{ave} and Θ_{WDW}, of about 0.1 °C. The main drop in temperature west of 20° E occurs in the vicinity north of Maud Rise (3-8° E) and between ~15 and 30° W. Between 0 and 20° W in Figs. 5.1 and 5.6, there is a patch of relatively warm water, which appears to be spreading northwards, which coincides with the slightly raised but uniform Θ_{max} in Fig. 5.8b, as observed between the two troughs discussed above. The temperature increase west of 40° W can also be identified in Figs. 5.1 and 5.6, where relatively warm water circulates northwards around the colder western circulation core.

East of the Prime Meridian, there are large positive and negative deviations from zero in the mean horizontal advection term (Fig. 5.8c), initially spiking to -65 Wm^{-2} before climbing up to 60 Wm^{-2}, occurring west of 10° W. The peaks and troughs reduce

in magnitude west of the Prime Meridian. This is reflected in the cumulative sum of the heat budget terms in Fig. 5.8d, where mean horizontal advection dominates the heat tendency east of the Prime Meridian. As a result of mean horizontal advection, the heat tendency initially decreases to -70 TW at ~15° E before returning to zero at the Prime Meridian (Fig. 5.8d). West of the Prime Meridian, a sharp decrease followed by a sharp increase occurs between 0 and 10° W in Fig. 5.8c, after which a gradual increase in the heat tendency is observed in Fig. 5.8d, resulting in an overall gain of 6 ± 31 TW (Table 5.3. The error is described in Section 5.2, and is mainly due to the ascribed ranges in horizontal and vertical diffusivity). While the mean horizontal advection term dominates the heat budget east of the Prime Meridian, horizontal turbulent diffusivity plays a more important role west of the Prime Meridian, in balancing with the mean horizontal advection term. Horizontal turbulent diffusivity gradually increases in Fig. 5.8d, resulting in a net contribution of +51 ± 26 TW, while mean horizontal advection provides a net loss of -37 ± 6.4 TW (Table 5.3). The vertical terms are invariant throughout (Fig. 5.8c), and, after taking into account the possible range of values for κ_v, the terms more or less balanced (Table 5.3 and Fig. 5.8d).

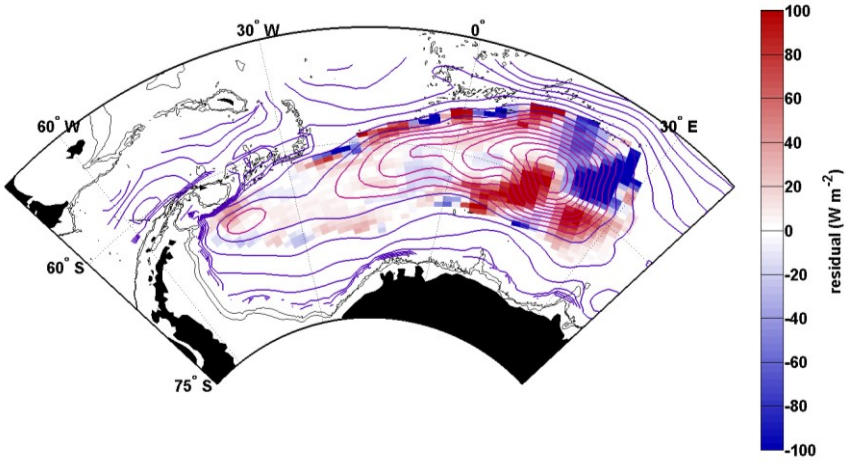

(5.8a)

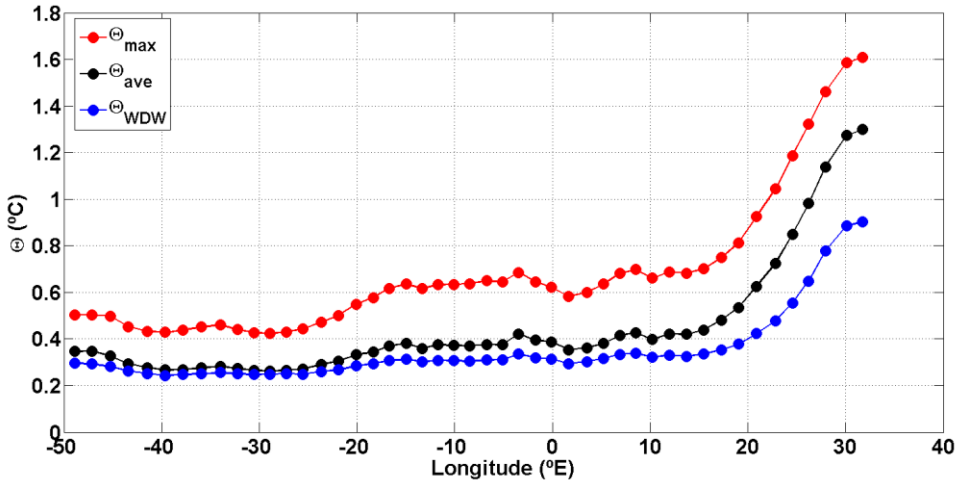

(5.8b)

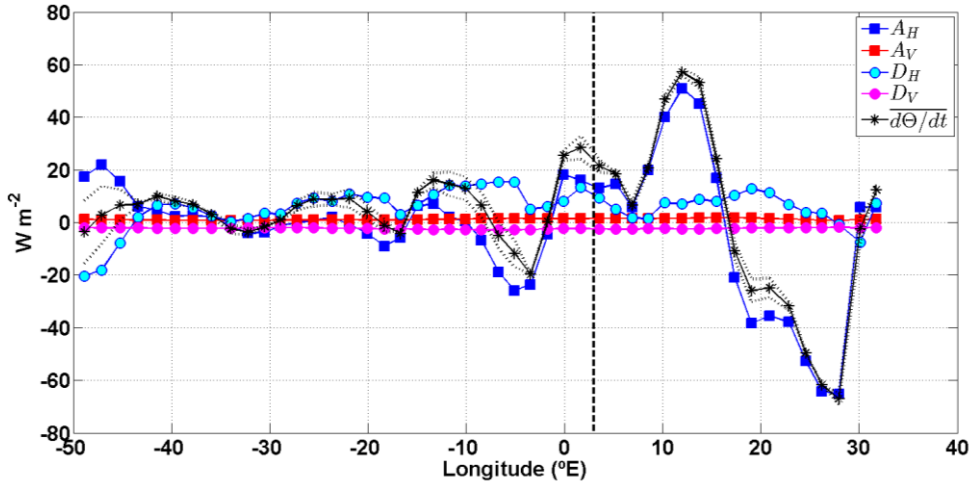

(5.8c)

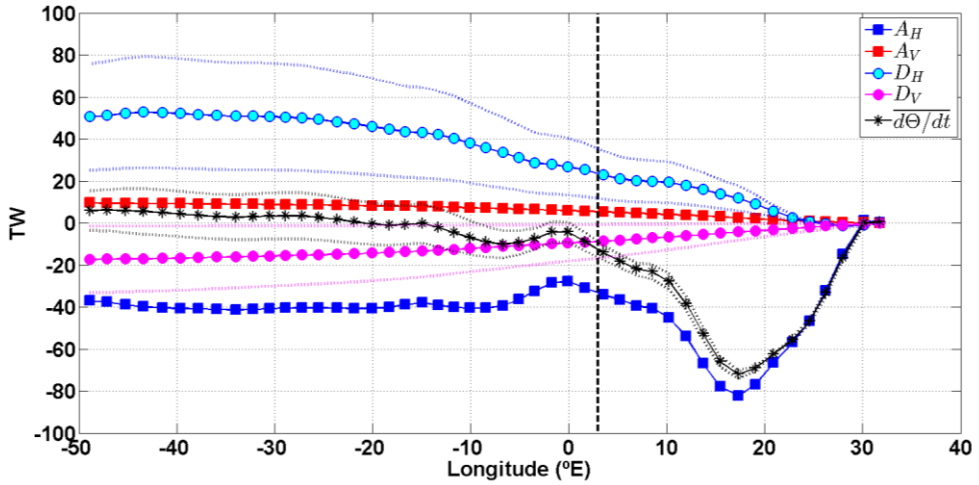

(5.8d)

Figure 5.8. As in Fig. 5.7, but for the interior circulation cell of the Weddell Gyre, as shown in panel **(a)**.

Table 5.3. Total heat budget contribution (TW) of the different terms in Eq. 1 for the interior circulation zone of the Weddell Gyre (Fig. 5.8a), and an estimate of temperature change (dT/dt), using a time period of 14 years, and the change in Θ_{ave} from east to west.

Heat Budget Term (interior circulation cell – enclosed streamlines)	**W m^{-2}**	**Total (TW) (temperature: °C)**
Mean Air-Sea flux	+8	+60
Mean horizontal advection	-4.9 ± 0.85	-37 ± 6.4
Mean vertical advection	+1.3 ± 0.13	+10 ± 1
Horizontal turbulent diffusion	+6.8 ± 3.4	+51 ± 26
Vertical turbulent diffusion	-2.3 ± 2.1	-17 ± 16
Heat tendency (i.e. sum of the heat budget terms)	+0.81 ± 0.55	+6 ± 31
Temperature tendency over 14 years		+ 0.09±0.45 °C or 0.006±0.032 °C/yr
Depth-averaged zonal temperature decrease (Θ_{ave})		0.95 ± 0.09 °C

5.5 Discussion

In this study, velocity and temperature derived from Argo floats were used to determine the heat budget of the Weddell Gyre, for a 1000 m thick layer of water extending from the mid-point of the thermocline, encompassing the core of the WDW layer.

5.5.1 Study limitations

Before interpreting the results, several limitations of the study require discussion. The first challenge, regarding vertical boundary limits, was already addressed in Section 5.2.1. Since the Argo float data were objectively mapped as a snapshot data set, incorporating all available data within the Weddell Gyre, the upper 50 dbar were omitted from the profiles prior to mapping, to avoid the highly seasonally varying surface waters. Generally, the heat budget is integrated to the surface, requiring the inclusion of the net surface heat flux term (Qnet) in the heat budget equation, so that the role of heat loss/gain through the surface of the ocean is an integral component to the heat budget. In this study, we remove the surface heat fluxes completely. Since we are

interested in the distribution of heat throughout the Weddell Gyre (which is primarily found within the core of WDW), we applied boundary conditions which ensures the Winter Water layer (defined by its temperature-salinity minimum) is not included within the layer, and the core of WDW (i.e. Θ_{max}) is fully included within the layer. The vertical boundary conditions allow us to consider the varying depths at which we find different water masses, while also avoiding bias by fixing the thickness of the vertical layer. However, this may introduce some noise into the analysis from grid cell to grid cell, owing to the different depths of the water column the heat budget is integrated over. This may partly explain why there is noise in the maps in Section 5.4.1, and in Figs. 5.7c and 5.8c, while the noise cancels out in Figs. 5.7d and 5.8d. The implication is that our heat budget analysis is reasonable on large-scales, but would introduce considerable noise when assessed on local-scales (which indeed is the case, as revealed by additional analyses not included in this paper).

Another limitation in the study is a suitable estimate for vertical velocity. Vertical Ekman pumping velocity is used to represent vertical velocity, which is constant with depth (Section 5.3.2). However, reanalysis products are also limited in their accuracy, largely due to lack of in-situ data in the Southern Ocean. Vertical velocity is positive (indicating upwelling) throughout the whole of the Weddell Gyre, with the exception of alongside the Antarctic Peninsula. Due to the cyclonic nature of the Weddell Gyre, some downwelling is expected along the periphery of the gyre. This is not revealed by the 2002-2016 wind-stress derived mean. However, there is considerable monthly variation in Ekman pumping velocity, with large downwelling zones found in various regions throughout the Weddell Gyre. It is thus possible that, while overall upwelling dominates the region, frequent pulses of downwelling may also have an important impact in the heat budget, which is unresolved in this study. Additionally, vertical velocities resulting from eddies, fronts and along steeply sloping bathymetry are not taken into account in this study, which might be important in resolving the mean vertical advection of the upper ocean. However, since we derive the horizontal velocity field from the stream function, we assume that the system is non-divergent (a mathematical requirement for deriving the stream function). Therefore, we can expect that vertical advection would play a minor role in the heat budget in this study.

The work presented within this paper is based on a long-term mean gridded dataset derived from Argo floats between 2002 and 2016. Therefore, without a time

component within the objective mapping method applied (Section 5.3.1), we are unable to directly incorporate an eddy component into the analysis, which requires fluctuations from the mean temperature and velocity. Thus, we rely on parameterised eddy-influences by using the concept of horizontal turbulent diffusion. Unresolved eddying fluctuations are most likely to be an important factor when assessing the heat budget east of the Prime Meridian in the Weddell Gyre, a region we know is dominated by a mesoscale eddy field (e.g. Leach et al., 2011; Ryan et al., 2016). Meanwhile, within this study, we rely on the parameterization of eddy-influences through the estimation of horizontal turbulent diffusion, and the parameterization of vertical instabilities through the estimation of vertical diffusion. The two diffusion terms include unknowns in Eq. 1, horizontal and vertical diffusivity, κ_H and κ_v respectively, which deliver considerable uncertainty to this study. Horizontal diffusivities are scale dependent (Okubo, 1971; Ledwell et al., 1998), and therefore require some decision regarding the length scales. Ledwell et al (1998) demonstrate the importance of length scales by estimating values of 2 m^2 s^{-1} for length scales of 1-10 km, and as much as 1000 m^2 s^{-1} for length scales of 30-300 km. For the entire Southern Ocean, Zika et al. (2009) estimate a value of 300 ± 150 m^2 s^{-1}. Within the Weddell Gyre, Leach et al. (2011) provide estimates of κ_H and κ_v derived from observations in the Maud Rise region, and estimate κ_H to be in the range of 70 - 140 m^2 s^{-1}. Leach et al. (2011) consider their estimate for κ_H appropriate, albeit on the low side, for mesoscale eddies. Also in the Weddell Gyre, Donnelly et al. (2017) provide estimates derived from observations on a larger scale than that of individual eddies, where κ_H is estimated as 247 ± 63 m^2 s^{-1}. Cole et al. (2015) use salinity anomalies from Argo floats and velocity fluctuations from the ECCO2 product (Menemenlis et al., 2005, 2008) to investigate horizontal mixing and the associated length scales. In Fig. 4 in Cole et al. (2015), at about 50 to 60° S in the Atlantic Ocean (the most southerly extent of the authors analysis resulting in omitting the Weddell Gyre), the estimated values of κ_H range from $10^{2.3}$ to $10^{3.3}$ m^2 s^{-1} (or, 200 to 2000 m^2 s^{-1}) in the depth range of 0 to 2000 m. In this study, we are focused on the large-scale, and have a grid of data representative of the long-term mean from 2002-2016. Our grid cell resolution varies slightly with changing latitude (for further details, see Reeve et al., in review), but is on the order of ~80 x 60 km, which is nearly double the station spacing of 55 km in Leach et al. (2011). We make the decision to provide three different estimates for horizontal diffusivity, in the range of that provided by Donnelly et al.

(2017), Zika et al. (2009) and Cole et al. (2015), of 200, 400 and 600 $m^2\ s^{-1}$ (the ranges from which are provided as dotted lines in Figs. 5.7-5.12).

Leach et al. (2011) provide particularly small estimates for κ_v, of 3 x 10^{-6} $m^2\ s^{-1}$ for the core of WDW, which they suggest is due to the timing of the survey – having taken place late spring/early summer, when sea-ice had just melted, and the wind had not yet had time to stir up the water column. Other studies provide larger estimates for κ_v, for various regions throughout the global ocean. Donnelly et al. (2017) estimate κ_v as 2.39 ± 2.83 x 10^{-5} $m^2\ s^{-1}$. Over rough topography, such as in the Brazil basin, Ledwell et al. (2000) provide an estimate for κ_v of 3 x 10^{-4} $m^2\ s^{-1}$. In the deep ocean however, Polzin et al. (1997) and Ledwell et al. (1998) estimate κ_v to be about 1 x 10^{-5} $m^2\ s^{-1}$. Naveira Garabato et al. (2004a, 2004b, 2007) provide larger numbers for deep water in the Scotia Seas of 3 x 10^{-4} to 1 x 10^{-2} $m^2\ s^{-1}$, which they attribute to breaking internal waves. Also within the Southern Ocean, Cisewski et al (2005, 2008) acquired 7 x 10^{-4} $m^2\ s^{-1}$ in the upper pycnocline of the Antarctic Circumpolar Current at 20° E and Forryan et al. (2013) obtained a value of 18.8 x 10^{-6} $m^2\ s^{-1}$ based on observations in close proximity to a vigorous frontal system between 60 and 80° E, at the northern edge of the Kerguelen Plateau.

Initially, we attempted to estimate κ_v through the use of the Richardson Number, following Forryan et al. (2013). The Richardson Number is defined as the ratio of buoyancy frequency (N) squared to vertical shear squared, and is often used to describe the stability of stratified shear flow. Forryan et al. (2013) provide a Richardson Number parameterisation that delivers estimates of vertical diffusivity in stratified shear flow associated with mesoscale eddies and fronts. For large Richardson Numbers, the resulting diffusivity tends towards a background diffusivity coefficient provided by the authors. In the Weddell Gyre, the circulation is mostly barotropic, and so the vertical shear is small, leading to large Richardson Numbers, especially when one is focused on the long-term mean. Thus, with this method, the resulting diffusivity tends back towards a background diffusivity parameter. Hence, based on the range of values available from the literature, we made the decision to provide three estimates of vertical diffusivity, of 2 x 10^{-4}, 2.6 x 10^{-5}, and 5 x 10^{-5} $m^2 s^{-1}$. The range of resulting vertical diffusivity estimates are presented as dotted lines in Figs. 5.7-5.8.

An obvious way to improve the robustness of the results presented in the paper is therefore obtaining adequate estimates for the isopycnal and diapycnal diffusivity,

which are not assumed to be spatially constant, both horizontally and vertically, unlike in this study. There are ways to estimate horizontal diffusivity from Argo floats, as demonstrated by Cole et al. (2015). The horizontal diffusivity range in Fig. 4 of Cole et al. (2015) provided guidelines for the values we arbitrarily prescribe in our analysis (though the upper range in this study is only 600 $m^2 s^{-1}$, since we are not focussed on the more dynamic Antarctic Circumpolar Current just to the north of the Weddell Gyre). Future work to improve the current knowledge of the heat budget in the Weddell Gyre requires adding to the existing knowledge of turbulent diffusivity within the gyre, and Argo floats provide us with an excellent opportunity to do so, by providing information about the water column every 10 days, from which temperature and salinity anomalies on isopycnal surfaces can be obtained, along with corresponding velocity fluctuations derived from float trajectories.

With improved diffusivities we can reduce the error estimated for the zonal variation in the heat budget, where the range in diffusivities results in especially large error estimates for the interior circulation cell in Section 5.4.2. We can also improve the estimate of uncertainty by including further perturbations to the heat budget and obtaining a mean deviation from the non-perturbed state, as described in Reeve et al. (in review). So far the error has only been determined based on a single perturbation, which is established using a velocity field derived from (1) Argo float trajectory data that has not been corrected for horizontal surface drift, and (2) gridded Argo profile data, where we determine density from gridded temperature and salinity plus their respective mapping errors. The perturbation is also established by the temperature field, which is adjusted by adding the objective mapping error to the gridded temperature. This means that the total error is also representative of the length scales applied in the objective mapping (Reeve et al., 2016). In Reeve et al. (2016), the length scales were assigned based on an investigation which showed that 95 % of the grid points have at least 40 Argo profiles within a distance of 500 km, which was thus the length scale applied in the second stage of the objective mapping, along with a fractional scale on the effect of f/H, which alters the shape of the area of influence about a grid point from circular (i.e. when the bottom bathymetry is flat) to elongated (i.e. especially when a grid point is in close proximity to changing bathymetry. See Figs. 8-10 in Reeve et al., 2016, for further explanations on the length scales applied). Since the focus is a climatological mean from 2002 to 2016, large length scales are chosen to represent the large-scale field of

the entire Weddell Gyre (Reeve et al., 2016). The resulting mapping errors are large in regions where bathymetry is complex and data coverage is sparse, and low in regions where the bathymetry is flat or where data density is high. Thus, in the perturbation, regions where the heat budget is perturbed the most includes the northern periphery of the gyre, where data are relatively abundant but the bathymetry is complex, and the western edge of the Weddell Gyre, where data is sparse (Fig. 5.9).

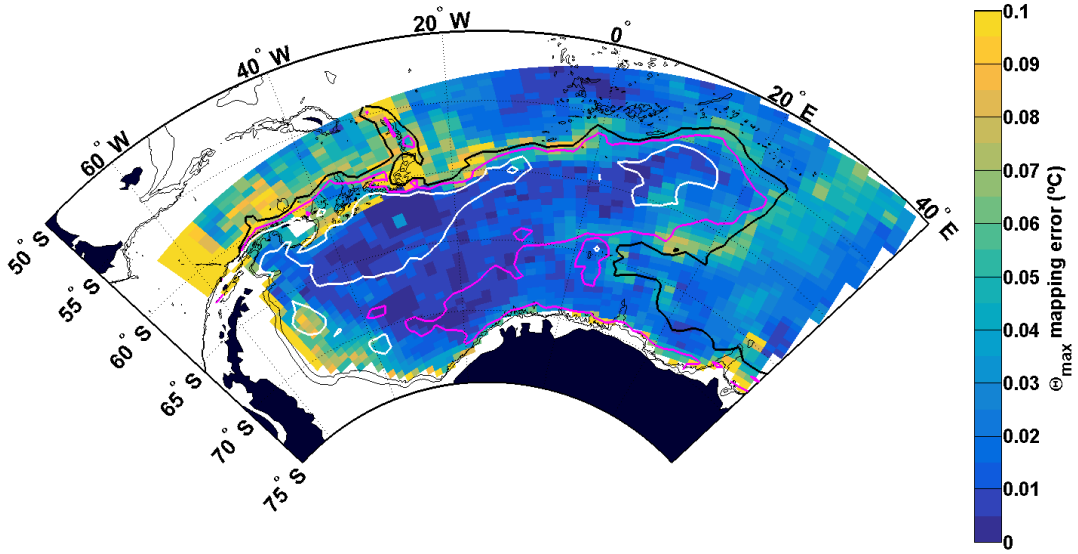

Fig. 5.9. Mapping error for Θ_{max} (ºC). The gridded Θ_{max} field is shown in Fig. 5.1. The white, magenta and black contours show the 0.5, 0.8 and 1.1 ºC isotherms respectively. The grey contours are as in Fig. 5.1.

5.5.2 The Weddell Gyre heat budget

In most regions of the Weddell Gyre, for the core of WDW, the terms dominating the heat budget are mean horizontal geostrophic advection (Fig. 5.5a), and horizontal turbulent diffusion (Fig. 5.5c). For the most part, mean vertical advection is virtually negligible, which could in part be due to the assumption of geostrophic flow, which is derived from a non-divergent stream function. Vertical turbulent diffusion is the dominant vertical term (Fig. 5.5d), where heat is diffused upwards through the thermocline.

While there is a lot of noise, particularly in Figs. 5.5a and 5.5c, the heat budget closes within uncertainty defined by the ranges in diffusivity used in Section 5.2, when

integrated over a large spatial scale. For both the southern limb of the Weddell Gyre (Fig. 5.7), and the interior circulation cell defined by the fully enclosed streamlines in Fig. 5.8a, there is a balance between the mean horizontal geostrophic advection and the horizontal turbulent diffusivity. The vertical terms provide smaller contributions to the heat budget, which may be a result of assuming non-divergent flow and avoiding the surface mixed layer. When integrating over smaller regions, the heat budget does not close (not shown, although indicated by Fig. 5.5e), indicating that noise is cancelled when integrating over larger areas. The noise is likely a result of (1) discrepancies in the depth range from grid cell to grid cell, (2) the nature of differentiating across grid cells, and (3) due the presence of mesoscale eddies not resolved by the data grids used. The latter is particularly important east of the Prime Meridian. East of the Prime Meridian, there appears to be a lot of noise, where mean horizontal geostrophic advection shows its largest convergence and divergence values (Fig. 5.5a). This could be due to unresolved eddy fluxes, since Gordon and Huber (1984), Leach et al. (2011), and Ryan et al. (2016) have shown the eastern inflow area of the Weddell Gyre to be a region dominated by a dynamic eddy field. This region is of particular dynamic interest: it is the region where interactions can occur between the so-called “warm-regime” WDW and the “cold-regime” WDW (Gordon and Huber, 1984). The “warm-regime” WDW is relatively warm WDW advected into the gyre at the eastern inflow zone at about 30° E, driven by mesoscale eddies (Deacon 1979; Orsi et al. 1993; Orsi et al. 1995; Gouretski and Danilov 1993, 1994; Ryan et al., 2016), whereas the “cold-regime” WDW is the colder WDW that has been recirculating within the central Weddell Gyre and has been modified primarily through heat loss (e.g. Gordon and Huber, 1984). The patches of strong positive and negative mean horizontal advection in the region suggests that strong eddy interaction may play an important role in this area, which is not resolved by parameterization through the turbulent diffusion term, and thus may require the need for a time series analysis where the direct impact of fluctuations from the mean state can be considered.

The noise to the east of the Prime Meridian is also revealed in the zonal variation of the integrated heat budgets for the southern limb and recirculation cell of the Weddell Gyre, in Figs. 5.7c and 5.8c respectively. However, the zonal variation cancels out and results in a smoothed field when integrating zonally (Figs. 5.7d and 5.8d respectively). West of the Prime Meridian, the zonal variation is considerably smaller, and, for the

zonally integrated heat budget of the interior circulation cell in Fig. 5.8d, the variation in mean horizontal advection is negligable between 10 and 40° W.

Maud Rise, a submersed seamount at 3º E, 65º S, is prominent feature in temperature (Figs. 5.1 and 5.6; Θ_{max} and Θ_{ave} respectively), mean horizontal advection (Fig. 5.5a), horizontal turbulent diffusion (Fig. 5.5c) and to a lesser extent, vertical diffusion (Fig. 5.5d). It also stands out as a feature that perturbs the zonally depth-averaged temperature and the integrated heat budget terms in Fig. 5.7. The effect of Maud Rise in temperature is due to the presence of a Taylor column directly over Maud Rise, which has been previously observed as a stagnant column of cold water surrounded by a warm halo on the flanks of Maud Rise (e.g. Muench et al., 2001; Leach et al., 2011). Regarding the heat budget in Fig. 5.7, mean horizontal advection results in a heat flux convergence upstream of Maud Rise, which is partially balanced by heat flux divergence due to horizontal turbulent diffusion. In contrast, downstream of Maud Rise, heat flux divergence occurs due to both mean horizontal advection and horizontal turbulent diffusion in Fig. 5.7c. The effect of mean horizontal advection on the flanks of Maud Rise is probably due to the inadequate resolution of the gridded dataset, in particular of the velocity field, in resolving the localised flow around Maud Rise. Since the water overlying Maud Rise is cold, and the velocity field does not adequately resolve the flow circulating the seamount, the heat convergence upstream of Maud Rise and divergence downstream Maud Rise are likely caused by strong lateral temperature gradients between the water column overlying Maud Rise and the area surrounding it. The mean advective heat flux perturbs the overall heat tendency within the southern limb of the Weddell Gyre. However, the effects of mean horizontal advection upstream and downstream of Maud Rise partially cancel each other when integrating zonally in Fig. 5.7d. Furthermore, horizontal turbulent diffusion acts to balance the influence of mean horizontal advection upstream of Maud Rise (Fig. 5.7c). When zonally integrated, as provided in Fig. 5.7d (which smooths the noise seen in Fig. 5.7c), the overall heat tendency thus increases from 0 TW at 10° E to +8 TW at ~3° E (directly over Maud Rise), and then decreases to +4 TW west of 0° E.

To determine if Maud Rise contributes towards redistributing heat throughout the Weddell Gyre, a velocity field that can adequately resolve the flow around the Taylor column overlying Maud Rise is required. However, that turbulent diffusion results in heat flux divergence on the flanks of Maud Rise fits with the literature, which shows

that barooclinic instabilities on the flanks of Maud Rise are the source of recurrent eddies (Akimoto et al., 2006). Furthermore, Leach et al. (2011) and Ryan et al. (2016) have observed a merging of water properties downstream of Maud Rise, suggesting a mixing of WDW with modified recirculating WDW, which would explain the features observed in Figs. 5.7 and 5.8, where the variation is considerably smaller west of the Prime Meridian.

Direct comparison between the heat budget presented and the literature is not possible due to the novel nature of this research, owing largely to the restrictions in vertical boundaries applied, and the Weddell Gyre being substantially under-sampled. However, there are some similar studies that require mentioning here. Volkov et al. (2010) use a global ocean data synthesis product (from the ECCO2 project) to highlight the importance of the horizontal circulation in the poleward transport of heat in the Southern Ocean. Tamsitt et al. (2016) derive the heat budget for the upper 624 m derived from the Southern Ocean State Estimate (SOSE), and demonstrates that the geostrophic heat advection is an important term in the Atlantic sector of the ACC, where, in a seasonal time series, it more or less balances with the ageostrophic advection term. Both Volkov et al. (2010) and Tamsitt et al. (2016), as well as Dong et al. (2007), integrate to the surface, and highlight the importance of ageostrophic advection due to Ekman transport. Ageostrophic advection would be an important term to include if we were to integrate to the surface, which is excluded from our analysis. Tamsitt et al. (2016) suggests that vertical heat advection assumes a lesser role than geostrophic eddy heat fluxes, which act to warm the upper ocean in the Atlantic sector of the ACC. In our analyses, the vertical heat advection is also a minor contributing factor. However, we do not resolve the eddy component of the heat budget, and assume eddying fluxes are represented by horizontal turbulent diffusivity, which shows heat flux divergence on the northern side of the Weddell Gyre's northern boundary. Jullion et al. (2014) use an inverse model based on ship-based sections along 30º E to the coast and also along the northern periphery of the gyre at about 55-60º S and to diagnose the heat budget of full water column. Jullion et al. (2014) suggest that most of the heat advected into the Weddell Gyre occurs along the northern gyre periphery, rather than from the eastern periphery, and reaches the south-western Weddell Gyre through recirculation in the central Weddell Gyre, leading to an entrainment of heat into the Antarctic Slope Front (ASF). This analysis is not able to resolve localised features such

as the ASF, but there is an indication, especially from the streamlines, that recirculation of the eastern cell plays a role in the distribution of heat in the Weddell Gyre (Fig. 5.1).

According to Tamsitt et al. (2016) and Naveira Garabato et al. (2011), major topographic features result in a divergence of transient horizontal and vertical eddy heat fluxes, leading to substantial warming in association with regions of enhanced mesoscale energy, and Thompson & Salleé (2012) show that the enhancement of eddy kinetic energy (EKE) occurs downstream off topographic obstacles, which may explain the exchange of particles in the lee of topographic features. This could help to explain the fluctuations along the northern limb of the Weddell Gyre in Figs. 5.5a and 5.5e, where the topography is complex, creating an open northern boundary to the Weddell Gyre. Indeed, the alternating convergence and divergence along the northern limb of the gyre between 30° W and 20° E in Figs 5.5a and 5.5e appear to mimic the underlying bathymetry. It may also explain the heat flux divergence due to horizontal turbulent diffusion that occurs in the lee of Maud Rise (Fig. 5.5 and 5.7).

In western boundary currents, such as the Aghulas Return Current in Tamsitt et al. (2016), the convergence of geostrophic and vertical heat advection is balanced mainly by ocean heat loss, while a smaller contribution comes from the ageostrophic advection term (when integrating from 624 m to the surface). Dong & Kelly (2004) and Roemmich et al. (2005) suggest that heat budgets of western boundary currents are characterised by a balance of convergence due to geostrophic advection with heat loss to the atmosphere. Since we do not integrate to the surface, the surface heat flux is not included in the analysis. Instead, heat convergence due to mean horizontal geostrophic advection is balanced by heat divergence due to horizontal turbulent diffusion (Table 5.2 and Fig. 5.7).

Diffusion remains a negligible term in both Dong et al. (2007) and Tamsitt et al. (2016), though Tamsitt et al. (2016) state that diffusion is an important term in the surface mixed layer and is strong in the upper 100-200 m in the ACC, but that positive and negative signals cancel out when integrating to depths below the mixed layer (note that in the analysis in this study, we do not integrate to the surface and avoid the surface mixed layer altogether). Additionally, while Dong et al., (2007) apply a filter and use a weekly temporal resolution to supress the effect of mesoscale eddies, Tamsitt et al. (2016), whose dataset is a 1/6°, eddy-permitting, data-assimilating model, incorporate mean and eddy components into both horizontal and vertical advection terms, as well as

providing a diffusion term. While the horizontal eddy term is generally small in Tamsitt et al. (2016), it is found to be enhanced in regions of high eddy variability in the ACC, where its magnitude can be equal to that provided by mean geostrophic advection, whereas diffusion is negligible throughout. In contrast, Jullion et al. (2014) suggests that eddy-induced transport contributes significantly to the heat budget, with a heat flux of 5 ± 1 TW, out of a net heat flux of 36 ± 13 TW, which is primarily due to mean circulation. The observations provided in Section 5.4 show that horizontal turbulent diffusion almost balances with mean horizontal advection to nearly close the heat budget, when integrated over large scales. Furthermore, horizontal turbulent diffusion exhibits a particularly interesting spatial pattern in Fig. 5.5c, where the northern limb and the interior circulation cell of the Weddell Gyre are dominated by a convergence of heat due to horizontal diffusion (i.e. red hues in Fig. 5.5c). The northern limb of the gyre has considerably stronger convergence values than the relatively weak gyre interior (i.e. the darker red hues overlying the streamlines indicating a west-to-east flow, parallel to and south of the ACC in Fig. 5.5c). Both the southern limb and north of the Weddell Gyre, in contrast, exhibit heat flux divergence (or cooling) due to horizontal turbulent diffusion. There is also a relatively strong heat flux divergence along the southern boundary of the Weddell Gyre towards the coastline, between 40 and 10° W, and between Astrid ridge and Gunnerus ridge (between 10 and 30° E). This suggests that horizontal turbulent diffusion may constitute an important role in transporting heat into the Weddell Gyre along the open northern boundary, and in transporting heat towards the shelves along the southern coastline. Additionally, there may be a diffusive transport of heat out from the southern limb of the Weddell Gyre northwards into the interior circulation cell.

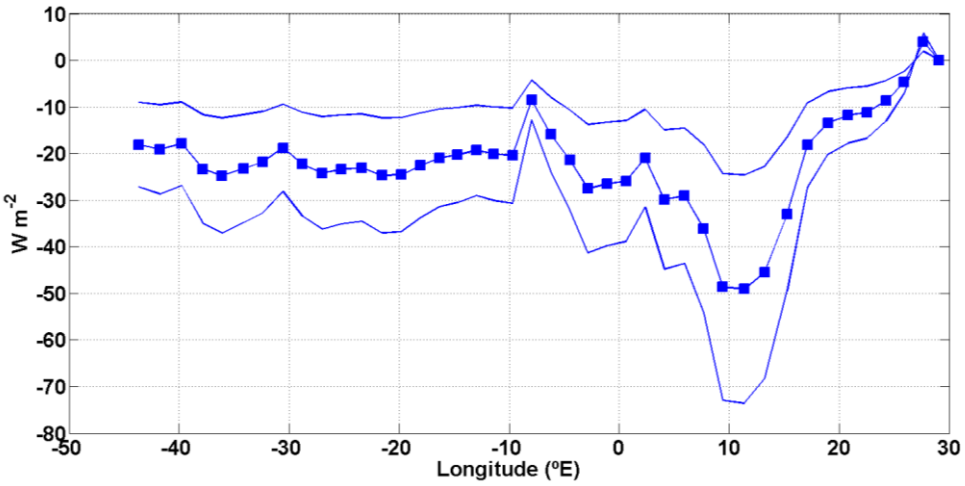

(5.10a)

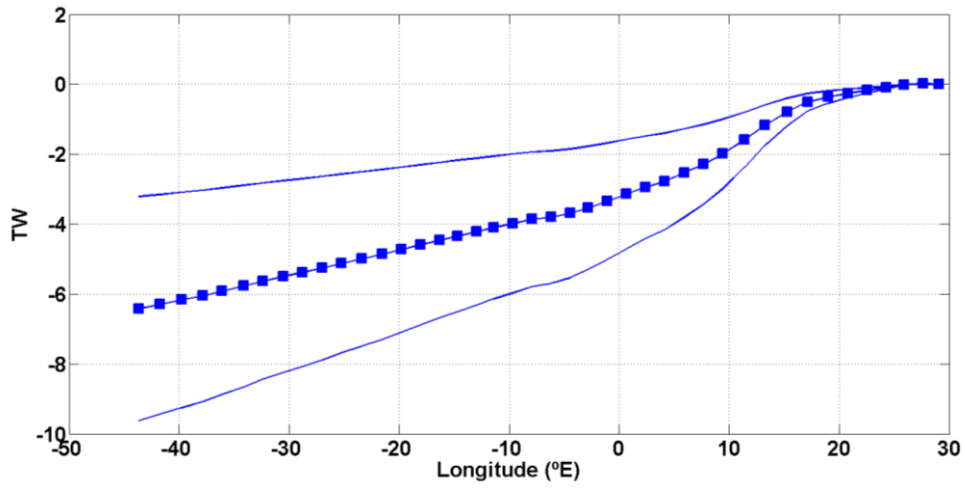

(5.10b)

Fig. 5.10. **(a)** The zonal variation of the diffusive heat flux along the boundary between the southern inflow limb and the interior circulation cell of the Weddell Gyre, in W m^{-2}. Panel **(b):** the cumulative sum of the diffusive heat flux from east to west, in TW. Negative values indicate a northward flux of heat from the southern limb into the interior circulation cell.

To determine whether horizontal turbulent diffusion is a mechanism by which heat is redistributed throughout the Weddell Gyre, horizontal turbulent diffusive heat fluxes were calculated along the boundary between the southern limb and the southern boundary of the interior circulation zone of the Weddell Gyre (Fig. 5.10), and across the northern boundary of the Weddell Gyre (Fig. 5.11). The northern boundary is defined as the northernmost streamline of the filled region in Fig. 8a (i.e. the streamline that, in Fig. 5.5c, marks the boundary between heat flux convergence within the Weddell Gyre (red) and heat flux divergence to the north of the Weddell Gyre (blue)).

Figure 5.10 shows a diffusive flux of heat northwards from the southern limb into the interior circulation cell, mostly at a rate of 23 ± 10 W m^{-2} (Fig. 5.10a). A maximum diffusive heat flux occurs at 10° E, of 50 ± 25 W m^{-2}, where the streamline along which we are integrating starts to curve northwards to meander around the northern flank of Maud Rise. The streamlines indicate a strong flow in this region, with a sharp meridional gradient between recirculated water close to the gyre axis, and the inflow of the southern limb. The total amount of heat diffused into the interior circulation cell from the southern limb of the gyre is 6.5 ± 3 TW (Fig. 5.10b). If we subtract this from the total heat flux divergence due to horizontal turbulent diffusion in Table 5.2, of 19 ± 10 TW, then we can infer that most of the remaining turbulent heat flux occurs southwards towards the ice-covered shelf seas (Fig. 5.5c), of 12.5 ± 10 TW.

At the boundary of the northern limb of the gyre, 20 ± 10 TW of heat is diffused southwards from north of the northern boundary (Fig. 5.11b). The strongest diffusive heat flux occurs between 5 and 10° W, with 100 ± 50 W m^{-2}, downstream of the south Sandwich trench (Fig. 5.11a), most likely due to the strong meridional temperature gradients characteristic of the boundary between the warmer ACC and the colder Weddell Gyre.

These results indicate that horizontal turbulent diffusion may play an important role in transporting heat southwards across the open northern boundary of the Weddell Gyre (Fig. 5.11), and also southwards towards the continental shelves along the Antarctic coast (Fig. 5.5c). Furthermore, the horizontal turbulent diffusion of heat may allow for the removal of some heat from the southern limb of the Weddell Gyre (Fig. 5.10), before advecting fully westwards towards the south-western corner of the gyre, where the large Filchner-Ronne ice shelves and the fragile Antarctic Peninsula are located. Since the diffusive turbulent heat fluxes are dependent on horizontal temperature gradients, this implies a complex interaction between the strength of the Weddell Gyre, thus mean horizontal advection, and the rate of meridional turbulent diffusion, which requires careful understanding if we are to understand the role of the Weddell Gyre in a changing climate perspective.

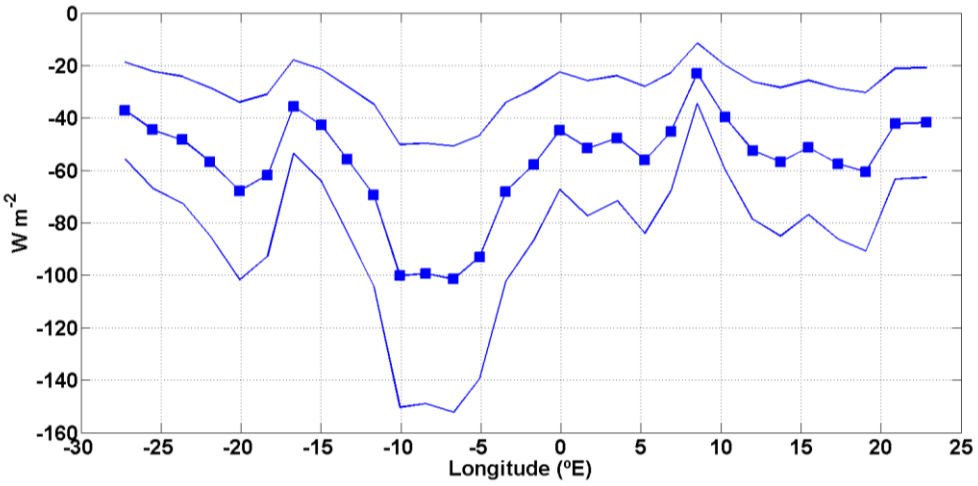

(5.11a)

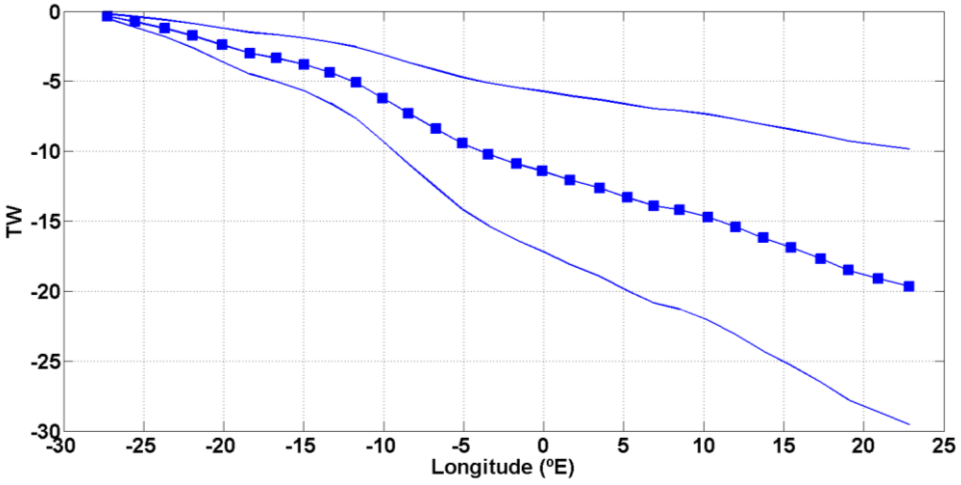

(5.11b)

Fig. 5.11. As with Fig. 5.10, but for the boundary between the eastward flowing northern limb of the Weddell Gyre and the eastward flow north of the Weddell Boundary, defined by the streamline that equals 25 Sv.

5.6 Summary: interpretation of results

Gridded climatologies of temperature and velocity derived from Argo floats spanning 2002-2016 were used to determine the heat budget of a 1000 m thick layer encompassing the core of WDW within the Weddell Gyre. This investigation was to establish the mechanisms by which heat is distributed throughout the Weddell Gyre, implicitly assuming non-divergent, geostrophic flow conditions. The mechanisms are summarised in the form of a basic schematic in Fig. 5.12, and interpreted below.

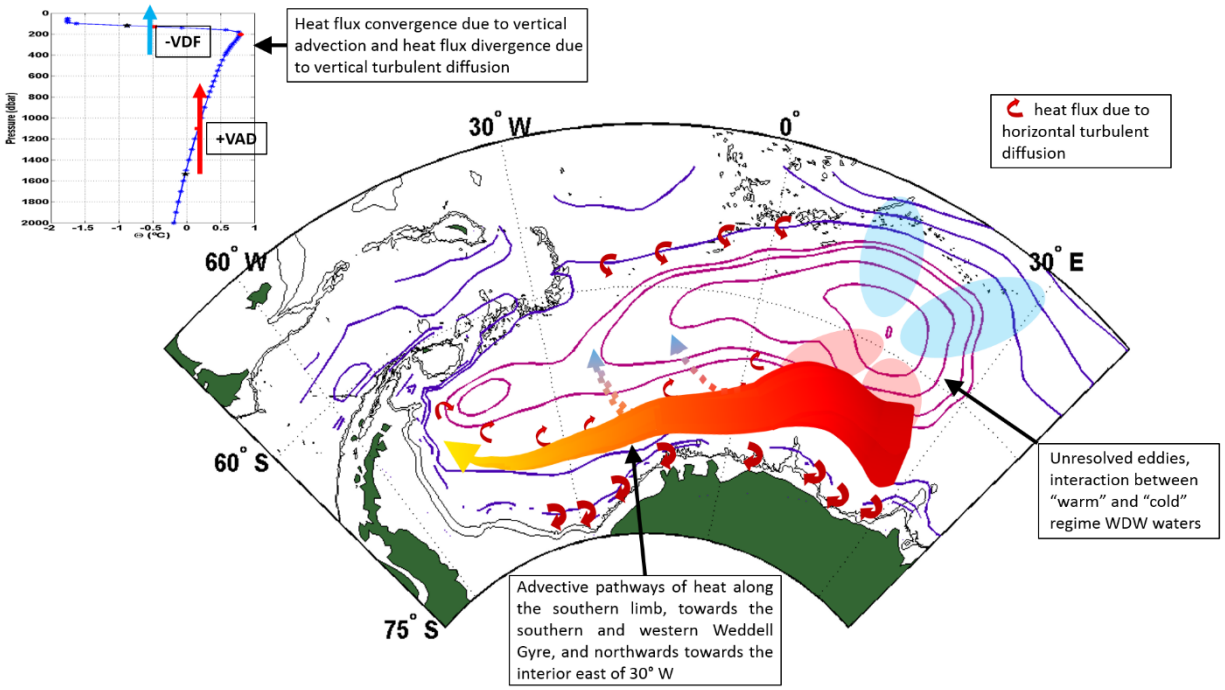

Figure 5.12. Schematic of proposed mechanisms by which heat is transported throughout the Weddell Gyre, based on interpretation of results in Section 5.4. The red-yellow line indicates the advection of heat into the southern limb of the gyre, with some of that heat being advected northwards at 20-30° W (dashed red-blue line). The tapering thickness of the line is representative of the east to west decrease in volume transport along the southern limb of the Weddell Gyre (e.g. see Reeve et al., under review). The red circular lines indicate the direction of turbulent diffusive heat fluxes (1) northwards into the interior circulation cell, (2) southwards towards the shelf seas, and (3) southwards into the Weddell Gyre's northern limb. Eddies dominate east of the Prime Meridian, with a strong interaction between incoming warm WDW and recirculated colder WDW, which is unresolved in the heat budget provided. The upper left figure shows an example of the vertical temperature profile, with –VDF indicating a vertical diffusion of heat upwards out of the layer through the thermocline, and +VAD indicating a vertical advection of heat upwards into the layer from below.

If we accept the potential sources of uncertainty discussed at the beginning of Section 5.5, we can interpret the results presented in this study as follows:

1. Heat convergence due to mean horizontal advection dominates the heat budget in the southern limb of the Weddell Gyre, balanced by a divergence of heat due to horizontal and vertical turbulent diffusion.

2. 26 ± 1 TW of heat flux convergence due to mean horizontal advection occurs along the southern limb of the Weddell Gyre

3. There is an advective pathway of heat northwards between 10 and 20° W, which has an impact on the spatial distribution of Θ_{max} and Θ_{ave}.

4. 6.5 ± 3 TW of heat is removed from the southern limb by horizontal turbulent diffusion northwards into the interior circulation cell.

5. At the southern boundary, there appears to be a diffusive flux of heat towards the shelf seas along the southern coastline, especially between 10 and 30° W, and 10 and 30° E. This may account for the remaining heat flux divergence due to horizontal turbulent diffusion along the southern limb of the Weddell Gyre (i.e. 19 ± 10 TW in Table 5.2, of which 6.5 ± 3 TW is diffused northwards, above (and Fig. 5.10b), leaving a divergence of 12.5 ± 10 TW to be diffused southwards along the southern boundary). While errors are likely to be high at the boundary since Argo floats cannot fully resolve shelf edge boundary currents, this may indicate that horizontal turbulent diffusion plays an important role in delivering heat to the ice-covered shelf seas.
6. The heat budget of the interior circulation cell is dominated by convergence of heat due to horizontal turbulent diffusion, which balances out with divergence due to mean horizontal advection.
7. 20 ± 10 TW of heat is diffused from the ACC into the northern limb of the Weddell Gyre, downstream of the South Sandwich Trench.
8. East of the Prime Meridian, a strong patchwork of heat divergence and convergence is found, possibly due to the occurrence of unresolved mesoscale eddies that are not represented by turbulent heat flux diffusion, possibly due to instabilities generated from the interaction between "cold" regime recirculating WDW and incoming "warm" regime WDW (Gordon and Huber, 1984 and Fig. 5.1).
9. Vertically, the advection term is nearly negligible, most likely due to the non-divergent conditions implicit in deriving velocity from the stream function. However, based on the wind field-derived boundary condition that Ekman pumping velocity is positive upwards throughout (Fig. 5.3b), and that the lower boundary of the layer is warmer than the upper boundary throughout (based on the vertical boundary conditions in Section 5.2.1), we can interpret the vertical terms as:
    a. heat is advected upwards into the layer
    b. heat is diffused upwards out of the top of the layer, due to the relatively strong vertical temperature gradient at the thermocline, and due to vertical instabilities at the thermocline. This heat may eventually be lost to the atmosphere.

While acknowledging the errors associated with this work, if we use a time period of 14 years (conceding that the data is a climatology and therefore more or less an average over the whole time period), we can speculate upon what temperature change occurs as a result of the sum of the heat budget terms, $d\Theta/dt$, which, while the heat budget comes close to closing when integrated over large spatial scales, does not close completely and thus does not equal to zero. Thus, over a period of 14 years, the 1000 m thick layer of water containing the core of WDW has warmed by 0.13 ± 0.5 °C

in the southern limb of the gyre (Table 2), and by 0.09 ± 0.45 °C in the interior circulation cell of the gyre (Table 5.3). This equates to a warming trend of 0.0095 ± 0.035 °C/year in the southern limb (Table 5.2), and 0.006±0.032 °C/year in the gyre interior (Table 5.3), which, while insignificant due to the assumptions involved, is in line with previous observations by Fahrbach et al. (i.e. Fig. 5a in Fahrbach et al., 2011), where a temperature increase from 0.28 °C in 2005 to 0.32 °C in 2008 indicates a warming of 0.013 °C/year, and by Kerr et al. (2017, Fig. 6a), where the core of WDW warmed from 0.35 to 0.4 °C over 10 years at the Prime Meridian, and from 0.33 to 0.36 °C over 5 years across the Kapp Norvegia - Joineville Island section (black line in Fig. 5.1), which indicates a warming of 0.005 °C/year.

From using Argo floats, we have described the heat budget of a 1000 m thick layer encompassing the core of WDW within the Weddell Gyre. The role of mean horizontal advection is evident in feeding heat towards the southwestern Weddell Gyre, where the Filchner-Ronne ice shelves and Antarctic Peninsula are located. What is also important, however, is understanding the respective roles of mean horizontal advection and horizontal turbulent diffusion in removing some of that heat from the southern limb of the Weddell Gyre before it is able to reach the southwestern interior. This is crucial since Hellmer et al. (2012) suggest that under future climate scenarios, a redirection of the coastal current toward the Filchner-Ronne ice shelf could lead to increased advection of waters into the ice-shelf cavity, leading to increased basal ice melt from 0.2 to 4 m/year. Further investigation of how heat is redistributed throughout the Weddell Gyre is required to ascertain the role of the Weddell Gyre in feeding heat to underneath the ice shelves, and also in supplying heat to deep and bottom water masses, which have been recently warming and reducing in volume (Kerr et al., 2017).

5.7 Acknowledgements

These data were collected and made freely available by the International Argo Program and the national programs that contribute to it (http://www.argo.ucsd.edu, http://argo.jcommops.org). The Argo Program is part of the Global Ocean Observing System. The GEBCO Digital Atlas is published by the British Oceanographic Data Centre on behalf of IOC and IHO, 2003. The mean velocities derived from mooring data were provided by Nicolas Le Paih, to whom the authors are indebted to.

6 Conclusions: The circulation and distribution of heat within the core of Warm Deep Water

In order to contribute to understanding the role of the Weddell Gyre in the Earth's climate system, the aim of this thesis is to determine the circulation and distribution of heat throughout the Weddell Gyre. To date, observation studies examining the circulation of the Weddell Gyre have been limited to single cross-sections across the gyre during ship-based expeditions. These investigations resulted in wide ranging volume transport estimates for the Weddell Gyre, and it has been unclear as to the cause of those differences, given the variation in time period of observation, instrumentation, methodology and placement of the cross-section in the Weddell Gyre. Argo floats give us an opportunity to expand our knowledge, by providing in-situ observations spanning the entire Weddell Gyre, for the upper 2000 dbar. Conveniently, Warm Deep Water (WDW) sits within the upper 2000 dbar of the water column. Given that WDW is the primary source of heat in the Weddell Gyre, the aim of this thesis is to establish the circulation and distribution of heat within the WDW layer, for the entire Weddell Gyre. To achieve this aim, three fundamental questions are addressed:

RQ 1. Is it possible to create gridded data sets of temperature and salinity throughout the entire Weddell Gyre, describing the spatial variation in the hydrography of the upper water column, which includes the WDW layer?

RQ 2. Can the large range in historical gyre strength estimates be reconciled with spatial inhomogeneity of the circulation of the Weddell Gyre?

RQ 3. In bringing together the outcomes from RQ.1 and RQ.2, what mechanisms contribute to distributing heat within the WDW layer of the Weddell Gyre?

In the following, a summary of the key findings that provide answers to each of the above research questions will be presented. Subsequently, some suggestions will be provided in terms of what limitations need to be addressed to improve the quality of the key findings, and future directions this research may take.

RQ. 1. Is it possible to create gridded data sets of temperature and salinity throughout the entire Weddell Gyre, describing the spatial variation in the hydrography of the upper water column, which includes the WDW layer?

The first paper (Chapter 3) was published in 2016 in *Earth Systems Science Data*, and provided a description of the distribution of temperature and salinity throughout the whole horizontal extent of the upper Weddell Gyre. This description was derived from Argo float profiles between 2002 and 2013, which were objectively mapped onto a regular grid to provide a climatology of temperature and salinity from 50 to 2000 dbar. Objective mapping was also applied to the level of the sub-surface temperature maximum, which represents the core of WDW.

The spatial distribution of temperature within the core of WDW is provided by a map of the subsurface temperature maximum. The warmest water, which exceeds 1º C, is found at the eastern gyre periphery south of 60º S, and progressively cools by ~0.5 ºC from east to west. A cold patch of water (~0.4 ºC) is found over Maud Rise, probably due to the presence of a Taylor Column (e.g. Leach et al., 2011; Cisewski et al., 2011; de Steur et al., 2007; Bersch et al., 1992). Throughout the central part of the gyre, the core of WDW is coldest, between 0.2 and 0.5 ºC, and appears to be split into two cold centres, east and west of 0-20º W. Between 0 and 20º W, relatively warm water appears to spread northwards from the southern limb of the gyre. This was a feature also observed by Bagriantsev et al. (1989). The northern limb of the gyre is narrow with sharp meridional gradients between the coldest water in the centre and the warmer water found north in the ACC. The subsurface temperature maximum, associated with the WDW layer, is shallowest in the central region of the gyre, especially between 20º W and 10º E, where it approaches 200 m. The subsurface temperature maximum is deepest at the gyre periphery, typically between 400 and 600 m, and also over Maud Rise, where it is found at 400-450 m. This is explained by the doming of the isopycnals that characterises a cyclonic gyre, whereas the deep temperature maximum over Maud Rise is associated with the upward heat loss to the atmosphere of a relatively stagnant water column, i.e. a Taylor Column, whose heat is not efficiently replenished by the advection of heat at the sub-surface level (e.g. Leach et al., 2011). The spatial variation of the subsurface temperature maximum derived here from Argo floats, shows agreement,

with additional detail, to various studies, such as Deacon (1979) and Bagriantsev et al. (1989), who also showed gradual cooling from >1 ºC in the east to 0.5 ºC in the west, but do not clearly show the double cell gyre structure, nor the cold water column over Maud Rise. There is also considerable agreement with the depth of the temperature maximum derived from Argo floats (Fig. 3.12), where a minimum depth of 200 m is located in the central Weddell Gyre and a maximum depth of 400-600 m is found at the gyre periphery in Deacon (1979). One advantage of the work presented in Reeve et al. (2016) is the provision of mapping errors and an investigation of the objective mapping performance by applying the objective mapping to the float profile locations.

Temperature at 800 dbar, the parking depth of Argo floats in the Weddell Gyre, shows a similar distribution of temperature to the subsurface temperature maximum, with fewer pertinent details such as the suggestion of a double cell structure. However, sharp meridional gradients are found along the narrow northern limb of the gyre, and an east to west temperature decrease is found in the broader southern limb of the gyre, whereas the coldest waters are found along the central zone of the gyre. Salinity shows a similar pattern to temperature, where warm water is associated with relatively high salinity and colder water is associated with relatively low salinity. Along the Prime Meridian, vertical sections show the doming of isopycnals, isotherms and isohalines, where a layer of cold, fresh water sits above the warm, salty WDW. Below the core of WDW, temperature and salinity gradually decrease with increasing depth, though the vertical gradient is most defined in temperature. The doming confirms the gyre's cyclonic structure, indicative of upwelling at the centre. These observations show excellent agreement with previous sections along the Prime Meridian observed during ship campaigns (e.g. Whitworth & Nowlin, 1987; Schröder & Fahrbach, 1999; Fahrbach et al., 2004, 2011). The advantage of the work presented in Reeve et al. (2016), is that it provides a comprehensive view of the distribution of heat and salt in the entire Weddell Gyre from observations independent of ship-based CTD surveys, where cross-sections can be extracted from any point in the Weddell Gyre, not just the Prime Meridian.

RQ. 2. Can the large range in historical gyre strength estimates be reconciled with spatial inhomogeneity of the circulation of the Weddell Gyre?

The second paper (Chapter 4), currently under review in *Progress in Oceanography*, provides a complete view of the offshore horizontal circulation of the Weddell Gyre derived solely from Argo float observations between 2002 and 2016. In addition to a description of the horizontal Weddell Gyre circulation, volume transports of the upper 2000 m, the WDW layer, and for the full water column are presented.

The results show clearly the elongated, cyclonic structure of the Weddell Gyre, confirming the entry of WDW into the gyre at the eastern periphery in the southern limb, established above. This work captures the southward flow of water at the eastern end of the gyre throughout the upper water column, between 20 and 30° E. This is in agreement with Orsi et al. (1993), use used dynamic topography maps derived from ship-based observations to investigate the Weddell Gyre circulation, and showed that a broad discontinuity in the Southwest Indian Ridge at about 25-32º E, allows for the southward flow of CDW, which eventually enters the Weddell Gyre from the east in the southern limb. Since the topography influences the path of the ACC (e.g. Gordon et al., 1978; Orsi et al., 1995), and the ACC curves southwards at this longitude, the Weddell and Southern ACC fronts converge, enhancing the meridional gradient of the zonal flow, which reduces relative vorticity (Schröder & Fahrbach, 1999). For the sake of conservation of potential vorticity, this leads to an increase in flow rotation and thus southward motion (Schröder & Fahrbach, 1999; Comiso & Gordon, 1996). As a result of the increased rotation, this region produces mesoscale eddies, which result in mixing between the modified recirculated WDW (or, cold-regime WDW, Schröder & Fahrbach, 1999; Gordon & Huber, 1984) and adjacent CDW (Schröder & Fahrbach, 1999). Ryan et al. (2016) show that an eddy-driven inflow region for CDW into the Weddell Gyre is found between 20 and 30° E, which drives an inflow just south of 60° S. South of the eddy-driven inflow region, an advection-driven inflow of CDW enters the gyre, which, in its southward journey from the ACC extends further east, prior to turning westward for its entry into the southern limb of the gyre (Ryan et al., 2016). There is some agreement in Fig. 4.4a, in which the streamlines at 50 dbar that make up the southern limb between 60 and ~65º S at 20º E are part of an enclosed circuit spanning the Weddell Gyre, whereas south of ~65º S, the streamlines are open from the east (i.e. the streamlines leave the grid domain). The boundary between the closed and

open streamlines shifts northwards with increasing depth, so that the closed streamlines at 800 dbar are found north of ~63º S, and below 800 dbar, the closed streamlines are found north of ~62º S, suggestive of some baroclinic influence of the circulation at the eastern periphery. An obvious limitation of this study is the exclusion of the strong boundary currents and frontal jets, in particular associated with the Antarctic coastal current, and the portion of the Weddell Gyre that flows between the Gunnerus and Astrid Ridges. This will be discussed later in this chapter, when describing the limitations of the research presented within this thesis.

Water masses circulate within the gyre in a clockwise direction, with 71±28 Sv (of which 15±8 Sv is within the WDW layer) flowing back northwards to join the eastern return flow between 18º E and 27º W. 50 Sv of this northward flow (12 Sv within the WDW layer) occurs between 15º E and 20º W, without circulating the full zonal extent of the gyre. This northward-flowing water circulates the eastern cell of the Weddell Gyre. There is another circulation cell in the west centred over 40º W, which is substantially weaker than the eastern cell. This double-cell structure has been suggested by past observations (e.g. Matano et al., 2002; Orsi et al., 1993) and also by numerical models such as BRIOS (Beckmann et al., 1999), but this is the first time, to the authors' knowledge, that the double cell structure of the Weddell Gyre has been depicted in detail by in situ observations only. The stronger eastern cell explains how some of the heat in the core of WDW spreads northward between 0 and 15º W (Chapter 3), which is also reflected in the heat budget (Chapter 5). It also explains why, in previous volume transport estimates provided from individual ship transects, weaker volume transports were observed in the western part of the gyre (e.g. Heywood & King, 2002) than at the Prime Meridian (e.g. Klatt et al., 2005; Schröder & Fahrbach, 1999). This implies that observations along the Prime Meridian are not indicative of the mean strength of the entire Weddell Gyre, but more closely represents the strength of the eastern cell. The double-cell structure of the gyre circulation is important and needs to be taken into account, as it influences the amount of heat that reaches the southwestern and western Weddell Sea, where some of the largest ice shelves of Antarctica are found, such as the Filchner-Ronne ice shelf. WDW, which breaches the continental shelf seas, can account for substantial basal ice melt, which, if it increases as in future climate scenarios, would contribute to global sea level rise (Timmermann & Hellmer, 2013). The WDW that flows northwards circulating the eastern cell before flowing along the full meridional

and zonal extent of the gyre is more likely to lose its heat to the atmosphere as it enters the central upwelling region of the gyre, which brings it into closer contact with the atmosphere, as was depicted in Chapter 3. Naveira Garabato et al. (2016) established the importance of the upwelling upper cell of the Weddell Gyre in terms of heat loss to the atmosphere and freshwater gain to the water column through sea-ice melt, but concluded that the upwelling in the Weddell Gyre presents a considerable gap in knowledge, and thus deserves greater attention in future research.

Regarding the vertical variation in the horizontal circulation of the Weddell Gyre, the western Weddell Gyre is almost invariant with depth, while the eastern sector of the gyre (especially east of the Prime Meridian) shows baroclinic contribution to the flow. There are two striking features in the vertical variation in horizontal circulation, both associated with the return-eastward flow in the northern limb of the Weddell Gyre. In the upper 50 to 1000 dbar, some of the water flows northwards through the Scotia ridge system, and joins the eastward return flow within the Weddell-Scotia Confluence, which was also observed by Heywood & King, (2002). This water curves south-eastwards, creating a surface inflow region to the northern limb of the gyre downstream of the South Sandwich Trench. Conversely, below 1000 dbar, the streamlines south of the Scotia Ridge appear to curve northwards downstream of the South Sandwich Trench, resulting in a deep water outflow. It should be noted that the most distinct outflow occurs at 3000 dbar, which should be treated with caution, as the stream function has been extrapolated to beyond the reach of the Argo floats (See Chapter 4.2.5). However, the outflow begins to take shape at 1200 dbar, well within the vertical reach of the Argo floats. The observations fit in the context of previous estimates, where Meredith et al., (2008) found that the South Sandwich Trench is an outflow region for WSDW, while Matano et al. (2002) used an inverse model to show that while there may be a deep water outflow, the net flow at the tip of the South Sandwich Trench is southward. The observations here provide a surprisingly distinct depiction of the circulation in a region where complex bathymetry would lead one to expect a poorly constrained flow regime when assessing the long-term mean circulation.

While the Weddell Gyre is itself largely barotropic, baroclinic shear appears to play an important role along the northern boundary of the gyre, and also in the north-eastern part of the gyre (Fig. 4.3). There is lack of a distinct eastward return flow in the northern limb of the gyre below 2000 dbar, where profiles have been extrapolated to full

ocean depth. In these regions where baroclinic contribution to the circulation is relatively large, surface measurements alone are not enough to resolve the circulation. This may be why, there is poor agreement with the literature regarding full depth volume transports in the northern limb at the Prime Meridian, which is in contrast to the excellent agreement with the literature of full depth volume transports in the southern limb and in the western sector of the Weddell Gyre (Klatt et al., 2005; Schröder & Fahrbach, 1999). This is despite excellent agreement with Klatt et al. (2005) for the volume transport of WDW in the northern limb at the Prime Meridian, implying that there is an important baroclinic contribution to the flow below 2000 dbar that is not resolved in our study.

The long-term mean strength of the Weddell Gyre depends on how one defines the gyre, especially given that it is an elongated gyre that consists of two cells with differing strengths. In Chapter 4.3.2, the Weddell Gyre is split into quadrants, defined by the zonal central axis of the gyre, and a meridional line that cuts through ~27º W at the central axis, which separates the northward flowing water circulating the eastern cell from the southward flowing water circulating the western cell. The mean offshore volume transports within these quadrants are determined, where the word offshore is used to emphasise that the means are derived for regions fully enclosed by streamlines in Fig. 4.9. The overall offshore mean transport is 32 ± 5 Sv, of which 12.5 ± 3 Sv occurs within the WDW layer. The southern limb mean westward transport of 38 ± 7 Sv, of which 14 ± 4 Sv is WDW, is larger than the northern limb mean eastward transport, which is 25 ± 7, with 11 ± 3 Sv of WDW. Lastly, the eastern sector of the Weddell Gyre, with a mean southern transport of 37 ± 6 Sv, with 14 ± 4 Sv of WDW, is considerably stronger than the weaker western Weddell Gyre, which has a mean northward transport of 23 ± 3 Sv, of which 10 ± 2 Sv occurs within the WDW layer. The volume transport of WDW occupies 36 % of the offshore full water column.

RQ. 3. In bringing together the outcomes from RQ.1 and RQ.2, what mechanisms contribute to distributing heat within the WDW layer of the Weddell Gyre?

The horizontal distribution of the sub-surface heat budget of the Weddell Gyre is provided for a layer encompassing the core of WDW. This was implemented by combining the results achieved in answering the first two research questions, regarding

the horizontal distributions of the flow field and temperature. Gridded horizontal velocity and temperature fields were combined, to assess mean advection and turbulent diffusion of heat. Vertical velocity, required for the estimate of the vertical heat advection term, was defined as the mean Ekman pumping velocity derived from ERA-Interim. The heat budget terms were integrated from the depth of the mid-thermocline, with the bottom boundary defined as 1000 m deeper than the mid-thermocline depth. The mid-thermocline is the defined upper boundary, to avoid surface water masses, whose properties are highly fluctuating due to seasonal variations. The vertical boundary conditions applied ensured that the core of WW was excluded. WW is characterised as the temperature minimum layer which sits on top of the thermocline. At the same time, defining the upper boundary as the mid-point of the thermocline ensured the inclusion of the core of the WDW layer, i.e. the subsurface temperature maximum, regardless of its depth in the water column, which varies throughout the gyre (as shown in Chapter 3). The bottom boundary was chosen to keep the thickness of the layer consistent across all grid cells, regardless of the depth of the upper boundary. Thus, surface heat fluxes do not directly enter into the heat budget for the sub-surface layer, and the heat equation is the sum of the horizontal and vertical mean advection and turbulent diffusion. For RQ. 3, the cost function that is minimised to provide a gyre-scale stream function of the Weddell Gyre at 800 dbar, was improved so that Neumann boundary conditions could be applied to a variable boundary, i.e. the southern coastline. This, plus the addition of long term mean velocities from moorings along the southern coast, and special treatment of the flow around Gunnerus Ridge, resulted in a greatly improved stream function that includes the southern inflow region between the Gunnerus and Astrid Ridges. The stream function describes the same features as from the second research question (Chapter 4), but reveals a slightly stronger inflow as it includes more of the region closer to the southern coastline west of the Prime Meridian.

The contribution of mesoscale eddies to the heat budget is not directly addressed in this study, and instead is parameterized in the horizontal turbulent diffusion term. It is assumed that mesoscale eddies constitute an important, yet poorly resolved contribution to the heat budget in the eastern region of the Weddell Gyre. Large variability in the mean horizontal advection is observed just east of the eastern circulation core. This is a region that has been described as a dynamic field of mesoscale eddies (Schröder & Fahrbach, 1999), which has been attributed to an eddy-driven inflow of WDW by Ryan

et al. (2016). When integrated over a large area depicted by the fully enclosed streamlines, the heat budget shows the strongest variation east of the Prime Meridian. The zonal variation of the heat budget is considerably smaller west of the Prime Meridian. Understanding the contribution of the mesoscale eddy field to the heat budget east of the Prime Meridian is mandatory for understanding the mixing between WDW (warm-regime) and modified WDW (cold-regime) in the Weddell Gyre, which is believed to take place in the region (Schröder & Fahrbach, 1999; Gordon & Huber, 1984).

Maud Rise has important consequences for the heat budget of the core of WDW, where a convergence of heat is observed upstream of Maud Rise, and heat divergence is observed downstream of Maud Rise. This is likely due to an inadequate resolution of the velocity field, in resolving the localised circulation around Maud Rise. Since the water directly atop of Maud Rise is colder than the surrounding water column, and the velocity field does not adequately resolve the flow around the seamount, the mean horizontal advection is reflective of the strong lateral temperature gradients on the flanks of Maud Rise. The presence of a Taylor column over Maud Rise impacts horizontal advection, and eddies shed on the flanks of the seamount contribute to enhanced lateral mixing in its lee (Leach et al., 2011). Maud Rise is a localised region in which baroclinic instabilities, particularly on the flanks of Maud Rise, lead to enhanced convection (e.g. Akitomo, 2007). The heat loss downstream of Maud Rise is about 30 W m^{-2} in Fig. 5.5e (in Chapter 5.4), which is similar to previous estimates by Muench et al. (2001), although these authors focus on the surface heat flux, using surface drifting buoys.

Over small scales, i.e. for each grid cell, the heat budget does not close. However, when integrated over large areas, the heat budget closes within uncertainty based on the assigned range of values for the diffusivity parameters, where heat convergence due to mean advection is mostly balanced by heat divergence due to turbulent diffusion. The distribution of heat throughout the Weddell Gyre can be explained by (1) heat convergence due to mean horizontal advection along the southern limb of the Weddell Gyre, (2) the southward turbulent diffusion of heat into the gyre along the northern boundary, (3) the northward turbulent diffusion of heat from the southern limb into the central recirculation cell of the gyre, where colder and fresher modified WDW is found, and (4) the turbulent diffusion of heat southwards towards the

continental shelf seas. While the turbulent diffusion of heat towards the southern coastline must be treated with caution due to the assumption of large errors at the southern boundary, it nevertheless suggests an important and possibly under-investigated mechanism for the transfer of heat onto the continental shelf seas, where it may come into contact with the ice shelf.

The turbulent diffusion of heat upwards through the thermocline also plays a role in heat loss from the core of WDW, which would then be mixed into WW, where it may be lost to the atmosphere or play a role in the melting of sea-ice. Studies have suggested that double diffusive convection is a mechanism that contributes to mixing in the central Weddell Sea, where cold, fresh WW sits on top of warm, salty WDW (Foster & Carmack, 1976). Vertical advection of heat is dependent on the temperature difference between the vertical boundaries, since the long-term mean of the Ekman pumping vertical velocity is constant with depth (since the layer is below the Ekman layer) and is positive upwards throughout most of the Weddell Gyre (the exception is on the continental shelf along the Antarctic Peninsula, Fig. 5.3b). However, vertical advection contributes very little to the overall heat budget, possibly due to the assumption of non-divergent flow conditions below the Ekman layer. Non-divergent flow conditions is an inherent assumption, since the velocity field is derived from a geostrophic stream function. However, it is justified, since the analysis is performed for a climatological dataset that represents the long-term mean, i.e. what is assumed to be steady state. The assumption of non-divergent flow may not be appropriate when analysing over shorter time periods, or when integrating to above/within the Ekman Layer, where Ekman transport becomes an important ageostrophic component of advection (i.e. such as in Tamsitt et al., 2016). Additionally, within the surface mixed layer, Ekman pumping velocity varies with depth.

Over a time period of 14 years, the heat tendency, i.e. the sum of the heat budget terms, indicates a mean warming of the 1000 m thick layer of water encompassing the core of WDW, from 2002 to 2016, with trends of 0.0095 ± 0.035 °C/year and 0.006±0.032 °C/year when integrated over the southern limb and central circulation cell of the gyre respectively. The error estimates are based on the summation in quadrature of (1) the range in horizontal and vertical diffusivity, defined as 400 ± 200 m^2s^{-1} and 2.6 x 10^{-5} ± 2.4x10^{-5} m^2s^{-1} respectively, and (2) a deviation in the heat budget due to a perturbation of the temperature and velocity fields, by using non-surface-drift-corrected

velocity and incorporating the mapping error in the temperature field (see Chapter 5.2 for further details). The defined ranges in the diffusivity parameters contribute most to the error estimates, which results in large estimates of uncertainty, diminishing the significance of the warming trends. Despite the large uncertainty, the temperature trend for the southern limb is similar to Fahrbach et al. (2011), whose observations along the Prime Meridian indicate a warming trend from 2005 to 2008 of 0.013 °C/year. Furthermore, the temperature trend for the interior circulation cell is similar to Kerr et al. (2017), whose time series analysis indicates a warming trend of 0.005 °C/year over 5 years along the western Weddell Gyre and over 10 years along the Prime Meridian.

Limitations of research

There are several limitations to this study, which mostly stem from the fact that we are in a data limited region periodically covered in sea-ice. The decision to base this research entirely on Argo Float observations was to produce a gridded climatology of the Weddell Gyre that is independent from CTD profiles from ship-based surveys. Also, the inclusion of ship-based CTD profiles would have required special statistical consideration to prevent bias to regions where the ship surveys on repeat transects. The work in Chapter 3 could be improved by incorporating additional data resources, such ship-based CTD profiles, data from seals, and mooring arrays. It would then be possible to investigate the full ocean depth, and provide an analysis of the Weddell Gyre deep circulation without needing to extrapolate below 2000 dbar in Chapter 4. However, it was useful to provide an independent Argo-derived data set which provides a basis for comparison with ship-based CTD data. This was especially useful in Chapter 4, where it was possible to directly compare volume transports to the literature, so that the transports across single ship transects could be placed in the context of the gyre-scale circulation. Since Argo floats drift freely in the water column, there are large regions where data coverage is particularly sparse, such as in the southwestern Weddell Gyre. Mapping errors are especially large along the eastern flank of the Antarctic Peninsula in Chapter, 3, where there is little data available.

Argo floats do not typically enter the continental shelf regions of the Weddell Gyre, as they tend to more or less follow contours of constant potential vorticity (as shown in Chapter 4.4.2). Thus, there are no data available for the on-shelf and shelf-edge regions, where important frontal dynamics and boundary currents exist, which

largely contribute to the overall circulation and transports of the Weddell Gyre (e.g. Heywood et al., 1998; Fahrbach et al. 1994). Thus, lack of data at the shelf edge was a substantial limitation in Chapter 4. A large section of the inflow region in the southern limb east of the Prime Meridian was omitted from the investigation of the circulation in Chapter 4. The grid was rotated by 14° to ensure the northern limb of the gyre east of the Prime Meridian was included in the analysis while avoiding, as much as possible, the inclusion of the ACC to the west of the Prime Meridian. This was appropriate at the time, as there were limited data along the shelf, and the cost function that was minimised to derive the stream function was not able to operate with a variable coastline. This issue, however, was resolved in time for the third manuscript in Chapter 5, which used an improved stream function, and also included long-term mean data from moorings along the southern coastline. Argo floats drifting along the coast were treated individually, where, if there were less data points available, the length scales were reduced, and in some cases, single data points were used in the mapping of velocity, though each individual was manually inspected. This presents a source of error in Chapter 5, since the boundary currents were partly constrained, and based on the use of single data points at some grid points. An example is at Gunnerus Ridge, where flow in opposing directions to each side of the ridge is observed, but were smoothed out entirely when subject to the objective mapping method, and so the nearest-values were used in this specific region. While these individual decisions greatly improved the resulting stream function, it does mean that in some regions the stream function is biased towards single time snapshots of when a float was passing through the data sparse region, likely in summer when it was possible for the float to surface, or where Katabatic winds were strong enough to push the sea-ice away from the coastline.

The mapping errors associated with objective mapping of both profile and velocity data derived from Argo floats are sensitive to the assigned length-scales. As mentioned above, it became necessary to adjust the length-scales in close proximity to the shelf edge, and to employ a nearest neighbour tactic for the flow around Gunnerus Ridge. Throughout the rest of the grid, however, the length-scales used were large, and has an impact on the resulting mapping errors (i.e. mapping errors are small in regions of sparse data coverage if the bathymetry is flat, and the properties of nearby data points have little variation). In Chapter 3.4, this is discussed in detail. The decision to incorporate a fractional length-scale that accounts for changes in *f/H* contours improved

the objective mapping, despite the large length-scales, by influencing the elliptical shape of the area of influence around a grid point (i.e. the area within which data are assigned a weight for the objective mapping).

Since data are too sparse to incorporate a time separation scale into the objective mapping procedure, it is necessary to use large-length scales, to avoid, as much as possible, the gridded-fields representing transient properties as opposed to the large-scale mean. For this reason, the upper 50 dbar were omitted from the study altogether. Seasonal variation is also not assessed within the scope of this research. Novel solutions were required for this when determining the heat budget in Chapter 5, since a heat budget is typically provided for the surface mixed layer and includes surface air-sea heat fluxes (such as in Dong et al., 2004, or Tamsitt et al., 2016). This problem was resolved by setting the upper boundary as the mid-point of the thermocline. However, this presents additional sources of error, since, from grid cell to grid cell, while the thickness of the layer is the same, the position of this layer within the water column can vary, leading to noise within the heat budget.

There may also be a seasonal bias of the available Argo float data, especially when deriving velocity from the float trajectories, which is only possible when the float is able to surface between drift dives. In the Austral winter when the Weddell Gyre is largely covered in sea-ice, less position data are available for deriving the drift velocity. This is a problem that will be solved in the near future, as acoustic positioning of Argo floats when drifting under sea-ice becomes available, from the triangulation of the floats using moored sound sources. Indeed, mapping of float profiles with no geolocation, whose positions are linearly interpolated between last known and first known positions, has been associated with large errors (Chamberlain et al., 2018), unless one applies suitably large length scales, which is necessary in this study due to the lack of a time – averaging component.

Furthermore, with no time series analysis component available with the objective mapping, owing to sparsity of available data, the contribution of mesoscale eddies to the distribution of heat and salt in the Weddell Gyre, and their subsequent contribution to the heat budget is unresolved, and therefore is indirectly taken into account by the turbulent diffusion term. Mesoscale eddies are especially important in the eastern Weddell Gyre, as implied by the heat budget in Chapter 5, but also by Schröder & Fahrbach (1999) and Ryan et al. (2016). Jullion et al., (2014) suggests that

overall the mesoscale eddy field contributes 14 % to the net amount of heat that enters the Weddell Gyre (5 TW in comparison to 31 TW of heat that enters the gyre via the mean horizontal circulation).

Another limitation with the work presented in this thesis is regarding dynamic regions where complex bathymetry and topographic obstacles are associated with enhanced mesoscale energy and baroclinic instabilities, which leads to transient horizontal and vertical eddy heat fluxes (Naveira Garabato et al., 2011; Tamsitt et al., 2016). Complex bathymetry is especially prominent along the northern boundary of the Weddell Gyre. Thus, when applying objective mapping to all data within a 14 year period (Chapter 3), without the consideration of time, one expects a large amount of noise, thus large mapping errors. The mapping errors are relatively large along the Scotia Ridge system until about 15° W (Chapter 3), and remain larger than in the gyre interior along the northern boundary of the gyre east of 15° W. However, the resulting sub-surface temperature maximum maps look rather convincing, showing the contours steering the South Sandwich Islands. It is likely that the objective mapping reduces lateral gradients in temperature and salinity and that the lateral gradients would be larger if smaller length-scales were defined for the objective mapping. Regardless, the streamlines in Chapter 4 also demonstrate some topographic steering about the South Sandwich Islands. The heat budget in Chapter 5, however, does not close in this region and results in large residuals, with heat loss over the South Scotia Ridge and downstream of the South Sandwich Trench, and heat gain over and slightly west of the South Sandwich Islands. In this analysis, the grid cell resolution and lack of time series analysis prevents adequate resolving of these tightly varying, dynamic features.

The final limitations discussed here are related to the heat budget in Chapter 5. Firstly, using a non-divergent horizontal stream function may reduce the importance of vertical advection to negligible. Since the Ekman layer is avoided in the heat budget analysis, the assumption is made that the vertical velocity is represented by the mean Ekman pumping vertical velocity between 2002 and 2016, which is assumed constant with changing depth below the Ekman Layer. However, Jullion et al. (2014) and Naveira Garabato et al. (2016), highlight the importance of two overturning cells in the Weddell Gyre through inverse modelling. This vertical overturning is not investigated in this research. Jullion et al. (2014) conclude that future research needs to include the upwelling processes within the gyre interior and not just sites of potential bottom water

formation. Based on the findings in Chapter 4, where it is shown that a large volume of water is circulated northwards towards the central gyre before reaching the southwestern Weddell Gyre, the research presented in this thesis agrees with that statement.

Lastly, an important limitation in the research presented in Chapter 5, is the lack of definite, spatially varying, horizontal and vertical diffusivities in the calculation of turbulent diffusion. Based on a range of estimates in the literature, such in Leach et al. (2011), Cole et al. (2015) and Donnelly et al. (2017), a range of three values are arbitrarily assigned for both horizontal and vertical diffusivity. The assumption is made that these values are constant both horizontally and vertically. However, this is not the case in the real-world. Ideally, diffusivities should be derived from observations, which is indeed possible to do with Argo floats (Cole et al., 2015). Regardless, when integrating over large areas, the heat budget closes within the range of uncertainty provided by the defined uncertainty in the diffusivity terms (i.e. κ_H is defined as 600±200 m^2 s^{-1} and κ_v is defined as $2.6x10^{-5}$ ± $2.4x10^{-5}$ m^2s^{-1}), which are based on previous estimates from the literature. This is something that can be improved upon.

6.1 Future Outlook

There are several avenues that can be explored to further the research presented in this thesis. Firstly, seasonal variations of the Weddell Gyre should be taken into account in future analyses. Resolving the seasonal cycle will be of primary importance in the near-surface ocean. This would allow me to overcome a major limitation of the study, namely the exclusion of the upper 50 dbar, and potentially provide an analysis of entrainment of WDW into WW and Surface Water, with major implications for the heat budget. It would also mean that we could determine the spatial structure and degree of the seasonal acceleration and deceleration of the gyre. This is an important topic that was investigated through satellite-derived sea-surface height by Armitage et al. (2018), who provide sea surface height fields in regions covered by sea-ice. Armitage et al. (2018) show that seasonal variability plays an important role in the circulation of the Southern Ocean. The analysis by Armitage et al. (2018), however, is limited to surface measurements, and lacks means of validation by in-situ measurements and lacks means of validation by in-situ measurements. The research presented in this thesis, if extended

to include seasonal analysis, could contribute greatly to Armitage et al.'s research, by extending the analysis downwards into the water column, especially if velocity data from moorings at the shelf-edge were included in the analysis, to improve the representation of the circulation at the shelf-edge. While a seasonal analysis was deemed unfeasible due to data sparsity in this work, it could become possible, once the time-variable position data of Argo floats when drifting under the sea-ice become available (using acoustic triangulation). Positioning of Argo floats under the sea-ice presents numerous possibilities for this research, namely, the additional velocity data could be incorporated into the stream function, greatly increasing the amount of data available to investigate the circulation of the Weddell Gyre. Under-ice float positioning and the subsequent improved sub-surface velocities could be used to investigate to what extent the circulation follows contours of constant potential vorticity over complex bathymetry, which was discussed in Chapter 4.4.2.

Resolving the seasonal variability is also important for isolating long-term trends in the upper ocean, since long-term trends in the temperature and salinity of WDW are difficult to extract due to strong decadal variability (Kerr et al., 2017; Fahrbach et al., 2011). Fahrbach et al. (2011) found that long-term trends in WDW and also WSDW and WSBW were masked by significant variability, from 1984 to 2008. In spite of the variability, however, the authors showed that the mean temperature and salinity of the whole water column exhibited a positive trend over the 24 year period. Hoppema et al. (2015) reported increasing trends in sub-surface nutrients, especially in the central of the section from Kapp Norvegia to Joineville Island over a period of 15 years. Given that the nutrient trends are synchronous with a significant increase in salinity in the WW layer, the author's hypothesise that the physical driver of the positive nutrient trends is increased upwelling in the centre of the Weddell Gyre. Given the month-to-month variability in the strength of the Weddell Gyre circulation, which is correlated with changes in the local wind stress curl (Armitage et al., 2018), determining long-term trends presents a significant challenge in investigating the response of the Weddell Gyre to modes of climate variability. This is especially prominent, seeing as the southerly shift and intensification of westerly winds over the Southern Ocean (i.e. shift to a more positive SAM index), is projected to increase under anthropogenic forcing in the near future (Zheng et al., 2013; Arblaster & Meehl, 2006), and a positive

SAM index has been associated with increased gyre strength and therefore upwelling in the centre of the Weddell Gyre (Cheon, 2013).

The research itself can be improved through the incorporation of all available data resources rather than Argo floats alone. This would include ship-based CTD data, temperature from instrumented seals, moorings, gliders and ice-tethered moorings for mapping the temperature and salinity to answer RQ. 1, and for providing the gridded density profiles from which the baroclinic contribution to the circulation was derived in RQ. 2. Velocity data from ADCP measurements from ship, moorings and surface buoy trajectories could be incorporated into the map of velocity, to which the stream function is fitted to answer RQ. 2. This could particularly help to resolve the flow (and heat advection) within boundary currents along the continental slope and shelf break, where float data are sparse and thus data from the other aforementioned platforms could fill important gaps. The flow within these boundary currents have been shown to contribute as much as 50-85 % to the overall flow and exhibit significant seasonal variability (Thompson & Heywood, 2008; Jullion et al. 2014; Armitage et al., 2018). With additional data, a time series of the gyre strength might become possible. The first simple step of splitting the climatology into shorter sub-periods was taken by Reeve et al. (2016) in Chapter 3. It was decided, however, that data density is inadequate to use these sub-periods in assessing the gyre circulation. It would be possible, if we limit the mapping to regions of adequate data density, to carry out a time series to determine the changes to water mass properties and maybe even velocities. This would be limited to regions where data density allow for it. The most recent time series of the hydrography in the Weddell Gyre was provided by Kerr et al. in 2017, for two sections, along the Prime Meridian, and for the section from Kapp Norvegia to Joineville Island. These are the two “traditional” cross-sections, from which three decades of data since 1984 are available. By focusing on available Argo float data (i.e. in the map of profile positions in Fig. 5.2c), the region with the largest data availability for a time series is also along the Prime Meridian. However, since profile data are available every 10 days, it would be possible to carry out a time series which incorporates seasonal variability, rather than ship-based analyses which are biased to summer conditions. In addition to the Prime Meridian, it may be possible to carry out a time series of available data (given the data density indicated in Fig. 5.2c) over the western circulation cell (indicated by the streamlines in Fig. 5.2c), the north-eastern part of the gyre (i.e. north of 65º S and east

of 20º E), and just downstream of the Prime Meridian, south of 65º S. There is, however, always a compromise between the time scale and length scale of the any analysis, which is sensitive to the density of available data, which may limit the feasibility of carrying out such a time series (Chapter 3.4.1).

In Chapter 5, it is shown that turbulent diffusion potentially plays an important role in (1) the distribution of heat once it has entered the Weddell Gyre (as is also indicated by Leach et al. 2011), (2) the import of heat along the northern boundary, and (3) as a mechanism by which heat could enter under the ice shelves along the southern coastline of the Weddell Gyre. There is also an indication that eddy-driven diffusion processes could be of particular importance in the Maud Rise region (Chapter 5.5.2), where the flanks of Maud Rise have been described as a region of extensive heat loss due to intense vertical convection (Muench et al., 2001; Akitomo, 2007). The Maud Rise region, and the region along the southern boundary of the southern limb of the gyre appear to be of considerable importance for the heat budget of the gyre, while the turbulent diffusion across the northern boundary accounts for a significant flux of heat into the Weddell Gyre. To confirm whether this is the case, one could carry out an investigation using eddy-resolving numerical model simulations, such as with FESOM (Finite Element Sea-Ice Ocean Model; Wang et al., 2014). In a recent study using the Massachusetts Institute of Technology (MIT) general circulation model, run at eddy- and tide- resolving horizontal resolution, Stewart et al., (2018) show that tidally-driven heat flux across the shelf break is compensated by offshore mean heat flux, so that the net shoreward heat flux agrees with the eddy heat flux, which cannot be accounted for by the eddy-driven cross-slope overturning circulation. The authors therefore suggest that eddy stirring along isopycnals is the main mechanism by which heat is transferred across the ASF (also Stewart & Thompson, 2016). A study by Hattermann et al. (2014) also highlights the central role of eddy processes in heat transport towards the Fimbul ice shelf, and subsequently basal melting. This mechanism agrees with the findings regarding the role of turbulent diffusion at the southern boundary in Chapter 5, but leads to further questions regarding the sensitivity of the eddy-driven shoreward heat flux to changes in the stratification of the water column (Stewart et al., 2018; Schmidtko et al., 2014) or in response to changing atmospheric conditions (Armitage et al., 2018).

Concerning observations, to further investigate the role of turbulent diffusion in distributing heat throughout the Weddell Gyre, estimates of diffusivity that vary

spatially and vertically need to be provided. Cole et al. (2015) has shown that this is possible to do with Argo floats, though the authors do not include the Weddell Gyre in their analysis. To determine estimates of heat diffusivity, would require velocity and temperature anomalies, which can both be obtained from Argo floats. While Cole et al. (2015) obtain velocity from the ECCO2 product (i.e. ocean state estimate), it is possible to obtain velocity estimates directly from the Argo floats, especially once the sub-surface float position data become available, which have been derived from the triangulation of the Argo float positions when drifting at depth. Donnelly et al., (2017) also obtain estimates of diffusivity directly from a combination of salinity observations (from various ship-based cross-sections within the Southern Ocean) and velocity data obtained from the ECCO model. Both Cole et al. (2015) and Donnelly et al., (2017) apply equations based on the second differential in the spatial distribution of salinity (i.e. $u\,\partial S'/\partial x = \kappa_H\,\partial^2 S/\partial y^2 + \kappa_V\,\partial^2 S/\partial y^2$, from Donnelly et al., 2017), which can also be applied to individual floats drifting within the Weddell Gyre. Thus, a useful way in which the research presented in this thesis could be extended and improved, is to calculate horizontal and vertical diffusivities from the Argo float profiles. This would allow us to determine more accurately to what extent turbulent diffusion plays a role in the three mechanisms described in the paragraph above.

The work presented in this thesis can also assist the decision making process regarding the future deployment of instruments. For example, the error maps in Chapter 3 highlight regions where additional measurements are required, though some of these gaps might be filled with already available data from other resources. The streamlines in Chapter 4 highlight the importance of obtaining adequate measurements to investigate how much of the WDW, and thus heat, actually reaches the southwest Weddell Gyre. For this purpose, the Prime Meridian appears not to be the best location due to the nearby influence of Maud Rise, and because of the large volume of water that flows northwards between 0 and 27° W. 27° W is identified as the mid-point between the northward flowing waters circulating the east core and the southward flowing waters that circulate the west core. A cruise campaign along the axis of the Weddell Gyre might be useful, especially one which identifies the mid-point between the two cores and uses this point to steam southwards towards the coast, to calculate how much water, and heat, enters the southwest region of the Weddell Gyre, where Deep- and Bottom-Water formation is known to occur.

Also, such a cruise could boost an investigation of upwelling along the central gyre axis (i.e. the upper cell of the overturning circulation in the Weddell Gyre), something that, to date, is lacking, as highlighted by Naveira Garabato et al. (2016), Jullion et al. (2014) and Hoppema et al. (2015). A useful tool for planning such a cruise might be satellite altimetry, providing the barotropic circulation as it varies from year to year (Armitage et al., 2018). In the north-eastern Weddell gyre, there is relatively large baroclinic shear, and a poorly constrained full-depth volume transport at 0° E, which indicates this to be a region where there could be bottom-intensified flow as an important component of the deep circulation. Thus, I would recommend the narrowest sector of the northern limb of the Weddell Gyre, at about 15-20° E, to be a region where future moorings might be deployed (if logistics allow for it), and perhaps even deep-sea profiling Argo floats, which are showing promise as a game-changer in autonomous deep-ocean oceanographic observations (Jayne et al., 2017).

The stream function could also be an invaluable observation-derived data resource for constraining regional climate models. This may be especially useful, as two open questions that stand out from this work are (1) to what extent is eddy-induced turbulent diffusion a mechanism for the transport of heat to underneath the ice shelves, and (2) how consistent, with seasonal variability and changing atmospheric conditions (such as that implied by the SAM index), is the double core structure of the Weddell Gyre? This second question is particularly important regarding the circulation and distribution of heat in the Weddell Gyre. For example, with changing wind conditions, the amount of heat that is circulated towards the gyre interior (where it may be upwelled and lost to the atmosphere), versus the amount of heat that is transported to the southwest Weddell Gyre (which brings it into close contact to regions of Deep- and Bottom Water formation and with the ice shelves), could also be subject to change. This has important consequences under a warming climate, since SAM has been shifting towards a more positive state possibly in part due to anthropogenic forcing, resulting in the southerly shift of more intensified Westerly winds (e.g. Marshall et al., 2004; Thompson & Solomon, 2002).

Lastly, the work presented in this thesis could provide a framework for the analysis of the circulation and distribution of heat in the Ross Gyre, as measurements in the Ross Gyre region become more abundant. According to the data selection tool on Coriolis (www.coriolis.eu.org), there are 320 Argo float profiles available in the region

of Ross Gyre (south of 60º S between 160º E and 120º W), a large number of which appear to have interpolated positions from being under the sea-ice (i.e. the green dots distributed along straight lines in Fig. 6.1). For comparison, data from 603 Argo floats were downloaded for the Weddell Gyre region in Chapter 4, and after quality control, this reduced to only 341 floats for trajectory data and 460 floats for profile data. There is an abundance of literature on the oceanography of the Weddell Gyre, while the Ross Gyre has comparatively little owing to the sparsity of data (Dotto et al., 2018). However, satellite altimetry data has led to useful insights to the drivers of Ross Gyre variability (Dotto et al., 2018). Other studies have shown that the Ross Gyre is an important region, regarding its contribution to basal ice-melt and therefore sea-level rise (Paolo et al., 2015; Rignot et al., 2013; Rye et al., 2014).

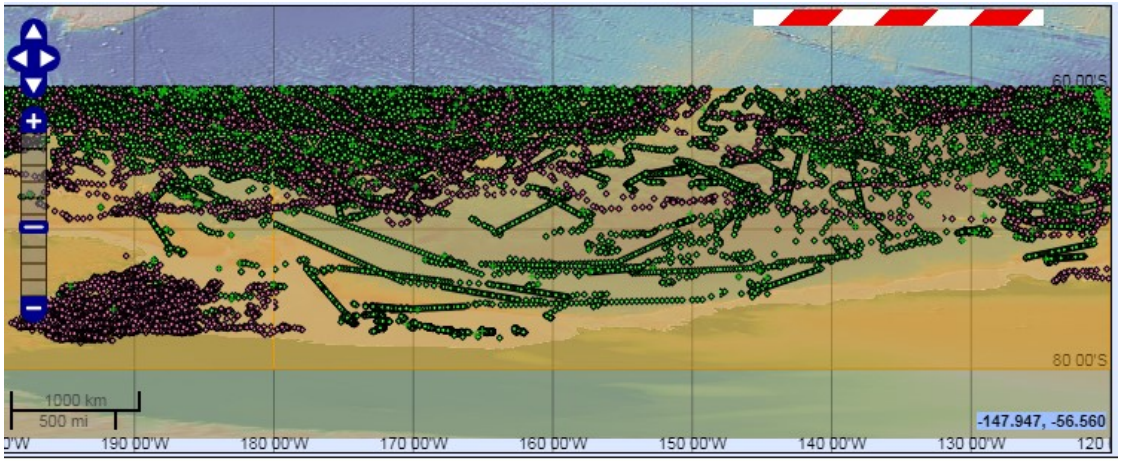

Fig. 6.1. Distribution of Argo float profiles (green) and animal-borne sensor profiles (pink), between 2000 and October 2018, from the data selection tool for Coriolis (www.coriolis.eu.org).

6.2 Final conclusion

The aim of this thesis was to determine the circulation and distribution of heat within the whole of the Weddell Gyre. The thesis achieved this, firstly by describing the distribution of heat contained in the core of WDW and the upper 50-2000 dbar, based on vertical profiles collected by Argo floats. The circulation was then described in detail through the provision of the stream function, derived from float trajectories and density profiles. The circulation was quantified through the calculation of volume transports across the central gyre axis and across various sections to provide comparisons and a

spatial context to the widely varying estimates in the literature. Lastly, the role of the circulation in distributing heat was assessed by providing a heat budget of a 1000 m layer of water encompassing the core of WDW for the entire Weddell Gyre.

Heat mostly enters the Weddell Gyre in the WDW through horizontal advection, where convergence due to mean horizontal advection contributes 26 ± 1 TW to the heat budget in the southern limb. 20 ± 10 TW of heat is diffused southwards into the Weddell Gyre along the northern boundary. There is a northward heat flux due to mean horizontal advection from the southern limb towards the gyre centre, owing to the distinct double cell structure of the Weddell Gyre, where the eastern cell is stronger and more elongated than the western cell. There is a turbulent heat flux of 6.5 ± 3 TW from the southern limb into the interior circulation cell of the Weddell Gyre, which is the region where the core of WDW (i.e. the sub-surface temperature maximum) is coldest and shallowest. Maud Rise influences the distribution of heat from the core of WDW, where, owing to a Taylor column on top of this sea mount, the subsurface temperature maximum is colder and deeper. The presence of Maud Rise perturbs the heat budget, resulting in a convergence of heat upstream and a divergence of heat downstream of Maud Rise, which is dominated by the mean horizontal advection, most likely due to the velocity field being unable to resolve the localised flow around Maud Rise. There is, however, and indication that horizontal turbulent diffusion, driven by eddy processes, are of particular importance on the flanks of Maud Rise. Upstream and north of Maud Rise, some of the streamlines are forced to veer around Maud Rise, resulting in increased intensity of flow. The intensified flow may influence the amount of water and heat that is transported towards the gyre centre rather than towards the southwestern Weddell Sea, though the question remains as to how permanent this feature is, or whether it is a consequence of mapping a data sparse region without time averaging.

Overall, when integrating over large areas, mean heat advection balances with turbulent heat diffusion, resulting in a mostly closed heat budget, where the warming indicated by the resulting heat tendency (sum of all heat budget terms) is comparable to warming trends in the literature for the corresponding time period, from 2002 to 2016. The southward turbulent diffusion of heat towards the continental shelves implies that turbulent diffusion may be an important mechanism by which heat enters under the ice shelves, which has also been implied by Hattermann et al. (2014), Daee et al. (2017) and Stewart et al., (2018), leading to basal ice melt (Hattermann et al., 2014). Thus,

understanding this mechanism is important in the context of sea level rise, especially in the context of anthropogenic forcing (Hellmer et al., 2017). Lastly, how the double cell circulation structure of the Weddell Gyre, and its role in distributing heat throughout the Weddell Gyre, might change with changing atmospheric conditions (such as the strengthening and southward migration of westerly winds associated with a positive SAM, e.g. Marshall, 2003), is an important open question that needs to be addressed in future research, if we are to truly understand the role of the Weddell Gyre in a global climate perspective.

7 Reference List

Abernathey, R.P., Cerovecki, I., Holland, P.R., Newsom, E., Mazloff, M. and Talley, L.D.: Water-mass transformation by sea ice in the upper branch of the Southern Ocean overturning. Nature Geoscience, 9(8), p.596, 2016.

Akitomo, K.: Thermobaric deep convection, baroclinic instability, and their roles in vertical heat transport around Maud Rise in the Weddell Sea, Journal of Geophysical Research, 111, C09027, doi:10.1029/2005JC003284, 2006.

Allen, J. T. and Smeed, D. A.: Potential Vorticity and Vertical Velocity at the Iceland-Færœs Front, Journal of Physical Oceanography, 26(12), pp. 2611-2634, 1996.

Anilkumar, N., Chacko, R., Sabu, P. and George, J. V.: Freshening of Antarctic Bottom Water in the Indian Ocean sector of Southern Ocean, Deep Sea Research Part II: Topical Studies in Oceanography, (0), 2015.

Antonov, J. I., Locarnini, R. A., Boyer, T. P., Mishonov, A. V., and Garcia, H. E.: World Ocean Atlas 2005, Volume 2: Salinity. S. Levitus, Ed. NOAA Atlas NESDIS 62, U.S. Government Printing Office, Washington, D.C., 182 pp., 2006.

Antonov, J. I., Seidov,D., Boyer, T. P., Locarnini, R. A., Mishonov, A. V., Garcia H. E., Baranova, O. K., Zweng, M. M., and Johnson, D. R.: World Ocean Atlas 2009, Volume 2: Salinity. S. Levitus, Ed. NOAA Atlas NESDIS 69, U.S. Government Printing Office, Washington, D.C., 184 pp., 2010.

Arblaster, J.M. and Meehl, G.A.: Contributions of external forcings to southern annular mode trends. Journal of climate, 19(12), pp.2896-2905, 2006.

Armitage, T.W., Kwok, R., Thompson, A.F. and Cunningham, G.: Dynamic topography and sea level anomalies of the Southern Ocean: Variability and teleconnections. Journal of Geophysical Research: Oceans, 123(1), pp.613-630, 2018.

Årthun, M., Nicholls, K.W., Makinson, K., Fedak, M.A. and Boehme, L.: Seasonal inflow of warm water onto the southern Weddell Sea continental shelf, Antarctica. Geophysical Research Letters, 39(17), 2012.

Bagriantsev, N.V., Gordon, A.L. and Huber, B.A.: Weddell Gyre: temperature maximum stratum. Journal of Geophysical Research: Oceans, 94(C6), pp.8331-8334, 1989.

Baker, D.J. Jr., Nowlin, W.D. Jr., Pillsbury, R.D., Bryden, H.L.: Antarctic circumpolar current: space and time fluctuations in the Drake Passage, Nature, 268, 696–699, 1977.

Barnes, S. L.: A technique for maximizing details in numerical weather map analysis. Journal of Applied Meteorology, 3, 396-409, 1964.

Barnes, S. L.,: Applications of the Barnes Objective Analysis Scheme, Part III: Tuning for Minimum Error. Journal of Atmospheric and Oceanic Technology, 11, 1459-1479, 1994.

Beckmann, A., Hellmer, H.H., Timmermann, R.: A numerical model of the Weddell Sea: large-scale circulation and water mass distribution. Journal of Geophysical Research 104, 23375–23391, 1999.

Behrendt, A., Fahrbach, E., Hoppema, M., Rohardt, G., Boebel, O., Klatt, O., Wisotzki, A., and Witte, H.: Variations of winter water properties and sea ice along the greenwich meridian on decadal time scales, Deep Sea Research Part II: Topical Studies in Oceanography, 58, 2524-2532, http://dx.doi.org/10.1016/j.dsr2.2011.07.001, 2011.

Bersch, M., Becker, G. A., Frey, H., and Koltermann, K. P.: Topographic effects of the Maud Rise on the stratification and circulation of the Weddell Gyre, Deep Sea Research, 39, 303–331, 1992.

Böhme, L., and Send, U.: Objective analyses of hydrographic data for referencing profiling float salinities in highly variable environments, Deep Sea Research Part II: Topical Studies in Oceanography, 52, 651-664, 2005. http://dx.doi.org/10.1016/j.dsr2.2004.12.014.

Brennecke, W.: Ozeanographische Ergebnisse der zweiten französischen, der schwedischen und der schottischen Südpolarexpedition. 1918.

Bretherton, F. P., Davis, R. E., and Fandry, C. B.: A technique for objective analysis and design of oceanographic experiments applied to mode-73, Deep Sea Research and Oceanographic Abstracts, 23, 559-582, 1976. http://dx.doi.org/10.1016/0011-7471(76)90001-2.

Brown, P.J., Jullion, L., Landschützer, P., Bakker, D.C., Naveira Garabato, A.C., Meredith, M.P., Torres-Valdés, S., Watson, A.J., Hoppema, M., Loose, B. and Jones, E.M.: Carbon dynamics of the Weddell Gyre, Southern Ocean. Global Biogeochemical Cycles, *29*(3), pp.288-306, 2015.

Callahan, J.E.: The structure and circulation of deep water in the Antarctic. Deep-Sea Research 19, 563—575, 1972.

Chamberlain, P., Talley, L.D., Mazloff, M., Riser, S., Speer, K., Gray, A.R. and Schwartzman, A.: Observing the ice-covered Weddell Gyre with profiling floats: position uncertainties and correlation statistics. Journal of Geophysical Research: Oceans, 2018. https://doi.org/10.1029/2017JC012990

Chang, Y.-S., Rosati, A. J., Zhang, S., and Harrison, M. J.: Objective analysis of monthly temperature and salinity for the world ocean in the 21st century: Comparison with world ocean atlas and application to assimilation validation, Journal of Geophysical Research: Oceans, 114, C02014, 10.1029/2008jc004970, 2009.

Cheon, W.G., Park, Y., Toggweiler, J.R., and Lee, S.: The Relationship of Weddell Polynya and Open-Ocean Deep Convection to the Southern Hemisphere Westerlies. Journal of Physical Oceanography, 44, 694–713, https://doi.org/10.1175/JPO-D-13-0112.1, 2014.

Chevanne, C.P., Heywood, K.J., Nicholls, K.W., Fer, I.: Observations of the Antarctic Slope Undercurrent in the southeastern Weddell Sea, Geophysical Research Letters, Vol. 37, 13, https://doi.org/10.1029/2010GL043603, 2010.

Cisewski, B., Strass, V.H., and Prandke, H.: Upper-ocean vertical mixing in the Antarctic Polar Front Zone, Deep-Sea Research II, 52:1087–1108. doi:10.1016/j.dsr2.2005.01.010, 2005.

Cisewski, B., V. H. Strass, M. Losch, and H. Prandke: Mixed layer analysis of a mesoscale eddy in the Antarctic Polar Front Zone, Journal of Geophysical Research, 113, C05017, 2008. https://doi.org/10.1029/2007JC004372.

Cisewski, B., Strass, V. and Leach, H.: Circulation and transport of water masses in the Lazarev Sea, Antarctica, during summer and winter 2006, Deep-Sea Research I, 58, pp. 186-199, 2011. https://doi.org/10.1016/j.dsr.2010.12.001.

Cole, S. T., C. Wortham, E. Kunze, and W. B. Owens: Eddy stirring and horizontal diffusivity from Argo float observations: Geographic and depth variability. Geophysical Research Letters, 42, 3989–3997, 2015. https://doi.org/10.1002/2015GL063827.

Coles, V.J., McCartney, M.S., Olson, D.B. and Smethie, W.M.: Changes in Antarctic Bottom Water properties in the western South Atlantic in the late 1980s. Journal of Geophysical Research: Oceans, 101(C4), pp.8957-8970, 1996.

Comiso, J. C., Gordon, A. L.: Cosmonaut polynya in the Southern Ocean: structure and variability. J.Geophys.Res.101,18297–18313, 1996.

Couldrey, M. P., Jullion, L., Naveira Garabato, A. C., Rye, C., Herráiz-Borreguero, L., Brown, P. J., Meredith, M. P. and Speer, K. L.: Remotely induced warming of Antarctic Bottom Water in the eastern Weddell gyre, Geophysical Research Letters, 40(11), pp. 2755-2760, 2013.

Cox, M.D.: An idealized model of the world ocean. Part I: The global-scale water masses. Journal of Physical Oceanography, 19, 1730-1752, 1989.

Cressman, G. P.: An operational objective analysis scheme. Monthly Weather Review, 87, 329-340, 1959.

Daae, K., T. Hattermann, E. Darelius, and I. Fer: On the effect of topography and wind on warm waterinflow—An idealized study of the southern Weddell Sea continental shelf system, Journal of Geophysical Research: Oceans,122, 2622–2641, 2017. https://doi.org/10.1002/2016JC012541.

Darelius, E., Fer, I. and Nicholls, K.W.: Observed vulnerability of Filchner-Ronne Ice Shelf to wind-driven inflow of warm deep water. Nature communications, 7, p.12300, 2016.

Deacon, G. E. R.: The hydrology of the Southern Ocean. Cambridge University Press, 1937.

Deacon, G.E.R,: The Weddell Gyre. Deep-Sea Research 26A, 981–995, 1979.

Deacon, G.E.R.: Physical and biological zonation in the Southern Ocean, Deep Sea Research Part I: Oceanographic Research Papers, vol. 29, 1, 1-15, 1982. https://doi.org/10.1016/0198-0149(82)90058-9.

Dong, S., and K. A. Kelly: Heat budget in the Gulf Stream region: The importance of heat storage and advection. Journal of Physical Oceanography, 34, 1214–1231, 2004. https://doi.org/ 10.1175/1520-0485(2004)034.

Dong, S, Gille ST, Sprintall J.: An assessment of the Southern Ocean mixed layer heat budget. Journal of Climate. 20:4425-4442, 2007.

Dong, J., Speer, K. and Jullion, L.: The Antarctic Slope Current near 30°E, Journal of Geophysical Research: Oceans, 121(2), pp. 1051-1062, 2016.

Donnelly, M., Leach, H. and Strass, V.: Modification of the deep salinity-maximum in the Southern Ocean by circulation in the Antarctic Circumpolar Current and the Weddell Gyre. Ocean Dynamics, 67(7), pp.813-838, 2017.

Dotto, T. S., Naveira Garabato, A., Bacon, S., Tsamados, M., Holland, P. R., Hooley, J., et al. Variability of the Ross Gyre, Southern Ocean: Drivers and responses revealed by satellite altimetry. Geophysical Research Letters, 45, 6195–6204, 2018. https://doi.org/10.1029/2018GL078607.

Fahrbach, E., de Baar, H.: The expedition of the research vessel "polarstern" to the antarctic in 2008 (ant-xxiv/3). Polar- und Meeresforschung 606, AWI, Bremerhaven, 228, 2010.

Fahrbach, E., Knoche, M. and Rohardt, G.: AN ESTIMATE OF WATER MASS TRANSFORMATION IN THE SOUTHERN WEDDELL SEA', Marine Chemistry, 35(1-4), pp. 25-44, 1991.

Fahrbach, E., Rohardt, G., Schröder, M. and Strass, V.: Transport and structure of the Weddell Gyre, Annales Geophysicae, 12, pp. 840-855, 1994.

Fahrbach, E., Rohardt, G., Scheele, N., Schröder, M., Strass, V. and Wisotzki, A.: Formation and discharge of deep and bottom water in the northwestern Weddell Sea, Journal of Marine Research, 53 (4), pp. 515-538, 1995.

Fahrbach, E., Hoppema, M., Rohardt, G., Schröder, M., and Wisotzki, A.: Decadal-scale variations of water mass properties in the deep weddell sea, Ocean Dynamics, 54, 77-91, 2004. https://doi.org/10.1007/s10236-003-0082-3.

Fahrbach, E., Rohardt, G. and Sieger, R.: 25 years of polarstern hydrography (1982 - 2007), WDC-MARE Reports 5, Alfred-Wegener-Institut, Bremerhaven, 94pp., 2007.

Fahrbach, E., Hoppema, M., Rohardt, G., Boebel, O., Klatt, O., and Wisotzki, A.: Warming of deep and abyssal water masses along the greenwich meridian on decadal time scales: The weddell gyre as

a heat buffer, Deep Sea Research Part II: Topical Studies in Oceanography, 58, 2509-2523, 2011. http://dx.doi.org/10.1016/j.dsr2.2011.06.007.

Fiekas, V., H. Leach, K. Mirbach, and J.D. Woods: Mesoscale Instability and Upwelling. Part 1: Observations at the North Atlantic Intergyre Front. Journal of Physical Oceanography, 24, 1750–1758, https://doi.org/10.1175/1520-0485, 1994.

Foldvik, A., Gammelsrød, T., Østerhus, S., Fahrbach, E., Rohardt, G., Schröder, M., Nicholls, K.W., Padman, L. and Woodgate, R.A.: Ice shelf water overflow and bottom water formation in the southern Weddell Sea. Journal of Geophysical Research: Oceans, 109(C2), 2004.

Forryan, A., Martin, A.P., Srokosz, M.A., Popova, E.E., Painter, S.C. and Renner, A.H.: A new observationally motivated Richardson number based mixing parametrization for oceanic mesoscale flow. Journal of Geophysical Research: Oceans, 118(3), pp.1405-1419, 2013.

Foster, T. D., Foldvik, A., and Middleton, J. H.: Mixing and bottom water formation in the shelf break region of the southern weddell sea, Deep Sea Research Part A. Oceanographic Research Papers, 34, 1771-1794, http://dx.doi.org/10.1016/0198-0149(87)90053-7, 1987.

Foster, T.D. and Middleton, J.H.: Bottom water formation in the western Weddell Sea. Deep Sea Research Part A. Oceanographic Research Papers, 27(5), pp.367-381, 1980.

Foster, T.D. and Carmack, E.C.: Temperature and salinity structure in the Weddell Sea. Journal of Physical Oceanography, 6(1), pp.36-44, 1976.

Gandin, L. S.: Objective analysis of meteorological fields, Israel Program for Scientific Translations, Jerusalem, 1965.

GiII, A.E., and Bryan, K.: Effects of geometry on the circulation of a three-dimensional southern hemisphere ocean model. Deep Sea Research, 18. 685-721, 1971.

Gille, S. T.: Float Observations of the Southern Ocean. Part I: Estimating Mean Fields, Bottom Velocities, and Topographic Steering, Journal of Physical Oceanography, 33(6), pp. 1167-1181, 2003.

Gordon, A.L.: Deep antarctic convection west of Maud Rise. Journal of Physical Oceanography, 8(4), pp.600-612, 1978.

Gordon, A.L., Huber, B.A.: Thermohaline stratification below the Southern Ocean sea ice. Journal of Geophysical Research, 89 (C1), 641–648, 1984.

Gordon, A.L., Huber, B.A.: Southern Ocean winter mixed layer. Journal of Geophysical Research 95, 11655–11672, 1990.

Gordon, A.L., Martinson, D.G. and Taylor, H.W.: The wind-driven circulation in the Weddell-Enderby Basin. Deep-Sea Research Part A. Oceanographic Research Papers, 28(2), pp.151-163, 1981.

Gordon, A.L., Visbeck, M. and Huber, B.: Export of Weddell Sea deep and bottom water. Journal of Geophysical Research: Oceans, 106(C5), pp.9005-9017, 2001.

Gordon, A.L., Huber, B., McKee, D. and Visbeck, M.: A seasonal cycle in the export of bottom water from the Weddell Sea. Nature Geoscience, 3(8), p.551, 2010.

Gouretski, V.V., and Danilov, A.I.: Weddell Gyre: structure of the eastern boundary. Deep-Sea Research I, 40:561–582. doi:10.1016/0967-0637(93)90146-T, 1993.

Gouretski, V.V., and Danilov, A.I.: Characteristics of warm rings in the African sector of the Antarctic circumpolar current. Deep-Sea Research I, 41:1131–1157, 1994. https://doi.org/doi:10.1016/0967-0637(94)90037-X.

Gouretski, V.V. and K.P. Koltermann,: WOCE Global Hydrographic Climatology. 35/2004, Berichte des Bundesamtes fur Seeschifffahrt und Hydrographie, 52 pp., 2004.

Gray, A. R. and Riser, S. C.: A Global Analysis of Sverdrup Balance Using Absolute Geostrophic Velocities from Argo, Journal of Physical Oceanography, 44(4), pp. 1213-1229 2014.

Hadfield, R. E., Wells, N. C., Josey, S. A., and Hirschi, J. J. M.: On the accuracy of north atlantic temperature and heat storage fields from argo, Journal of Geophysical Research: Oceans, 112, C01009, 2007. https://doi.org/10.1029/2006jc00382.

Hattermann, T., Smedsrud, L.H., Nøst, O.A., Lilly, J.M. and Galton-Fenzi, B.K.: Eddy-resolving simulations of the Fimbul Ice Shelf cavity circulation: Basal melting and exchange with open ocean. Ocean Modelling, 82, pp.28-44, 2014.

Hayakawa, H., Shibuya, K., Aoyama, Y., Nogi, Y., Doi, K.: Ocean bottom pressure variability in the Antarctic Divergence Zone off Lützow-Holm Bay, East Antarctica, Deep Sea Research Part I: Oceanographic Research Papers, Vol. 60, 22-31, 2012. https://doi.org/10.1016/j.dsr.2011.09.005.

Hellmer, H.H., Kauker, F., Timmermann, R., Determann, J. and Rae, J.: Twenty-first-century warming of a large Antarctic ice-shelf cavity by a redirected coastal current. Nature, 485(7397), p.225, 2012.

Hellmer, H.H., Kauker, F., Timmermann, R. and Hattermann, T.: The fate of the southern Weddell Sea continental shelf in a warming climate. Journal of Climate, 30(12), pp.4337-4350, 2017.

Heywood, K. J. and King, B. A.: Water masses and baroclinic transports in the South Atlantic and Southern oceans, Journal of Marine Research, 60(5), pp. 639-676, 2002.

Heywood, K.J. and Stevens, D.P.: Meridional heat transport across the Antarctic Circumpolar Current by the Antarctic Bottom Water overturning cell. Geophysical research letters, 34(11), 2007.

Heywood, K. J., Locarniniu, R. A., Frew, R. D., Dennis, P. F. and King, B. A.: TRANSPORT AND WATER MASSES OF THE ANTARCTIC SLOPE FRONT SYSTEM IN THE EASTERN WEDDELL SEA', ANTARCTIC RESEARCH SERIES, 75, pp. 203-214, 1998.

Heywood, K.J., Naveira Garabato, A.C., Stevens, D.P. and Muench, R.D.: On the fate of the Antarctic Slope Front and the origin of the Weddell Front. Journal of Geophysical Research: Oceans, 109(C6), 2004.

Holland, P.R. and Kwok, R.: Wind-driven trends in Antarctic sea-ice drift. Nature Geoscience, 5(12), p.872, 2012.

Hoppema, M., Klatt, O., Roether, W., Fahrbach, E., Bulsiewicz, K., Rodehacke, C. and Rohardt, G.: Prominent renewal of Weddell Sea Deep Water from a remote source, Journal of Marine Research, 59(2), pp. 257-279, 2001.

Hoppema, M., Bakker, K., van Heuven, S.M., van Ooijen, J.C. and de Baar, H.J.: Distributions, trends and inter-annual variability of nutrients along a repeat section through the Weddell Sea (1996–2011). Marine chemistry, 177, pp.545-553, 2015.

IOC, IHO and. BODC: Centenary edition of the gebco digital atlas, in, Published on CD-ROM on behalf of the Intergovernmental Oceanographic Commission and the International Hydrographic Organization as part of the General Bathymetric Chart of the Oceans;, British Oceanographic Data Centre, Liverpool, 2003.

IOC, SCOR and IAPSO: The international thermodynamic equation of seawater - 2010: Calculation and use of thermodynamic properties., Intergovernmental Oceanographic Commision, 196, 2010.

Jacobs, S. S.: On the nature and significance of the Antarctic Slope Front, Marine Chemistry, 35, 9–24, 1991. https://doi.org/ 10.1016/S0304-4203(09)90005-6.

Jayne, S.R., Roemmich, D., Zilberman, N., Riser, S.C., Johnson, K.S., Johnson, G.C. and Piotrowicz, S.R.: The Argo Program: present and future. Oceanography, 30(2), pp.18-28, 2017.

Jeffreys, H.: On fluid motions produced by differences of temperature and humidity, Q.J.R. Meteorol. Soc., 51, 347–356, 1925.

Johnson, G. C.: Quantifying antarctic bottom water and north atlantic deep water volumes, Journal of Geophysical Research: Oceans, 113, C05027, 2008. https://doi.org/10.1029/2007jc004477.

Johnson, G. C. and Doney, S. C.: Recent western South Atlantic bottom water warming, Geophysical Research Letters, 33(14), 2006.

Johnson, G.C., Purkey, S.G. and Bullister, J.L.: Warming and freshening in the abyssal southeastern Indian Ocean. Journal of Climate, 21(20), pp.5351-5363, 2008.

Jones, R. W., I. A. Renfrew, A. Orr, B. G. M. Webber, D. M. Holland, and M. A. Lazzara: Evaluation of four global reanalysis products using in situ observations in the Amundsen Sea Embayment, Antarctica, Journal of Geophysical Research, Atmosphere, 121, 6240–6257, 2016. https://doi.org/ 10.1002/2015JD024680.

Jullion, L., Jones, S.C., Naveira Garabato, A.C. and Meredith, M.P.: Wind-controlled export of Antarctic Bottom Water from the Weddell Sea. Geophysical Research Letters, 37(9), 2010.

Jullion, L., Garabato, A.C.N., Bacon, S., Meredith, M.P., Brown, P.J., Torres-Valdés, S., Speer, K.G., Holland, P.R., Dong, J., Bakker, D. and Hoppema, M.: The contribution of the Weddell Gyre to the lower limb of the Global Overturning Circulation. Journal of Geophysical Research: Oceans, 119(6), pp.3357-3377, 2014.

Kawano, T., Fukasawa, M., Kouketsu, S., Uchida, H., Doi, T., Kaneko, I., Aoyama, M. and Schneider, W.: Bottom water warming along the pathway of lower circumpolar deep water in the Pacific Ocean. Geophysical Research Letters, 33(23), 2006.

Kerr, R., Dotto, T.S., Mata, M.M. and Hellmer, H.H.: Three decades of deep water mass investigation in the Weddell Sea (1984–2014): temporal variability and changes. Deep Sea Research Part II: Topical Studies in Oceanography, 2017.

Killworth, P. D.: An equivalent-barotropic mode in the Fine Resolution Antarctic Model, Journal of Physical Oceanography, 22, 1379–1387, 1992.

Killworth, P. D., and Hughes, C. W.: The Antarctic Circumpolar Current as a free equivalent-barotropic jet, J. Mar. Res., 60, 19–45, 2002.

Klatt, O., Fahrbach, E., Hoppema, M., and Rohardt, G.: The transport of the weddell gyre across the prime meridian, Deep Sea Research Part II: Topical Studies in Oceanography, 52, 513-528, 2005. http://dx.doi.org/10.1016/j.dsr2.2004.12.015.

Klatt, O., Boebel, O., and Fahrbach, E.: A profiling float's sense of ice, Journal of Atmospheric and Oceanic Technology, 24, 1301-1308, 10.1175/jtech2026.1, 2007.

Koenig, Z., C. Provost, R. Ferrari, N. Sennéchael, and M.-H. Rio: Volume transport of the Antarctic Circumpolar Current: Production and validation of a 20 year long time series obtained from in situ and satellite observations, Journal of Geophysical Research: Oceans, 119, 5407–5433, 2014. https://doi.org/10.1002/2014JC009966.

Komuro, Y. and Hasumi, H.: Effects of surface freshwater flux induced by sea ice transport on the global thermohaline circulation. Journal of Geophysical Research: Oceans, 108(C2), 2003.

Koshlyakov, M. N. and Tarakanov, R. Yu.: Water Transport across the Subantarctic Front and the Global Ocean Conveyer Belt, Oceanology, 2011, Vol. 51, No. 5, pp. 721–735, 2011. https://doi.org/10.1134/S0001437011050110.

Koszalka, I., LaCasce, J.H. and Orvik, K.A.: Relative dispersion in the Nordic Seas. Journal of Marine Research, 67(4), pp.411-433, 2009.

LaCasce, J. H.: Floats and f/H', Journal of Marine Research, 58(1), pp. 61-95, 2000.

Leach, H., Strass, V. and Cisewski, B.: Modification by Lateral Mixing of the Warm Deep Water entering the Weddell Sea in the Maud Rise Region, Ocean Dynamics, 61 (1), pp. 51-68, 2011 https://doi.org/10.1007/s10236-010-0342-y.

Lebedev , K. V., H. Yoshinari, H., Maximenko, N. A. and Hacker, P.: YoMaHa'07: Velocity data assessed from trajectories of Argo floats at parking level and at the sea surface. IPRC Technical Note No. 4(2), 2007.

Ledwell, J.R., Watson, A.J., and Law, C.S.: Mixing of a tracer in the pycnocline. Journal of Geophysical Research-Oceans, 103:21499– 21529, 1998.

Ledwell, J.R., Montgomery, E.T., Polzin, K.L., St Laurent, L.C., Schmitt, R.W., and Toole, J.M.: Evidence for enhanced mixing over rough topography in the abyssal ocean, Nature 403:179–182, 2000.

Levitus,S., Conkright, M.E., Reid, J.L., Najjar, R.G., Mantyla, A.: Distribution of nitrate, phosphate and silicate in the world oceans, Progress in Oceanography, Vol. 31, 3, 245-273, 1993.

Levitus, S., Antonov, J. I., Boyer, T. P., Baranova, O. K., Garcia, H. E., Locarnini, R. A., Mishonov, A. V., Reagan, J. R., Seidov, D., Yarosh, E. S., and Zweng, M. M.: World ocean heat content and thermosteric sea level change (0–2000 m), 1955–2010, Geophysical Research Letters, 39, L10603, 10.1029/2012gl051106, 2012.

Locarnini, R. A., Whitworth, T. and Nowlin, W. D.: The importance of the Scotia Sea on the outflow of Weddell Sea Deep Water, Journal of Marine Research, 51(1), pp. 135-153, 1993.

Locarnini, R. A., Mishonov, A. V., Antonov, J. I., Boyer, T. P., and Garcia, H. E.: World Ocean Atlas 2005, Volume 1: Temperature. S. Levitus, Ed. NOAA Atlas NESDIS 61, U.S. Government Printing Office, Washington, D.C., 182 pp., 2006.

Locarnini, R. A., Mishonov, A. V., Antonov, J. I., Boyer, T. P., and Garcia, H. E., Baranova, O. K., Zweng, M. M., and Johnson, D. R.: World Ocean Atlas 2009, Volume 1: Temperature. S. Levitus, Ed. NOAA Atlas NESDIS 68, U.S. Government Printing Office, Washington, D.C., 184 pp., 2010.

Locarnini, R. A., Mishonov, A. V., Antonov, J. I., Boyer, T. P., and Garcia, H. E., Baranova, O. K., Zweng, M. M., Paver, C. R., Reagan, J. R., Johnson, D. R., Hamilton, M., and Seidov, D.: World Ocean Atlas 2013, Volume 1: Temperature. S. Levitus, Ed., A. Mishonov Technical Ed.; NOAA Atlas NESDIS 73, 40 pp., 2013.

Lumpkin, R. and Elipot, S.: Surface drifter pair spreading in the North Atlantic. Journal of Geophysical Research: Oceans, 115(C12), 2010.

Lyman, J. M., and Johnson, G. C.: Estimating annual global upper-ocean heat content anomalies despite irregular in situ ocean sampling, Journal of Climate, 21, 5629-5641, 2008. https://doi.org/10.1175/2008jcli2259.1.

Lyman, J. M., Good, S. A., Gouretski, V. V., Ishii, M., Johnson, G. C., Palmer, M. D., Smith, D. M., and Willis, J. K.: Robust warming of the global upper ocean, Nature, 465, 334-337, 2010. http://www.nature.com/nature/journal/v465/n7296/suppinfo/nature09043_S1.html.

Marshall, G.J.: Trends in the Southern Annular Mode from Observations and Reanalyses. Journal of Climate, 16, 4134–4143, 2003. https://doi.org/10.1175/1520-0442(2003)016.

Marshall, G.J., Stott, P.A., Turner, J., Connolley, W.M., King, J.C. and Lachlan-Cope, T.A.: Causes of exceptional atmospheric circulation changes in the Southern Hemisphere. Geophysical Research Letters, 31(14), 2004.

Marshall, J. and Speer, K.: Closure of the meridional overturning circulation through Southern Ocean upwelling. Nature Geoscience, 5(3), p.171, 2012.

Matano, R. P., Gordon, A. L., Muench, R. D. and Palma, E. D.: A numerical study of the circulation in the northwestern Weddell Sea, Deep Sea Research Part II: Topical Studies in Oceanography, 49(21), pp. 4827-4841, 2002.

Mazloff, M.R., Heimbach, P. and Wunsch, C.: An eddy-permitting Southern Ocean state estimate. Journal of Physical Oceanography, 40(5), pp.880-899, 2010.

McDougall, T. J. and Barker, P. M.: Getting started with TEOS-10 and the Gibbs Seawater (GSW) Oceanographic Toolbox, 28pp., SCOR/IAPSO WG127, 2011.

McIntosh, P. C.: Oceanographic data interpolation: Objective analysis and splines, Journal of Geophysical Research: Oceans, 95, 13529-13541, 1990. https://doi.org/10.1029/JC095iC08p13529.

McKee, D.C., Yuan, X., Gordon, A.L., Huber, B.A. and Dong, Z.: Climate impact on interannual variability of Weddell Sea Bottom Water. Journal of Geophysical Research: Oceans, 116(C5), 2011.

Menemenlis, D., I. Fukumori, and T. Lee: Using Green's Functions to calibrate and Ocean General Circulation Model, Monthly Weather Review, 133, 1224–1240, 2005.

Menemenlis, D., Campin, J.M., Heimbach, P., Hill, C., Lee, T., Nguyen, A., Schodlok, M., and Zhang, H.: ECCO2: High resolution global ocean and sea ice data synthesis, Mercator Ocean Quarterly Newsletter, 31, 13–21, 2008.

Meredith, M. P., Locarnini, R. A., Van Scoy, K. A., Watson, A. J., Heywood, K. J. and King, B. A.: On the sources of Weddell Gyre Antarctic Bottom Water', Journal of Geophysical Research-Oceans, 105(C1), pp. 1093-1104, 2000.

Meredith, M.P., Garabato, A.C.N., Gordon, A.L. and Johnson, G.C.: Evolution of the deep and bottom waters of the Scotia Sea, Southern Ocean, during 1995–2005. Journal of Climate, 21(13), pp.3327-3343, 2008.

Meredith, M.P., Gordon, A.L., Naveira Garabato, A.C., Abrahamsen, E.P., Huber, B.A., Jullion, L., and Venables, H.J.: Synchronous intensification and warming of Antarctic Bottom Water outflow from the Weddell Gyre, Geophysical Research Letters, 38, L03603, 2011. https://doi.org/10.1029/2010GL046265.

Meredith, M.P., Ducklow, H.W., Schofield, O., Wahlin, A., Newman, L. and Lee, S.: The interdisciplinary marine system of the Amundsen Sea, Southern Ocean: Recent advances and the need for sustained observations. Deep Sea Research II, 123, pp.1-6, 2016.

Muench, R. D., Morison, J. H., Padman, L., Martinson, D., Schlosser, P., Huber, B. and Hohmann, R.: Maud Rise revisited, Journal of Geophysical Research, 106, C2, 2423-2440, 2001.

Muench, R. D., Morison, J. H., Padman, L., Martinson, D., Schlosser, P., Huber, B., and Hohmann, R.: Maud Rise revisited, Journal of Geophysical Research, 106, 2423–2440, 2001.

Munk, W. and Wunsch, C.: Abyssal recipes II: Energetics of tidal and wind mixing. Deep Sea Research Part I: Oceanographic Research Papers, 45(12), pp.1977-2010, 1998.

Naveira Garabato, A. C., McDonagh, E. L., Stevens, D. P., Heywood, K. J. and Sanders, R. J.: On the export of Antarctic Bottom Water from the Weddell Sea', Deep-Sea Research Part Ii-Topical Studies in Oceanography, 49(21), pp. 4715-4742, 2002.

Naveira Garabato, A.C., Oliver, K.I.C., Watson, A.J. and Messias, M.J.: Turbulent diapycnal mixing in the Nordic Seas, Journal of Geophysical Research, 109:C12010, 9 pp., 2004a https://doi.org/10.1029/2004JC002411.

Naveira Garabato, A.C., Polzin, K.L., King, B.A., Heywood, K.J., and Visbeck, M.: Widespread intense turbulent mixing in the Southern Ocean, Science 303:210–213, 2004b. https://doi.org/10.1126/science.1090929.

Naveira Garabato, A.C., Stevens, D.P., Watson, A.J., and Roether, W.: Short-circuiting of the overturning circulation in the Antarctic circumpolar current, Nature, 447:194–197, 2007. https://doi.org/10.1038/nature05832.

Naveira Garabato, A.C., Ferrari, R., and Polzin, K.L.: Eddy stirring in the Southern Ocean. Journal of Geophysical Research: Oceans 116: C09019, 2011. https://doi.org/10.1029/2010jc006818.

Naveira Garabato, A.C., Zika, J.D., Jullion, L., Brown, P.J., Holland, P.R., Meredith, M.P., and Bacon, S.: The thermodynamic balance of the Weddell Gyre, Geophysical Research Letters, 43, 317–325, 2016. https://doi.org/10.1002/2015GL066658.

Nowlin Jr., W. D., and J. M. Klinck: The physics of the Antarctic Circumpolar Current, Reviews in Geophysics, 24(3), 469–491, 1986. https://doi.org/10.1029/RG024i003p00469.

Núñez-Riboni, I. and Fahrbach, E.: Seasonal variability of the Antarctic Coastal Current and its driving mechanisms in the Weddell Sea. Deep Sea Research Part I: Oceanographic Research Papers, 56(11), pp.1927-1941, 2009.

Okubo, A.: Oceanic diffusion diagrams. Deep Sea Research and Oceanographic Abstracts, 18:789–802. doi:10.1016/0011-7471(71) 90046-5, 1971.

Orsi, A.H., Nowlin, W.D. Jr, and Whitworth, T. III: On the circulation and stratification of the Weddell gyre, Deep-Sea Research I, 40:169–203, 1993. https://doi.org/10.1016/0967-0637(93)90060-G.

Orsi, A.H., Whitworth, T. III, and Nowlin, W.D. Jr: On the meridional extent and fronts of the Antarctic circumpolar current. Deep-Sea Research I, 42:641–673, 1995. https://doi.org/10.1016/0967-0637(95) 00021-W.

Orsi, A. H., Johnson, G. C., and Bullister, J. L.: Circulation, mixing, and production of antarctic bottom water, Progress in Oceanography, 43, 55-109, 1999. https://doi.org/10.1016/S0079-6611(99)00004-X.

Orsi, A. H., Smethie, W. M. and Bullister, J. L.: On the total input of Antarctic waters to the deep ocean: A preliminary estimate from chlorofluorocarbon measurements', Journal of Geophysical Research: Oceans, 107(C8), pp. 31-1-31-14, 2002.

Orsi., A. H., Whitworth, III., T.: Hydrographic Atlas of the World Ocean Circulation Experiment (WOCE). Volume 1: Southern Ocean (eds. M. Sparrow, P. Chapman and J. Gould), International WOCE Project Office, Southampton, U.K., ISBN 0-904175-49-9. 2005.

Owens, W. B., and Wong, A. P. S.: An improved calibration method for the drift of the conductivity sensor on autonomous ctd profiling floats by θ–s climatology, Deep Sea Research Part I: Oceanographic Research Papers, 56, 450-457, 2009. http://dx.doi.org/10.1016/j.dsr.2008.09.008.

Paolo, F. S., H. A. Fricker, and L. Padman: Volume loss from Antarctic ice shelves is accelerating, Science, 348(6232), 327–331, 2015.

Park, J. J., Kim, K. and Crawford, W. R.: Inertial currents estimated from surface trajectories of ARGO floats, Geophysical Research Letters, 31(13), 2004.

Park, J. J., Kim, K., King, B. A. and Riser, S. C.: An Advanced Method to Estimate Deep Currents from Profiling Floats, Journal of Atmospheric and Oceanic Technology, 22(8), pp. 1294-1304, 2005.

Park, Y.-H., F. Vivier, F. Roquet, and E. Kestenare: Direct observations of the ACC transport across the Kerguelen Plateau, Geophysical Research Letters, 36, L18603, 2009. https://doi.org/10.1029/2009GL039617.

Peña-Molino, B., S. R. Rintoul, and M. R. Mazloff: Barotropic and baroclinic contributions to along-stream and across-stream transport in the Antarctic Circumpolar Current, Journal of Geophysical Research: Oceans, 119, 8011–8028, 2014. https://doi.org/10.1002/2014JC010020.

Pollard, R. T. and Regier, L. A.: Vorticity and Vertical Circulation at an Ocean Front, Journal of Physical Oceanography, 22(6), pp. 609-625, 1992.

Polzin, K.L., Toole, J.M., Ledwell, J.R., and Schmitt, R.W.: Spatial variability of turbulent mixing in the abyssal ocean. Science 276:93–96, 1997. https://doi.org/10. 1126/science.276.5309.93.

Purkey, S. G. and Johnson, G. C.: Global Contraction of Antarctic Bottom Water between the 1980s and 2000s, Journal of Climate, 25(17), pp. 5830-5844, 2012.

Purkey, S. G. and Johnson, G. C.: Antarctic Bottom Water Warming and Freshening: Contributions to Sea Level Rise, Ocean Freshwater Budgets, and Global Heat Gain', Journal of Climate, 26(16), pp. 6105-6122, 2013.

Rabe, B., Karcher, M., Schauer, U., Toole, J. M., Krishfield, R. A., Pisarev, S., Kauker, F., Gerdes, R., and Kikuchi, T.: An assessment of arctic ocean freshwater content changes from the 1990s to the 2006–2008 period, Deep Sea Research Part I: Oceanographic Research Papers, 58, 173-185, 2011. http://dx.doi.org/10.1016/j.dsr.2010.12.002.

Rahmstorf, S., Thermohaline Circulation: the current climate, Nature, 421, 699, 2003. https://doi.org/10.1038/421699a.

Reeve, K. A., Boebel, O., Kanzow, T., Strass, V., Rohardt, G. and Fahrbach, E.: A gridded data set of upper-ocean hydrographic properties in the Weddell Gyre obtained by objective mapping of Argo float measurements, Earth System Science Data, 8(1), pp. 15-40, 2016.

Rhein, M., S.R. Rintoul, S. Aoki, E. Campos, D. Chambers, R.A. Feely, S. Gulev, G.C. Johnson, S.A. Josey, A. Kostianoy, C. Mauritzen, D. Roemmich, L.D. Talley and F. Wang: Observations: Ocean. In: Climate Change 2013: The Physical Science Basis. Contribution of Working Group I to the Fifth Assessment Report of the Intergovernmental Panel on Climate Change [Stocker, T.F., D. Qin, G.-K. Plattner, M. Tignor, S.K. Allen, J. Boschung, A. Nauels, Y. Xia, V. Bex and P.M. Midgley (eds.)]. Cambridge University Press, Cambridge, United Kingdom and New York, NY, USA, 2013.

Rignot, E., S. Jacobs, J. Mouginot, and B. Scheuchl: Ice-shelf melting around Antarctica, Science, 341(6143), 266–270, 2013. https://doi.org/10.1126/science.1235798.

Rintoul, S., Hughes, C. & Olbers, D.: The Antarctic Circumpolar Current system. International Geophysics. 77, 2001. https://doi.org/10.1016/S0074-6142(01)80124-8.

Roemmich, D., Gilson, J., Willis, J., Sutton, P., and Ridgway, K.: Closing the Time-Varying Mass and Heat Budgets for Large Ocean Areas: The Tasman Box. Journal of Climate, 18, 2330–2343, 2005. https://doi.org/10.1175/JCLI3409.1.

Roemmich, D., and Gilson, J.: The 2004–2008 mean and annual cycle of temperature, salinity, and steric height in the global ocean from the argo program, Progress in Oceanography, 82, 81-100, 2009. http://dx.doi.org/10.1016/j.pocean.2009.03.004.

Ryan, S., Schröder, M., Huhn, O. and Timmermann, R.: On the warm inflow at the eastern boundary of the Weddell Gyre. Deep Sea Research Part I: Oceanographic Research Papers, 107, pp.70-81, 2016.

Ryan, S., Hattermann, T., Darelius, E. and Schröder, M.: Seasonal cycle of hydrography on the eastern shelf of the Filchner Trough, Weddell Sea, Antarctica. Journal of Geophysical Research: Oceans, 2017.

Rye, C. D., Naveira Garabato, A. C., Holland, P. R., Meredith, M. P., Nurser, A. J. G., Hughes, C. W., et al.: Rapid sea-level rise along the Antarctic margins in response to increased glacial discharge. Nature Geoscience, 7(10), 732–735, 2014. https://doi.org/10.1038/ngeo2230

Saenko, O.A., Gregory, J.M., Weaver, A.J. and Eby, M.: Distinguishing the influence of heat, freshwater, and momentum fluxes on ocean circulation and climate. Journal of Climate, 15(24), pp.3686-3697, 2002.

Sandström, J.W.: Meteorologische Studien im Schwedischen Hochgebirge, Göteborgs K. Vetensk. Vitterhetssamhällets Handkl., 27, 48 pp, 1916.

Sarmiento, J.L., Gruber, N., Brzezinski, M.A., Dunner, J.P.: High-latitude controls of thermocline nutrients and low latitude biological productivity, Nature, vol. 427, pages 56–60, 2004.

Schmidtko, S., Heywood, K.J., Thompson, A.F. and Aoki, S.: Multidecadal warming of Antarctic waters. Science, 346(6214), pp.1227-1231, 2014.

Schodlok, M.P., Hellmer, H.H. and Beckmann, A.: On the transport, variability and origin of dense water masses crossing the South Scotia Ridge. Deep Sea Research Part II: Topical Studies in Oceanography, 49(21), pp.4807-4825, 2002.

Schröder, M. and Fahrbach, E.: On the structure and the transport of the eastern Weddell Gyre. Deep Sea Research Part II: Topical Studies in Oceanography, 46(1-2), pp.501-527, 1999.

Schwerdfeger, W.: The climate of the Antarctic. In: Landsberg, H.E. (Ed.), Climates of the Polar Regions. World Survey of Climatology. Elsevier, Amsterdam, pp. 255–355, 1970.

Sloyan, B.M. and S.R. Rintoul, 2001: The Southern Ocean Limb of the Global Deep Overturning Circulation. Journal of Physical Oceanography, 31, 143–173, 2001. https://doi.org/10.1175/1520-0485.

Smith, D.A., Hofmann, E.E., Klinck, J.M., Lascara, C.M.: Hydrography and circulation of the West Antarctic Peninsula Continental Shelf, Deep-Sea Research I, Vol. 46, 925-949, 1999.

Sterl, A.: On the impact of gap-filling algorithms on variability patterns of reconstracted oceanic surface fields. Geophysical Research Letters, 28, N12, p.2473-476., 2001.

von Schuckmann, K., and Le Traon, P. Y.: How well can we derive global ocean indicators from argo data?, Ocean Science, 7, 783-791, 10.5194/os-7-783-2011, 2011.

de Steur, L., Holland, D.M., Muench, R.D. and McPhee, M.G.: The warm-water "Halo" around Maud Rise: Properties, dynamics and impact. Deep Sea Research Part I: Oceanographic Research Papers, 54(6), pp.871-896, 2007.

Stewart, A. L., & Thompson, A. F.: Eddy generation and jet formation via dense water outflows across the Antarctic continental slope. Journal of Physical Oceanography, 46(12), 3729–3750, 2016.

Stewart, A. L., Klocker, A., & Menemenlis, D.: Circum-Antarctic shoreward heat transport derived from an eddy- and tide-resolving simulation. Geophysical Research Letters, 45, 834–845, 2018. https://doi.org/10.1002/2017GL075677.

Stoessel, A.: The Impact of Southern Ocean Sea Ice on the Mean State and Variability of a Global Ocean Model. World Meteorological Organization-Publications-Wmo Td, pp.258-260, 1998.

Talley, L. D.: Closure of the Global Overturning Circulation Through the Indian, Pacific, and Southern Oceans: Schematics and Transports. Oceanography, 2013.

Tamsitt, V., Talley, L.D., Mazloff, M.R., and Cerovecki, I.: Zonal Variations in the Southern Ocean heat budget, Journal of Climate, 29, 6563-6579, 2016. https://doi.org/10.1175/JCLI-D-15-0630.1.

Tamsitt, V., Drake, H.F., Morrison, A.K., Talley, L.D., Dufour, C.O., Gray, A.R., Griffies, S.M., Mazloff, M.R., Sarmiento, J.L., Wang, J. and Weijer, W.: Spiraling pathways of global deep waters to the surface of the Southern Ocean. Nature communications, 8(1), p.172, 2017.

Taylor, H. W., A. L. Gordon, and E. Molinelli: Climatic characteristics of the Antarctic Polar Zone. Jounral of Geophysical Research, 83, 4572–4578, 1978.

Thompson, D.W. and Solomon, S.: Interpretation of recent Southern Hemisphere climate change. Science, 296(5569), pp.895-899, 2002.

Thompson, A. F. and Heywood, K. J.: Frontal structure and transport in the northwestern Weddell Sea, Deep Sea Research Part I: Oceanographic Research Papers, 55(10), pp. 1229-1251, 2008.

Thompson, A., Salleé, J.B.: Jets and topography: Jet transitions and the impact on transport in the Antarctic Circumpolar Current, Journal of Physical Oceanography, 42, 956-972, 2012.

Timmermann, R., and H. H. Hellmer: Southern Ocean warming and increased ice shelf basal melting in the twenty-first and twenty-second centuries based on coupled ice-ocean finite-element modelling, Ocean Dynamics, 63(9–10), 1011–1026, 2013. https://doi.org/10.1007/s10236-013-0642-0.

Toggweiler, J. R., and B. Samuels: Effect of Drake Passage on the global thermohaline circulation, Deep Sea Research, Part I, 42, 477–500, 1995.

Toole, J.M., Schmitt, R.W. and Polzin, K.L.: Estimates of diapycnal mixing in the abyssal ocean. Science, 264(5162), pp.1120-1123, 1994.

Turner, J., Phillips, T., Marshall, G.J., Hosking, J.S., Pope, J.O., Bracegirdle, T.J. and Deb, P.: Unprecedented springtime retreat of Antarctic sea ice in 2016. Geophysical Research Letters, 44(13), pp.6868-6875, 2017.

Venegas, S.A. and Drinkwater, M.R.: Sea ice, atmosphere and upper ocean variability in the Weddell Sea, Antarctica. Journal of Geophysical Research: Oceans, 106(C8), pp.16747-16765, 2001.

Volkov, D.L., Fu, LL. and Lee, T.: Mechanisms of the meridional heat transport in the Southern Ocean, Ocean Dynamics 60(4): 791-801, 2010. https://doi.org/10.1007/s10236-010-0288-0.

Wang, Q., Danilov, S., Sidorenko, D., Timmermann, R., Wekerle, C., Wang, X., Jung, T., and Schröter, J.: The Finite Element Sea Ice-Ocean Model (FESOM) v.1.4: formulation of an ocean general circulation model, Geosciences Model Development, 7, 663-693, 2014 https://doi.org/10.5194/gmd-7-663-2014.

Whitworth, T. and Nowlin, W.D.: Water masses and currents of the Southern Ocean at the Greenwich Meridian. Journal of Geophysical Research: Oceans, 92(C6), pp.6462-6476, 1987.

Whitworth, T.III, A. H. Orsi, S.-J. Kim, and W. D. Nowlin Jr.: Water masses and mixing near the Antarctic Slope Front, in Ocean, Ice, and Atmosphere: Interactions at the Antarctic Continental Margin, Antarctic Research Ser., vol. 75, edited by S. S. Jacobs, and R. F. Weiss, pp. 1–27, AGU, Washington, D. C, 1998.

Wong, A. P. S., Johnson, G. C., and Owens, W. B.: Delayed-mode calibration of autonomous ctd profiling float salinity data by θ–s climatology, Journal of Atmospheric and Oceanic Technology, 20, 308-318, 20013. https://doi.org/10.1175/1520-0426(2003)020<0308:dmcoac>2.0.co;2.

Yaremchuk, M., Nechaev, D., Schroter, J., Fahrbach, E: A dynamically consistent analysis of circulation and transports in the southwestern Weddell Sea', Annales Geophysicae, 16, 1024-1038, 1998.

Zenk, W. and Morozov, E.: Decadal warming of the coldest Antarctic Bottom Water flow through the Vema Channel. Geophysical Research Letters, 34(14), 2007.

Zheng, F., Li, J., Clark, R.T. and Nnamchi, H.C.: Simulation and Projection of the Southern Hemisphere Annular Mode in CMIP5 Models. Journal of Climate, 26, 9860–9879, 2013. https://doi.org/10.1175/JCLI-D-13-00204.1.

Zhou, Q., Hattermann, T., Nøst, O.A., Biuw, M., Kovacs, K.M. and Lydersen, C.: Wind-driven spreading of fresh surface water beneath ice shelves in the Eastern Weddell Sea. Journal of Geophysical Research: Oceans, 119(6), pp.3818-3833, 2014.

Zika, J.D., Sloyan, B.M. and McDougall, T.J: Diagnosing the Southern Ocean overturning from tracer fields. Journal of Physical Oceanography, 39(11), pp.2926-2940, 2009.

Zwally, H. J., Comiso, J. C. and Gordon, A. L.: Antarctic Offshore Leads and Polynyas and Oceanographic Effects. In Oceanology of the Antarctic Continental Shelf, S. S. Jacobs (Ed.), 2013. https://doi.org/10.1029/AR043p0203

Zweng, M. M., Reagan, J. R., Antonov, J. I., Locarnini, R. A., Mishonov, A. V., Boyer, T. P., Garcia, H. E., Baranova, O. K., Johnson, D. R., Seidov, D. and Biddle, M. M.: World Ocean Atlas 2013. Vol. 2: Salinity. S. Levitus, Ed., NOAA Atlas NESDIS 74, 39 pp., 2013.

8 Acknowledgements

As a child, whenever something would go wrong, my dad would say to me, “it is what it is”. It was only in my adult years that I came to appreciate what this means. “It is what it is”, means that when things go wrong that are beyond your control, you need to accept them in order to be able to move forwards, because, after all, it is what it is. This motto has helped me through the challenges of my PhD, which would not have been possible without the unfailing support of colleagues, friends and family, to whom I am forever grateful.

I will start by thanking a pioneering researcher who is sadly no longer with us today, but who is the very reason I moved to Germany to embark upon a career in polar ocean research. This work is dedicated to the memory of Eberhard Fahrbach, who was always kind and caring to me. The last thing that Eberhard ever said to me was that it was his hope that I would become the Argo lady of the Weddell Gyre. I hope that this thesis would have done him proud.

The next person I must thank is Olaf Boebel, whose door was open to me during a time when I was in a state of despair, who listened to me and showed interest in my work, and who set upon re-building my confidence step by step. Thank you for your support, for listening to me, and most of all, for your patience.

My deepest gratitude is extended towards Torsten Kanzow, who has provided incredible support over the years, and would always go above and beyond to give me his invaluable time, and to provide advice, guidance and feedback to help me through the challenges always knocking at my door. You have helped me to overcome so much, both on an academic and personal level, and I will always be thankful to you for it.

Next, a special thank you goes to Rüdiger Gerdes and Volker Strass, who have never faltered in their support of me, whom I could always rely on for feedback, and for precious problem-solving discussions. Hartmut Hellmer and Ralf Timmermann also deserve special mention, for their encouragement and interest in my research, helping me to find my confidence. Thank you to Laurenz Thomsen and Andreas Muenchow, for sportingly agreeing to be committee members for this thesis.

A big shout out goes to all the colleagues in the oceanography work group at AWI, especially my fellow PhD students, who have always been kind and empathetic towards me, with a smile and general attitude of good humour, especially my old office buddies, Svenja and Janin, thank you for tolerating my madness!

Last but not least, I would like to thank my family and friends for putting up with me over these last few years. Thank you to Paul Gierz and to my hero cabin buddy Caro Hauer, for always being there for me, whether it’s to help with German paperwork, visiting me in hospital (AGAIN!), or spending time with me over a drink. This also extends to my flatmates who have endured my madness over the years, especially Jude and Magni, who have been there for me through thick and thin, and always ready to point out the humour in any situation I somehow found myself in. I would also like to thank my sister in heart if not blood, Lys. We have been through so much together, and you have always been there for me, whether it’s to vent, to laugh, to cry or to breath fire. I probably would not have survived without all of you, or at the very least I’d be missing a few limbs or organs, and my sanity…

I am grateful to my parents, who, from as early as I can remember have encouraged me to pursue anything that interested me, whether it was to dress up in a bin bag and pretend I'm a wicked witch, or to be the next David Attenborough while watching the Little Mermaid on repeat. Thank you to my sister, who has been there, always, and provided a source of comfort, understanding, and an ear to rant and rage to.

And lastly, to my rock, to my James, a thousand times thank you. For everything.